

Development of FAIR-Relevant X-Ray Diagnostics Based on the Interaction of Lasers and Particle Beams with Matter

Dissertation
zur Erlangung des Doktorgrades
der Naturwissenschaften

vorgelegt beim Fachbereich Physik
der Johann Wolfgang Goethe - Universität
in Frankfurt am Main

von
Şero Jakob Zähler
aus Frankfurt am Main

Frankfurt 2020
(D 30)

vom Fachbereich Physik der
Johann Wolfgang Goethe - Universität als Dissertation angenommen.

Dekan: Prof. Dr. Michael Lang
Gutachter: Apl. Prof. Dr. Olga Rosmej
Prof. Dr. Joachim Jacoby
Datum der Disputation: 22.09.2020

“Everything you desire is outside your comfort zone - otherwise, you would already have it.”

Zan Perrion

Abstract

This Dissertation deals with the development of FAIR-relevant X-ray diagnostics based on the interaction of lasers and particle beams with matter. The associated experimental methods are supposed to be employed in the HIHEX-experiments in the HHT-cave of the GSI Helmholtz Center for Heavy-Ion Research GmbH (GSI) in Phase-0 and in the APPA-cave at the Facility for Antiproton and Ion Research in Darmstadt, Germany.

Diagnostic of high aerial density targets that will be used in FAIR experiments demands intense and highly penetrating X-ray sources. Laser generated well-directed relativistic electron beams that interact with high Z materials is an excellent tool for generation of short-pulse high luminous sources of MeV-gammas.

In pilot experiments carried out at the PHELIX laser system, GSI Darmstadt, relativistic electrons were produced in a long scale plasma of near critical electron density (NCD) by the mechanism of the direct laser acceleration (DLA). Low density polymer foam layers preionised by a well-defined nanosecond laser pulse were used as NCD targets. The analysis of the measured electron spectra showed up to 10-fold increase of the electron "temperature" from $T_{Hot} = 1-2$ MeV, measured for the case of the interaction of $1-2 \times 10^{19} \text{ W cm}^{-2}$ ps-laser pulse with a planar foil, up to 14 MeV for the case when the relativistic laser pulse propagates through the by a ns-pulse preionised foam layer. In this case, up to 80-90 MeV electron energy was registered. An increase of the electron energy was accompanied by a strong increase of the number of relativistic electrons and well-defined directionality of the relativistic electron beam measured to be $12 \pm 1^\circ$ (FWHM). This directionality increases the gamma flux on target by far compared to the soft X-ray sources.

Additionally to laser based active diagnostics, passive techniques involving inherent X-ray fluorescence radiation of projectile and target emitted during heavy-ion target interaction can be used to measure the ion beam distribution on shot. This information is of great importance, since the target size is chosen to be smaller than the beam focus in order to ensure homogeneous heating of the HIHEX-target by the ion beam. High amounts of parasitic radiation and activation of experimental equipment is expected for experiments at the APPA-cave. For this reason, all electronic devices must be placed at a safe distance to the target chamber. In order to transport the signal over a large distance, the X-ray image of the target irradiated by heavy-ions has to be converted into an optical one.

For these purposes, the X-ray Conversion to Optical radiation and Transport (XCOT)-system was developed in the frame of a BMBF-project and commissioned in two beamtimes at the UNILAC, GSI during this work.

In experiments, we observed intense radiation of target atoms (K-shell transitions in Cu at 8–8.3 keV and L-shell transition in Ta) ionised in collisions with heavy ions as well as Doppler-shifted L-shell transitions of Au-projectiles passing through targets. This radiation can be used for monochromatic (dispersive elements like bent crystals) or polychromatic (pinhole) 2D X-ray mapping of the ion beam intensity distribution in the interaction region during the beam-target interaction. We measured the efficiency of the X-ray photon production depending on the target thickness and the number of ions passing through the target. The spatial resolution of the XCOT-system based on the multi-pinhole camera was measured to be $91 \pm 17 \mu\text{m}$ for the image magnification factor $M = 2$. It was considerably improved by application of a toroidally bent quartz crystal and reached $30 \mu\text{m}$ at $M = 6$. This resolution is optimal to image the distribution of a 1 mm in diameter ion beam. As next step, the XCOT-system will be tested during the SIS18 beam-time at the HHT-experimental area.

Zusammenfassung

Diese Dissertation beschäftigt sich mit der Entwicklung von FAIR-relevanten Röntgendiagnostiken basierend auf der Interaktion von Lasern und Teilchenstrahlen mit Materie. Die damit im Zusammenhang stehenden experimentellen Methoden sollen in zukünftigen Experimenten im HHT-Cave des GSI Helmholtzzentrums für Schwerionenforschung GmbH (Gesellschaft für Schwerionenforschung (GSI)), Darmstadt in Phase-0 und später im APPA-cave an FAIR (Anlage für Antiprotonen- und Ionenforschung, Englisch: Facility for Antiproton and Ion Research) zum Einsatz kommen. Sie können aber auch in anderen Forschungsbereichen von Interesse sein.

0.1 Laser Generierte Ultrarelativistische Elektronen

Unsere Experimente wurden an der Nd:Glass Petawatt Hochenergielaser für Schwerionenexperimente (PHELIX) Anlage am GSI Helmholtzzentrum für Schwerionenforschung GmbH in Darmstadt durchgeführt. Elektromagnetische (EM) Strahlung, die auf ein Plasma trifft, kann entweder absorbiert (Laserfrequenz entspricht Plasmafrequenz), reflektiert (Laserfrequenz unterhalb Plasmafrequenz) oder transmittiert (Laserfrequenz oberhalb Plasmafrequenz) werden. Die Elektronendichte, bei der die Plasmafrequenz der Laserfrequenz entspricht, wird kritische Dichte genannt ($n_e = 10^{21} \text{ cm}^{-3}$ bei 1053 nm Laserwellenlänge für PHELIX). Ein Laser wird deshalb an einem Plasma oberhalb der kritischen Dichte reflektiert. In Plasmen nahe der kritischen Dichte (Englisch: Near critical density, NCD) kann der Laser propagieren und effizient Energie an die Elektronen des Plasmas übertragen. Die Erzeugung von NCD Plasmen erweist sich als herausforderung. Die Wechselwirkung relativistischer Laserpulse mit durch ns-Laserpulsen vorionisierten Folien führen zu einem effizienten Beschleunigungsprozess auf Strecken von 10–30 μm . Der auf das unterkritische Plasma treffende Laser erzeugt durch seine Intensitätsverteilung und die damit zusammenhängende ponderomotorische Kraft (Elektronen wandern im zeitlichen Mittel zu geringeren Intensitäten) Elektronen mit relativistischen kinetischen Energien. Um die Beschleunigungsstrecke von 10–30 μm auf einige 100 μm zu erhöhen und bessere Bedingungen für den Mechanismus der direkten Laserbeschleunigung (Englisch: direct laser acceleration (DLA)) zu schaffen, haben wir die Interaktion von relativistischen Laserpulsen mit sub-mm langen vorionisierten Schaumtargets (2 mg cm^{-3} Triacetat Cellulose (TAC), $n_e = 7 \times 10^{20} \text{ cm}^{-3}$) vorgeschlagen. Wir haben im Experiment gezeigt, dass die Verwendung von Schaumtargets eine effiziente Konversion der Laserenergie in relativistische Elektronenstrahlen liefert und damit die Energie der

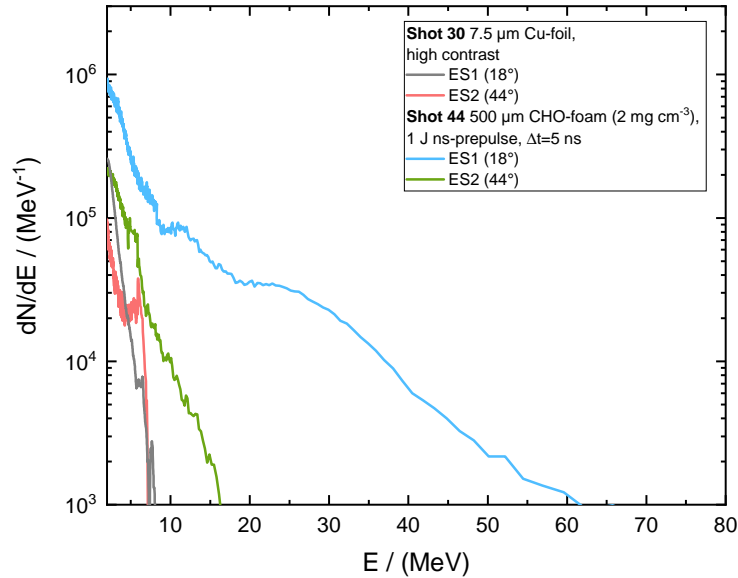


FIGURE 1: Elektronen Energieverteilung für verschiedene Targettypen bei gleichen Laserparametern: Cu-Folie (Shot 30) und 500 μm TAC-Schaum (Shot 44). Elektronenspektrometer bei 18° (ES1) and 44° (ES2) platziert. Die Spektrometer haben einen Raumwinkel von $\Omega = 1.5 \times 10^{-5}$ sr abgedeckt.

Elektronen erhöht. Der Laserpuls erzeugt durch die ponderomotorische Kraft einen Kanal geringerer Elektronendichte im Plasma. Der Laserpuls kann durch den Elektronendichtegradienten im Kanal weiter fokussiert werden. Wenn die Größe des Laserfokuses viel größer als die Eindringtiefe im Plasma ist, dann filamentiert dieser Kanal zu einer Reihe kleinerer Kanäle. Die Übertragung der Energie des Lasers auf die Elektronen im Kanal geschieht unter Gegenwart von quasistatischen E- (erzeugt von den Kanalelektronen) und B-Feldern (erzeugt von den beschleunigten Elektronen), die zusätzlich zum Laserfeld auf die beschleunigten Elektronen wirken und sie im Kanal einschließen. Ein im Kanal gefangenes relativistisches Elektron erfährt Betatronoszillationen und gewinnt effizient Energie vom Laserpuls wenn die Frequenz der Betatronoszillationen in Resonanz mit der Dopplerverschobenen Frequenz des Laserpulses ist. Elektronen, die mit dem E-Feld des Lasers kopropagieren, erhalten Energie durch das E-Feld des Lasers und werden von den vorhandenen B-Feldern in Vorwärtsrichtung umgelenkt. Dieser Mechanismus wird DLA genannt. Charakteristische Eigenschaften dieser Elektronenstrahlen sind ihre hohen Energien von bis zu 100 MeV für relativ moderate Intensitäten bis zu $5 \times 10^{19} \text{ W cm}^{-2}$ im Vergleich zu 10–15 MeV bei Schüssen auf Standardfolien sowie eine große Anzahl von Elektronen (einige zehn nC) und eine starke Richtungsabhängigkeit. Das Spektrum der so erzeugten relativistischen Elektronen ähnelt einer Maxwell-Boltzmann-Verteilung (siehe Fig. 1). Dadurch lässt sich eine Art Elektronentemperatur definieren. In Schüssen auf Folien liefert die ponderomotorische Kraft Temperaturen von 1–2 MeV.

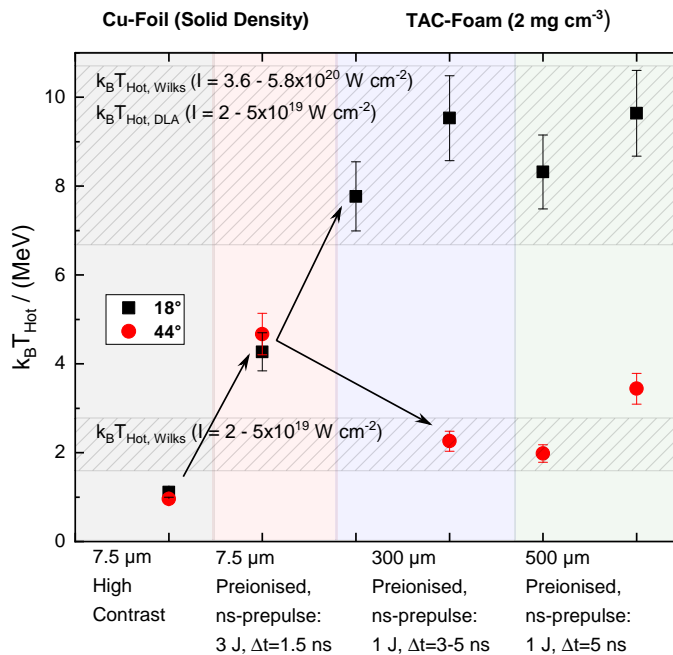


FIGURE 2: Vergleich der experimentellen Ergebnisse aus Fig. 4.9, Fig. 4.10 und Fig. 4.11 mit den theoretischen Werten aus dem Diagramm gezeigt in Fig. 4.12.

Durch DLA messen wir eine weitere Temperatur, die bis zu einem Faktor 10 (10 MeV) über der ponderomotorischen Temperatur liegt. Solche Elektronen werden als superponderomotorisch bezeichnet.

Die Elektronen und Ionen Energieverteilungsmessung wurde unter dem Einsatz von zwei Elektron- ($\approx 18 \pm 1^\circ$ und $\approx 44 \pm 1^\circ$) und zwei Ionenspektrometern ($\approx 29 \pm 1^\circ$ und $\approx 52 \pm 1^\circ$) mit statischen Magnetfeldern durchgeführt. Eine ortsauflösende Zylinderdiagnostik wurde verwendet um die Winkelverteilung von Elektronen zu messen. Absolut kalibrierte Imaging Plate (IP, Deutsch: Bildplatte) Detektoren kamen in beiden Diagnostiken zum Einsatz. IPs sind eine Art wiederverwendbarer Film zum Nachweis von hochenergetischen Teilchen und Photonen. Diese Ergebnisse sind zum Vergleich in Fig. 2 zusammengefasst. Die Messung der emittierten relativistischen Elektronen in Schüssen mit hohem Laserkontrast auf Folientargets unter zwei Winkeln zeigt, dass die Temperaturen gleich sind. Eine Erhöhung der Temperaturen in Schüssen auf vorionisierte Folientargets wird erreicht. Diese Temperaturen liegen zwischen den Messwerten für ponderomotorische und superponderomotorische Elektronen. Die Einführung von CHO-Schäumen als Targets erhöht die Temperatur von in Vorwärtsrichtung beschleunigten Elektronen gemäß den theoretischen Vorhersagen für DLA weiter, während die Temperatur für Elektronen bei großen Winkeln zur Laser Propagationsrichtung den Vorhersagen für ponderomotorische Beschleunigung entspricht. Diese Beobachtung unterstützt klar die Vorhersage einer Richtungsabhängigkeit von superponderomotorischen Elektronen die in NCD Plasmen erzeugt wurden. Erste Abbildungen von Radiographie-Proben wurden aufgenommen.

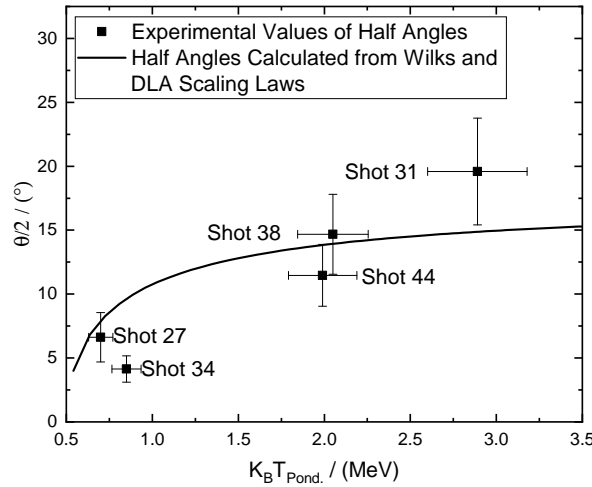


FIGURE 3: Halbwinkel für Schüsse auf unterschiedliche vorionisierte Targetsorten berechnet aus den Werten der Temperaturdaten in Tab. 4.1 in Abhängigkeit der Werte des ponderomotorischen Teils des Spektrums. Die durchgezogene Linie deutet die Halbwinkel, berechnet aus den ponderomotorischen und dem DLA Skalierungsgesetzen an.

Das Experiment wurde von 3D-Particle in Cell (PIC)-Simulationen unterstützt, welche die verwendeten Laserparameter und die Geometrie des experimentellen Aufbaus berücksichtigten. Die Abschätzung der absoluten Anzahl der Elektronen, ihre Energie- und Winkelverteilung sind in guter Übereinstimmung mit den experimentellen Ergebnissen.

Der Emissionswinkel der ultrarelativistischen Elektronen kann mit Hilfe der relativistischen Energie-Impuls-Beziehung (siehe. Gl. 4.1) und den Daten aus Fig. 2 abgeschätzt werden. Fig. 3 zeigt diese Halbwinkel im Vergleich zu theoretischen Werten, berechnet aus ponderomotorischen und DLA Vorhersagen. Die so berechneten Werte liefern Halbwinkel bis zu 20° . Wobei die meisten Werte im Bereich von $5\text{--}15^\circ$ liegen. Dies entspricht den Werten, die mit der Zylinderdiagnostik erhalten wurden. Es wurde mit der Zylinderdiagnostik ebenfalls die Entstehung von filamentierenden Kanälen innerhalb des Plasmas beobachtet. Die Ausgänge dieser Kanäle lagen sowohl in horizontaler als auch in vertikaler Richtung bis zu 30° voneinander entfernt, während ihre Halbwinkel kleiner als 10° blieben.

Fig. 4 (a) zeigt die Elektronenverteilung für einen Schuss mit hohem Laserkontrast auf eine Au-Folie von Dicke $10\ \mu\text{m}$. Das Signallevel ändert sich über einen Bereich von 30° (vertikal und horizontal) nur um einen Faktor zwei. Es ist keine Vorzugsrichtung des Signals zu erkennen. Das Signal eines Schusses auf einen CHO-Schaum von $300\ \mu\text{m}$ Dicke plus eine $10\ \mu\text{m}$ dicke Goldfolie die als Radiator fungiert zeigt eine starke Richtungsabhängigkeit des Signals (siehe Fig. 4 (b)). GEANT4 Simulationen deuten darauf hin, dass das von den Elektronen erzeugte Signal, eine Größenordnung größer als das der Gammas ist. Daher ist die Inhomogenität der Winkelverteilung

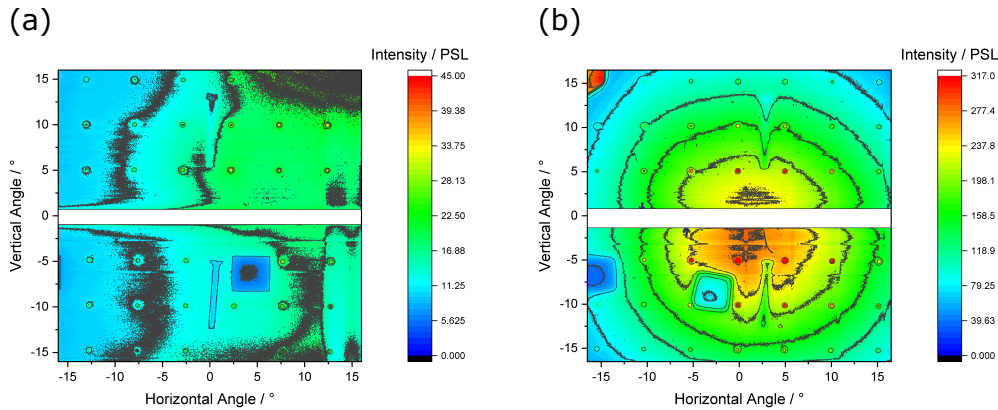


FIGURE 4: Verteilung von Elektronen für einen Schuss auf (a) eine Goldfolie von Dicke $10\ \mu\text{m}$ und (b) auf einen CHO-Schaum von $300\ \mu\text{m}$ Dicke plus eine $10\ \mu\text{m}$ dicke Goldfolie die als Radiator fungiert. Die Punkte zeigen die Löcher, die in den Stahlzylinder gebohrt wurden.

von Elektronen stets sichtbar.

Verschiedene Forschungsfelder werden durch diese ersten Experimente zur Erzeugung von ultrarelativistischen Elektronen in unterkritischen Plasmen an der PHELIX-Anlage eröffnet. Phasenkontrast-Abbildungstechniken könnten von der Betatronstrahlung profitieren, die von den durch die Laserfelder innerhalb der Laserkanäle zur Oszillation angeregten Elektronen erzeugt wird. Lasererzeugte relativistische Elektronenstrahlen können hervorragend zur Erzeugung von ultrakurzen MeV-Gamma- und Neutronenquellen, THz- und Betatronstrahlung verwendet werden. Bei gut gerichteten Hochstromstrahlen relativistischer Elektronen kann man eine extrem hohe Brillianz der sekundären Laserquellen erreichen und diese für radiographische Anwendungen, zur laserbasierten Kernphysik und zur Herstellung von Radioisotopen für die Nuklearmedizin verwenden.

0.2 Röntgenfluoreszenz von Target und Schwerionenstrahl

Die Ionenstrahlintensitätsverteilung ist ein wichtiger Inputparameter für numerische Simulationen der hydrodynamischen Antwort des HIHEX-Targets auf die vom Ionenstrahl deponierte Energie. Zusätzlich muss sichergestellt werden, dass das Target isochor geheizt wird, damit Dichte und Volumen statische Parameter bleiben. Das ist der Fall, wenn es sich während der Schwerionenstrahl-Target-Wechselwirkung nicht beginnt auszudehnen, sondern erst, wenn die Energie deponiert ist. Wenn ein hydrodynamischen Verhalten doch schon während der Wechselwirkung auftritt, dann können wir das mit Hilfe der Röntgenfluoreszenz Messungen registrieren. Das Ziel des durchgeführten Experiments war die Untersuchung der möglichen Nutzung von Projektil- und Targetröntgenfluoreszenz zur on Shot Diagnostik der Ionenstrahlintensitätsverteilung auf dem HIHEX-Target und der Energiedeposition. Unsere Testexperimente wurden an der Universal Linear Accelerator (UNILAC)-Anlage des GSI

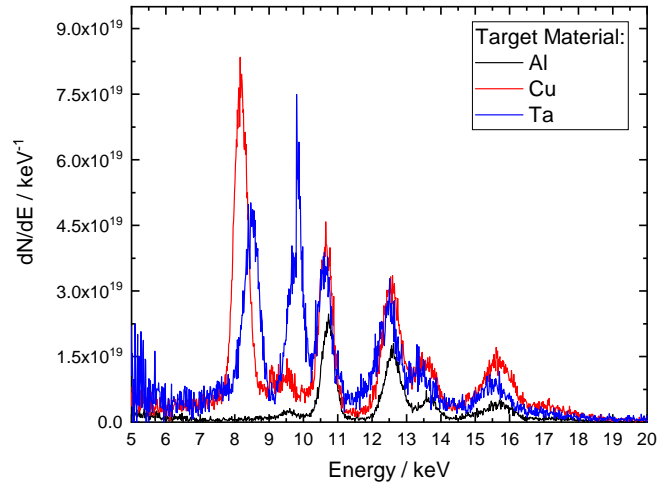


FIGURE 5: Mit dem CdTe-Spektrometer gemessenes Spektrum. Spektrale Auflösung ungefähr 1 keV. Eine Anzahl von 6.2×10^{13} Au^{26+} -Ionen passierten die Folie, was die Ionen weiter zu Au^{50+} strippte. Das Spektrum wurde auf die Anzahl der Röntgenfluoreszenzphotonen in 4π sr pro keV, pro C von Au^{50+} -Ionen und pro μm der Targetdicke normiert.

Helmholtzzentrums für Schwerionenforschung GmbH in Darmstadt durchgeführt. Weiteres Ziel ist es, diese Diagnostik an den SIS18 Experimenten während Phase-0 im APPA-cave einzusetzen.

Die Interaktion eines $6.5 \text{ MeV/u Au}^{26+}$ -Strahls mit Folientargets verschiedener Materialien (Al, Cu, Ta) mit Dicken von $6\text{--}10 \mu\text{m}$ erlaubte es Röntgenfluoreszenz von Strahl und Targets zu charakterisieren. Röntgenspektren im Bereich von 5 keV bis 20 keV wurden gemessen und die Wechselwirkungszone wurde im Röntgenbereich sowohl polychromatisch als auch monochromatisch abgebildet. Fig. 5 zeigt das Spektrum, dass mit der CdTe-Diode gemessen wurde. Es sind eindeutig unverschobene Linien des Targets und Dopplerverschobene Linien der Strahlionen zu erkennen. Die Dopplerverschiebung hängt vom Beobachtungswinkel und der Energie der Projektionen ab. Dies ermöglichte die Berechnung der Fluoreszenzausbeute von Au L_{α} -Strahlung in 4π sr pro keV, pro C des durch das Target gelaufenen Au-Strahls und pro μm des Targetmaterials (siehe Tab. 1). Deshalb erlauben Röntgenfluoreszenzmessungen die absolute Messung der deponierten Energie innerhalb des Targets in zukünftigen Experimenten während Phase-0 im Hochenergie, Hochtemperatur (HHT) Cave und im Atomphysik, Plasmaphysik und Anwendungen (APPA) Cave an FAIR.

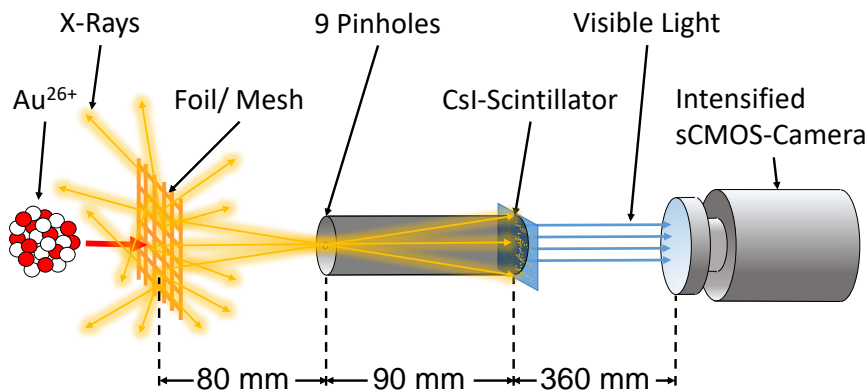


FIGURE 6: Schematische Darstellung des XCOT-Systems. Cu-Gitter werden von einem Au^{26+} -Strahl bestrahlt. Die Cu-Gitter emittieren Röntgenfluoreszenz welche auf einen CsI-Szintillator abgebildet wird. Der Szintillator konvertiert die Röntgenstrahlung in sichtbares Licht. Dieses Licht wird zu einem auf MCPs basierenden Bildverstärker transportiert und von einer sCMOS-Kamera detektiert.

Fluoreszenzausbeute	
Targetmaterial	Au L_{α} -Strahlung in 4π sr / Photonen/C/ μm
Al	1.66×10^{19}
Cu	2.89×10^{19}
Ta	2.05×10^{19}

TABLE 1: Die aus dem Spektrum in Fig. 5 berechnete Fluoreszenzausbeute.

Bei der Wechselwirkung eines $11.4 \text{ MeV/u Au}^{26+}$ -Strahls mit Folientargets und Cu-Gittern von unterschiedlichen Maschenweiten wurde die Anwendung von Röntgenfluoreszenzstrahlung als Diagnostikmethode erforscht und das X-ray Conversion to Optical Radiation (XCOT, Deutsch: Röntgen- Konversion in optische Strahlung und Transport)-System kam zum ersten mal zum Einsatz (siehe Fig. 6). Messungen mit Folientargets ließen uns die Ionenstrahlintensitätsverteilung in der Ebene der Folie abbilden (siehe Fig. 7). Die Verwendung von Multipinholes hat es erlaubt, das Signalintensitätslevel, das Signal-Rausch-Verhältnis und das Kontrast-Rausch-Verhältnis zu verbessern. Es wird erwartet, dass eine Kombination aus gebogenen Kristallen für Abbildungszwecke und dem XCOT-System dies weiter verbessert.

Die Ortsauflösung des XCOT-Systems wurde bestimmt. Die Maschenweite von

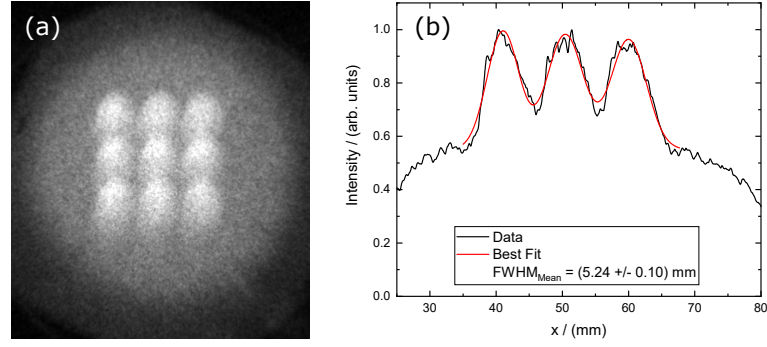


FIGURE 7: (a) Polychromatische Abbildung der Ionenstrahlverteilung auf einer Ta-Folie mit dem XCOT-System mit einer Gesamtexpositionszeit von 3 s. Das entspricht einer Anzahl von 1.2×10^9 Au-Ionen, die die Ta-Folie passieren. Die neun Bilder der selben Verteilung werden von den Multipinholes erzeugt. (b) Lineout in horizontaler Richtung der Integration von drei der Bilder in (a).

60 μm des Cu100-Gitters wurde für diese Abschätzung verwendet. Die Ortsauflösung des XCOT-Systems bei Vergrößerung von $M = 2$ ist mit $91 \pm 17 \mu\text{m}$ ausreichend für die Systemanforderungen von 100 μm . Die Ortsauflösung der monochromatischen Abbildungstechnik mit toroidal gebogenen Kristallen bei einer Vergrößerung von $M = 6$ kann mit wenigstens 30 μm abgeschätzt werden. Fig. 8 zeigt den Vergleich von Abbildungen mit Hilfe des (a) XCOT-Systems, der (b) und (c) toroidal gebogenen Si-Kristalle und (d) der Kombination des XCOT-Systems mit Kristall (Vergrößerung von $M = 7.5$). Der Unterschied zwischen Fig. 8 (b) und (c) ist eine Verschiebung des Targets um 0.5 mm relativ zur Kristallposition. Fig. 9 zeigt 3D-Darstellungen dieser Abbildungen. Das ist ein vielversprechendes Ergebnis für die Kombination von toroidal gebogenen Kristallen und dem XCOT-System.

Diese Experimente haben das Potential der Röntgenfluoreszenz als Diagnostikwerkzeug für zukünftige FAIR-Experimente, wie HIHEX (siehe Fig. 10), demonstriert. Wir haben intensive Strahlung von ionisierten Targetatomen (K-Schalen Übergänge in Cu bei 8–8.3 keV und L-Schalen Übergänge in Ta) sowie Dopplerverschobene L-Schalen Übergänge von Au-Projektilen, welche sich durch Folientargets und Cu-Gitter bewegt haben, im Photonenenergiebereich von 10 keV beobachtet. Diese Strahlung kann für monochromatische (dispersive Elemente wie gebogene Kristalle) oder polychromatische (Pinhole) Röntgenkartierung der Ionenstrahlintensitätsverteilung in der Wechselwirkungszone genutzt werden (siehe Fig. 11). Die Dopplerverschiebung erlaubt beispielsweise die Feinabstimmung bei Verwendung von gebogenen Kristallen, die für ihre Abbildungen nur einen kleinen Arbeitsbereich der Röntgenenergien besitzen. Durch die Nutzung von Daten, die mit dem CdTe-Röntgenspektrometer und einer Faraday-Tasse aufgenommen wurden, konnte die Anzahl der Au L_α Photonen pro 1 C der Au-Ladung, die sich durch die Al-, Cu- und Ta-Folien bewegt haben und pro 1 μm Targetdicke in 4π bestimmt werden. Diese Zahl erlaubt uns zu folgern, dass 10–100-fache Verstärkung des Signals benötigt wird, um diese Methode bei U-Strahlintensitäten von 10^{10} particles/pulse anzuwenden. Um dieses Ziel zu erreichen,

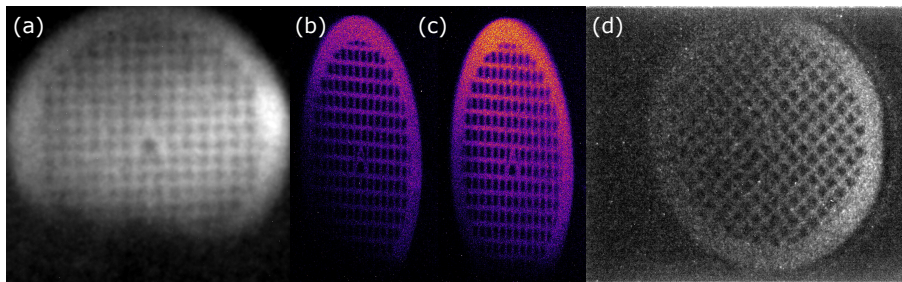


FIGURE 8: (a) Polychromatische Abbildungen eines Cu150-Gitters aufgenommen mit dem XCOT-System. Die Belichtungszeit betrug 180 min (entsprechend 2.3×10^{12} Au-Ionen). (b) und (c) sind Abbildungen des gleichen Cu150-Gitters bei 8.028 keV aufgenommen mit einem toroidal gebogenen Si-Kristall (siehe Tab. 5.1). Die Akkumulationszeit betrug 50 min (4.9×10^{11} Au-Ionen). Der Unterschied zwischen (b) und (c) ist eine Verschiebung des Targets um 0.5 mm relativ zur Kristallposition. Unterschiede im Signalintensitätslevel entstehen vorwiegend dadurch, dass (b) nicht im Focus liegt. (d) zeigt die die Abbildung des Cu150-Gitters mit der Kombination des Si-Kristalls mit dem XCOT-System. Die Belichtungszeit betrug 25 min (entsprechend 1.1×10^{11} Au-Ionen).

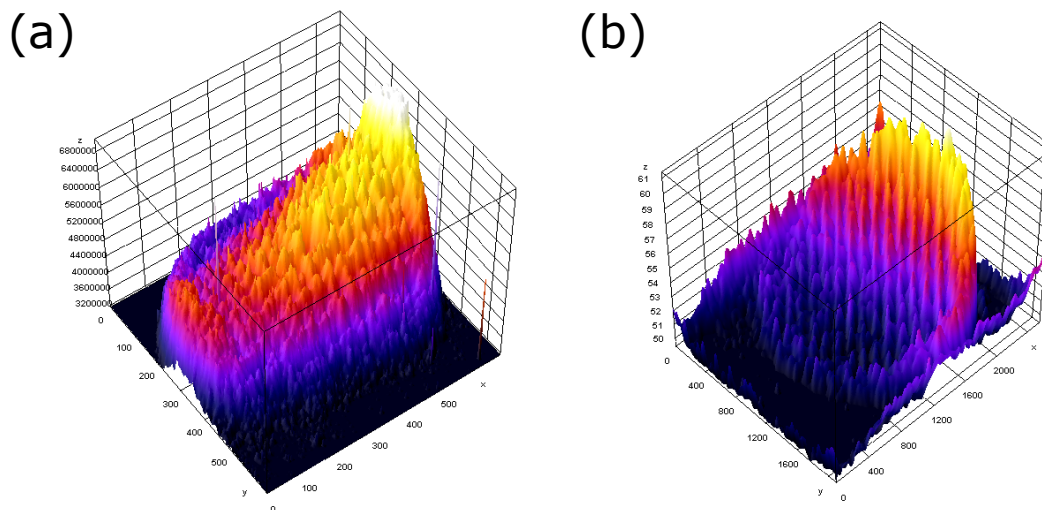


FIGURE 9: 3D-Darstellung der Ionenstrahlverteilung auf Gittertarget: (a) zeigt die 3D-Darstellung von Fig. 8 (a) und (b) zeigt die 3D-Darstellung von Fig. 8 (d).

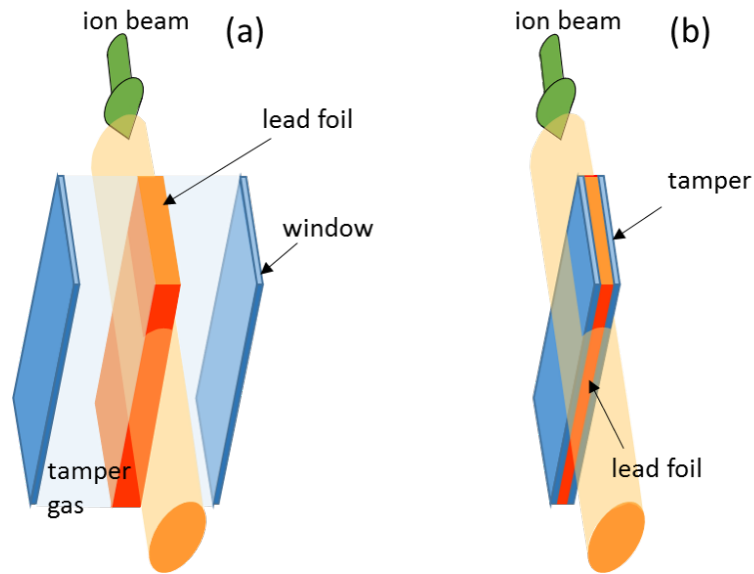


FIGURE 10: (a) HIHEX-Schema mit einer dicken Targetfolie von einigen hundert μm Dicke. Es ist geplant ein Tamper-Gas von 100 bar Druck zu verwenden. (b) dünne Targetfolien von einigen wenigen μm Dicke. Es ist geplant einen Festkörper-Tamper in diesem Schema zu verwenden.

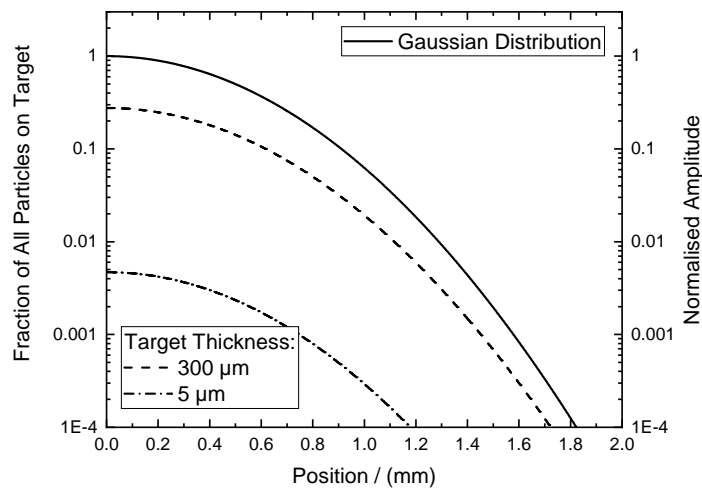


FIGURE 11: Der Anteil der Schwerionen, der, wie in Fig. 10 gezeigt, die Targetfront tatsächlich passiert. Es wird eine gaußförmige Strahlverteilung mit Halbwertsbreite um 1 mm angenommen (rechte Achse). Gezeigt sind die Abschätzungen für zwei unterschiedliche planare Folientargetdicken mit einer unendlichen Ausdehnung der Folien in einer Dimension, wie für die beiden HIHEX-Schemata vorgeschlagen. Der Anteil der Gesamtzahl der Strahlteilchen, der mit der Folie interagiert, ist auf der linken Achse aufgetragen.

wurde zu Beginn von 2020 eine weitere Strahlzeit durchgeführt. Das XCOT-System wurde mit dem Si-Kristall, der in dieser Arbeit eingesetzt wurde, gekoppelt, um das Signalintensitätslevel, das Signal-Rausch-Verhältnis und das Kontrast-Rausch-Verhältnis zu verbessern. Die Daten dieses Experiments befinden sich gerade in der Auswertung und ein Manuskript, welches die Resultate dieser Arbeit zu den Röntgenabbildungstechniken behandelt, wird vom Autor et al. vorbereitet. Das erste Resultat ist, dass das optische System des XCOT-Systems für die HIHEX-Experimente im HHT-Cave verbessert werden muss.

Contents

Abstract	v
Zusammenfassung	vii
0.1 Laser Generierte Ultrarelativistische Elektronen	vii
0.2 Röntgenfluoreszenz von Target und Schwerionenstrahl	xi
1 Motivation and introduction	1
2 Theory	7
2.1 Interaction of Electromagnetic Radiation with Matter	7
2.1.1 Interaction of a Plane Electromagnetic Wave with a Single Charged Particle	7
2.1.2 Behaviour of Electromagnetic Waves at Interfaces	7
2.1.3 Ionisation Processes in Laser-Matter-Interaction	8
2.1.4 Keldysh-Parameter	10
2.1.5 Interaction of Electromagnetic Radiation with Plasma	11
Plasma Frequency	11
Critical Density	12
Skin Depth	13
2.2 Laser Plasma and Particle Acceleration by Laser	13
2.2.1 Preplasma Expansion	14
2.2.2 Supersonic Ionisation in Structured Low Density Targets	15
2.2.3 Lorentz Force	16
2.2.4 Ponderomotive Potential	16
2.2.5 Ponderomotive Force	17
2.2.6 Generation of Relativistic Laser-Accelerated Electrons	18
2.2.7 Formation of Relativistic Laser Channels in Plasma	20
2.2.8 Limits of Magnetic Self-Focusing at relativistic Intensities and Super-Channel Formation	20
2.2.9 Direct Laser Acceleration (DLA)	22
2.2.10 Inverse Free Electron Laser at the Channel Betatron Resonance	22
2.2.11 Hot electron scaling laws	24
2.3 Interaction of Heavy-Ions and Electrons with Cold Matter	27
2.3.1 Stopping Power in Cold Matter	27
2.3.2 The Beer-Lambert Law	29
2.3.3 Bremsstrahlung	30

2.3.4	Relativistic Doppler Effect	31
2.3.5	Characteristic Line Radiation and X-Ray Fluorescence Radiation	31
2.3.6	Inner Shell Vacancy Production in Heavy-Ion-Atom Collisions	33
2.3.7	Atomic Radiative and Radiationless Yields and Line Widths for K-Shells	35
3	Experimental Environments at GSI and FAIR	39
3.1	UNILAC	39
3.1.1	Z6 Experimental Area	40
3.2	PHELIX	41
3.2.1	PHELIX Petawatt Experimental Area	42
3.3	FAIR	45
3.3.1	APPA Experimental Area	45
4	Laser Generated Ultrarelativistic Electrons	47
4.1	Experimental Setup	50
4.2	Diagnostic Methods	55
4.2.1	Electron and Ion Spectrometers	55
4.2.2	Angular Distribution of Electrons	57
4.3	Experimental Results	58
4.3.1	Generation of Ultra Relativistic Electrons	59
4.3.2	Angular Distribution of Ultrarelativistic Electrons	66
4.3.3	Generation of Quasi Monoenergetic Protons of few MeVs	70
4.3.4	Comparison of X-Ray Radiography by X-Ray Tube and Laser Experiment	78
5	X-Ray Fluorescence of Target and Heavy-Ion Beam	83
5.1	Experimental Setup	86
5.2	Diagnostic Methods	87
5.3	Experimental Results	90
5.3.1	Fluorescence Yield Measurements	90
5.3.2	Polychromatic X-Ray Fluorescence Imaging of the Ion Beam distribution on Target Using the XCOT-System	93
5.3.3	Polychromatic X-Ray Fluorescence Imaging of a Cu100-Mesh Irradiated by an Ion Beam Using the XCOT-System and Imag- ing Plates as Detectors	95
5.3.4	Polychromatic X-Ray Fluorescence Imaging of a Cu150-Mesh Irradiated by an Ion Beam Using the XCOT-System as Detector	99
5.3.5	Monochromatic X-Ray Fluorescence Imaging Using Toroidally Bent Crystals	101
6	Discussion and Outlook	107
6.1	Laser Generated Ultrarelativistic Electrons	107

6.2	X-Ray Fluorescence of Target and Heavy-Ion Beam	111
A	Electron and Ion Diagnostics	117
A.1	Geometry of the magnet spectrometers	117
A.2	Dispersion of the magnet spectrometers	118
A.2.1	Dispersion of the magnet spectrometers assuming a homoge- neous magnetic field	118
	Side-On IP	119
	Back-On IP	120
A.2.2	Dispersion of the Magnet Spectrometers Assuming an Inhomo- geneous Magnetic Field	121
A.3	Normalisation due to Non Linear Dispersion	122
A.4	Background corrections	124
B	Imaging Plate Detectors (IPs)	125
B.1	IP Response Functions	126
B.1.1	IP Response to Photons and Electrons	128
B.1.2	IP Response to Protons	128
B.2	IP Angular Response Function	130
B.3	IP Signal Fading	130
B.4	IP Properties in X-Ray Radiography Applications	133
B.4.1	Quantum Efficiency, Signal-to-Noise-Ratio (SNR) and Contrast- to-Noise-Ratio (CNR)	134
B.4.2	Multiple Scanning Procedures of IPs	136
B.4.3	Mean Intensities in the Scanning Process of IPs	138
B.4.4	Signal-to-Noise Ratio in the Scanning Process	140
B.4.5	Spatial Resolution in the Scanning Process	141
C	X-Ray Diagnostics	147
C.1	X-Ray CdTe-Diode	147
C.2	HOPG X-Ray Spectrometer in von Hámos Geometry	147
C.3	XCOT-System	149
C.4	Pinhole Cameras	155
C.5	X-Ray Crystal Microscope	156
	Bibliography	159
	Acknowledgements	171

List of Abbreviations

ADC	A nalogue- t o- d igital
APPA	A tomic-, P lasma- P hysics and A pplications
ASE	A mplified S pontaneous E mission
ATI	A bove T hreshold I onisation
BIF	B eam I nduced F luorescence
CNR	C ontrast- t o- N oise- R atio
CPA	C hirped P ulse A mplification
CSDA	C ontinuous S lowing D own A pproximation
DLA	D irect L aser A cceleration
EOS	E quation of S tate
FAIR	F acility for A ntiproton and I on R esearch
FWHM	F ull W idth at H alf M aximum
GSI	G esellschaft für S chwer I onen f orschung
HED	H igh E nergy D ensity
HHT	H igh energy, H igh T emperature
HOPG	H ighly O riented P yrolytic G raphite
IP	I maging P late
MPI	M ulti- P hoton- I onisation
MTF	M odulation T ransfer F unction
OTBI	O ver T he B arrier I onisation
NHELIX	N anosecond H igh- E nergy L aser for Heavy Ion E Xperiments
PIC	P article I n C ell
PHELIX	P etawatt H igh- E nergy L aser for Heavy Ion E Xperiments
PMMA	P oly M ethyl M eth A crylate
PMT	P hoto M ultiplier T ube
PSL	P hoto S timulated L uminescence
PSP	P hotostimulabel P hosphor
NCD	N ear C ritical D ensity
RBS	R utherford b ackscattering
sCMOS	s cientific C omplementary M etal- O xide- S emiconductor
SIS18	S chwer I onen S ynchrotron18
SIS100	S chwer I onen S ynchrotron100
SNR	S ignal- t o- N oise- R atio
TE	T hermodynamic E quilibrium
TI	T unnel- I onisation

TLD	T hermo L uminescence D etector
TNSA	T arget N ormal S heath A cceleration
UNILAC	U NIversal L inear A Ccelerator
uOPA	u ltrashort O ptical P arametric A mplifier
WDM	W arm D ense M atter
XCOT	X ray C onversion to O ptical and T ransport

Physical Constants

Electron Rest Mass	$m_e = 9.1093837015(28) \times 10^{-31} \text{ C}$
Elementary Charge	$e = 1.602\,176\,634 \times 10^{-19} \text{ C (exact)}$
Planck Constant	$h = 6.626\,070\,15 \times 10^{-34} \text{ J s (exact)}$
Reduced Planck Constant	$\hbar = h/2\pi = 1.054\,571\,817 \times 10^{-34} \text{ J s}$
Speed of Light in Vacuum	$c_0 = 2.997\,924\,58 \times 10^8 \text{ m s}^{-1} \text{ (exact)}$
Vacuum Permittivity	$\epsilon_0 = 8.8541878128(13) \times 10^{-12} \text{ F m}^{-1}$

*Dedicated to the adventure of my life and everybody who gets
caught up in it...*

Chapter 1

Motivation and introduction

The experimental investigation of high energy density (HED) matter states created with intense laser (Sebastien Le Pape et al. 2010; Morace et al. 2014; Schönlein et al. 2016) and heavy-ion beams (Tahir, Deutsch, et al. 2005; Tahir, Stöhlker, et al. 2010) requires, on the one hand, active backlighting with highly penetrating gamma-rays and energetic particles that provide important diagnostic tools to access plasma parameters and structural information from inside the high areal density samples. On the other hand, passive diagnostics using X-ray fluorescence of target atoms and projectiles for gaining precise knowledge of the energy density distribution deposited by the heavy-ion beam into the target are needed (O N Rosmej, S. A. Pikuz, et al. 2005; O N Rosmej, Blazevic, et al. 2005; Rzadkiewicz et al. 2010). This is an important input parameter for simulations concerning the equation-of-states (EOS) (Tahir, Deutsch, et al. 2005; Tahir, Stöhlker, et al. 2010).

The heavy-ion heating and expansion (HIHEX) experiment planned by the collaboration HED@FAIR at the facility for antiproton and ion research (FAIR) (V. Mintsev et al. 2016; Schoenberg et al. 2020) will involve intense uranium beams that will be available after the commissioning of the new synchrotron SIS100 at the GSI Helmholtz Centre for Heavy-Ion Research GmbH (Society for Heavy-Ion Research, german: Gesellschaft für Schwerionenforschung (GSI)) in Darmstadt, Germany. Numerical simulations have demonstrated that intense heavy-ion beams can be a very efficient tool to study the EOS properties of HED matter using the HIHEX technique (see fig. 1.1) (Hoffmann et al. 2002; Tahir, Deutsch, et al. 2005; Golubev and V. B. Mintsev 2012; V. Mintsev et al. 2016). The intense ion beam of duration 50–100 ns is expected to heat the sample isochorically. After heating, the target expands isentropically and reaches many interesting physical states. Depending on the ion beam intensity, the target can states like the two-phase liquid-gas region, expanded hot liquid, the critical point and strongly coupled plasmas. That is in comparison to the application of the traditional method of shock compression where these states are either difficult to access or even inaccessible.

Various experimental schemes are proposed for the experiments in the atomic-plasma-physics-and-applications(APPA)-cave at FAIR. The first experiments with these schemes will take place at the High energy, High Temperature (HHT)-cave situated after the synchrotron SIS18 in FAIR Phase-0. Macroscopic samples of matter

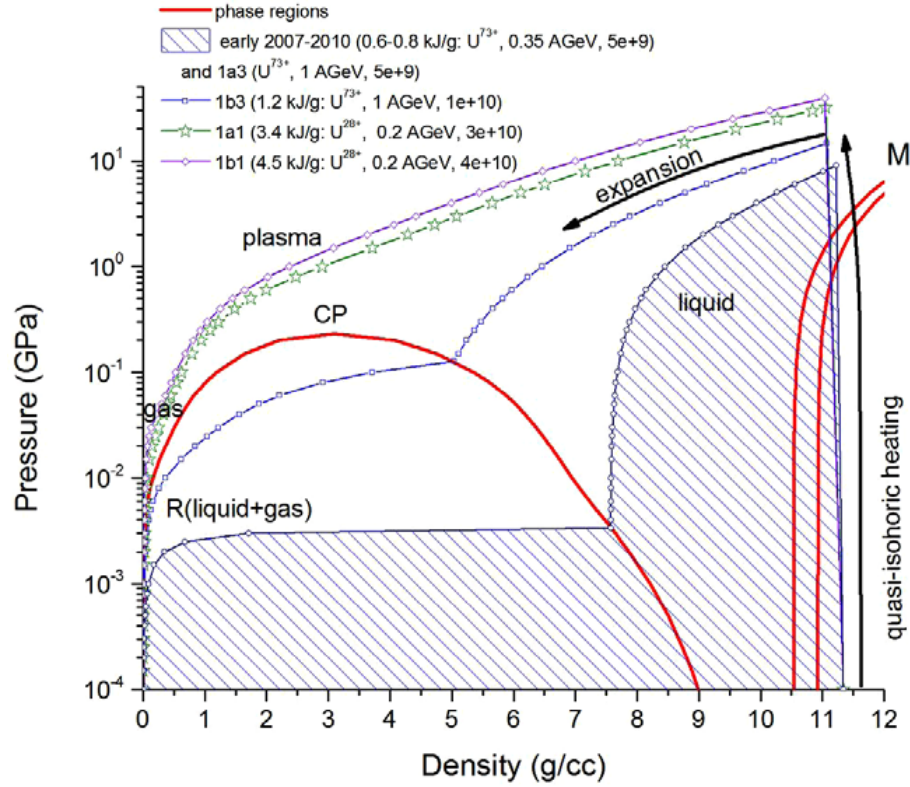


FIGURE 1.1: Pressure-density diagram for lead. Phase regions along with cases for HIHEX study for different beam parameters are shown (V. Mintsev et al. 2016).

in form of foils (or wires) of different materials like Al, Cu and Pb will be irradiated by the intense ion beams (2×10^9 – 10^{10} particles of 400 MeV/u U^{73+} at HHT (GSI Helmholtz Centre for Heavy-Ion Research GmbH 2020) and 5×10^{11} particles of up to 1 GeV/u U^{28+} at FAIR (Appel, Boine-Frankenheim, and Geithner 2019)). Two of these schemes involving foil-targets are shown in fig. 1.2. The length of the samples along the ion beam propagation direction is chosen to be much smaller than the range of the ions in the material so that the Bragg peak does not lie inside the target and the energy deposition is uniform along the ion trajectories. Additionally, the diameter of the target is assumed to be much less than that of the ion beam which, in fact, is the full width at half maximum (FWHM) of the Gaussian power distribution in the beam focal spot along the transverse direction. Fulfilment of these conditions ensures a fairly uniform energy deposition along the target radius as well as the length. The heated material expands perpendicular to the plane in the case of a foil-target (radial in the case of a wire-target). As the fringe effects are minimised by the choice of the aspect ratios, the problem is reduced to a one dimensional expansion. Typically, for the case of 350–1000 GeV/u ions, the focal spot size (FWHM) is 0.5–1.5 mm and the ion range in lead corresponding to this energy band is 3.5–15.5 mm (while the length of the wire would be 60–80 % of the range) (Tahir, Deutsch, et al. 2005; Tahir, Adonin, et al. 2005). In fig. 1.2 (a), a thick target foil of several hundred μm thickness is shown. To actively diagnose layers of high Z material (like Pb) deep inside the

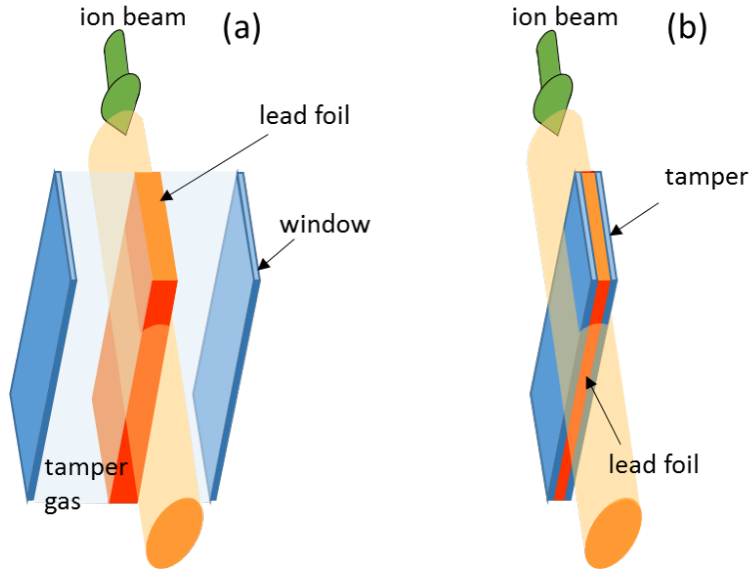


FIGURE 1.2: (a) HIHEX scheme with a thick target foil of several hundred μm thickness. A tamper gas of 100 bar pressure is planned to be used. (b) thin target foils of a few μm thickness. A solid state tamper is planned to be used in this scheme (Vincent Bagnoud 2020).

target, either hard X-rays or gamma-rays are needed. Passive diagnostics of the energy deposition by the beam inside the target during the beam target interaction are possible by observing inner atomic shell emissions of heavy-ion beam or target atoms. Fig. 1.2 (b) shows the scheme for thin target foils.

One of the unique features of the GSI Helmholtz Centre is the possibility to combine heavy-ion and high energy lasers at the same experimental area. The Petawatt High Energy Laser for Heavy Ion eXperiments (PHELIX) facility can be operated in long (1 kJ, ns) and short pulse (200 J, sub-ps) mode (Vincent Bagnoud et al. 2010). The short pulse mode is available in the PHELIX laser bay. However, the long pulse mode is also available at either the Z6 experimental area situated after the UNiversal Linear ACcelerator (UNILAC) or, in the near future, at the HHT experimental area (Major et al. 2019).

Active backlighting with highly penetrating gamma-rays and energetic particles is proposed for thick targets in the HIHEX-scheme at FAIR. Intense and well directed beams of photons with energies far above 100 keV is the best candidate for such radiographic applications. Relativistic particle beams for the production of gamma-radiation can be generated by TW- and PW-class laser systems that deliver laser pulses of relativistic intensities. Spatial and temporal resolution for radiographic purposes by these sources is achieved by the micrometer-small size laser focus on a target surface and a short laser pulse duration. By providing up to $10\mu\text{m}$ spatial resolution and snap shots of the Warm-Dense-Matter (WDM)-object density distribution in ps- up to fs-time scale, the analysis of the hydrodynamic motion of heated matter is facilitated (Ravasio et al. 2008; K. Li et al. 2014).

For such kind of backlighter sources and if the laser parameters cannot be changed,

the properties of the secondary laser sources have to be optimised. In pilot experiments carried out at the PHELIX laser system, GSI Darmstadt, relativistic electrons were produced in a long scale plasma of near critical electron density (NCD) by the mechanism of the direct laser acceleration (DLA). Low density polymer foam layers preionised by a well-defined nanosecond laser pulse were used as NCD targets (N. G. Borisenko, Akimova, et al. 2006; Khalenkov et al. 2006; N. G. Borisenko, Khalenkov, et al. 2007). The analysis of the measured electron spectra showed up to 10-fold increase of the electron "temperature" from $T_{Hot} = 1-2$ MeV, measured for the case of the interaction of $1-2 \times 10^{19}$ W cm⁻² ps-laser pulse with a planar foil, up to 14 MeV for the case when the relativistic laser pulse propagates through the by a ns-pulse preionised foam layer. In this case, up to 80–90 MeV electron energy was registered. An increase of the electron energy was accompanied by a strong increase of the number of relativistic electrons and well-defined directionality of the relativistic electron beam measured to be $12 \pm 1^\circ$ (FWHM). This directionality increases the gamma flux on target by far compared to the soft X-ray sources.

Additionally to laser based active diagnostics, passive techniques involving inherent X-ray fluorescence radiation of projectile and target emitted during heavy-ion-target interaction can be used to measure the ion beam distribution on shot in experiments with the intense ion-beams available at HHT in Phase-0 and the APPA-cave at FAIR. This is the case in particular if no short pulse laser option is available. In order to ensure the homogeneous heating of the HIHEX-target by the ion beam, the target size is chosen to be smaller than the beam focus size (see fig. 1.2). A Beam Induced Fluorescence (BIF) monitor based on radiation of residual gas in the visible range was developed for measurement of the heavy-ion beam distribution on target before the shot (Becker et al. 2006; Varentsov et al. 2008). During the shot, vacuum conditions are required. Therefore, BIF in the visible range is not possible, but the mapping of the heavy-ion beam distribution by X-ray fluorescence on shot is possible. Therefore, the X-ray fluorescence yield is a good measure for the energy deposition of the projectiles into the target during the interaction.

The X-ray-Conversion-to-Optical-radiation-and-Transport(XCOT)-system was developed at the Goethe University Frankfurt in the frame of a BMBF-Project (FKz. 05P15RGFAA, (El Houssaini 2017; Gesell 2018; Gyrdymov 2019)) for application in Phase-0 and at FAIR, where one expects strong parasitic radiation of particles and gammas capable of destroying the experimental equipment. In the XCOT-concept, the X-ray image of the beam-target interaction region is performed by means of a pin-hole camera (polychromatic imaging) or a crystal (monochromatic imaging). Monochromatic imaging allows to discern between target and beam fluorescence. The X-rays are then converted into optical light using a thin CsI(Tl)-scintillator plate. The optical image is transported for registration over a meters long distance to a Micro Channel Plate (MCP)-based image intensifier module by using optical fibres or a telescope objective. After amplification, the image is registered by a sCMOS-camera. The scheme of the XCOT-system is shown in fig. 1.3. Our experiments were

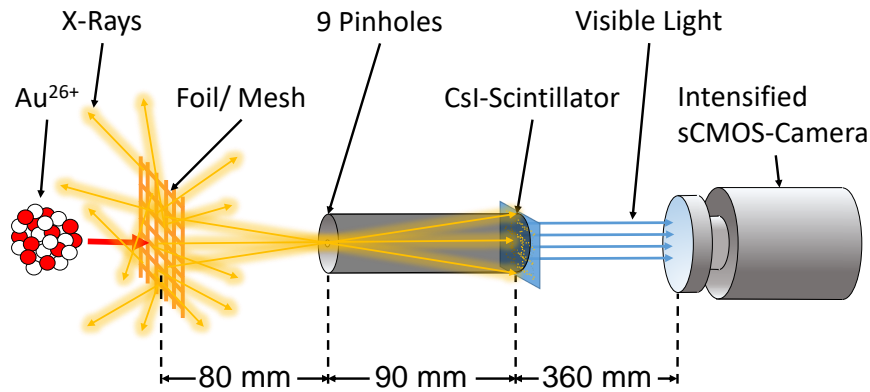


FIGURE 1.3: Schematic view of the XCOT-system. Cu-Meshes are irradiated by an Au^{26+} -beam. The Cu-meshes emit X-ray fluorescence which is imaged onto a CsI-scintillator. The scintillator converts the X-rays into visible light. That light is transported to an MCP based image intensifier and then registered by a sCMOS-camera.

performed at the UNILAC-facility using Au^{26+} ion-beams of energies 6.5 MeV/u and 11.4 MeV/u. Solid state targets of different materials were used for the measurement of fluorescence yields and for imaging purposes. Spatial resolution was tested using mesh targets of different materials and mesh widths. Multi pin holes were used for the reduction of the signal-to-noise-ratio. This allowed for measuring the ion beam distribution on the target spatially resolved and to measure the X-ray fluorescence yield from different target materials spectrally resolved.

In this work, the results from first pilot experiments on the characterisation of MeV electron beams generated by the interaction of the PHELIX-laser pulse with low density CHO-foams as foundation for the development of MeV gamma-sources (P138, October 2017 and P176, September 2019) and X-ray fluorescence imaging of heavy-ion beam cold target interaction (U305, June 2016 and U317, February 2019) are presented. The experiments were performed in the frame of FAIR Phase-0 at the PHELIX and UNILAC facilities at GSI Helmholtz Centre for Heavy-Ion Research GmbH in Darmstadt, Germany.

Chapter 2

Theory

The first part discusses the theoretical foundations of the interaction of lasers and particles beams with matter. The first part will deal with the interaction between electromagnetic radiation with matter. The second part handles the interaction of light and heavy particles with matter.

2.1 Interaction of Electromagnetic Radiation with Matter

The interaction of electromagnetic waves and matter is governed by the forces enacted by the oscillating electric and magnetic fields of the wave on charged particles inside of matter. New collective phenomena become important when cold matter transitions into the plasma state. The following section will also describe mechanisms of electron acceleration in plasmas of near critical density.

2.1.1 Interaction of a Plane Electromagnetic Wave with a Single Charged Particle

In electromagnetic waves, both electric fields \vec{E} and magnetic fields \vec{B} are present. The fields are perpendicular to each other. A linear polarised plane electromagnetic wave which is propagating in z -direction is described by their oscillating electric and magnetic field in space (x, y, z) and time t :

$$\vec{E}(x, y, z, t) = E_0(t) e^{-i(\omega_L t - kz)} \vec{e}_x \quad (2.1)$$

$$\vec{B}(x, y, z, t) = B_0(t) e^{-i(\omega_L t - kz)} \vec{e}_y \quad (2.2)$$

where ω_L is the angular frequency of the laser, k is the wave vector and from the Maxwell equations follows $B_0(t) = E_0(t) / c$.

2.1.2 Behaviour of Electromagnetic Waves at Interfaces

The behaviour of electromagnetic waves on the interfaces between media is governed by the Fresnel equations. The plane in which the electromagnetic wave propagates

before and after hitting the interface is called the plane of incidence. The fraction of power of the electromagnetic wave reflected at the interface is called the reflectance R and the transmitted power the transmittance T . R is depending on the polarisation of the electric field of the electromagnetic wave. S -polarised is denoted as the direction of the E -field perpendicular to the plane of incidence while the wave is P -polarised for the case of E parallel to that plane. The reflectance of a S -polarised wave is:

$$R_S = \left| \frac{Z_2 \cos(\theta_i) - Z_1 \cos(\theta_t)}{Z_2 \cos(\theta_i) + Z_1 \cos(\theta_t)} \right|^2 \quad (2.3)$$

The reflectance of a P -polarised wave is:

$$R_P = \left| \frac{Z_2 \cos(\theta_t) - Z_1 \cos(\theta_i)}{Z_2 \cos(\theta_t) + Z_1 \cos(\theta_i)} \right|^2 \quad (2.4)$$

with $Z_{1/2}$ the wave impedances of the media and $\theta_{i/t}$ the angles of incidence and transmittance. The angles $\theta_{i/t}$ are connected by Snell's law through the refractive indexes $n_{i/t}$:

$$\frac{\sin(\theta_i)}{\sin(\theta_t)} = \frac{n_t}{n_i} \quad (2.5)$$

Note that this does not include attenuation of the wave due to absorption inside of media.

2.1.3 Ionisation Processes in Laser-Matter-Interaction

For the generation of a plasma on the surface of matter, enough energy has to be transferred from the laser onto the electrons bound in the atoms of said matter, so that they can leave the atomic shell. Different mechanisms are known that lead to ionisation of the atom by a laser.

Optical Field-Ionisation A bound electron situated in an electric laser-field, that is of the order of magnitude of the Coulomb-field created by the core of the atom, can be separated from the atom by gaining enough energy from the laser-field (see fig. 2.1). The laser-intensity I_L is connected to the electric laser-field E by (Protopapas, Keitel, and Knight 1997):

$$I_L = \frac{1}{2} \varepsilon_0 c_0 E^2. \quad (2.6)$$

For example, the Coulomb-field of the hydrogen atom is around $5 \times 10^9 \text{ V cm}^{-1}$. From eq. 2.6 we can calculate an intensity of $3 \times 10^{16} \text{ W cm}^{-2}$. This process of ionisation is called optical field-ionisation.

Optical Field/Direct Ionisation (1 Photon)

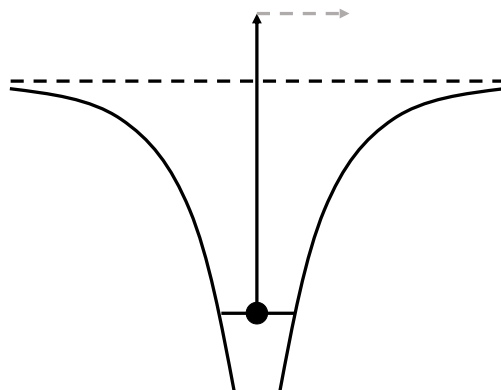


FIGURE 2.1: An atom is directly ionised by a single photon with enough energy to elevate the electron out of the potential well. This is called optical field ionisation.

Multi-Photon-Ionisation (MPI) However, ionisation can happen below intensities of $3 \times 10^{16} \text{ W cm}^{-2}$ already. One possible ionisation process is the multi-photon-ionisation (MPI). In contrast to the classical (outer) photoelectric effect, MPI describes the transition of a bound electron into an unbound state through the instantaneous absorption of multiple photons to surpass the ionisation threshold (see fig. 2.2). The ionisation-rate Γ_N is given by (Protopapas, Keitel, and Knight 1997):

$$\Gamma_N = \sigma_N I_L^N \quad (2.7)$$

with N the minimal number of photons that have to be involved in a single ionisation process and σ_N the, so called, generalised cross-section. However, eq. 2.7 is only valid below a critical intensity, called the saturation intensity. This saturation is reached, when the intensity is so high, that, because of the complete ionisation of the atoms, MPI is not possible anymore (Protopapas, Keitel, and Knight 1997).

A special case of MPI is the above-threshold-ionisation (ATI). It describes the ionisation processes when the number of photons exceeds N . The ionisation-rate of eq. 2.7 is then corrected (Protopapas, Keitel, and Knight 1997):

$$\Gamma_{N+s} \propto I_L^{N+s} \quad (2.8)$$

The number of excess photons (excess but still absorbed) is expressed by s . Therefore, the energy E of the freed electron is given by (Protopapas, Keitel, and Knight 1997):

$$E = (N + s) h\nu - W_I \quad (2.9)$$

where W_I is the ionisation-energy and ν the frequency of the absorbed photon.

Multiphoton Ionisation (MPI)

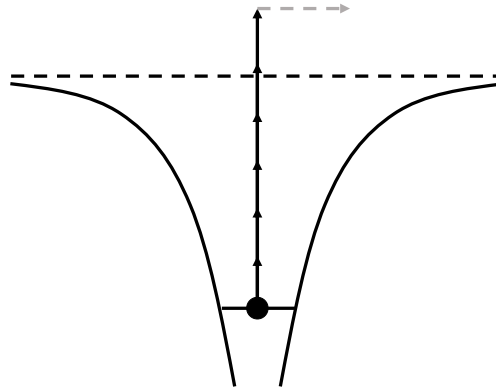


FIGURE 2.2: An atom is ionised by absorption of multiple photons. The sum of the energies of the photons is high enough to elevate the electron out of the potential well. This is called multi-photon ionisation.

Tunnel-Ionisation (TI) Another possible ionisation process is the tunnel-ionisation (TI) (Keldysh et al. 1965). The requirement for the occurrence of that process is, that the Coulomb potential of the atom becomes reduced by the laser-field enough to increase the probability of the electron tunnelling through the barrier (see fig. 2.3). A continuous increase of the laser-intensity and thus the strength of the laser-field, can be used for the complete compensation of the Coulomb potential. This kind of ionisation is called Over The Barrier Ionisation (OTBI) and is associated with the field-ionisation (Protopapas, Keitel, and Knight 1997).

2.1.4 Keldysh-Parameter

In essence, the above mentioned ionisation mechanisms are paramount for the generation of laser-plasma, though there can be different scopes of application distinguished between the different ionisation mechanisms. For low intensities, MPI is dominating. With increasing intensity, the TI process gains in importance. At very high intensities, where the electrical field strength of the laser-field corresponds to the Coulomb-potential or even exceeds it, the optical field ionisation dominates (Keldysh et al. 1965).

A straightforward estimation for the decision between the applicability of field ionisation and MPI is possible by introducing the Keldysh-parameter γ_κ (Keldysh et al. 1965; Gibbon 2004):

$$\gamma_\kappa = \omega_L \sqrt{\frac{2E_{ion}}{I_L}} \sim \sqrt{\frac{E_{ion}}{\Phi_{pond}}} \quad (2.10)$$

where E_{ion} is the ionisation energy and

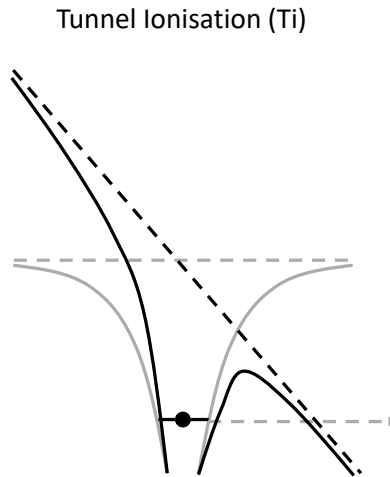


FIGURE 2.3: The Coulomb potential of the atom becomes reduced by the laser-field enough to increase the probability of the electron tunnelling through the barrier. This is called tunnel ionisation.

$$\Phi_{pond} = \frac{e^2 E_L^2}{4m_e \omega_L^2} \quad (2.11)$$

is the so called ponderomotive potential of the laser field, expressing the quiver energy acquired by an oscillating electron.

$\gamma_\kappa \geq 1$ signifies that a bound electron can only gain half of the energy necessary for the ionisation at maximum. Therefore, MPI dominates in this region. Hence, for $\gamma_\kappa \leq 1$ the field ionisation is dominating.

The generation of a laser plasma and which processes are dominating in the ionisation is therefore depending on the laser parameters, as energy, pulse duration and focal spot size, as well as on material properties, as atomic number and phase of the matter.

2.1.5 Interaction of Electromagnetic Radiation with Plasma

The interaction between an electromagnetic wave and ionised matter leads to collective phenomena not present in cold matter. The following section deals with important properties of plasmas in respect to electromagnetic waves propagating through them.

Plasma Frequency

Under the presence of free electrons, like in solid state matter with metals which possess a conduction band or in a plasma, the collective behaviour of the electrons can be described by several quantities described in this section. Under the assumption of a thermodynamic equilibrium (TE), electrons and positive charge carriers possess the same temperature. As the positive charge carriers also possess a much higher

mass than the electrons, they can be treated as stationary. Electrons, and ions in the case of a plasma, moved from the rest position by a force and then released, will perform oscillatory motions in in the material or plasma. The eigenfrequency of that motion is called the plasma-frequency and given by (Wiesemann 2014):

$$\omega_{p_{e,i}} = \sqrt{\frac{n_{e,i} (Z_i e)^2}{\epsilon_0 m_{e,i}}} \quad (2.12)$$

where $n_{e,i}$ is the electron or ion density, Z is the charge of the ion in units of e or, in the case of an electron, equal to one, and $m_{e,i}$ is the mass of the electron or ion. The plasma frequency is therefore only depending on the density and mass of a certain kind of particle.

There are three physically interesting cases ($\omega_{em} < \omega_{p_e}$, $\omega_{em} > \omega_{p_e}$ and $\omega_{em} = \omega_{p_e}$) for the interaction of photons of an electromagnetic wave with plasmas. Due to the fact that the mass of the electrons is much smaller than the mass of the ions in the plasma, the following observations are dominated by the electron plasma frequency and therefore we chose $\omega_{p_e} = \omega_p$ further on.

Firstly, the frequency of the electromagnetic wave is smaller than the plasma frequency ($\omega_{em} < \omega_{p_e}$). The electrons can follow the disturbance of the electromagnetic wave easily and therefore reflect the wave.

Secondly, the frequency of the electromagnetic wave is bigger than the plasma frequency ($\omega_{em} > \omega_{p_e}$). The mass of the electrons is too high to follow the driving force of the electromagnetic field. They can not follow and thus, the wave is transmitted. That is also the reason, why the electrons dominate the interaction with electromagnetic waves. Due to the higher mass of ions in the plasma, the ion plasma frequency is smaller and therefore, even if transmission through the ions is possible, electrons can still reflect at higher frequencies. Only if the frequency of the electromagnetic wave is higher than each plasma frequency, the wave is transmitted.

At last, the frequency of the electromagnetic wave is equal to the plasma frequency ($\omega_{em} = \omega_{p_e}$). That is the special case of resonant absorption. The oscillation of the electrons in the plasma is amplified by the incident electromagnetic wave and energy is transferred resonantly. As the energy of the electrons is increased by this, that can be understood as a heating process.

There is no clear border for the existence of the three different regions of reflexion, transmission and absorption. Only the ratios are shifting.

Critical Density

The plasma frequency is primarily depending on the electron density in the plasma. Therefore, a so called critical density n_c can be calculated for every frequency ω_{em} or wavelength λ_{em} of the electromagnetic wave at which that electromagnetic wave would be absorbed resonantly. Hence, the critical density n_c is the density at which $\omega_{p_e} = \omega_p$ holds true (Gibbon 2004):

$$n_c = \frac{\varepsilon_0 m_e}{e^2} \times \omega_{em}^2 = \frac{4\pi^2 \varepsilon_0 m_e c_0}{e^2} \times \frac{1}{\lambda_{em}^2} \quad (2.13)$$

with ω_{em} the frequency and λ_{em} the wavelength of the electromagnetic wave respectively. For example, the critical density for a laser of wavelength 1053 nm is $n_c = 1 \times 10^{21} \text{ cm}^{-3}$.

Vice versa, a plasma with a density $n_e = n_c$ is called critical, a plasma with a density $n_e > n_c$ is called over-critical or supercritical or overdense and a plasma with a density $n_e < n_c$ is called under- or subcritical or underdense. For densities just below critical density there is also the term near-critical-density (Bin et al. 2015).

Skin Depth

In the absence of absorption, an electromagnetic wave impinging on a steep density gradient plasma or solid density metal will form a standing wave pattern in front of the target. An evanescent component of the wave will penetrate into the overdense region of the target beyond the critical density to a characteristic skin depth (Gibbon 2004):

$$l_s = \frac{c_0}{\omega_p} \quad (2.14)$$

where ω_p is the plasma frequency.

2.2 Laser Plasma and Particle Acceleration by Laser

As mentioned above, the plasma generated by the laser pulse on a surface will begin to expand. The expansion can be described by a rarefaction wave that moves away from the target with almost sound velocity (see below). Additionally, through ablation of material on the target surface, a shock wave is generated and travels through the material and generates high energy density matter states. Fig. 2.4 shows qualitatively the development of density and temperature during the first few nano seconds of the laser matter interaction.

The laser can penetrate the thinner volume of matter until it reaches the critical density n_c . Lower densities than critical density are called underdense or sub critical. The highest absorption of laser energy is reached at the layer of critical density. Where the plasma frequency ω_p is approaching the laser frequency ω_L and the energy transfer becomes resonant. The maximum of the temperature is reached in a volume with smaller density than critical density as secondary heating processes like radiation heating or particle heating take place. Densities exceeding the critical densities are called overdense or over critical. Overdense volumes of the plasma are only heated by secondary heating processes. The temperature is declining with depth in the target as the secondary heating processes lose their importance.

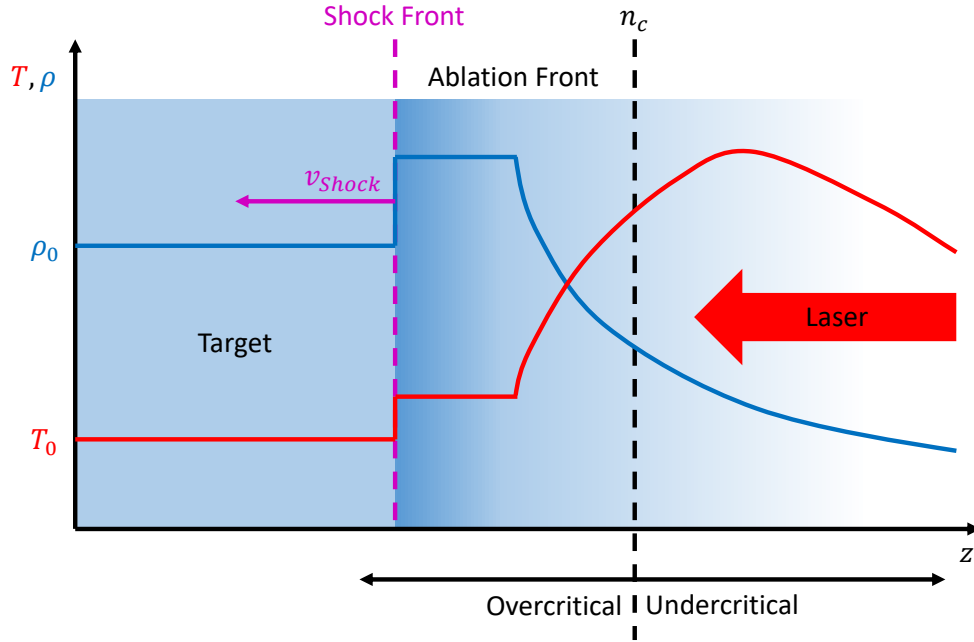


FIGURE 2.4: Qualitative progression of temperature and density in laser matter interaction on ns timescale.

While the above mentioned rarefaction wave is propagating against laser propagation direction and causes an exponential density evolution, the shock wave traversing the target is moving in laser propagation direction and leads to a density and temperature increase with strong gradient. The spatial extent of the different regions described in fig. 2.4 depend essentially on the timescales and laser intensities.

2.2.1 Preplasma Expansion

When the incident laser interacts with a solid state material surface and produces a plasma. The electrons of this plasma will gain energy by the laser pulse and their mean kinetic energy defined by the temperature T_e will increase. Some of these electrons will have an energy high enough to leave the target. This produces an electric field on the surfaces of the target in which ions are accelerated. Consequently, the plasma will expand. The velocity of expansion into vacuum is the ion acoustic velocity. The velocity of expansion follows from the two-fluid model:

$$v_s = \sqrt{\frac{k_B (ZT_e + T_i)}{m_i}} \quad (2.15)$$

where Z is the atomic number, T_e the electron temperature, T_i the ion temperature and m_i the ion mass. The plasma expands isothermally and possesses an exponentially decreasing density profile. After the time t the density profile perpendicular to

the surface is:

$$n(z, t) = n_0 e^{-\frac{z}{v_s t}} \quad (2.16)$$

with n_0 the density of the target material. A typical measure to characterise such a plasma is the scale length L_S of the density profile. This indicates the strength of the density change regarding the direction of the expansion. With expansion in z -direction and eq. 2.16 follows:

$$L_S = n_0 \left(\frac{\partial n}{\partial z} \Big|_{n(z,t)} \right)^{-1} = v_s t. \quad (2.17)$$

Typical scale lengths lie in the range of a few μm . The incident electromagnetic wave will propagate inside the preplasma up to the critical density n_c and an evanescent component will penetrate into the overdense region (see sec. 2.1.5).

2.2.2 Supersonic Ionisation in Structured Low Density Targets

Ionised targets with low mean density can be produced using gas or even solid state matter. 2 mg cm^{-3} triacetate cellulose (TAC, $\text{C}_{12}\text{H}_{16}\text{O}_8$) layers with thicknesses of $300 \mu\text{m}$ and $500 \mu\text{m}$ were used in the presented experiments (Khalenkov et al. 2006; N. G. Borisenko, Akimova, et al. 2006; N. G. Borisenko, Khalenkov, et al. 2007). TAC-layers are optically transparent and characterised by a highly uniform 3D network structure consisting of $1\text{--}2 \mu\text{m}$ pores, $0.1 \mu\text{m}$ thick and $1 \mu\text{m}$ long fibres with density of approximately 0.1 g cm^{-3} . The density fluctuations on the focal-spot size area of $100 \times 100 \mu\text{m}^2$ do not exceed 0.5% . Due to their open cell structure, air contained by pores can be evacuated.

When the incident laser interacts with a structured surface like a foam, it interacts with a material of mean density much below the critical density, but the membranes and fibres of the foam structure are still at solid density and their dimensions are larger than the skin depth. These membranes are ionised by the laser pulse. Therefore, the expansion of the plasma into the pores and consequently the decrease of the density to undercritical electron densities and allowing further propagation of the laser pulse through the 3D-structure of the aerogel takes time. It was shown analytically (Gus'kov et al. 2011) and experimentally (Nicolai et al. 2012) that the velocity of the super-sonic ionisation front propagation in an initially porous matter is lower than in a homogeneous medium of sub-critical density, like in a gas. An estimation of the ionisation front velocity V_p is given by (O N Rosmej, Suslov, et al. 2015):

$$V_p \approx 9.7 \times 10^4 \frac{A^{\frac{2}{3}} I_{14}^{\frac{1}{3}}}{Z_m^{\frac{2}{3}} \lambda_L^{\frac{4}{3}} \rho_a^\alpha \rho_s^{1-\alpha}} \text{ cm s}^{-1} \quad (2.18)$$

with A the atomic mass, I_{14} the laser intensity in normalised to $10^{14} \text{ W cm}^{-2}$, Z_m the mean atomic number of the foam, λ_L the wavelength of the laser, ρ_a the mean foam density, ρ_s the fibre density and a power factor α that reflects the geometry

of the foam (Gus'kov et al. 2011). Therefore the intensity of a ns-prepulse can be matched to the target density and target thickness in such a way that the velocity of the ionisation front will be much faster than the ion acoustic velocity. There is no notable expansion of the region that is heated during the propagation of the supersonic ionisation wave. The mean volume density of 2 mg cm^{-3} of the TAC-foam corresponds to $1.7 \times 10^{20} \text{ atoms/cm}^3$ and a mean ion charge $Z_{mean} = 4.2$. Full ionisation of all CHO-atoms would correspond to an electron density of $7 \times 10^{20} \text{ cm}^{-3}$, which is slightly lower than critical density (10^{21} cm^{-3}) for the fundamental wavelength of the Nd:glass laser ($\lambda_L = 1053 \text{ nm}$).

2.2.3 Lorentz Force

Electric fields \vec{E} and magnetic fields \vec{B} couple to electrically charged particles via the Lorentz force:

$$\vec{F}_L = \frac{d\vec{p}}{dt} = q \left(\vec{E} + \vec{v} \times \vec{B} \right) \quad (2.19)$$

where \vec{p} is the momentum, q is the charge and \vec{v} is the velocity of the particle present. This means that electric charges are accelerated alongside \vec{E} and perpendicular to \vec{B} . In the static case, this leads to straight trajectories in \vec{B} fields. The momentum is corrected in the relativistic case by $\vec{p} = \gamma m_e \vec{v}$ with $\gamma = \left(1 - \beta^2\right)^{-1/2} = \left(1 - (v/c)^2\right)^{-1/2}$ the Lorentz factor. In the non relativistic case ($v \ll c$), the electrons will experience a force according to eq. 2.19. This force acts perpendicular to the propagation direction of the electromagnetic wave (dominated by \vec{E}). The electron performs harmonic oscillations during the interaction with the laser field. When an electron is accelerated to velocities near the speed of light $v \leq c$, the Lorentz factor increases and the electron experiences an additional acceleration along the propagation direction of the electromagnetic wave (due to \vec{B}). Note that time averaged an indefinitely extended plane electromagnetic wave does not accelerate charged particles. A charged particle has to experience a spatial inhomogeneous electromagnetic wave distribution to be accelerated over time. This is the case in a laser which usually has a Gaussian shape in space and time.

2.2.4 Ponderomotive Potential

The so-called ponderomotive potential Φ_p is induced by the oscillatory motion of a free charge (Bauer, Mulser, and Steeb 1995). A free electron, situated in a laser-field, gains additional oscillational energy to its kinetic energy due to the ponderomotive potential of the laser-field. The corresponding ponderomotive potential Φ_p is given by (Freeman, Bucksbaum, and McIlrath 1988; Protopapas, Keitel, and Knight 1997):

$$\Phi_p = \frac{e^2 \vec{E}_0^2(\vec{r}, t)}{4m_e \omega_L^2} \quad (2.20)$$

with ω the angular frequency of the laser-field. $\vec{E}_0^2(\vec{r}, t)$ is related to the intensity $I_L(\vec{r}, t)$ by (Freeman, Bucksbaum, and McIlrath 1988):

$$I_L(\vec{r}, t) = \frac{\vec{E}_0^2(\vec{r}, t)}{8\pi c_0} \quad (2.21)$$

where

$$I_L(\vec{r}, t) = \left(\frac{r_0^2 P_0}{r^2(z)} \right) \times \exp \left(- \left(\frac{r}{r(z)} \right)^2 - \frac{\left(t - \frac{z}{c_0} \right)^2}{\left(\frac{\tau}{2} \right)^2} \right) \quad (2.22)$$

with $r^2(z) = r_0^2 \left(1 + (z/z_0)^2 \right)$, r_0 the spot size of the laser at the waist, the Rayleigh length z_0 of the focus

$$z_0 = (\pi/\lambda) r_0^2, \quad (2.23)$$

τ the pulse length, and P_0 the peak intensity at $r = z = t = 0$. That is related to the energy E_{beam} in the laser pulse by

$$P_0 = - \frac{2E_{beam}}{\pi^{3/2} \tau r_0^2}. \quad (2.24)$$

The ponderomotive energy is therefore proportional to the square of the local instantaneous electrical field-strength \vec{E}_0 and following that also to the laser-intensity I_L . For very high intensities, that also means that bound electrons experience that field so that a shift of the energy level, in accordance with the dynamic stark-effect, has to be taken into account. As a result, the modulus of the ponderomotive potential Φ_p is added to the ionisation energy W_I for high laser-intensities. Therefore, the energy balance of the electron leaving the atom from eq. 2.9 becomes:

$$E = (N + s) h\nu - (W_I + \Phi_p) \quad (2.25)$$

The ionisation through simultaneous absorption of multiple photons is already possible below intensities of $3 \times 10^{16} \text{ W cm}^{-2}$. The energy contained in the laser-pulse and the associated number of photons is the deciding factor.

2.2.5 Ponderomotive Force

The force that is introduced by the ponderomotive potential Φ_p is called the ponderomotive force F_p . The ponderomotive force is a nonlinear force that a charged particle experiences in an inhomogeneous oscillating electric field. In contrast to the oscillation of a charged particle around an initial point in a homogeneous field, the particle will move toward the area of the weaker field strength. This occurs as the particle sees a greater magnitude of force during one half of the oscillation periods while it is in the stronger field. The net force in the second half of the oscillation does not compensate the net force experienced in the first half of the oscillation. Therefore

a particle experiences the time averaged ponderomotive force F_p over a hole period (Freeman, Bucksbaum, and McIlrath 1988):

$$\vec{F}_p = -\frac{q^2}{4m\omega_L^2} \nabla \left(\vec{E}_0^2(\vec{r}, t) \right) \quad (2.26)$$

where q and m are the charge and mass of a particle in the laser field respectively, ω_L^2 is the angular frequency of the laser and \vec{E}_0 the local instantaneous electrical field-strength as above. This force is independent on the sign of the charge of a particle and therefore, all charged particles experience a ponderomotive force that is expelling them from Gaussian laser beams. A small longitudinal component of the ponderomotive force acts on a charged particle in a focussed laser beam as the beam is not a plane wave anymore. That makes the scattering radial symmetric (Alexander Pukhov 2003). Additionally, the relativistically normalised laser amplitude or normalised vector potential a_0 is defined by (Gordienko and Pukhov 2005; Arefiev et al. 2016; Kluge et al. 2011):

$$a_0 = \frac{eA_0}{m_e c_0^2} = \frac{eE_0}{m_e \omega_L c_0} = 100 \times \sqrt{\frac{2e^2 \times I_{18} [10^{18} \text{ W cm}^{-2}]}{m_e^2 c_0^3 \varepsilon_0 \omega_L^2}} \quad (2.27)$$

with ω_L the angular frequency of the laser, A_0 and E_0 either the amplitude of the vector potential or of the electric field inside the laser pulse, ε_0 the vacuum permittivity and I_{18} the laser intensity in units of $10^{18} \text{ W cm}^{-2}$. The parameter a_0 is roughly the ratio of the transverse electron momentum induced by the oscillating laser electric field to $m_e c_0$. Therefore, a laser pulse with a normalised amplitude of $a_0 \geq 1$ would induce relativistic electron motion. At these intensities, the electrons are also accelerated in forward direction by the $v_{\perp} \times \vec{B}$ part of the Lorentz force.

2.2.6 Generation of Relativistic Laser-Accelerated Electrons

As mentioned above, part of the laser energy can be transferred to bound electrons during the laser matter interaction. Depending on the ionisation process, the transferred energy can exceed the binding energy of the atom so that the excess energy is available as kinetic energy for the electron. Furthermore, these then free electrons and other free electrons can interact with the laser itself directly. The electrons are accelerated by that and can reach, due to their small mass more easily compared to other heavier particles in the plasma, relativistic energies. There is no complete understanding of the different absorption mechanisms, which are depending on a lot of different laser and target parameters (Davies 2008).

The free electrons in the plasma interact with the electric and magnetic parts of the laser field. The electric field accelerates them perpendicular (transversally) to the laser propagation direction and the magnetic field accelerates along (longitudinally) the laser propagation direction. In the frame of reference of the electron, the electron is moving on a trajectory that is forming an eight (Gibbon 2004). For very high laser intensities the electrons reach relativistic velocities and therefore the interaction

between laser and electrons becomes dominated by relativistic effects. This regime of laser intensities is reached when the mean energy an electron can gain during one half cycle of the laser wave exceeds the rest energy of the electron (Mourou, Tajima, and S. V. Bulanov 2006):

$$eE_0\lambda > 2\pi m_e c_0^2 \quad (2.28)$$

where E_0 is the amplitude of the laser field. For a laser of wavelength $\lambda = 1 \mu\text{m}$, this is reached for intensities above $10^{18} \text{ W cm}^{-2}$ (Mourou, Tajima, and S. V. Bulanov 2006).

However, absorption can already occur below the relativistic limit. In this case, one of the dominating mechanisms is the inverse bremsstrahlung (Langdon 1980). In that process the energy is transferred through collisions with the target-ions to free electrons. Thus, collisions are of great importance for that process. But the collisional frequency is already decreasing strongly below the relativistic limit due to the increase in temperature of the matter. An estimation of the collisional frequency of electrons with ions is given by (Dendy 1995):

$$\nu_{ei} = \frac{4(2\pi)^{1/2}}{3} \frac{n_e Z e^4}{m^2 v_{te}^3} \ln \Lambda \approx 2.91 \times 10^{-6} \frac{Z n_e [\text{cm}^{-3}] \ln \Lambda}{(T_e [\text{eV}])^{3/2} \text{s}} \quad (2.29)$$

here Z is the number of free electrons per atom, n_e the electron density in cm^{-3} , T_e is the electron temperature in eV and $\ln \Lambda$ is the Coulomb-logarithm, accounting for the usual limits, b_{min} and b_{max} , of the electron-ion scattering cross-section. Here, these are determined by the classical distance of closest approach and the Debye-length respectively, so that (Gibbon 2004):

$$\Lambda = \frac{b_{max}}{b_{min}} = \lambda_D \times \frac{k_B T_e}{Z e^2} = \frac{9 N_D}{Z} \quad (2.30)$$

where

$$\lambda_D = \sqrt{\frac{k_B T_e}{4\pi n_e e^2}} = \frac{v_{te}}{\omega_p}, \quad (2.31)$$

and

$$N_D = \frac{4\pi}{3} \lambda_D^3 n_e \quad (2.32)$$

is the number of particles in a Debye-sphere.

The higher the laser intensity the higher the reachable electron temperature. That means that the probability for the collisions between electrons and ions decreases. Effective absorption above intensities of $10^{18} \text{ W cm}^{-2}$ are therefore only possible through collisionless absorption mechanisms (Davies 2008).

2.2.7 Formation of Relativistic Laser Channels in Plasma

Different nonlinear and relativistic effects lead to focussing of a Gaussian laser pulse inside a plasma. Firstly, the refractive index in matter is reduced along the intensity profile at high intensities. The wave fronts are bent in the direction of the beam axis. This is due to the Kerr-effect:

$$n(I_L) = n_0 + n_2 I_L \quad (2.33)$$

where n_2 is the Kerr-coefficient. Secondly, at relativistic intensities, the mass of the electrons is increased with the Lorentz-factor γ . The closer to the beam axis an electron is accelerated the higher γ . This changes the plasma frequency and consequently the refractive index. Thirdly, the ponderomotive force pushes electrons away from the beam axis which produces a density gradient. Altogether, a relativistically intense laser beam propagating in an underdense plasma modifies the plasma permittivity and the refractive index (Alexander Pukhov 2003):

$$n_{rel}^2 = \varepsilon = 1 - \frac{\omega_{p,rel}^2}{\omega_L^2} \quad (2.34)$$

where $\omega_{p,rel}^2 = 4\pi n_e / \gamma m_e$ is the relativistically corrected plasma frequency. The relativistic mass γm_e of electrons quivering in the electric field of the laser pulse increases. In addition, the ponderomotive force of the laser pulse pushes the plasma electrons radially out of the focal spot. Both these effects diminish the local plasma frequency and increase the plasma refractive index n_{rel} . The medium then acts as a positive lens. One may show that when the laser power P exceeds the critical value (Alexander Pukhov 2003)

$$P_{cr} \approx 17 \left(\frac{\omega_L}{\omega_p} \right)^2 GW, \quad (2.35)$$

the laser pulse experiences relativistic self-focusing and channels through the plasma (Max, Arons, and Langdon 1974; Borisov et al. 1992). This effect is known as relativistic filamentation.

Fig. 2.5 shows the results of simulations that were performed in preparation of the experiments discussed in this work (Pugachev, N E Andreev, et al. 2016). The formation of a relativistic laser channel and its filamentation inside a foam is visible.

2.2.8 Limits of Magnetic Self-Focusing at relativistic Intensities and Super-Channel Formation

The threshold for relativistic self-focusing/filamentation depends on the laser power only. If the laser pulse is wide enough self-focusing occurs even at moderate laser intensities. Electrons are accelerated by the Lorentz force in the forward direction when the intensity becomes $a_0 \geq 1$. In plasma, all electrons trapped in the laser channel are

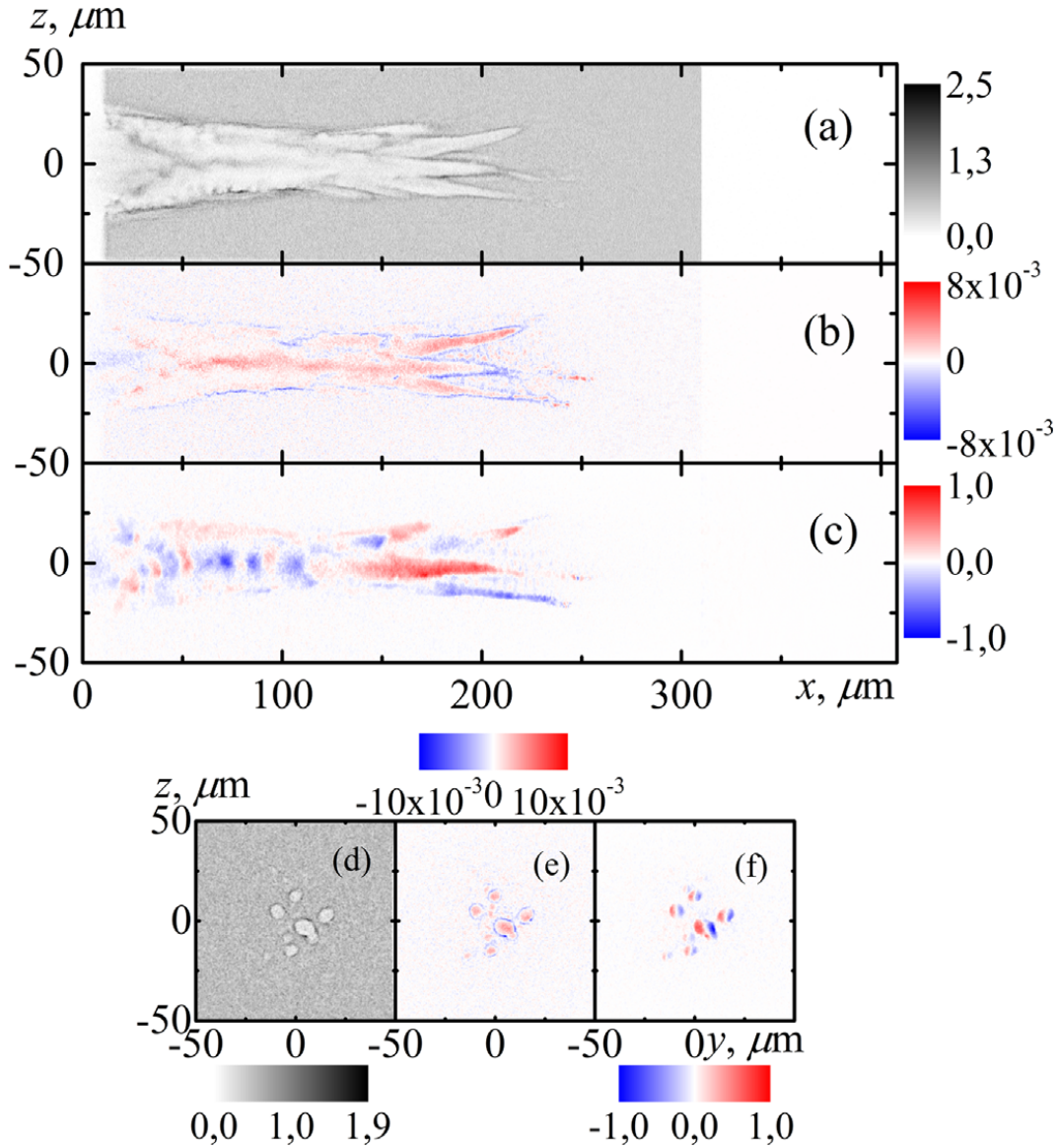


FIGURE 2.5: Simulation with the target thickness $l = 300 \mu\text{m}$ at $c_0 t = 300 \mu\text{m}$, a Gaussian spatial and temporal pulse profile with $I_L = 4 \times 10^{19} \text{ W cm}^{-2}$, $d_{FWHM} = 25 \mu\text{m}$ and $\tau_{FWHM} = 400 \text{ fs}$. The pulse is polarised in y -direction. Distributions in the plane $y = 0$: (a) electron density, (b) averaged over the laser period current density $\langle j_x \rangle$, (c) averaged over the laser period magnetic field $\langle b_z \rangle$. Distributions in the plane $x = 200 \mu\text{m}$: (d) electron density, (e) averaged over the laser period current density $\langle j_x \rangle$, (f) averaged over the laser period magnetic field $\langle b_z \rangle$ (Pugachev, N E Andreev, et al. 2016).

driven, and each laser filament carries a strong electron current (Alexander Pukhov 2003).

These currents of relativistic electrons pushed forward by the laser pulse magnetize the plasma. This generates quasi static magnetic fields $B_{s,\perp}$ at the distance r (Alexander Pukhov 2003):

$$B_{s,\perp} = B_0 \left(\frac{fn_e}{n_{crit}} \right) \frac{\pi r}{\lambda} \quad (2.36)$$

where $B_0 = mc_0\omega/e$, n_e is the background electron density, n_{crit} is the critical electron density for a certain wavelength λ , and f is the fraction of $en_e c_0$. $B_{s,\perp}$ can reach an order of magnitude of 10^4 T for $\lambda = 1 \mu\text{m}$.

The multiple filaments of the laser pulse inside the plasma can coalesce into one super-channel due to the large magnetic fields pinching the currents. The light channels follow the currents, guided by the refractive index modified by the fast electrons. Coalescence only occurs if the laser width is small enough. Indeed, if the laser pulse is much wider than the plasma skin length $l_s = c_0/\omega_p$, the distance between the individual filaments may be so large that their individual magnetic fields are shielded in the surrounding plasma. These filaments do not feel each other anymore and cannot coalesce. The skin depth for the foam targets with $n_e = 7 \times 10^{20} \text{ cm}^{-3}$ used in this work would require a laser spot size of $0.2 \mu\text{m}$ to let coalescence occur.

2.2.9 Direct Laser Acceleration (DLA)

A further mechanism for the generation of ultra-relativistic laser accelerated electrons is the mechanism of Direct Laser Acceleration (DLA) (Pukhov, Sheng, and Meyer-ter-Vehn 1999). This mechanism is very efficient in the Near Critical Density (NCD) regime of a plasma where the laser pulse channels due to relativistic and ponderomotive effects (Sun et al. 1987). Both experiments (Key et al. 1998; Wharton et al. 1998; G. Malka et al. 1997), and Particle in Cell (PIC) simulations (Pukhov and Meyer-ter-Vehn 1996; Pukhov and Meyer-ter-Vehn 1997; Pukhov and Meyer-ter-Vehn 1998) suggest that this conversion does operate with significant efficiency, up to 30–40%. The spectra of these electrons usually show a quasi-thermal Maxwellian-like behaviour in the spectra, which can be characterised by an exponential slope with some effective 'temperature' (Alexander Pukhov 2003). The normal ponderomotive scaling in the spectra is superceeded by far by the tail of these spectra. The electron acceleration in laser-plasma channels is very different to the simple picture of a single free electron in a plane electromagnetic wave (Alexander Pukhov 2003).

2.2.10 Inverse Free Electron Laser at the Channel Betatron Resonance

When a laser-plasma channel is formed, it is accompanied by the presence of quasi static radial electric and azimuthal magnetic fields inside the channel. They are created when the ponderomotive force of the laser-pulse expels electrons from the

channel. A significant amount of electrons are driven from the laser propagation axis while ions stay in place during the time of the laser-matter interaction. Hence, a charge density distribution is formed that has an inwardly directed radial quasi-static (on the timescale of the laser pulse) electric field. Electrons still inside this channel are trapped by this field. An amount of electrons is accelerated in forward direction alongside the laser propagation direction. This electron current generates a quasi-static azimuthal magnetic field, which has field strengths in the range of a few kT (Pukhov, Sheng, and Meyer-ter-Vehn 1999). Both these fields depend approximately linearly on the radius and reach their maxima at the channel boundaries. The contribution of the electric and magnetic forces on the electron motion inside the channel depend on the fraction f of cavitation inside the channel. The electric field dominates for small $\beta = v/c_0$ if f is large and the total force becomes independent of f for $\beta \rightarrow c_0$ (M. Kaluza n.d.). The Larmor-radius for electrons with velocities approaching the speed of light in a magnetic field of 1 kT is in the order of $2 \mu\text{m}$ and therefore, smaller than the laser spot sizes used in this work.

Simulation suggest that there is no complete cavitation inside the channel. This is because of the strong heating of plasma electrons in the channel by the laser pulse (Pukhov and Meyer-ter-Vehn 1997; Tzeng, Mori, and Katsouleas 1999). We may introduce the effective charge neutralisation factor $f = n_e/n_i$ in the channel. Typically, $f \sim 0.5$ (Borghesi, MacKinnon, et al. 1997). The channel works as a potential well. A relativistic electron trapped in the channel oscillates radially at the betatron frequency which is roughly $\omega_\beta = \omega_p/2\gamma^{1/2}$ and does not depend on the degree of channel cavitation. For the betatron oscillation with frequency ω_β and amplitude x_0 in x-direction follows (Alexander Pukhov 2019):

$$\vec{x} = x_0 \cos(\omega_\beta t) \vec{e}_x \quad (2.37)$$

and consequently the betatron phase ϕ_β is given by:

$$\phi_\beta = \omega_\beta t. \quad (2.38)$$

The real part of the E-field of the laser in eq. 2.1 is:

$$\text{Re}(e^{-ix}) = \text{Re}(\cos(x) - i \sin(x)) = \cos(x). \quad (2.39)$$

Therefore, the laser electric field running in z -direction with the phase velocity v_{ph} is:

$$\vec{E}_L = E_0 \cos(\omega_L t - kz) \vec{e}_z \quad (2.40)$$

and hence the laser phase is:

$$\phi_L = \omega_L t - kz = \omega_L \left(t - \frac{z}{v_{ph}} \right) \quad (2.41)$$

where $v_{ph} = \omega/k$ is the laser phase velocity. with the particle velocity v_z follows for the position z of the particle:

$$z = v_z t \quad (2.42)$$

The betatron resonance condition is:

$$\phi_\beta = \phi_L \quad (2.43)$$

This leads to:

$$\omega_\beta t = \omega_L \left(t - \frac{z}{v_{ph}} \right) = \omega_L \left(t - \frac{v_z t}{v_{ph}} \right) = \omega_L t \left(1 - \frac{v_z}{v_{ph}} \right) \quad (2.44)$$

An efficient energy coupling of the laser energy into electrons is possible as the oscillations are along the laser polarisation. An electron running along the laser propagation with velocity v_z witnesses a strongly downshifted optical frequency. This downshift can be so strong that the transverse betatron oscillations are in resonance with the laser. Both frequencies are electron energy dependent, which allows for a broadband resonant energy transfer, as the two frequencies remain matched over a wide range of electron energies during the electron energy gain (Khudik et al. 2016). The resonance condition for the driving force of the laser is hit when (Alexander Pukhov 2003):

$$\omega_\beta = \left(1 - \frac{v_z}{v_{ph}} \right) \omega_L \quad (2.45)$$

with ω_β the betatron frequency, v_z the longitudinal velocity of an electron and v_{ph} the phase velocity of the laser inside the channel respectively. This resonance condition states that when an electron makes one oscillation, the electromagnetic wave, which propagates with a phase velocity $v_{ph} > c_0$, overtakes it exactly by one period (see fig. 2.6). This is the inverse free electron laser mechanism. The only difference is that instead of the usual spatially periodic wiggler we have the betatron channel frequency.

2.2.11 Hot electron scaling laws

Due to the fact that the mass of the electron is much smaller than the mass of the nuclei in the plasma, the laser energy is transferred to the electrons but not the nuclei. Only a small fraction of hot electrons is created (in the range of 10^{-3} –1%) (Forslund, Kindel, and Lee 1977). Hot electrons transverse the target and dissipate some of their energy by collisions. In that process they heat up the material and emit bremsstrahlung radiation. The displacement of the hot electrons will also produce strong electric fields either inside the target or near the target surface that induce return currents of bulk electrons and acceleration of protons and other ions on the target surface. To characterise the hot electron energy distribution, 'effective

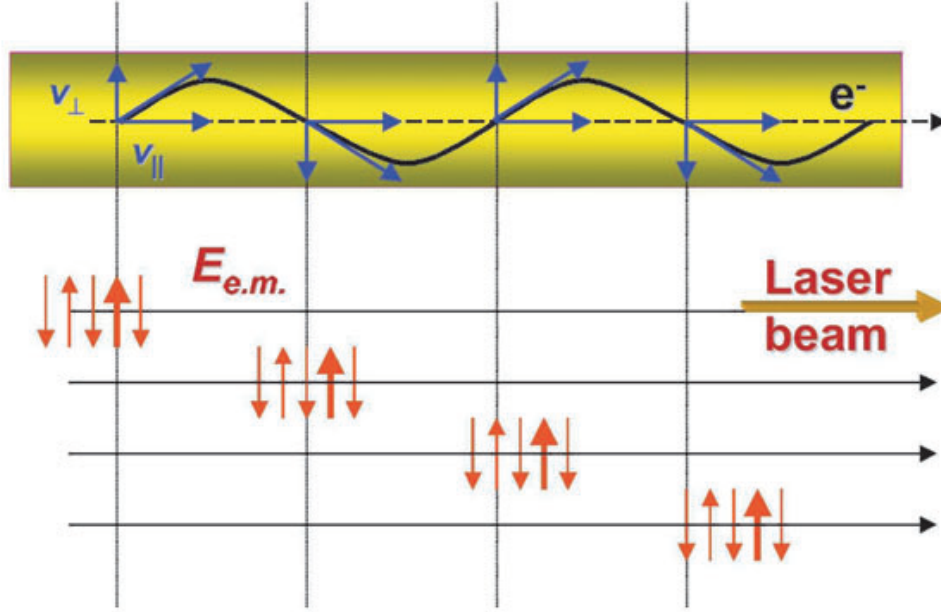


FIGURE 2.6: Resonance between the electromagnetic wave and a co-propagating relativistic electron. The electron makes transverse oscillations in the channel fields along the laser polarisation and stays in phase with the electric field of the wave, when the resonance condition eq. 2.45 is satisfied (Alexander Pukhov 2003).

temperature' laws are introduced to take different physical mechanisms and their mixture into account. However, the term 'effective temperature' does not mean that the electrons underwent enough collisions to reach thermal equilibrium, but rather the fact that they show quasi-maxwellian energy distributions. Experimental results often show that several maxwellian-like distributions of electrons are present in a single laser-target interaction and therefore cannot be described by a single 'effective temperature'.

Wilks Scaling The scaling law after Wilks et al. is based on 2D-PIC simulations and shows a similarity to the hot electron temperature estimate based on the relativistic ponderomotive force, with an analytical equation of (Wilks et al. 1992):

$$T_{Hot}^W = 511 \text{ keV} \times \left(\sqrt{1 + 0.73 \times I_L [10^{18} \text{ W/cm}^2] \times (\lambda_L [\mu\text{m}])^2} - 1 \right) \quad (2.46)$$

where I_L is the laser intensity and λ_L the laser wavelength.

Direct Laser Acceleration The Maxwellian-like shape of the electron spectra generated in the laser channel was evaluated theoretically in 3D-PIC-simulation and show an approximately exponential behaviour (Pukhov, Sheng, and Meyer-ter-Vehn 1999):

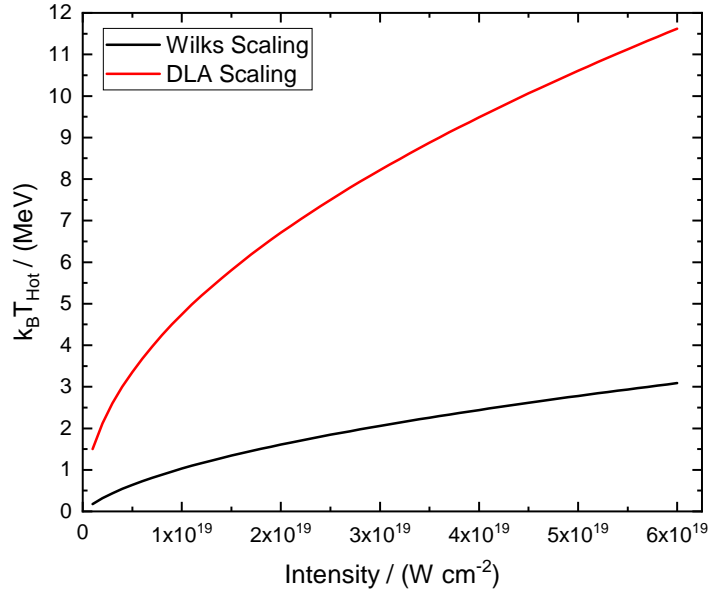


FIGURE 2.7: Comparison of the hot electron temperature scaling laws of Wilks et al. (Wilks et al. 1992) and in DLA by Pukhov et al. (Pukhov, Sheng, and Meyer-ter-Vehn 1999).

$$n_e(\varepsilon) \sim n_0 \exp\left(-\frac{\varepsilon}{T_{eff}}\right) \quad (2.47)$$

with an 'effective temperature' T_{eff} growing with laser intensity. The results of the numerical simulations suggest that T_{eff} grows like the square root of the intensity:

$$T_{eff}^{DLA} \sim \alpha \left(\frac{I}{I_{18}}\right)^{1/2} \quad (2.48)$$

where the coefficient is $\alpha \approx 1.5 \text{ MeV}$. These results with the behaviour of $I^{1/2}$ coincide with 2D-PIC-simulations but show a significantly higher α . This higher temperature is due to the presence of a long laser channel and the mechanism of DLA.

Comparison of Hot Electron Temperatures The above mentioned mechanisms of generation of hot electrons have in common, that their energy distribution can be described by a temperature T_{Hot} according to their maxwellian like behaviour. Hence, the different processes produce in general electrons of different temperatures, the hot electron distribution can show a lot of different temperature profiles in their spectrum. Also, inhomogeneities in the laser focus or target density can have influence on the hot electron temperature. Therefore, in general, for i different mechanisms involved, the hot electron numbers per energy interval result in:

$$\frac{dN(E_{kin})}{dE} [MeV^{-1}] \approx \sum_{i=1}^n a_i [MeV^{-1}] \times \exp\left(-\frac{E_{kin} [MeV]}{k_B T_i [MeV]}\right) \quad (2.49)$$

with E_{kin} the kinetic energy of the electrons, T_i the characteristic temperatures and a_i their weighting factors.

2.3 Interaction of Heavy-Ions and Electrons with Cold Matter

The particles accelerated by either laser or ion accelerator can be used in various applications. The interaction with cold matter plays a great role in e.g. the generation of X- and gamma-rays. In this section, the interaction processes between energetic particles and cold matter is discussed. In particular, the stopping power, generation of bremsstrahlung, characteristic line radiation, X-ray fluorescence absorption of electromagnetic radiation in matter are introduced.

2.3.1 Stopping Power in Cold Matter

Particles moving through matter will interact with the surrounding particles and hence lose kinetic energy on their track (M J Berger et al. 1993; Weick et al. 2002). The lost energy can either be transferred to the particles of said matter, and thus heat it, or be emitted by radiation. The radiation can either be emitted by the traversing particle or a particle in the matter itself. As the traversing particles are losing kinetic energy during the passage through the matter, that property of matter is called stopping power. It is, as mentioned, due to collisional and radiative losses (Physical Measurement Laboratory 2019a; Bethe 1930; Bethe 1932; Rudolph M Sternheimer 1952; R M Sternheimer, S M Seltzer, and M J Berger 1982; R M Sternheimer, S M Seltzer, and M J Berger 1983; Stephen M Seltzer and Martin J Berger 1985; Pratt et al. 1977; Sigmund 2006).

Collisional losses describe losses that are due to inelastic scattering with the particles in the matter. The inelastic Coulomb-scattering leads to excitation or ionisation of the traversing particles and the matter they are moving through. For energies high enough, that can heat the matter. The stopping of the passing particle for the same path length is only depending on the kinetic energy of the particle and on the properties of the matter.

Estimations about the applicability of classical or quantum mechanical calculations can be achieved using the Sommerfeld parameter η (Breit 1967; Rolfs, Rodney, and Rodney 1988):

$$\eta = \frac{Z_1 Z_2 e^2}{4\pi\epsilon_0 \hbar v} = \alpha Z_1 Z_2 \sqrt{\frac{\mu c_0^2}{2E}} \quad (2.50)$$

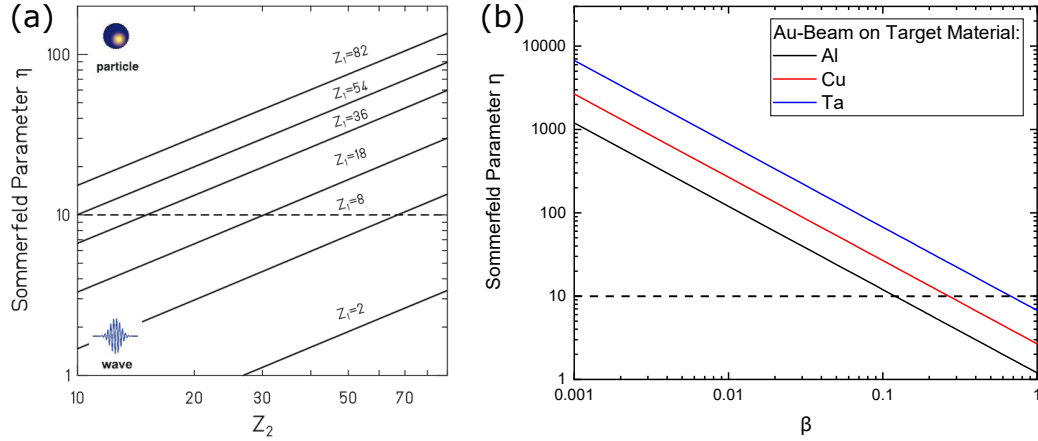


FIGURE 2.8: Sommerfeld parameter η (a) at a bombarding energy of 100 A MeV as a function of the target charge number Z_2 for various projectiles (Wollersheim 2011) and (b) for an Au-ion beam with velocity $\beta = v/c$ onto Al-, Cu- and Ta-target material. The boundary to quantum mechanical corrections is determined at lower beam energies and indicated by the dashed line.

with Z_1 and Z_2 the atomic numbers of two interacting nuclides respectively, v the magnitude of the relative incident velocity in the center-of-mass frame, α the unitless fine-structure constant, and μ the reduced mass of the two nuclides of interest. Classical calculations can be applied in the case of $\eta \gg 1$. Quantum mechanical correction have to be considered for $\eta \ll 1$ (Wollersheim 2011). Fig. 2.8 (a) shows the Sommerfeld parameter for a wide range of Z_1 and Z_2 . Additionally, Fig. 2.8 (b) shows η for the Au-ion beam with velocity $\beta = v/c$ onto Al-, Cu- and Ta-target material as used in this work. This shows $\eta > 1$ always and $\eta \gg 1$ for moderate values of β of the Au-ions.

The stopping power is given by the Bethe-Bloch-formula in the relativistic version for a particle with speed v , charge z in multiples of the elementary charge e , and Energy E , travelling a distance x into a target of electron number density n_e and mean excitation potential I (Bethe 1930; Bethe 1932; Sigmund 2006):

$$-\left\langle \frac{dE}{dx} \right\rangle = \frac{4\pi}{m_e c_0^2} \times \frac{n_e z^2}{\beta^2} \times \left(\frac{e^2}{4\pi\epsilon_0} \right)^2 \times \left[\ln \left(\frac{2m_e c_0^2 \beta^2}{I \times (1 - \beta^2)} \right) - \beta^2 \right] \quad (2.51)$$

where $\beta = \frac{v}{c_0}$. Here, the electron density of the material can be calculated by

$$n_e = \frac{N_A Z \rho}{A M_u} \quad (2.52)$$

where ρ is the mass density of the material, Z its atomic number, A its relative atomic mass, N_A the Avogadro constant and M_u the molar mass constant. An example for gold particles traversing cold copper target material is shown in fig. 2.9.

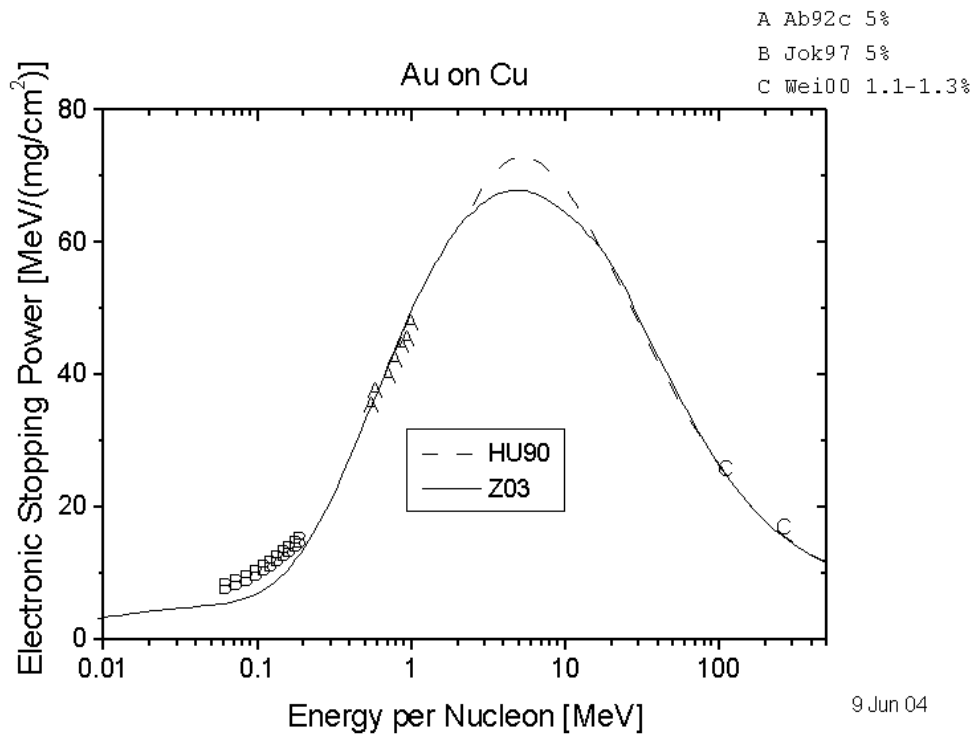


FIGURE 2.9: Electronic stopping power of gold on cold copper (Nuclear Data Services 2019).

2.3.2 The Beer-Lambert Law

The intensity of transmitted radiation is reduced continuously by matter. This is depending on the path length travelled by photons through the matter. The attenuation of radiation in matter is given by the Beer-Lambert law (Swinehart 1962; Creagh and Hubbell 1987):

$$I(x) = I_0 e^{-\mu_l x}, \quad (2.53)$$

where I_0 is the intensity of the incident electromagnetic radiation and I is the emergent radiation. The directions of the incident and emergent radiation must be exactly the same. The path travelled through the material by the radiation is x .

In eq. 2.53, the linear attenuation coefficient μ_l of the material, which is dependent on the sample density, is used. Additionally, it depends on the effective atomic weight and atomic structure properties of the sample. Furthermore, as the density of a given elemental substance can vary widely (allotropic versus various crystalline forms, vapour/liquid/solid phases, thermal expansion etc.), a coefficient more uniquely characterising a given substance is the density-independent mass attenuation coefficient μ_m .

The mass attenuation coefficient is defined as

$$\mu_m = \mu_l / \rho \quad (2.54)$$

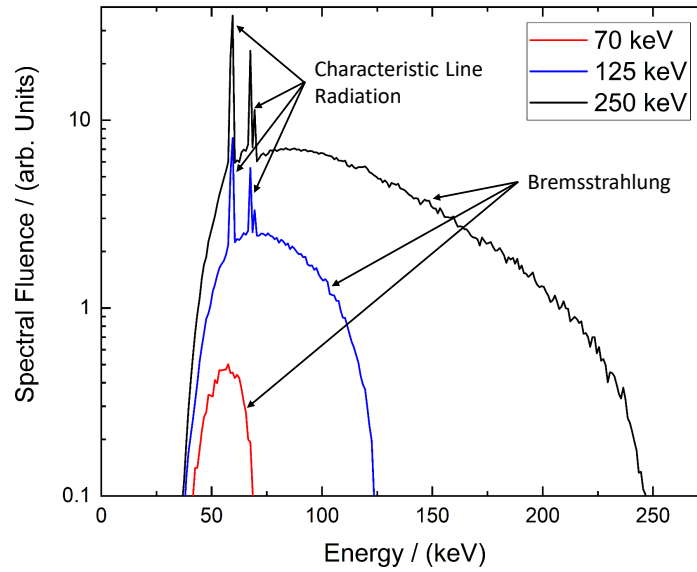


FIGURE 2.10: Simulated spectrum of an X-ray tube with different acceleration voltages. The spectrum consists of bremsstrahlung and characteristic line radiation. The low energy cut-off is due to an X-ray window between Cu-anode and detector. Calculations by Felix Horst.

where ρ is the mass density of the medium.

The mass attenuation coefficient is proportional to the total photon interaction cross section per atom,

$$\sigma = \mu_m M / N_A \quad (2.55)$$

where N_A is the Avogadro number and M is the atomic weight of the sample material.

2.3.3 Bremsstrahlung

Radiative losses, mentioned above, originate from the loss of energy through the emission of radiation. Acceleration of charged particles leads to the emission of electromagnetic waves. That is a direct consequence of the classical theory of electrodynamics (Jackson 1999). In quantum mechanics, there is a small but finite probability that a photon is emitted each time a charged particle is accelerated. As the particles are decelerated during this process, that radiation is called bremsstrahlung (deceleration radiation, german: Bremsstrahlung). The radiation is produced by the interaction of the traversing particle with the fields of electrons and nuclei of the atoms of the target material. As the particles are decelerated continuously, the spectrum of the Bremsstrahlung is also continuous (see fig. 2.10).

Due to conservation of energy, a cut-off of wavelengths λ_{min} appears where all of the kinetic energy E_{kin} of a single particle would be converted into a single photon of the radiation:

$$\lambda_{min} = \frac{hc_0}{E_{kin}}. \quad (2.56)$$

As a particle that is accelerated in matter is accelerated in the field of a nucleus, the angular distribution is that of a radiating dipole (Haug and Nakel 2004):

$$\frac{dI}{d\Omega} \propto \sin^2 \theta \quad (2.57)$$

where θ is the emission angle relative to the dipole axis. Radiation of this kind is called dipole radiation. The radiation patterns are shown qualitatively in fig. 2.11. For $v \ll c$ no energy is radiated in forward or backward direction along the direction of the acceleration and the maximum of the radiation is perpendicular to this direction. When the acceleration is perpendicular to the direction of motion of the charged particle, the maximum of the radiation is in direction of the motion. For both cases, the radiation pattern is toroidal. For the case of $v \rightarrow c$, the distribution is not symmetric about $\theta = 90^\circ$ anymore and becomes increasingly forward peaked for increasing incident energy. Both, the non relativistic and the relativistic case are shown qualitatively in fig. 2.11. For electron energies $E > 2m_e c_0^2 \approx 1$ MeV, the energy loss of electrons in matter becomes increasingly dominated by pair production while pair production from bremsstrahlung photons produced in thick targets contributes significantly to pair production as well (Tsai 1974; Gryaznykh, Kandiev, and Lykov 1998).

2.3.4 Relativistic Doppler Effect

The radiation of particles moving at a velocity v relative to the detector will experience a Doppler-shift. The wavelength λ_0 of a photon emitted under an angle θ is shifted in the relativistic case to λ_D according to:

$$\lambda_D = \lambda_0 \gamma (1 + \beta \sin(\theta)) = \lambda_0 \left(\frac{1}{\sqrt{1 - \beta^2}} + \frac{\beta \sin(\theta)}{\sqrt{1 - \beta^2}} \right) \quad (2.58)$$

with $\beta = v/c_0$, and the Lorentz factor $\gamma = \frac{1}{\sqrt{1 - \beta^2}}$.

2.3.5 Characteristic Line Radiation and X-Ray Fluorescence Radiation

Particles and electromagnetic radiation traversing matter will transfer energy to the material they are penetrating as mentioned above. There is not only a continuous part in the emission of radiation, that might stem from that interaction but also characteristic line radiation, also called fluorescence radiation, may occur (Beyer and

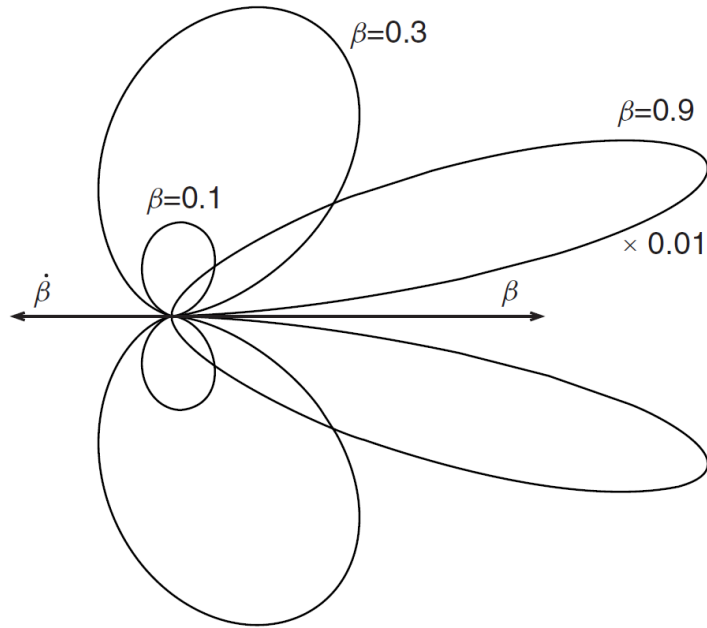


FIGURE 2.11: The theoretical emission pattern of solid-target bremsstrahlung. The curve for $\beta = 0.9$ was multiplied by 0.01. It clearly reveals the strong forward boost at high particle velocity (Beyer and Shevelko 2016).

Shevelko 2016; Beckhoff et al. 2007; Jenkins 2012). The radiation is called characteristic, as the energy of the emitted photons is characteristic to an element and, in particular, to the electronic transitions in their hull. For inner shell transitions in heavier elements, the energy of the emitted photons may lie in the X-Ray range (see fig. 2.10).

When a particle with mass or a photon hit the material, they can interact inelastically with the atoms in the matter and transfer energy to the electrons and, therefore, either excite the electron from one shell in the hull to a higher shell, or even, if they carry enough energy ($E_{transf} > W_I$), ionise the atom by lifting the electron to the continuum. There, it is not bound anymore and carries the energy $E_{kin} = E_{transf} - W_I$ away from that reaction. A so created hole in a shell of the atom can then be filled by either another electron from a shell inside the atom or an electron from outside the atom. If no Auger-effect, dielectronic recombination, or three-body recombination occurs, the difference in the energy for that electron is emitted by a photon due to photo-recombination. The energy of the emitted photons due to photo recombination is continuous (Beyer and Shevelko 2016).

If only bound electrons are involved and the excess energy of a deexcitation is carried away by a photon, the the spectrum of the photons is a line-spectrum, where the energy of the photons satisfy Mosley's law (Moseley 1913):

$$E = h\nu = E_i - E_f = Z_{eff}^2 Ry \left(\frac{1}{n_i} - \frac{1}{n_f} \right) \quad (2.59)$$

where

$$Ry = hc_0 R_\infty = \frac{m_e e^4}{8\epsilon_0^2 h^2} \approx 13.6 \text{ eV} = 2.179 \times 10^{-18} \text{ J} \quad (2.60)$$

is the Rydberg unit of energy, R_∞ is the Rydberg-constant, Z_{ee} is the effective atomic number. This can be refined to account for the masses of the electron m_e and the total mass of the nucleus M by replacing R_∞ with R_M (Beyer and Shevelko 2016):

$$R_M = R_\infty / (1 + m_e/M) \quad (2.61)$$

2.3.6 Inner Shell Vacancy Production in Heavy-Ion-Atom Collisions

When a heavy-ion is traversing a target it can deposit energy in different channels as mentioned above. One of them is ionisation of target atoms and heavy-ions of the beam itself by the interaction between their respective Coulomb fields of nuclei and shell electrons. This is for example applied in gas and solid foil strippers (Baron 1972) and was studied semi-empirically (Sayer 1977). Projectiles traversing a target thick enough will reach an equilibrium charge state where ionisation and electron capture are equal. These projectiles are called equilibrated.

Ionisation and electron transfer involving inner shells are the two dominant processes in case of heavy-ion collisions (Kadhane, Montanari, and Tribedi 2003). The precise theoretical description for multi electron systems is challenging (Beyer and Shevelko 2016; C. Foster et al. 1976; Eichler 1977). We define Z_p and Z_t as the nuclear charges of the projectile and target respectively. Additionally, the scaled projectile velocity v_{sp} is defined as (Randall et al. 1976):

$$v_{sp} = \sqrt{\frac{E}{1840} MU_k} \quad (2.62)$$

with E and M the projectile laboratory energy in MeV and mass in amu, respectively, and U_k is the target K-shell binding energy. For Z_p/Z_t small compared to v_{sp} , the direct ionisation of the target K-electron by Coulomb interaction with the projectile nuclear charge should dominate the target K-vacancy-production cross section (Randall et al. 1976).

But not only the velocity of the projectile is of importance. Let Z_l and Z_h be the atomic number of the lower- Z and higher- Z collision partner, respectively, independent of which one is the projectile or the target. Then, if $Z_l \ll Z_h$, vacancy production in the higher- Z partner can be treated as the perturbative interaction of a charged point particle with the higher- Z electronic wave function (atomic regime). If $Z_l \approx Z_h$ and if $v_p \ll v_{en}$, where v_p is the projectile velocity and v_{en} the Bohr velocity of the ejected electron in the n -shell ($n = \text{K, L, M, ...}$), a molecular description becomes relevant. The velocity v_{en} is related to the binding energy U_{en} of the ejected electron by (Meyerhof and Taulbjerg 1977):

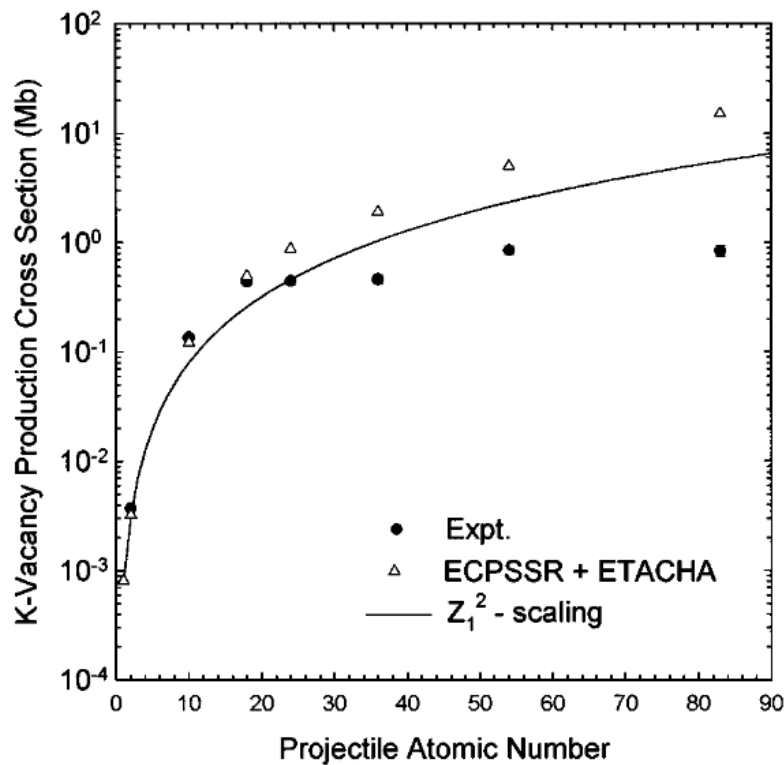


FIGURE 2.12: Comparison of the Cu K-shell vacancy production cross sections for equilibrated projectiles with energies of 10 MeV/u to theoretical total cross sections that were averaged over target thickness (Watson, Blackadar, and Horvat 1999).

$$v_{en} = \sqrt{\frac{2U_{en}}{m_e}}. \quad (2.63)$$

The above mentioned challenges in the theoretical description of total cross sections for the K-vacancy production are visible in comparison to experimental data (Watson, Blackadar, and Horvat 1999). Fig. 2.12 shows experimental and theoretical data of the K-shell vacancy production cross sections for equilibrated projectiles with energies of 10 MeV/u (in this figure $Z_p = Z_1$). It is assumed that the occurrence of plateaus in the region around $Z_p = 27$ where $Z_p/Z_t \approx 1$ and $Z_p = 54$ can be accounted for by electron capture to the projectile K- and M-shells.

The production of a K-vacancy in the projectile or target atom can be accompanied by the production of another K-vacancy or one or more L-vacancies in the same atom. The K X-rays from decays of excited states with such multiple inner shell vacancies have higher energies than that from a single K-vacancy state. Therefore, X-ray spectra from the collisions have satellite and hyper satellite structures that can be observed in high-resolution X-ray measurements (Awaya, Kambara, and Kanai 1999). The involvement of multiple inner shells in the reactions increases the complexity of the problem even further than already mentioned above. In asymmetric systems where $Z_p + Z_t \geq 100$, with the K-level of the lighter collision partner lying

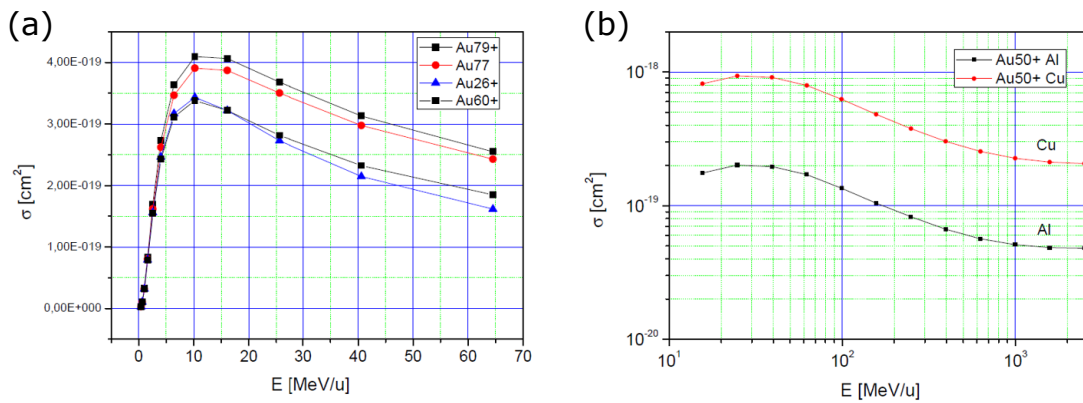


FIGURE 2.13: (a) Cross sections of Cu-target K-vacancy production by Au-ions of different charge states between 26+ and 79+ and energies up to 65 MeV/u. (b) Cross sections of Au^{50+} -ions L-vacancy production in Cu- and Al-targets between 10 (energies provided by the UNILAC at GSI Helmholtz Centre) and 3000 MeV/u (energies provided by SIS18 at GSI). Calculations by Viacheslav P. Shevelko (Olga N Rosmej 2016).

energetically above the L-level of the heavier one, the M-shell of the heavier particle is correlated to the united atom M-shell (Warczak et al. 1983).

2.3.7 Atomic Radiative and Radiationless Yields and Line Widths for K-Shells

After the generation of a hole in an ion during beam-target interaction, this hole will be filled by other electrons of that ion. There exist two competing processes in heavy-ion-atom collisions that lead to the filling: The emission of fluorescence radiation by deexcitation of electrons in the ion and the Auger-effect. The Auger-effect describes the filling of an inner-shell vacancy accompanied by the emission of another electron, both by electrons of another shell in the same ion. The ratio between the yields of both processes depends on Z (see fig. 2.14) (Krause 1979).

The lifetime τ of a single hole in a given level is related to the natural width Γ of that level by the uncertainty principle (Krause 1979):

$$\Gamma\tau = \hbar. \quad (2.64)$$

The rate $S = 1/\tau$ of all processes to fill the hole then leads to:

$$S = \frac{\Gamma}{\hbar} \quad (2.65)$$

With the assumption of the different decay modes being independent, the total rate S will be given by the sum of the partial rates

$$S = S_R + S_A + S_C \quad (2.66)$$

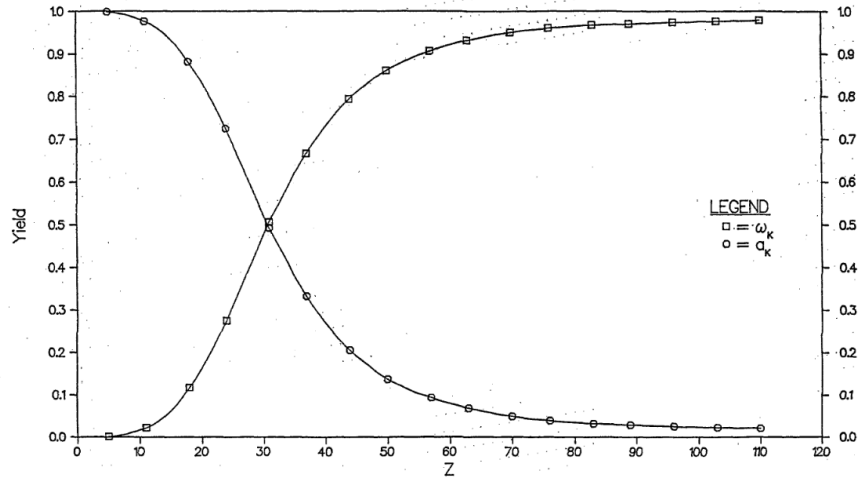


FIGURE 2.14: K-shell fluorescence and Auger yields (Krause 1979).

and the total level width (natural width) by

$$\Gamma = \Gamma_R + \Gamma_A + \Gamma_C \quad (2.67)$$

where subscripts denote the radiative, Auger, and Coster-Kronig (similar to Auger effect but by electron from higher subshell of the same shell) branches (see fig. 2.15). The yields for the various processes are defined as follows:

$$\omega = \Gamma_R / \Gamma \quad (2.68)$$

$$a = \Gamma_A / \Gamma \quad (2.69)$$

$$f = \Gamma_C / \Gamma \quad (2.70)$$

The sum of radiative yield ω and radiationless yields a and f is unity:

$$\omega + a + f = 1. \quad (2.71)$$

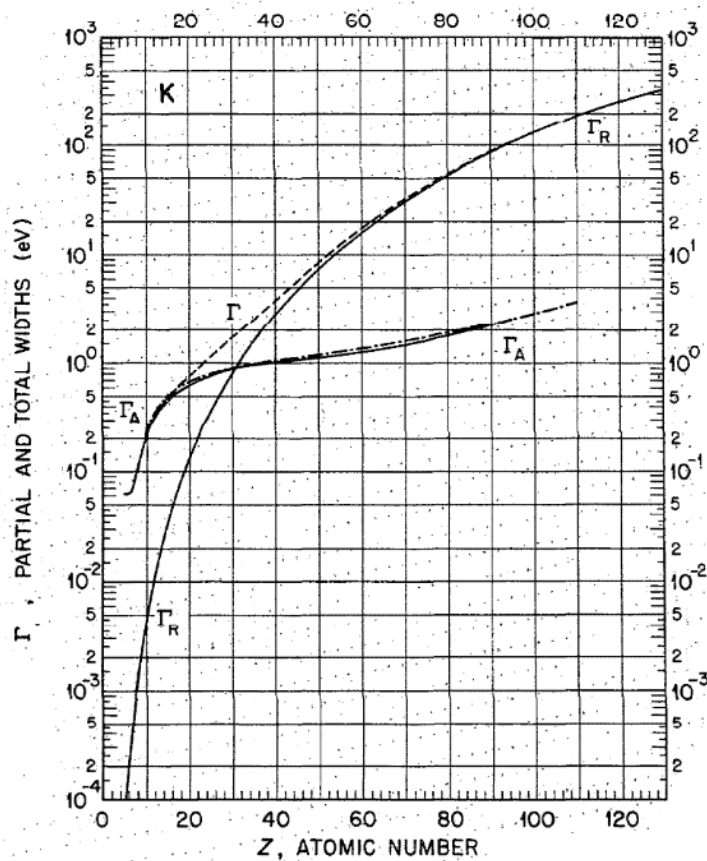


FIGURE 2.15: Theoretical partial and total atomic level widths for K-shell. Γ_A = Auger width, Γ_R = radiative width, Γ = total width. Dot-dash curve represents semi-empirical Γ_A = curve obtained from adopted ω_K values and theoretical Γ_R curve: $\omega_K \Gamma_A = (1 - \omega_K) \Gamma_R$ (Krause 1979).

Chapter 3

Experimental Environments at GSI and FAIR

This chapter describes the experimental areas at the GSI Helmholtz Center for Heavy Ion Research in Darmstadt where the experiments presented in this thesis were conducted. The plasma physics group at GSI possesses several experimental areas for either heavy-ion beam or high power laser experiments. The UNiversal Linerar ACcelerator (UNILAC) provides heavy-ion beams of low energy for the experimental areas Z4 and Z6. The heavy-ion synchrotron SIS18 (german: Schwerionensynchrotron, 18 stands for 18 Tm rigidity of the magnets in the synchrotron) accelerates the heavy-ions from the UNILAC further. The high energy, high temperature (HHT)-cave is situated behind the SIS18. First experiments of FAIR Phase-0 will be conducted there. The future facility for antiproton and ion research(FAIR) will increase the energy and intensity of the heavy-ion beams even further. After commissioning of the SIS100, warm dense matter (WDM) experiments will be performed at the atomic-, plasma-physics and applications(APPA) cave (Stöhlker et al. 2015; V. Bagnoud et al. 2017; GSI Helmholtz Centre for Heavy-Ion Research GmbH 2019b; GSI Helmholtz Centre for Heavy-Ion Research GmbH 2019a).

The **P**etawatt **H**igh-**E**nergy **L**aser for Heavy Ion **E**Xperiments (PHELIX) supplement the heavy-ion beam experiments. A second smaller laser system is the **N**anosecond **H**igh-**E**nergy **L**aser for Heavy Ion **E**Xperiments (NHELIX). A unique feature of GSI is the possibility to combine the ns-long high energy laser pulse of PHELIX or NHELIX with a heavy-ion beam at the same experimental area (Z6 now and HHT from 2020 on). Furthermore, a ps-experimental area for high intensities is available in the PHELIX laser bay. The following sections introduce GSI and FAIR as a whole and Z6 and the ps-experimental area in the laser bay of PHELIX in particular. The existing and future facilities at GSI and FAIR are shown in fig. 3.1.

3.1 UNILAC

The UNILAC is the linear accelerator part of the existing GSI Helmholtz Centre for Heavy-Ion Research GmbH facilities. It acts as injector for the SIS18 synchrotron

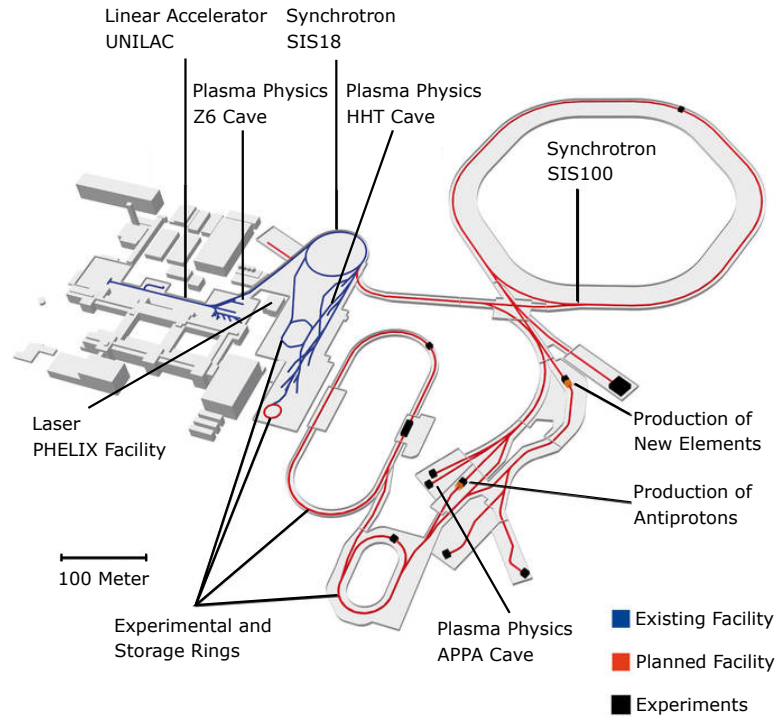


FIGURE 3.1: Schematic view of the GSI Helmholtz Centre for Heavy-Ion Research GmbH (existing) and the FAIR (future) facility in Darmstadt, Germany (GSI Helmholtz Centre for Heavy-Ion Research GmbH 2019b).

(see fig. 3.1). The following section shows the Z6 experimental area and the unique parameters of the combined ion and laser beams there.

3.1.1 Z6 Experimental Area

The Z6 experimental area provides the unique opportunity for experiments with low energy heavy-ion beams produced by the UNILAC as well as combined experiments with the PHELIX and NHELIX laser systems (see sec. 3.2). The UNILAC provides a large variety of elements with moderate energies. PHELIX and NHELIX bring ps- and ns-long laser pulses of up to several 100 J into the same target chamber as the ion beam. The provided beam parameters are shown in fig. 3.1 while fig. 3.2 shows a schematic view of the different beamlines entering the Z6 target chamber.

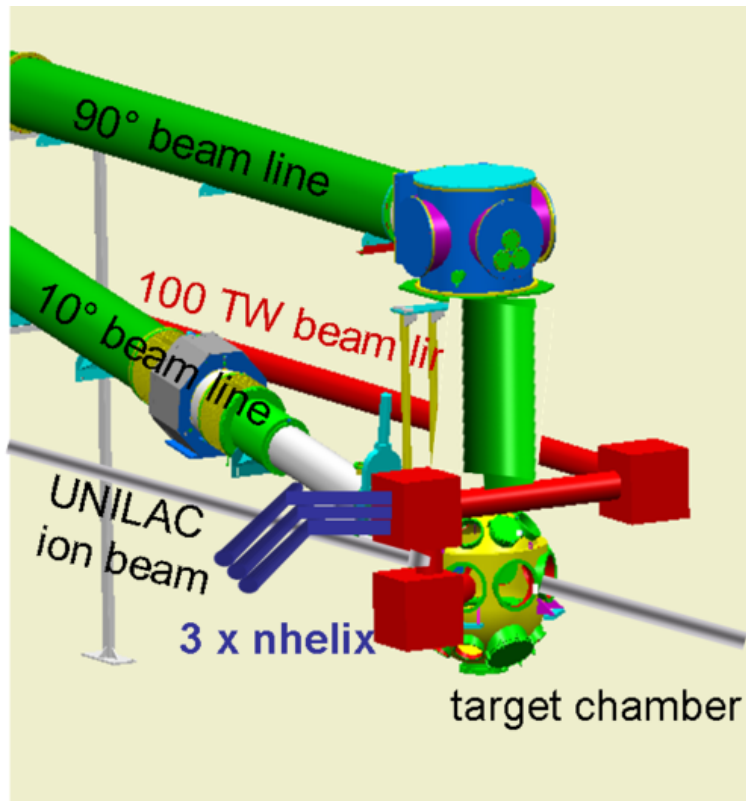


FIGURE 3.2: View of the Z6 experimental area. Also shown are the connections to the UNILAC, to PHELIX and NHELIX (GSI Helmholtz Centre for Heavy-Ion Research GmbH 2019c).

Available Experimental Parameters at the Z6 Cave		
UNILAC Ion Beam	PHELIX Laser Beam	NHELIX Laser Beam
$3 < Z < 92$	0.3–1 kJ @ 1–15 ns, 2ω	100 J @ 6–16 ns
$E = 3\text{--}13 \text{ MeV/u}$	50 J @ 0.5–2 ps = 100 TW	5 J @ 0.5 ns
$f = 108/36 \text{ MHz}$,	300 J @ \sim ns	< 1 mJ @ 0.5 ns
$\Delta t_{ion} = 3 \text{ ns (FWHM)}$		

TABLE 3.1: Available ion and laser parameters of the UNILAC and the PHELIX system at Z6 (GSI Helmholtz Centre for Heavy-Ion Research GmbH 2019c).

3.2 PHELIX

The PHELIX Laser system at the GSI Helmholtz Centre is one of the largest lasers and the only kJ-facility in Germany (Danson et al. 2019). It provides several ps- and ns-options for experiments conducted either in the petawatt experimental area or at Z6 with the unique opportunity to combine it with heavy-ion beams of all elements up to uranium.

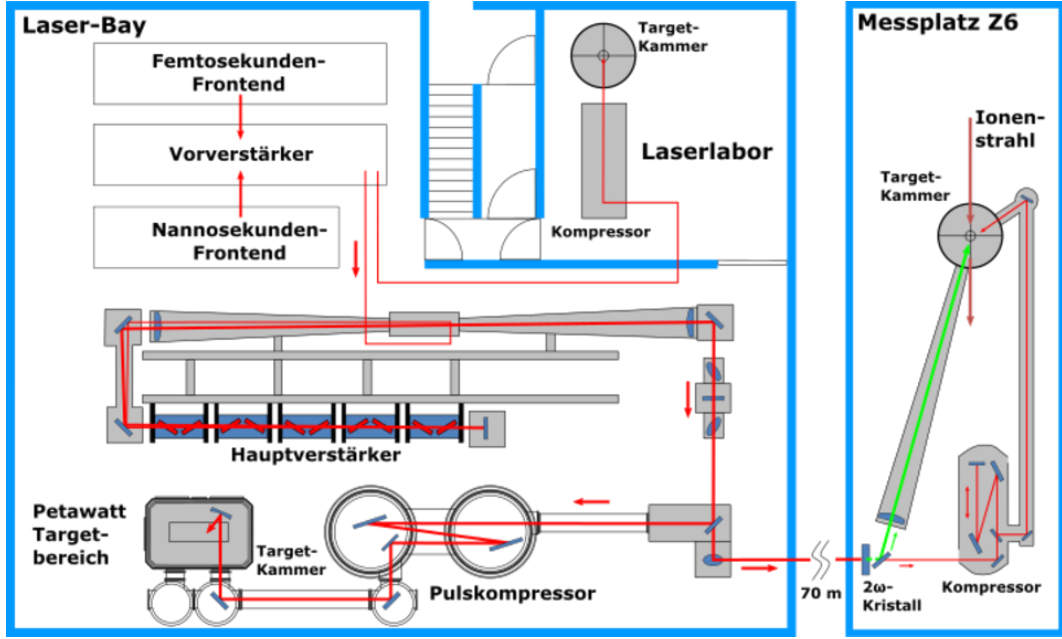


FIGURE 3.3: PHELIX laser bay with experimental areas (GSI Helmholtz Centre for Heavy-Ion Research GmbH 2018).

3.2.1 PHELIX Petawatt Experimental Area

PHELIX is able to produce laser pulses with energies up to 1 kJ as well as powers higher than 500 TW. PHELIX is a flashlamp pumped Nd-glas-system with a central wavelength of 1053 nm. It consists of two frontends, a preamplifier and a main amplifier (GSI Helmholtz Centre for Heavy-Ion Research GmbH 2018). One frontend produces femtosecond pulses (fs-frontend) and the other nanosecond pulses (ns-frontend). The PHELIX facility is shown in Fig. 3.3 and the available laser parameters can be found in tab. 3.2.

Laser Parameters Available		
	Long Pulse	Short Pulse
Pulse length	1–10 ns	0.5–20 ps
Energy E	0.3–1 kJ	up to 200 J
Max intensity I_{max}	$3 \times 10^{16} \text{ W cm}^{-2}$	$2 \times 10^{21} \text{ W cm}^{-2}$
Contrast	50 dB $\equiv 10^{-6}$	up to 120 dB $\equiv 10^{-10}$

TABLE 3.2: Available laser parameters of the PHELIX system.

The laser beam can be directed into three different target chambers: The Z6 target area allows for combined experiments of high intensity laser and heavy-ion beams from the UNILAC. In the PHELIX-building (laser bay) there is a target chamber for intense laser experiments. For powers under 10 TW there is a target chamber in the laser lab. After generation of the laser pulse in one of the frontends the pulse is amplified in a preamplifier and a main amplifier. The high intensities lead to the possibility of

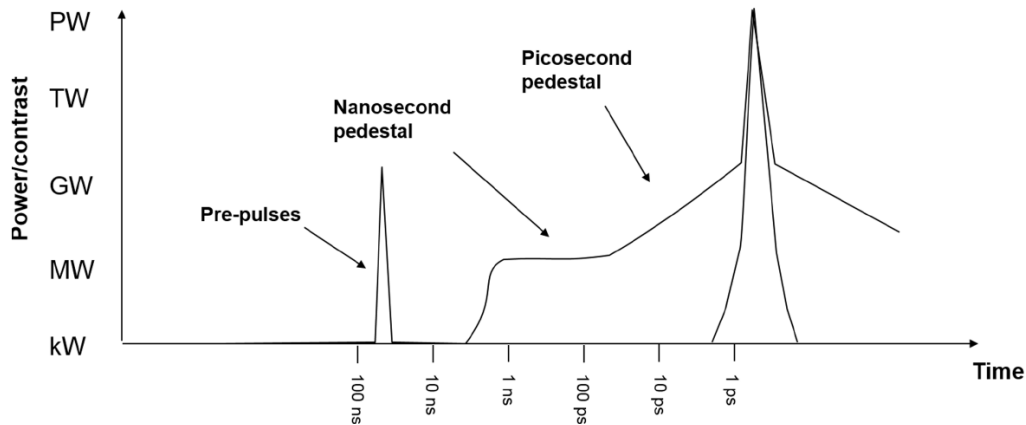


FIGURE 3.4: Illustration of laser contrast issues (Danson et al. 2019).

damage in the optical and amplifier components. Therefore the method of Chirped Pulse Amplification (CPA) is used to reach those high intensities at PHELIX.

The description of short laser pulses uses the theory of wave packages. The time-bandwidth-product $\Delta t \times \Delta f \geq k$ describes the fact that the product of pulse duration Δt and bandwidth Δf is always greater than a constant k . The shorter a laser pulse, the bigger its bandwidth. This relation is used in the CPA. At first a temporally short laser pulse is stretched by an optical grating ("chirped") by using the lengthening of the beam path through the dispersing properties of the grating. The intensity of the beam is reduced so much by the increasing pulse length that an amplification in the amplifier is possible without destroying it. Subsequently the pulse is temporally compressed again by use of optical gratings, and focussed. That allows to reach intensities of up to $10^{21} \text{ W cm}^{-2}$.

Since the high intense short pulse laser does not only consist of a short main pulse but also longer prepulse the laser contrast has to be taken into account (Danson et al. 2019). That is especially the case for investigations of interactions between the laser and matter (see fig. 3.4).

Fig. 3.5 shows the measurements of the laser contrast at PHELIX including the main pulse up to the ns-pedestal region (Wagner et al. 2014). In the case of the PHELIX laser system the prepulse pedestal is in the range of one ns. Although the intensity of the prepulse is lower than the intensity of the main pulse, the intensity of the main pulse might be sufficient to generate a plasma on the target surface before the main pulse arrives. That means that the main pulse does not interact with a cold surface but with an already expanding plasma.

The contrast as given in tab. 3.2 is the best reachable ratio between the intensities of the pre- and the mainpulse for the PHELIX laser system. Because the intensity is connected to the power of the laser pulse a contrast of 100 dB corresponds to a ratio of the intensity of 10^{10} .

The development of the prepulse can be traced back to the amplification of spontaneous emissions in the laser oscillators by the CPA-mechanism. Therefore the

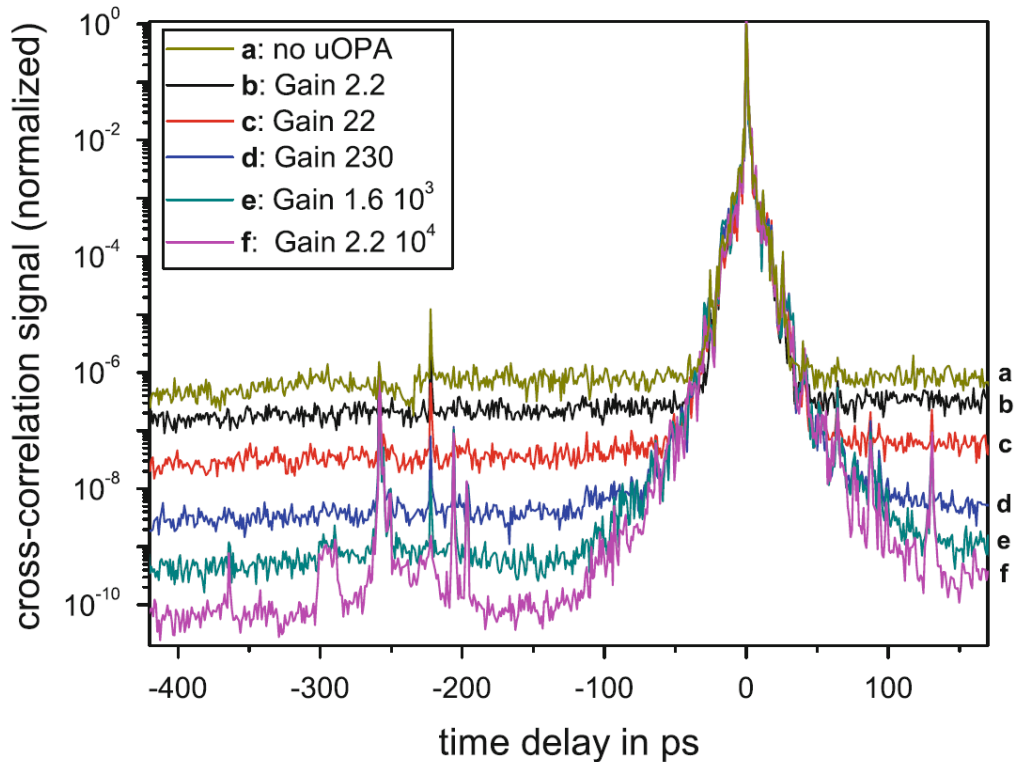


FIGURE 3.5: Improvement of the ASE contrast for different gain levels in the uOPA (Wagner et al. 2014).

prepulse is also referred to as amplified-spontaneous-emission (ASE). By now it is possible to control the ASE prepulse. This is achieved by an additional uOPA (ultrashort optical parametric amplifier) module. Through this uOPA it is possible to amplify the mainpulse immediately after the laser oscillators. In this way it is possible to reduce the amplification in the following amplifiers and hence the ASE prepulse is reduced. That can be seen in fig. 3.5 where the ASE prepulse of the PHELIX laser system is reduced drastically with increasing gain in the uOPA. That allows the experimentalists to investigate the influence of the prepulse on the interaction between the laser and matter.

The results presented here were produced using a ps main-pulse and a ns pre-pulse. The parameters used can be found in tab. 3.3.

Used Laser Parameters at the PHELIX Bay	
Main-pulse	
Wavelength λ	1053 nm
Polarisation	S
Energy E	100 J
Focus size	18.9 μm \times 13.2 μm
Intensity I	3×10^{19} – 4×10^{19} W cm $^{-2}$
Contrast	10^{-6} – 10^{-10}
Pulse duration τ	750 fs
Pre-pulse	
Wavelength λ	1053 nm
Energy E	20 mJ
Pulse duration τ	1.5 ns
Contrast	10^{-4}
dt	1–5 ns

TABLE 3.3: Parameters of the lasers during the experiment.

3.3 FAIR

The new facility for antiproton and ion research (FAIR) is under construction. After commissioning, the synchrotron SIS100 will provide high intensity beams for different experimental caves at FAIR. Plasma physics experiments will be performed at the APPA-cave (see fig. 3.1). The following sections presents the FAIR design parameters for the APPA-cave.

3.3.1 APPA Experimental Area

Experiments of the HED@FAIR collaboration will take place in the APPA-cave. Diagnostic setups have to take the design parameters of that experimental area into account. Tab. 3.4 shows the design parameters with respect to proton and uranium beams.

FAIR Design Parameters at the APPA Cave		
SIS100		
Reference Ion	U ²⁸⁺	Proton
Time Structure	Single Compressed Bunch	Single Compressed Bunch
Number of Ions per Cycle	5×10^{11}	2×10^{13}
Repetition Rate	2 – 10 shots per hour	2 – 10 shots per hour
Energy Range	0.4–2.0 GeV/u	3.0–10.0 GeV/u
Reference Energy	2 GeV/u	5 GeV/u
Pulse length (4σ)	50 ns	50 ns
Momentum Spread (2σ)	3×10^{-3}	1×10^{-2}
Transverse Emittance (2σ)	11 (<i>h</i>) \times 4 (<i>v</i>) mm mrad	7.8 (<i>h</i>) \times 2.6 (<i>v</i>) mm mrad
Beam Spot Radius (2σ)	0.8 (<i>h</i>) \times 1 (<i>v</i>) mm	5 mm

TABLE 3.4: Available ion parameters of the SIS100 at the APPA cave (Appel, Boine-Frankenheim, and Geithner 2019).

Chapter 4

Laser Generated Ultrarelativistic Electrons

As mentioned in chap. 1, active backlighting is an important tool for experimental investigation of high areal density HED matter states. Electrons with relativistic kinetic energies can be used to generate highly energetic gammas in the form of bremsstrahlung. One way to increase the number and energy of these relativistic electrons is to improve the laser system involved in the acceleration. If the modification of the laser system is impossible, the choice of the target can play an important role. Direct laser acceleration is an effective mechanism for the generation of a high number of relativistic electrons. This chapter discusses the generation of ultrarelativistic electrons by intense sub-picosecond laser pulses propagating in sub-mm long plasmas of near critical electron density (NCD) in comparison to the case of plane metal foil targets.

In the production of laser based sources of radiation and particles, the very first stage of laser-matter interaction is dominated by the interaction of the laser with electrons. Several mechanisms of laser energy transfer to high energy electrons can occur depending on the laser parameters and the type of targets. The density of the targets ranges from solid density to gaseous. This is accompanied by the existence of sharp boundaries in solid state targets in comparison to extended gas targets. The mechanism strongly depends on the gradients of the pre-plasma on the target surface in solids. It can be vacuum/Brunel (Brunel 1987), resonant absorption in critical density, the ponderomotive and the (JxB) mechanism of acceleration (Wilks et al. 1992; Gibbon 2004) or stochastic heating (Peter Mulser and Dieter Bauer 2010; Mulser, Weng, and Liseykina 2012; Bochkarev et al. 2014; N E Andreev, Pugachev, et al. 2016) etc. An effective acceleration of electrons to high energies can be achieved in the laser interaction with low density gas targets using the wakefields generated in preformed plasma channels (N E Andreev, Kuznetsov, et al. 2010; Leemans et al. 2014; Esarey, C. B. Schroeder, and Leemans 2009). This mechanism allows the generation of monoenergetic electron beams. The energy of electrons created in such a way is comparatively high. The obtained energies in experiments on the interaction of relativistic laser pulses with low density gas jets and capillary plasmas range from

hundreds of MeV up to several GeV (Faure et al. 2004; Pugacheva and Nikolai Evgen'evich Andreev 2018; Walker et al. 2013; Ju et al. 2014). However, the total charge of these electron beams does not exceed tens of pC. In experiments with a high level of background radiation, this charge does not suffice the requirements of the radiography of high aerial density HED-samples. Therefore, the electron beam charge has to be increased above a nC level while keeping the electron energy at a level of tens up to hundreds of MeV. One of the possibilities to achieve this goal is to use the advantages provided by relativistic laser interaction with plasmas of subcritical and near critical density (Willingale, Nilson, et al. 2011; Willingale, Thomas, et al. 2013; Willingale, Arefiev, et al. 2018; Toncian et al. 2018).

Particle acceleration in relativistic laser channels generated in near critical plasmas was studied initially in 3D PIC-simulations (Pukhov, Sheng, and Meyer-ter-Vehn 1999). These simulations demonstrated the formation of plasma channels and filamentation of the relativistic laser pulse in the NCD-part of expanding plasmas. Additionally, generation of strong currents of energetic (10–100 MeV) electrons that have Boltzmann-like energy distribution with an effective temperature was indicated. The effective temperature should depend, amongst other parameters, on the laser pulse intensity and the length of the NCD plasma region. The creation of this strong electron current results in the emergence of giant azimuthal quasi-static magnetic fields (Pukhov, Sheng, and Meyer-ter-Vehn 1999; Borghesi, AJ Mackinnon, et al. 1998). As the mechanism of electron acceleration in NCD plasmas involves many physical processes simultaneously, it has an intrinsically complex nature. A mechanism of direct laser energy coupling into hot electrons that occurs in relativistic laser channels was proposed (Pukhov, Sheng, and Meyer-ter-Vehn 1999). This coupling would require strong self-generated static electric fields additional to the strong magnetic fields mentioned above. These electric and magnetic fields confine the fast electrons to the relativistic channels formed by the laser. Effective energy coupling can be achieved when the electrons experience resonant transverse betatron oscillations. Resonance happens when the betatron frequency of the electrons approaches the Doppler shifted laser frequency (Pukhov, Sheng, and Meyer-ter-Vehn 1999). Assuming an exponential electron density profile with the scale length $L = 30 \mu\text{m}$, the effective electron temperature obtained numerically for the case of the relativistic laser interaction with expanding plasmas was 4.5 MeV for $I_L = 10^{19} \text{ W cm}^{-2}$ and 14 MeV for $I_L = 10^{20} \text{ W cm}^{-2}$.

Further studies supported these results and extended the analysis of the relativistic laser pulse interaction with sub-critical plasmas (Arefiev et al. 2016; Khudik et al. 2016). The process of direct laser acceleration (DLA) of relativistic electrons undergoing betatron oscillations in a plasma channel and the role played by transverse and longitudinal quasi-static electric fields was examined as well. A universal scaling for the maximum attainable electron energy was derived analytically and the final energy gain of the electrons shows a threshold dependence on the laser intensity (Gray et al. 2014).

This DLA mechanism of electrons and the demonstration of its advantages were only studied in a few experiments up until now. The energy transfer from an ultra-intense laser pulse with an intensity of $1 \times 10^{20} \text{ W cm}^{-2}$ to hot electrons in NCD plasmas depends on the pre-plasma scale length (Gray et al. 2014). It was partially investigated experimentally and partially using 2D PIC-simulations. A separate 5 ns long laser pulse with a $100 \mu\text{m}$ large focal spot was used for the production of one-dimensional expansion of the plasma with a well-controlled scale length. The coupling of the energy of the ultra-intense laser pulse into hot electrons was analysed indirectly using measurements of Cu K_α -intensity and proton spectra depending on the pre-plasma scale length in the experiment. Additionally, the pre plasma scale length was simulated in 1D approximation for different energies of the long pulse. The energy distribution of energetic electrons was not measured directly but simulated using a 2D PIC-code. A density gradient optimum that ensures strong laser pulse self-focussing and channelling processes was found as explanation for an one order of magnitude variation in the coupling efficiency of the laser energy into fast electrons.

Measurements of electrons accelerated by a relativistic laser pulse propagating across a mm-long extended sub-NCD plasma plume were reported (Willingale, Thomas, et al. 2013). A strong increase of the effective temperature and number of superponderomotive electrons caused by the increased length of a relativistic ion channel was shown in these experiments. Likewise, experiments conducted at the Titan laser system using pre-ionised foam layers as targets for electron acceleration were published recently (Willingale, Arefiev, et al. 2018). There, $250 \mu\text{m}$ thick foam layers with mean densities from 3 up to 100 mg cm^{-3} ($n_e = 0.9\text{--}30 \times 10^{21} \text{ cm}^{-3}$) were pre-ionized by a ns ASE-prepulse. The intensity of the 1 kJ, 8–10 ps short laser pulse was $5.3 \pm 1.8 \times 10^{19} \text{ W cm}^{-2}$. The high energy tail of the measured electron spectra was approximated by a maxwellian-like distribution. The effective electron temperature increased by two and up to four times than $E_{pond} \approx 5.4 \text{ MeV}$ for $a_0 = 6.5$.

The so generated beams of ultra relativistic electrons can, for their part, be applied to generate highly penetrating gamma-rays for radiographic purposes in experiments with high aerial densities. Spatial and temporal resolution for radiographic purposes by these sources is achieved by the micrometer-small size laser focus on a target surface and a short laser pulse duration. The analysis of the hydrodynamic motion of heated matter is facilitated by providing up to $10 \mu\text{m}$ spatial resolution and snap shots of the Warm-Dense-Matter (WDM)-object density distribution in ps- up to fs-time scale (Ravasio et al. 2008; K. Li et al. 2014).

Two experimental campaigns were performed on the generation and characterisation of ultra relativistic hot electrons accelerated in underdense pre-ionised foam targets and their usage in backlighter applications (P138 in 2017 and P176 in 2019).

In P138, first pilot experiments at the PHELIX laser showed promising results in the generation of electrons up to 80 MeV, on which was build upon in P176 with the addition of angular resolving electron diagnostics for the characterisation of the acceleration with respect to backlighter applications. The following sections show the

setups, diagnostic methods and the results of these experiments.

4.1 Experimental Setup

This section describes the experimental setup for the laser acceleration of electrons in NCD plasmas. The production of a hydrodynamically stable NCD-plasma layer remains an important issue for such types of experiments. 3D PIC simulations of the relativistic laser interaction with large-scale NCD plasmas (Pugachev, N E Andreev, et al. 2016; Pugachev and N E Andreev 2019) demonstrated that low density CHO-aerogel (Khalenikov et al. 2006; N. G. Borisenko, Akimova, et al. 2006; N. G. Borisenko, Khalenikov, et al. 2007) is a very prospective material for the creation of sub-mm long NCD plasmas and efficient electron acceleration. As part of the preparation of the experimental campaign, an optimisation study was performed for the range of the current PHELIX-laser parameters and various areal densities of the NCD-plasmas (Pugachev, N E Andreev, et al. 2016). Effects of self-focusing and filamentation of the laser pulse, the formation of relativistic plasma channels, their bifurcation and the generation of strong quasi-static magnetic fields were demonstrated in the results of 3D-PIC-Simulations. Due to the self-focussing effect in the NCD-plasma, it was shown that part of the energy spectrum of the accelerated electrons can be approximated by the ponderomotive scaling with the laser pulse amplitude increased up to three times. The additional energy gained by the electrons was attributed to the energy gained directly from the high-frequency laser field through the mechanism of direct laser acceleration (DLA). Where the emerging quasi-static azimuthal magnetic field can keep electrons trapped during the acceleration process.

To compare the hot electron temperatures produced in different plasma conditions, shots onto metallic foils and onto pre ionised foam layers were performed. The electron and ion energy distribution measurement was performed using two electron ($\approx 18 \pm 1^\circ$ and $\approx 44 \pm 1^\circ$) and two ion ($\approx 29 \pm 1^\circ$ and $\approx 52 \pm 1^\circ$) spectrometers with static magnetic fields. A spatial resolving cylinder diagnostic was used to measure the angular distribution of electrons. For comparison of the direct measurement of the electron energy distribution, gamma-yield measurements were performed by N. Zahn using a TLD-dosimeter cards based filter spectrometer. 3D-PIC simulations, that considered the used laser parameters and the geometry of the experimental set-up, supported the experiment. The results of these simulations could be used to calculate the absolute number of accelerated electrons, their energy, and their angular distribution.

The goal of the experiments was the characterisation of the ultra relativistic hot electrons accelerated by intense sub-picosecond laser pulses propagating in sub-mm long plasmas of near critical electron density (NCD), the results are compared to expected values computed by the scalings shown in sec. 2.2.11. The hot electron temperature, generated in laser matter interaction with relativistic laser intensities, can be estimated using the Wilks-scaling. The interaction of laser pulses of relativistic

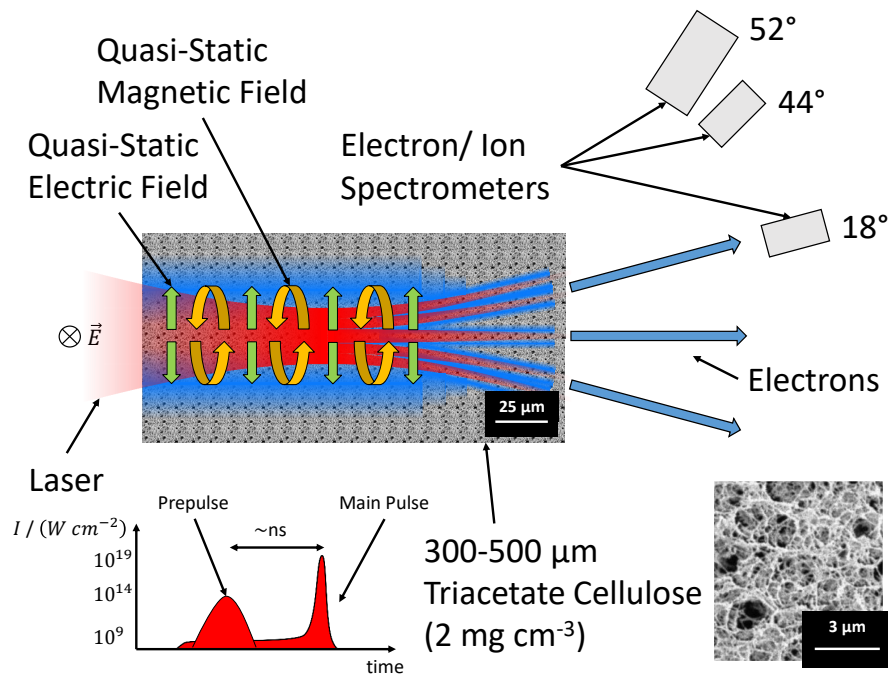


FIGURE 4.1: Schematic view of the experiment P138. A vertical cut through the foam target is shown. The laser (red) irradiates the foam-target. The electron density is increased around the laser channel by the laser (blue). This generates quasi static electric fields (green) and the forward motion of electrons quasi static magnetic fields (orange). The diagram shows the used laser pulses schematically.

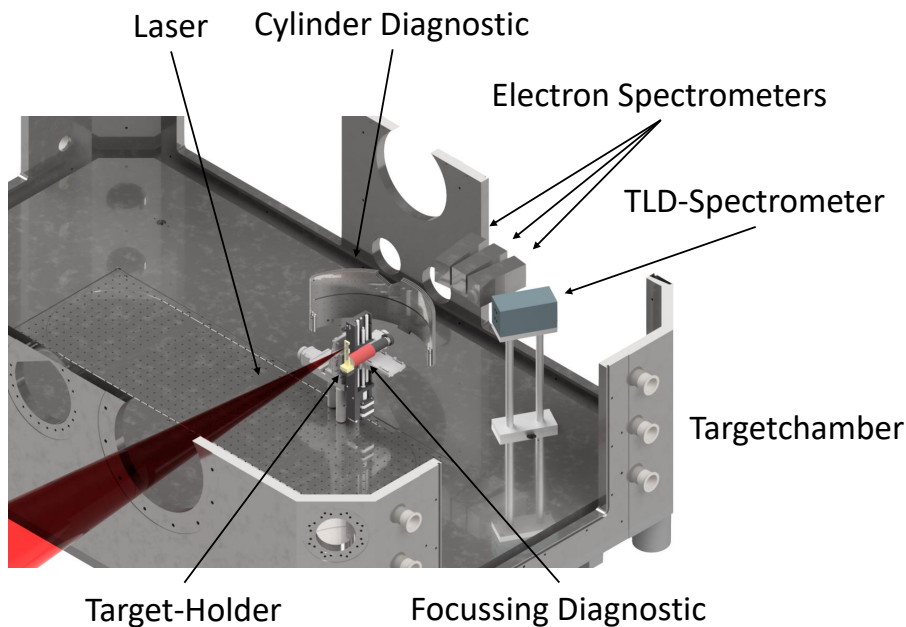


FIGURE 4.2: Schematic view of the targetchamber used in both experiments. The laser (red) is focussed into the chamber onto target position (yellow) which was the same in both experiments but diagnostics are shown for experiment P176.

intensities with foam targets of NCD provides an efficient conversion of the laser energy into relativistic electron beams, which therefore should enhance the electron energies far above those predicted by Wilks (Pugachev, N E Andreev, et al. 2016; Pugachev and N E Andreev 2019). Distinctive features of these beams are their up to 100 MeV high energy accompanied by a large number of electrons (tens of nC) and a strong directionality. This prediction was realised experimentally by the application of under-dense polymer foams while keeping the laser parameters fixed.

Our experiments were performed at the Nd:glass PHELIX-laser facility at the GSI Helmholtz Centre for Heavy-Ion Research GmbH in Darmstadt, Germany. A s-polarised laser pulse of 1053 nm fundamental wavelength, 80–100 J energy and 750 ± 250 fs pulse duration was focused onto the target by means of a 150 cm 90° off-axis parabola under 5° to the target normal. In this way, up to 60 % of the laser energy was concentrated in the focal spot with a FWHM-size of $14 \pm 1 \times 19 \pm 1 \mu\text{m}^2$ (see fig. 4.3). Shot-to-shot deviations of the laser energy and 30 % uncertainties in the laser pulse duration resulted in the rather large confidence interval of the laser intensities ranging from 1.5 up to $5.0 \times 10^{19} \text{ W cm}^{-2}$. The corresponding normalised vector potentials are $a_0 = 3.5 - 6.4$. The ns laser contrast was kept at the highest level between 10^{-11} and 10^{-12} . The shot to shot variations of the laser spot can be understood with fig. 4.3. The intensity of a shot is estimated by imaging the reduced intensity profile directly before a shot as on shot measurement of laser intensities is not possible. This energy distribution is then scaled up to full energy. The intensity range of the experiment was estimated by comparison of the images of 15 shots.

Foams in the form of low density polymer aerogels with 2 mg cm^{-3} volume density and conventional metallic foils (Cu, Ti) were used as targets. A 1.5 ns long pulse with a triangular temporal shape and 1–3 J energy, forerunning the relativistic short main pulse, irradiated these foils and foams in order to create the NCD plasma. The delay between the peak of the ns pulse and the relativistic main pulse was varied from 0 ns up to 5 ns. A schematic view of the experiment P138 is shown in fig. 4.1 while the setup of P176 can be seen in fig. 4.2. The diagnostics setup of both experiments included two portable electron spectrometers with 250 mT nominal static magnetic field. The spectrometers were placed in the target chamber in the horizontal plane perpendicular to the laser polarisation vector. The distance between the interaction point and the entrance holes of both spectrometers was 450 mm in P138. In order to measure an angular distribution of super ponderomotive electrons predicted in simulations (Pugachev, N E Andreev, et al. 2016), the first spectrometer ES1 was placed under 18° and the second one (ES2) under 44° to the laser pulse propagation direction (x-axis, fig. 4.1). A thermo-luminescence dosimetry (TLD)-based ten channel system was used by N. Zahn for the spectrometry of the hard bremsstrahlung caused by MeV electrons interacting with a 17 mm thick Fe-flange that separated the evacuated target chamber from the environment. Ten TLD-cards were placed inside a shielding cylinder with a collimator window between the absorbers, which are manufactured from lower to higher Z materials of different thickness (Horst et al. 2015). The incident

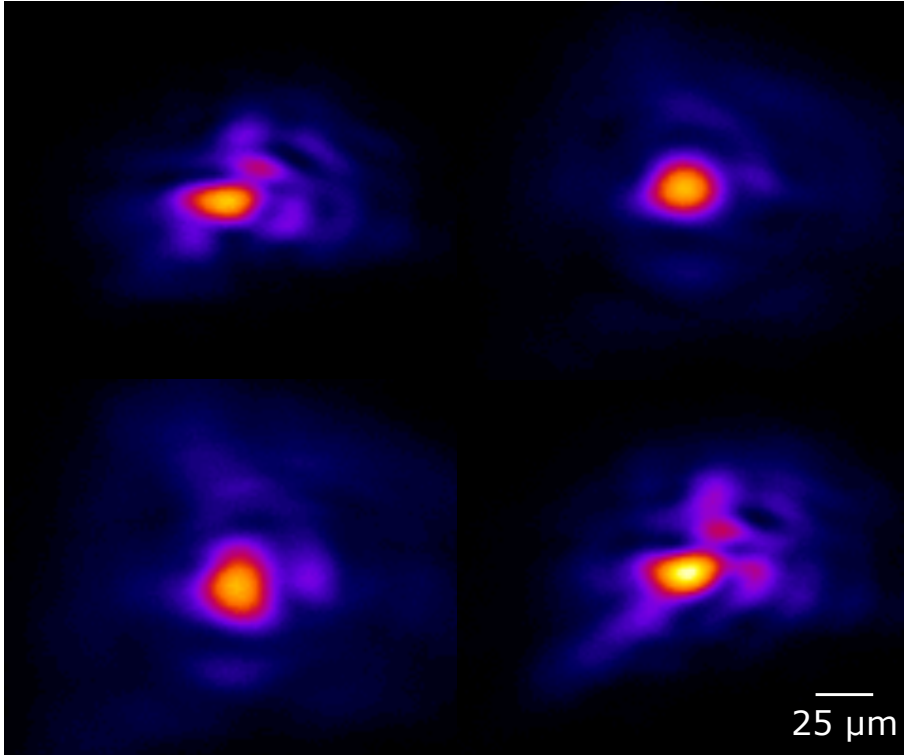


FIGURE 4.3: Focus images taken before four subsequent shots on the same day. False colour images in same colour scale.

X-rays penetrate different absorbers and cause a corresponding TLD-signal (dose) in all ten channels. The spectrometer was designed for an energy range from 30 keV up to 100 MeV. The TLD detector was placed for one set of shots in the direction of the laser pulse propagation and for another set in perpendicular direction to measure an angular dependence of the MeV bremsstrahlung radiation produced by supra-thermal electrons.

The main difference in P176 is the addition of a cylindrical diagnostic made of three layers of steel for the measurement of the angular distribution of electrons in laser propagation direction. Imaging plate detectors were placed between the 3 mm thick steel plates of 200 mm radius. As the cylinders were placed concentric in the same plane as other diagnostics, it covered an angle of 100° on the backside of the target in that plane. Furthermore, the TLD-spectrometer was replaced by a more compact version that is vacuum capable.

In both experiments, high aspect ratio homogeneous plasma targets with a slightly under-critical electron density were produced by the application of foams. 2 mg cm^{-3} triacetate cellulose (TAC, $\text{C}_{12}\text{H}_{16}\text{O}_8$) layers with thicknesses of 300 μm and 500 μm were used (Khalenkov et al. 2006; N. G. Borisenko, Akimova, et al. 2006; N. G. Borisenko, Khalenkov, et al. 2007). TAC-layers are optically transparent and characterised by a highly uniform 3D network structure consisting of 1–2 μm pores, 0.1 μm thick and 1 μm long fibres with density of approximately 0.1 g cm^{-3} . The density fluctuations on the focal-spot size area of $100 \times 100 \mu\text{m}^2$ do not exceed 0.5%. Due

to their open cell structure, air contained by pores can be evacuated. The mean volume density of 2 mg cm^{-3} TAC-foam corresponds to 1.7×10^{20} atoms/cm³ and a mean ion charge $Z_{mean} = 4.2$. Full ionisation of all CHO-atoms would correspond to an electron density of $7 \times 10^{20} \text{ cm}^{-3}$, which is slightly lower than critical density (10^{21} cm^{-3}) for the fundamental wavelength of the Nd:glass laser ($\lambda_L = 1053 \text{ nm}$).

The foam is not instantaneously converted into plasma. A supersonic wave is propagating through the foam after the ns-pulse starts to irradiate the surface. During the interaction, the laser heats the membranes/fibres until they get ionised and expand. The plasma created by the ionisation of the 0.1 g cm^{-3} (8×10^{21} atoms/cm³) dense, 100 nm thick fibres has an overcritical electron density and the fibre thickness is larger than the thickness of the skin layer ($\sim 30 \text{ nm}$). Therefore, the created plasma has to expand into the pores, reaching undercritical electron density and allowing further propagation of the laser pulse into the 3D-like aerogel structure. This process takes time and, hence, determines the delay between the fs main pulse and the ns pulse. The intensity of the ns-pulse can be matched to the target density and target thickness in such a way that the velocity of the ionisation front will be much faster than the ion acoustic velocity. During the propagation of the supersonic ionisation wave the heated high aspect ratio plasma region does not undergo notable expansion. Estimations of the ionisation front propagation velocity V_p that considered the delay caused by hydro homogenisation processes on the micrometer scale were made in accordance with eq. 2.18 for the following values that describe the laser parameters and C₁₂H₁₆O₈ foam structure used in the experiment: mean $A = 8$; mean ion charge $Z_m = 4.2$, mean foam density $\rho_a = 2 \text{ mg cm}^{-3}$, fibre density $\rho_s = 0.1 \text{ g cm}^{-3}$, laser wave length $\lambda_L = 1 \mu\text{m}$, normalised to $10^{14} \text{ W cm}^{-2}$ laser intensity $I_{14} = 0.5$ and a power factor $\alpha = 0.8$ that reflects the geometry of the foam structure.

These values lead to a velocity of the ionisation front of $V_p = 2 \times 10^7 \text{ cm s}^{-1}$. The time required for the ionisation of the 300–500 μm thick foam layers by a 1 J ns-pulse reaches 1.5–2.5 ns.

The foam targets were enclosed in Cu-washers. Therefore, the electron density profile in dependence on time could not be measured. The front part of the created plasma expands towards the incident laser at large delays between the ns- and main pulses. PIC-simulations made for a plasma layer with a constant NCD electron density and for a combination of the linear density profile with a density plateau showed no noticeable difference in the electron energy distribution and charge.

In the case of metallic foils, an inhomogeneous plasma plume that expands toward the main laser pulse with an exponentially decaying electron density was produced by the same 1–3 J ns pulse forerunning the relativistic short main pulse with the delay varied from 0 up to 5 ns.

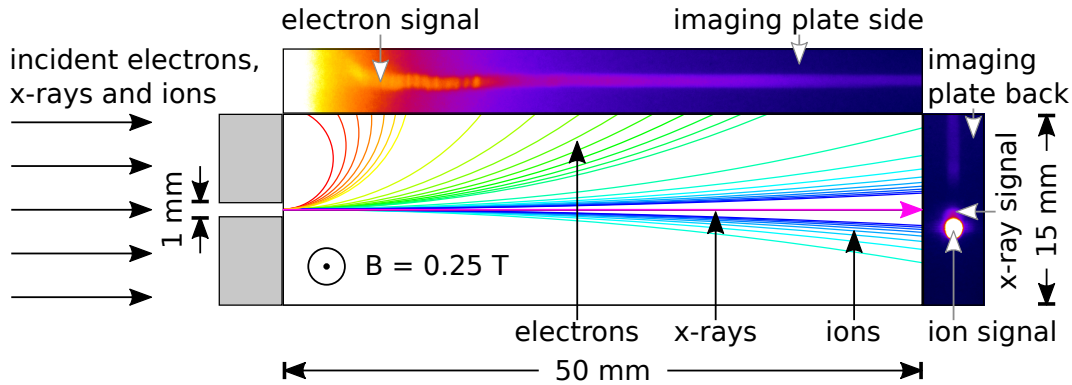


FIGURE 4.4: Schematic view of the electron spectrometers used in the experiments. The ion spectrometers are similar but have bigger dimensions and a stronger nominal magnetic field.

4.2 Diagnostic Methods

A variety of particle detection (keV to MeV) and radiometrical (keV to MeV) diagnostics were applied at the PHELIX laser bay during the experiment. The photons in the range of keV to MeV energies were produced by the interaction of the laser accelerated electrons and ions with a cold metallic foil or the target chamber wall. In experiments with intense short pulse lasers, and also at the new FAIR facility, the diagnostics will be exposed to extreme conditions in which they have to work. In particular, electronic devices like CCD- and CMOS-Cameras can be heavily influenced by parasitic electromagnetic radiation, bombardment with high energy particles, as well as debris. By that, either the measurement process can be disrupted or the devices can be damaged. Experiments have to be performed largely without electronic measurement and readout processes near the interaction region to avoid these problems. Reduction of malfunctions by increasing the distance or the shielding of the diagnostics is only possible if suitable optics are available for the imaging of the interaction region in the desired spectral region. As a result, it is necessary to use diagnostics that are capable of withstanding those extreme conditions as mentioned above. Therefore, analogue detectors like imaging plates and TLD-cards are used as detectors for radiation and particles in laser experiments. The following section describes the measurement method of the electron and particle energy distribution measured in a small solid angle as well as the measurement of the angular distribution of particles over a large solid angle. Imaging plates were used as detectors in both cases. A description of Imaging Plate detectors and details about their properties can be found in Appendix A.

4.2.1 Electron and Ion Spectrometers

For the measurement of the kinetic energy of charged particles, spectrometers with static magnetic fields as dispersive elements can be applied. Charged particles that pass through electromagnetic fields are deflected in these fields according to the

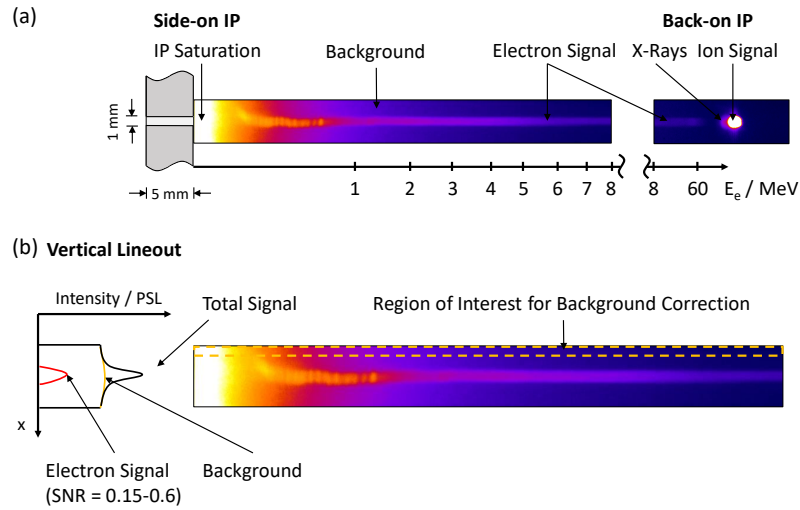


FIGURE 4.5: Principle of interpretation of the raw data after the scanning process of the IPs in the magnet spectrometers. (a) Two images of the side-on and back-on IP of fig. 4.4 are shown. The energy scale for electrons is given. (b) The region of interest allows to estimate the background intensity level. by subtracting the background calculated individually for each energy bin, the electron signal level can be obtained in each energy bin.

Lorentz force. If only a homogeneous magnetic field is present, the charged particle will perform a circular motion in the field with a turning radius called the Larmor radius. The following section describes the scheme and evaluation of the data of such a spectrometer used in the experiments described in this work.

Spectra of the hot electrons and ions leaving the target were obtained by applying a static magnetic field to disperse particles with different charge to mass ratios and energies. The detection of the particles was performed using imaging plates as detectors. The energy range of detection was up to around 100 MeV for both the electron and ion spectrometers. Fig. 4.4 shows a schematic view of the used electron spectrometers (the ion spectrometers have a similar design but doubled proportions and four times higher nominal magnetic field strength). The spectrometers consist of a stainless steel box that contains two iron/neodymium magnets. Between these magnets a static magnetic field B is present. The deflected electrons are detected by IPs on the side and in the back of the spectrometer. The geometry of the box and the nominal strength of the magnetic field is chosen according to the type of particle that the spectrometer is designed to detect. Corrections to the data were introduced considering the magnetic field inhomogeneity, non-linear dispersion, background inhomogeneity, IP-response functions, particle types, angular response, and fading.

Fig. 4.5 shows an example of the raw data obtained by the magnet spectrometers. In fig. 4.5 (a), electrons entering the spectrometer through the 5 mm steel front plate

deposit energy in the IP detector. After scanning the IPs, an electron signal is visible on the side-on IP. Additionally, for shots onto foam targets, a strong background is present and can lead to saturation of the image especially near the entrance aperture (for more details about saturation of IPs and saturation in their scanning procedure see. Appendix B.4.2). This is due to ultrarelativistic electrons of tens of MeV penetrating the steel front plate and their energy deposition in the IP. Perpendicular to the electron propagation direction, the background is rather homogeneous. The back-on IP also registers the X-ray radiation emitted in the target region. This spot is centred on the IP for a well adjusted spectrometer. That allows to estimate the error of the angular adjustment of the spectrometer and also the verification of the entrance angle of the electrons into the spectrometer. Furthermore, the ions accelerated by the laser are deflected to the opposite side of the X-ray spot due to the opposite sign of their charge and also detected by the IP. The basics of the data evaluation of these images is shown in fig. 4.5 (b). The left side shows a vertical lineout of the IP image. The Signal-to-Noise-ratio between the signal intensity level and the background intensity level indicated by the orange box spans a large range from 0.15 to 0.6 in different parts of the IP and for different shots where the noise is largest in shots onto foam layers. A region similar to the orange box was chosen in every image to account for the background. The energy region below 2 to 4 MeV was omitted from the data analysis due to saturation of signal, oscillations in the electron signal and the rather complicated IP-response in that energy range. An automated procedure calculated the mean background in x-direction for each energy bin. The mean value was subtracted from each pixel in that bin, and the remaining electron signal was integrated in each energy bin.

4.2.2 Angular Distribution of Electrons

The angular distribution of electrons could be obtained by the diagnostic setup shown in fig. 4.6. Three steel plates of 3 mm thickness with a bending radius of around 200 mm were placed behind each other. A horizontal cut and a cutout on the upper edge allowed to use particle diagnostics behind the cylinder without obstructing direct line of sight. Holes were drilled into the plate in the direction of the target. The distance between the holes, both in horizontal and vertical direction, was $d = 20$ mm which corresponds to an angle of $\alpha = 5^\circ$ for the distance of $d = 220$ mm used due to technical restraints during the experiment. These holes allow for the angular calibration of the images obtained by imaging plates. Two IPs were placed behind the first and second layer of steel. Electrons with an energy exceeding $E = 3.5$ MeV will penetrate 3 mm of steel and $E = 7.5$ MeV electrons will penetrate 6 mm of steel respectively (see fig. A.6). Gammas with energies in the range of 1–5 MeV have a transmission of over 90 % while gammas reach a plateau for the transmission of 99 % for 3 mm of steel and 98 % for 6 mm in the range of 5–20 MeV. The rest of the signal stems from the gammas produced by the relativistic electrons emitting bremsstrahlung while traversing the cylinder material

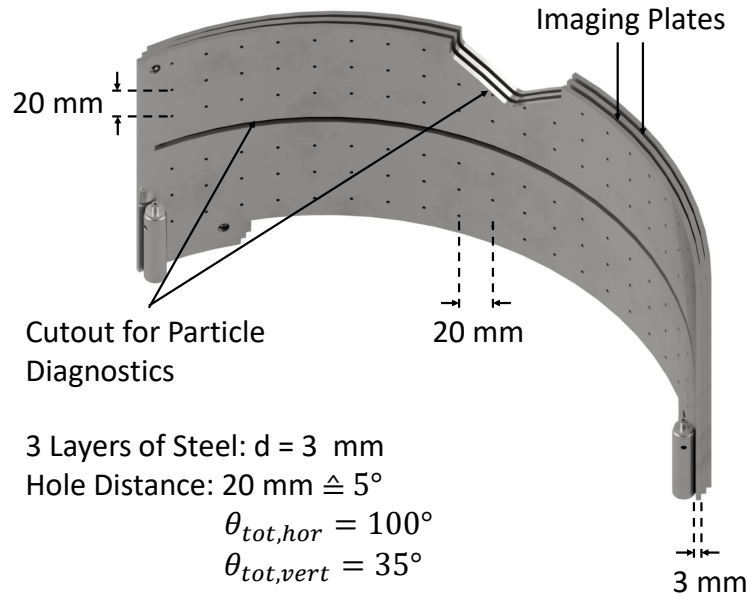


FIGURE 4.6: Schematic view of the cylinder diagnostic for the measurement of the angular distribution of electrons.

4.3 Experimental Results

The following section discusses experimental results on the interaction of relativistic sub-picosecond laser pulses with sub-mm long NCD plasmas. Hydrodynamically stable, large scale, quasi-homogeneous plasma targets were created by using polymer foam layers of 2 mg cm^{-3} and up to $500 \mu\text{m}$ thickness. Foam layers with density of a thousandth of solid density and $300\text{--}400 \mu\text{m}$ thickness were used as targets. By using a mechanism of super-sonic ionisation, a homogeneous NCD-plasma was produced when a well-defined separate ns laser-pulse with $1\text{--}3 \text{ J}$ energy was sent onto the foam-target forerunning the relativistic main pulse. The energy and the duration of the ns-pulse were well matched to the mean volume density and the thickness of foam layers in order to optimise the velocity of the supersonic ionisation wave that creates high aspect ratio NCD-plasma. A mean ion charge $Z = 4.2$ is achieved in the case of fully ionised CHO-atoms. In comparison to the case of freely expanding plasmas created in the interaction of ns-laser pulses with solid foils, the application of sub-mm thick low density foam layers provided a substantial increase of the electron acceleration path in a NCD-plasma. The total energy of the main laser pulse used in the experiment was 100 J , the pulse length was 750 fs and the intensity reached $2\text{--}5 \times 10^{19} \text{ W cm}^{-2}$. Supporting 3D-PIC and FLUKA simulations, which took the laser parameters and the geometry of the experimental setup into account, showed evidence for an increase in the mean electron energy and temperature in the case of foam-targets in comparison to foil-targets (Rosmej, Olga N. et al. 2019). The tendency towards a strong increase in those electrons is reinforced by the results of gamma-yield measurements that showed a 1000-fold increase of the measured doses. Additionally, the simulations suggest a high directionality of the acceleration process.

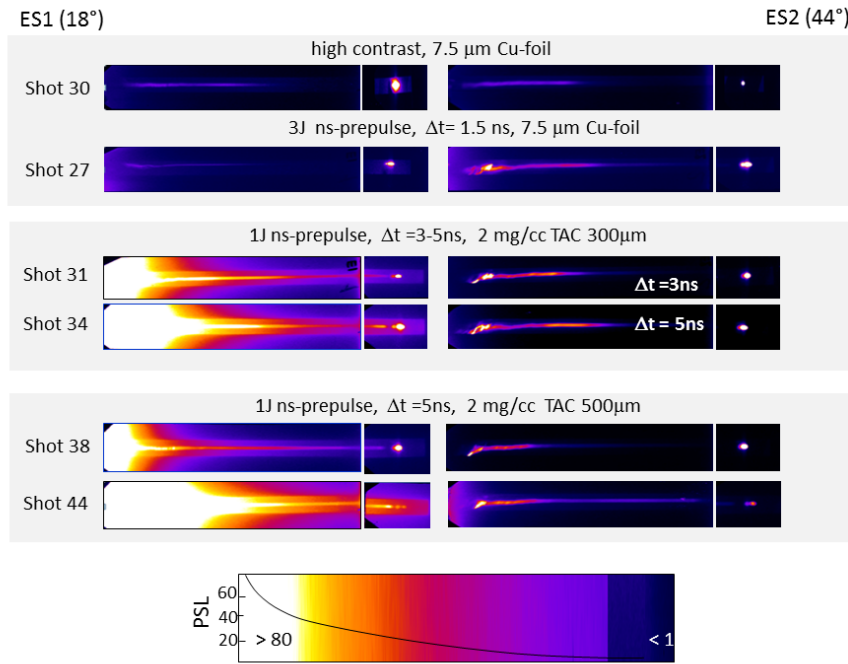


FIGURE 4.7: Raw electron spectra measured by means of electron spectrometers ES1 and ES2 under 18° and 44° to the laser propagation direction for various combinations of the ns-pulse energy and the delay Δt between the ns- and fs-pulses. The colour scale of the IP signal expressed in PSL is the same for all presented spectra (Rosmej, Olga N. et al. 2019).

4.3.1 Generation of Ultra Relativistic Electrons

The electron energy distribution was measured directly using two electron spectrometers with a static magnetic field. The comparison between shots onto metallic foils and onto pre-ionised low density foam layers demonstrated that the effective temperature of supra-thermal electrons increased from 0.4 to 1.1 MeV in the case of the relativistic laser interaction with a metallic foil at high laser contrast up to 10 MeV for the laser shots onto the pre-ionised 300 μm and 500 μm thick foam layers. These results of a strong increase of the mean electron energy and number of ultra-relativistic electrons was supported by gamma-yield measurements. In the case of pre-ionised polymer foams, a 1000-fold increase of the measured doses in all 10 channels of the gamma-spectrometer covering the photon energy range from 30 keV up to 100 MeV was shown. For interpretation of the measured doses by means of the Monte Carlo multi-particle transport code FLUKA, the electron spectra were approximated by a Maxwell-like distribution with two effective temperatures. The best fit of the measured values obtained with a deviation less than 10% resulted in $T_1 \approx 12$ MeV and $T_2 \approx 2\text{--}5$ MeV which is in good agreement with direct measurements made by means of the two electron spectrometers.

The laser shots that are presented here were made onto Cu-foils and CHO-foams at a ns-contrast of the laser of 10^{-11} with and without an additional ns-pulse. The

results of electron spectra measured by two electron spectrometers ES1 (18°) and ES2 (44°) and the TLD-dose caused by the bremsstrahlung radiation were very stable from shot to shot for every type of laser pulse and target combination.

The two electron spectrometers had a static magnetic field with nominal field strength of 250 mT. The scheme of the electron spectrometer is shown in fig. 4.4. The spectrometer consisted of an Fe-housing that held two imaging plates (IPs). A signal on the long side-on IP corresponds to electron energies $1 < E < 8$ MeV (ES 1) or $1 < E < 6$ MeV (ES2) and the short, end-on IP covers the electron energy range from 8 MeV or 6 MeV up to 100 MeV. A 2D-map of the magnetic field distribution inside the spectrometer at the height of the entrance hole was made by means of a hall-probe. In the center of the Neodymium-magnets the measured B-field reached 245–250 mT with a gradient of 2–5 mT mm⁻¹. The B-field dropped down to 190 mT at a distance of 1 mm from the magnet edges. The dispersion curve that accounts for this gradient dynamics was used to calculate electron trajectories. The response of BASF MS IPs to an electron impact accounting for the electron energy and angle of incidence was considered (Bonnet, Comet, Denis-Petit, Gobet, Hannachi, Tarisien, Versteegen, and Aléonard 2013; Tanaka et al. 2005).

Shots onto Cu-foils and foam layers were performed with high laser contrast and a well defined ns prepulse. Fig. 4.7 shows the raw data for several shots with different target and prepulse conditions. The left side shows the data for the spectrometer ES1 under 18° and the right side the data for ES2 under 44° to laser propagation direction. Shot 30 and shot 27 were performed on Cu-foils while high laser contrast was used in shot 30 and a ns-prepulse was applied in shot 27. Shots 31 to 44 used CHO-foams as targets (300 μ m in shots 31 and 34 and 500 μ m in shots 38 and 44). Two spots can be seen in the middle of the end-on IP. These spots correspond to X-rays (low signal intensity level) and positively charged ions (saturated signal) that experience only a slight deviation in the magnetic field due to their higher mass (see fig. 4.4). The position of the X-ray signal would correspond to infinitely large electron or ion energy. Low background intensity levels can be observed on the side-on IP in high contrast shots onto Cu-foil targets (shot 30). This background as well as the signal intensity levels and maximum energy of electrons increase for shots on Cu-foils with prepulse (shot 27) or preionised foam layers (shots 31, 34, 38 and 44). In shot 27, a pinhole with a third of the diameter (0.3 mm opposed to the other shots 1 mm) was mounted onto the ES1-spectrometer. Thus the amplitudes of the signals of ES1 and ES2 are not easily comparable in these pictures. This was accounted for in the spectra shown in fig. 4.9. A oversaturation in the electron energy range below 1 MeV was detected regularly for the shots onto foam targets. This is probably caused by a strongly increased amount of laser accelerated electrons with $E > 6$ –8 MeV (see fig. 4.8). The stopping range in iron for electrons above this energy is large enough to allow electrons to penetrate the 5 mm thick steel front plate of the electron spectrometer directly. Inside the spectrometer, they were deflected by the static magnetic field according to their final energy. This energy region is excluded from the analysis and results are

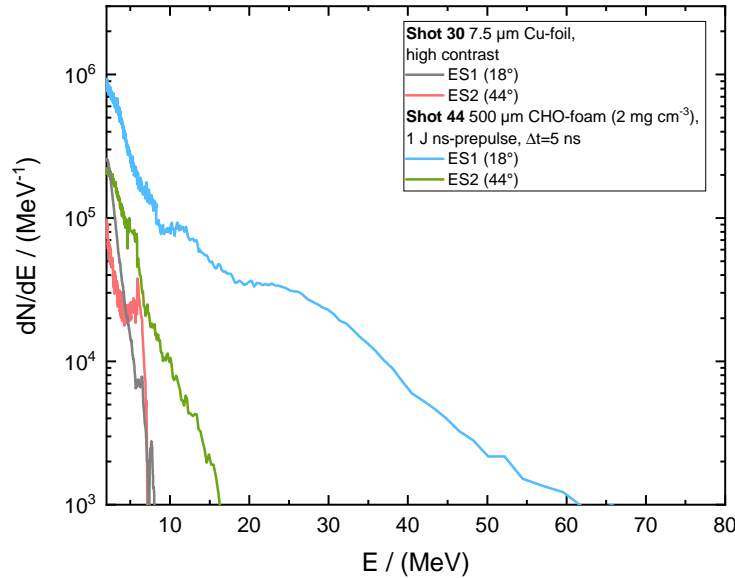


FIGURE 4.8: Electron energy distributions for different target types at same laser parameters: Cu-foil (shot 30) and 500 μm TAC-foam (shot 44). Electron Spectrometer placed at 18° (ES1) and 44° (ES2). The spectrometers observed a solid angle of $\Omega = 1.5 \times 10^{-5}$ sr.

presented for electrons that entered the spectrometer through the 1 mm collimator hole with energies above 2 MeV. The signals from electrons with energies between 8 (ES1) or 6 (ES2) and 100 MeV are accumulated in fewer pixels than on the side-on IP. But the lower energy resolution on the back-on IP still allowed the registration of the pronounced effect of the effective laser energy coupling into electrons in NCD-plasmas and their acceleration up to tens of MeV.

Data from the absolute calibration of the image plates for relativistic electrons with energies up to 100 MeV and the dependence of the absolute signal on the electron angle of incidence onto the IP (Bonnet, Comet, Denis-Petit, Gobet, Hannachi, Tarisien, Versteegen, and Aléonard 2013; Tanaka et al. 2005) were used to evaluate the number of electrons in different energy ranges.

The first two shots (27 and 30) were shots onto a 7.5 μm thick Cu-foil target. Shot 30 was a shot performed with high laser contrast. Therefore, the main laser pulse interacted predominantly with the foil and no expanding plasma layer. The main difference in shot 27 is the application of a 3 J ns-prepulse forerunning the main pulse by $\Delta t = 1.5$ ns to pre-ionise the Cu-foil. The main laser pulse is then able to interact with the expanding plasma at the depth where critical density can be found. This increases the energy and number of electrons accelerated by the laser. As the acceleration path of the electrons is short, pondermotive forces perpendicular to the laser propagation direction lead to a higher signal at 44° compared to 18° . The foams were ionised by a ns-prepulse preceding the main pulse by $\Delta t = 3$ to

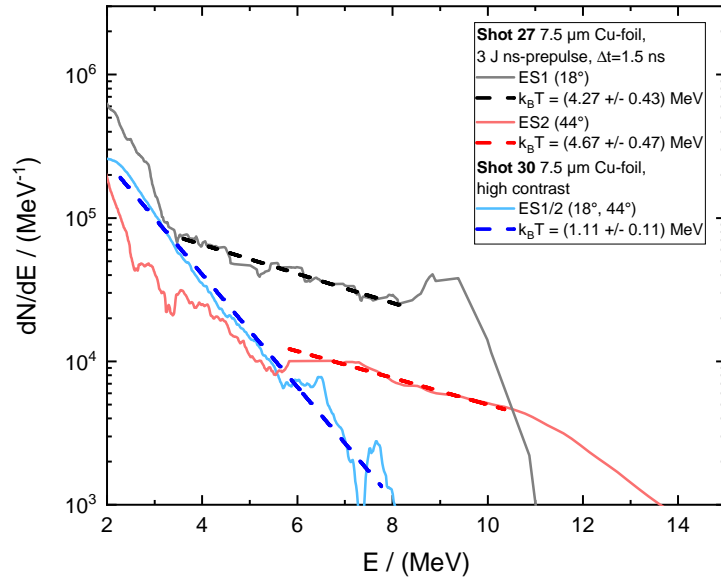


FIGURE 4.9: Electron energy distributions and temperatures for a Cu-foil target. Electron Spectrometer placed at 18° (ES1) and 44° (ES2). The spectrometers observed a solid angle of $\Omega = 1.5 \times 10^{-5}$ sr.

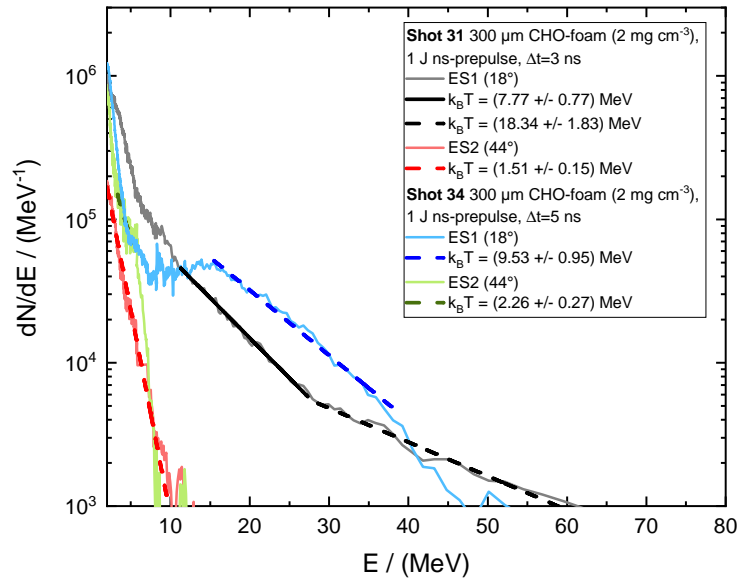


FIGURE 4.10: Electron energy distributions and temperatures for a 300 μm TAC-foam target. Electron Spectrometer placed at 18° (ES1) and 44° (ES2). The spectrometers observed a solid angle of $\Omega = 1.5 \times 10^{-5}$ sr. About 18 to 34% of all electrons at 18° reach energies $E > 10$ MeV.

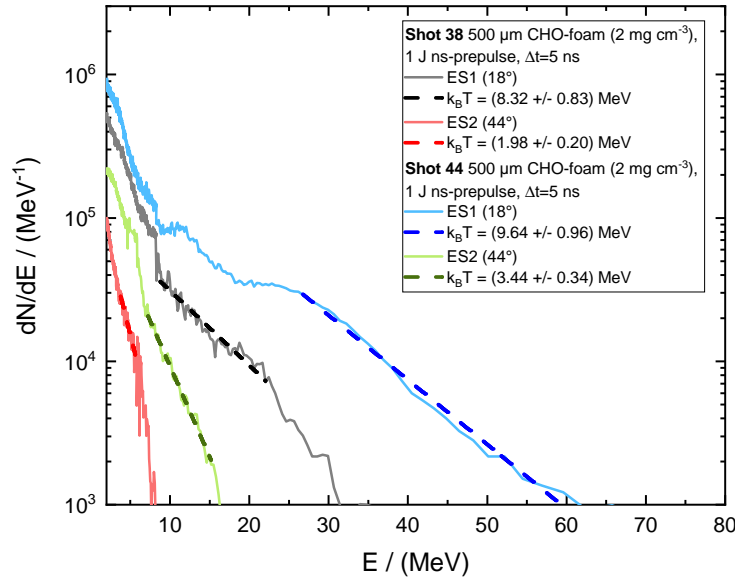


FIGURE 4.11: Electron energy distributions and temperatures for a 500 μm TAC-foam target. Electron Spectrometer placed at 18° (ES1) and 44° (ES2). The spectrometers observed a solid angle of $\Omega = 1.5 \times 10^{-5}$ sr. About 14 to 31 % of all electrons at 18° reach energies $E > 10$ MeV.

5 ns. The energy distributions of electrons with energies between 2 and 50 MeV that entered the spectrometer through the 1 mm collimator hole in the mentioned shots are presented in fig. 4.9, fig. 4.10, and fig. 4.11.

The measured electron spectra were fitted by several Maxwell-like distributions with different temperatures (dashed lines in fig. 4.9, fig. 4.10 and fig. 4.11). One part of the electron spectra that can be well approximated by a ponderomotive hot electron temperature of 0.4–2.9 MeV is present in all shots onto the foil and CHO-foams under 18° and 44° . This is in agreement with the scaling by Wilks et al. (Wilks et al. 1992) for intensities in the range of 3×10^{18} – 6×10^{19} MeV as shown in fig. 4.12. A 10-fold increase of the number of hot electrons with $E < 10$ MeV measured by ES1 and ES2 and a dramatic increase of the number of ultra-relativistic electrons with energies above 20 MeV measured by means of ES1 under 18° can be observed when shooting onto the pre-ionised CHO-foams (see fi. 4.13). A fraction of 14 to 34 % of all electrons above 2 MeV reach energies above 10 MeV.

These results are summarised for comparison in fig. 4.14. It is clearly visible that temperatures of emitted relativistic electrons are isotropic for shots onto foil targets. An increase of the temperatures in shots onto preionised foil-targets is achieved. These temperatures lie between the ponderomotive- and DLA-scaling (see sec. 2.2.11). The introduction of CHO-foams as targets further increases the temperature of electrons accelerated in forward direction according to the DLA-scaling while the temperature

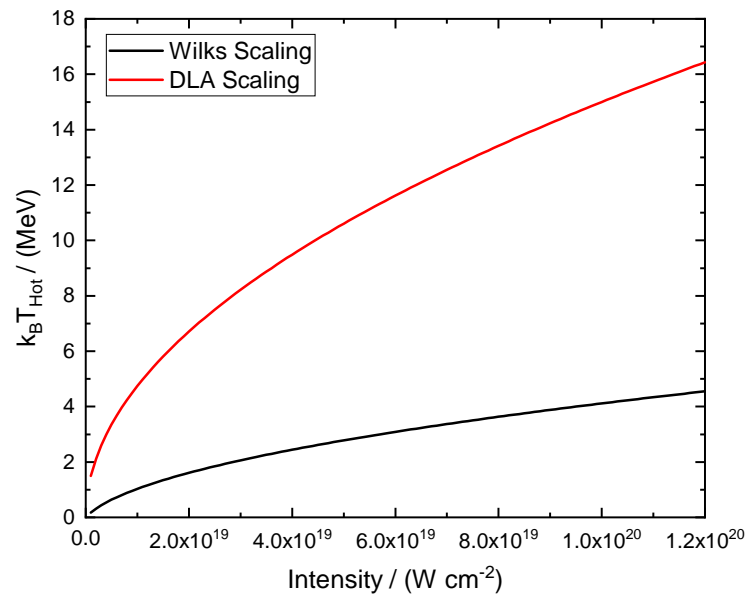


FIGURE 4.12: Comparison of the hot electron temperature scaling laws of Wilks et al. (Wilks et al. 1992) and in DLA by Pukhov et al. (Pukhov, Sheng, and Meyer-ter-Vehn 1999) for $\lambda_L = 1053$ nm.

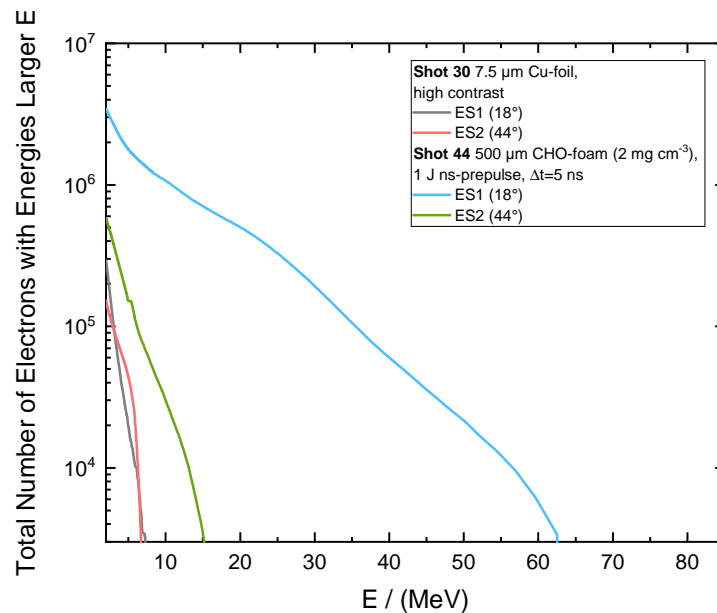


FIGURE 4.13: Evaluated total number of electrons that enter the spectrometer with energies above the given one.

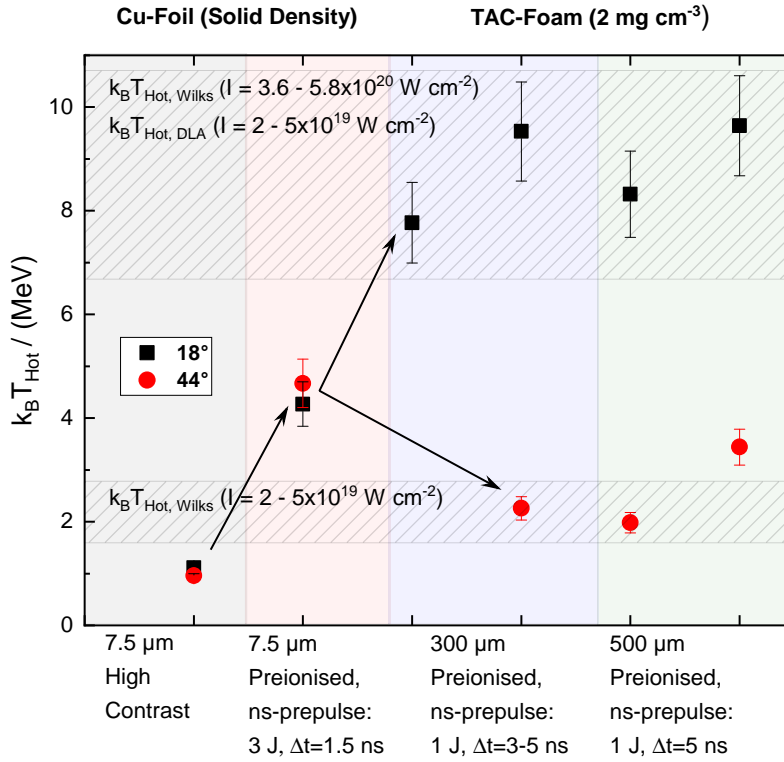


FIGURE 4.14: Comparison of the experimental results from fig. 4.9, fig. 4.10 and fig. 4.11 with the theoretical values from the diagram shown in 4.12.

for electrons at large angles to the laser propagation direction matches the ponderomotive scaling. This observation clearly supports the prediction of a directionality of superponderomotive electrons generated in NCD plasmas.

Tab. 4.1 shows the summary of the fitted temperatures for the fits in fig. 4.9, fig. 4.10 and fig. 4.11. The maximum effective electron temperature $T_h \approx 9.6$ MeV was achieved in the case of 300 μm and 500 μm thick pre-ionised CHO-foam layers of 2 mg cm^{-3} mean density and 5 ns delay between the pre-pulse and the main pulse under 18° to laser propagation direction (shots 34 and 44). This is at least 3 – 11 times higher than predicted by the Wilks scaling determined by the vacuum laser pulse intensity $2.1\text{--}5.1 \times 10^{19} \text{ W cm}^{-2}$ ($T_h = 1.7\text{--}2.8$ MeV) and measured in the high contrast laser interaction with Cu-foils ($T_h = 0.96\text{--}1.11$ MeV in shot 30). The energy distribution of electrons detected under 18° and 44° is very similar in the case of shots with a high laser contrast (compare raw spectra and electron energy distribution measured by ES1 and ES2 in shot 30 in fig. 4.7 and fig. 4.9). A predominant effect in the spectra of the accelerated electrons measured by ES1 under 18° to the laser propagation direction in the shots with foam targets is visible. An approximation of the high energy tails ($E > 10\text{--}15$ MeV) with a Maxwell-like distribution function results in 7.8–9.6 MeV effective electron temperature. Fig. 4.13 shows the total number of electrons that entered the spectrometer with energies above the given

one. The measured number of electrons with energies $E > 30$ MeV that entered the spectrometers through the 1 mm hole (solid angle $\Omega = 1.5 \times 10^{-5}$ sr) reached 2×10^5 particles (see fig. 4.13). The IP signal of the electron spectra measured by ES2 caused by electrons with $E > 10$ –15 MeV is at the background level (fig. 4.8 and fig. 4.13).

Electron Temperatures for Different Target Types				
ES1 (18°)				
Shot	Target	$k_B T_1$ / MeV	$k_B T_2$ / MeV	Max. Measured Energy / MeV
27	7.5 μ m Cu-foil Preionised 3 J, $\Delta t = 1.5$ ns	0.70 ± 0.07	4.27 ± 0.43	11.0 ± 0.1
30	7.5 μ m Cu-foil Prepulse foams 1 J, $\Delta t = 3$ –5 ns	1.11 ± 0.11	N/A	7.27 ± 0.1
31	300 μ m foam	2.05 ± 0.21	7.77 ± 0.78	61.1 ± 0.1
34	300 μ m foam Prepulse foams 1 J, $\Delta t = 5$ ns	0.85 ± 0.09	9.53 ± 0.95	52.2 ± 0.1
38	500 μ m foam	2.89 ± 0.29	8.32 ± 0.83	31.4 ± 0.1
44	500 μ m foam	1.99 ± 0.20	9.64 ± 0.96	61.5 ± 0.1
ES2 (44°)				
Shot	Target	$k_B T_1$ / MeV	$k_B T_2$ / MeV	Max. Measured Energy / MeV
	details see above			
27	Cu-foil	0.44 ± 0.04	4.67 ± 0.47	13.6 ± 0.1
30	Cu-foil	0.96 ± 0.10	N/A	7.1 ± 0.1
31	300 μ m foam	1.51 ± 0.15	N/A	11.6 ± 0.1
34	300 μ m foam	0.60 ± 0.06	2.26 ± 0.27	11.9 ± 0.1
38	500 μ m foam	1.24 ± 0.12	1.98 ± 0.20	8.2 ± 0.1
44	500 μ m foam	2.23 ± 0.22	3.44 ± 0.34	16.3 ± 0.1

TABLE 4.1: Electron temperatures and maximum energies for Cu-foil and foam targets (300 μ m and 500 μ m TAC-foam). Electron Spectrometer placed at 18° (ES1) and 44° (ES2). The spectrometers observed a solid angle of $\Omega = 1.5 \times 10^{-5}$ sr.

4.3.2 Angular Distribution of Ultrarelativistic Electrons

The angular distribution of the laser accelerated electrons was measured directly only in two angular positions around the target in P138. A directionality along the laser propagation direction for superponderomotive electrons is visible for shots onto CHO-foam layers (see 4.8) as well as an increase in the temperature of the electrons along

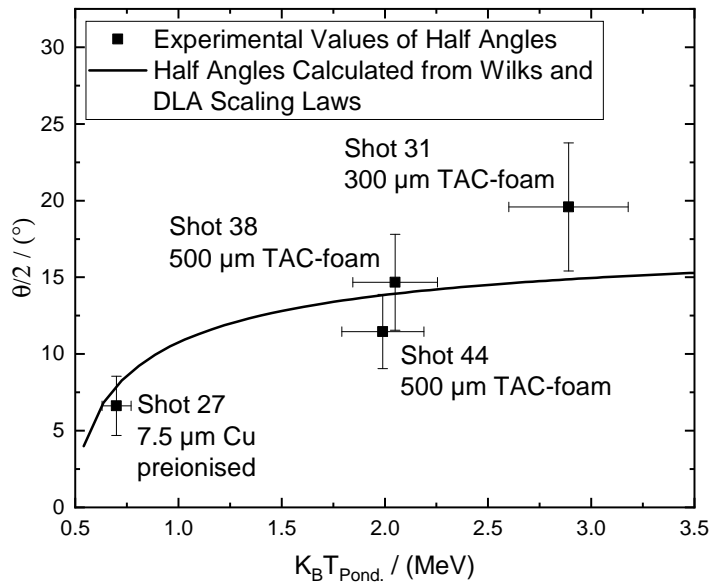


FIGURE 4.15: Half angles for shots onto different preionised target types calculated from the temperature data in tab. 4.1 depending on the values of the ponderomotive part of the spectrum. Solid line indicates the Half angles calculated from the Wilks and DLA scaling laws.

that direction (see tab. 4.1). 3D-Pic simulations show the occurrence of a cone along which the emission of electrons from the target reach a maximum (Rosmej, Olga N. et al. 2019; Pugachev and N E Andreev 2019). A simple estimation of the opening angle for that emission can be achieved using the values of the temperatures in tab. 4.1. The ponderomotive force predominantly accelerates perpendicular to the laser propagation direction while the DLA mechanism is directed along the laser. As the two different processes are responsible for the different temperature regimes in the electron spectra, the temperatures account for the mean kinetic energy of particles accelerated by each process individually. The opening half angle $\theta/2$ is estimated by the ratio of the momentum of the electrons of the ponderomotive part and the superponderomotive part of the electron spectra obtained from the total energy $E = k_B T$ by the relativistic energy momentum relation $E^2 = (pc_0)^2 + (m_0c_0)^2$:

$$\frac{\theta}{2} = \frac{1}{2} \arctan \left(\sqrt{\frac{E_{\text{Ponderomotive}}^2 - (m_e c_0^2)^2}{E_{\text{Superponderomotive}}^2 - (m_e c_0^2)^2}} \right) \quad (4.1)$$

with $E_{\text{Ponderomotive}}$ and $E_{\text{Superponderomotive}}$ the total energy of the ponderomotive and superponderomotive parts of the electron spectra respectively.

Fig. 4.15 shows the calculation of the half angles in dependence on the ponderomotive temperatures using the data from tab. 4.1. The solid line represents the half angle calculated from the hot electron temperatures from the Wilks and DLA scalings

(see fig. 4.12). Both, the ponderomotive and the superponderomotive temperature increase with intensity and subsequently the half angle. The values lie within the error on the calculated curve.

In P176, the angular distribution of the laser accelerated electrons was measured directly using imaging plate detectors placed on a cylinder with radius $r = 200$ mm concentric to the target position (see fig. 4.2 and fig. 4.6). The cylinder covered an angle of $\alpha = 100^\circ$ behind the target. The Cylinder consisted of three layers of thickness 3 mm magnetic steel. The imaging plate detectors were placed in between the three layers of steel to have a fixed distance between the detector surface and the target position. A slit was cut into the surface of each metal layer in the horizontal plane at height of the laser-target interaction region in order to allow for a free path for particles leaving the target to be measured behind the cylinder diagnostic by electron and ion spectrometers. As the imaging plate detectors only allow to obtain spatial and intensity information, the angular calibration was obtained by drilling holes in the surface of the first cylinder (e.g. see fig. 4.16). The distance of the holes was $d = 20$ mm which corresponds to an angle of $\alpha = 5^\circ$ for the distance of $d = 220$ mm used due to technical restraints during the experiment. Two screws (± 5 – 12.5° in vertical direction) are placed horizontally in laser propagation direction. Several layers of square pieces of activation samples were placed near the laser propagation direction and at around 15° to the laser propagation direction on the surface of the cylinder facing the target. Both, the shadows of the screws and of the activation samples can be seen clearly in the corresponding figures (see fig. 4.16, fig. 4.19 and fig. 4.26). The signal measured by the IP is the sum of the signal produced by electrons and gammas penetrating the cylinder. Geant4 simulations suggest that the the amount of electrons and gammas penetrating the frontal steel is shared 50 % each by electrons and gammas. But as electrons produce one order of magnitude more signal in the IP than gammas, the signal on the IP is dominated by electrons. Electrons with an energy exceeding $E = 3.5$ MeV will penetrate 3 mm of steel and $E = 7.5$ MeV electrons will penetrate 6 mm of steel respectively (see fig. A.6). Gammas with energies in the range of 1–5 MeV have a transmission of over 90 % while gammas reach a plateau for the transmission of 99 % for 3 mm of steel and 98 % for 6 mm in the range of 5–20 MeV. The rest of the signal stems from the gammas produced by the relativistic electrons emitting bremsstrahlung while traversing the cylinder material. For shots onto CHO-foam targets, multiple scanning procedures had to be performed as the first scan showed oversaturation. The first scan was always performed with 50 μ m spatial resolution, latitude 5 and sensitivity 4000. The sensitivity was then reduced to 1000 for subsequent scanning procedures. In sec. B.4.2, it is shown that multiple scanning procedures still allow to obtain information even after a presumed oversaturation in a single scanning procedure.

The angular distribution is depending on the choice of type of target. The results for three shots are shown for comparison in fig. 4.16, fig. 4.19 and fig.4.26. 0° corresponds to laser propagation direction, both horizontally and vertically.

Fig. 4.16 shows the angular distribution for a shot of high laser contrast (10^{-11}) on a $10\ \mu\text{m}$ thick gold foil. The picture from the first scanning procedure is shown. As only electrons with maximum energy of around 8 MeV are created in the foil (see. fig. 4.9), most of those electrons are stopped in the 6 mm thick steel of the cylinder (second layer of IP). Vertically, the distribution is homogeneous, while horizontally in the laser propagation plane there is a slight increase in the measured signal in the direction normal to the target surface (the target was turned in clockwise direction 10° from laser propagation direction). Fig. 4.18(a) and (b) show a vertical and horizontal lineout of the intensity profile in 4.16 respectively.

Changing the target to $300\ \mu\text{m}$ thick CHO-foam results in fig. 4.19. The picture from the third scanning procedure is shown. A clear directionality can be seen in this picture. The highest intensity which is much higher than for the case of a foil-target points towards the target normal again while the lower intensity areas are more symmetrically distributed around the axis of laser propagation direction. The homogeneity is also stronger in vertical direction than in horizontal direction. A filamentation of the laser-channel inside the plasma was predicted by simulations (Rosmej, Olga N. et al. 2019; Pugachev and N E Andreev 2019). Fig. 4.22, fig. 4.23, fig. 4.24 and fig. 4.25 support these results experimentally. Fig. 4.21(a) and (b) show a vertical and horizontal lineout of the intensity profile in 4.19 respectively. Fig. 4.21 (a) shows the lineout in horizontal direction at -2° of vertical direction of fig. 4.19. The signal intensity level shows a maximum in laser propagation direction (0°). As the signal is in part due to the filamented electron beam generated in the ionised foam, multiple Gaussian fits can be used to approximate the signal shape (half angles $\theta/2$: $23 \pm 16^\circ$ (orange), $3.8 \pm 0.4^\circ$ (turquoise), $5.4 \pm 0.8^\circ$ (magenta), $2.1 \pm 0.1^\circ$ (light green), $1.7 \pm 0.1^\circ$ (dark green) and $7.0 \pm 1.0^\circ$ (blue)). Fig. 4.21 (b) shows the lineout in vertical direction at 0° of horizontal direction of fig. 4.19. The signal intensity level shows a maximum in laser propagation direction (0°). As the signal is in part due to the filamented electron beam generated in the ionised foam again, multiple Gaussian fits can be used to approximate the signal shape here as well (half angles $\theta/2$: $5.8 \pm 2.3^\circ$ (magenta), $3.2 \pm 1.3^\circ$ (turquoise), $1.4 \pm 0.1^\circ$ (light green), $5.4 \pm 2.1^\circ$ (dark blue), $5.0 \pm 1.0^\circ$ (orange) and $1.5 \pm 0.2^\circ$ (dark green)). The angular distribution shown by fig. 4.22 and fig. 4.24 show half angles in the range of a few degrees as well.

The results for a combination of a $10\ \mu\text{m}$ thick gold foil and $300\ \mu\text{m}$ CHO-foam can be seen in fig.4.26. The picture from the second scanning procedure behind 6 mm of steel is shown. The gold-foil was placed behind the CHO-foam in order to be used as a radiator for the relativistic electrons produced in the CHO-foam plasma. This setup seems to increase the homogeneity and symmetry of the signal measured by the cylinder diagnostic. This homogenisation is possibly due to the generation of fields by return currents inside the metal foil. The signal shows a similar half angle in vertical (IP in the back behind 6 mm steel: $\theta_{vertical}/2 = 9.42 \pm 0.05^\circ$; IP at the front behind 3 mm steel at second scan: $\theta_{vertical}/2 = 9.84 \pm 0.12^\circ$ and at third scan: $\theta_{vertical}/2 = 10.39 \pm 0.05^\circ$) and in horizontal (IP at the front behind 6 mm

steel: $\varphi_{horizontal}/2 = 11.49 \pm 0.04^\circ$; IP at the front behind 3 mm steel at second scan: $\varphi_{horizontal}/2 = 11.07 \pm 0.05^\circ$ and at third scan: $\varphi_{horizontal}/2 = 12.88 \pm 0.06^\circ$) direction.

Angular Distribution of electrons generated in Different Target Types			
Values Calculated from Temperatures			
Shot	Target	Horizontal $\theta/2 / ^\circ$	
27	7.5 μm Cu-foil Preionised 3 J, $\Delta t = 1.5$ ns	6.6 ± 1.9	
	Prepulse foams 1 J, $\Delta t = 3\text{--}5$ ns		
31	300 μm Foam	19.6 ± 4.2	
34	300 μm Foam	4.1 ± 1.0	
	Prepulse foams 1 J, $\Delta t = 5$ ns		
38	500 μm Foam	14.7 ± 3.1	
44	500 μm Foam	11.5 ± 2.4	
Values Measured by Cylinder-Diagnostic			
Shot	Target	Horizontal $\theta/2 / ^\circ$	Vertical $\theta/2 / ^\circ$
41	300 μm Preionised Foam	23 ± 16	5.8 ± 2.3
		3.8 ± 0.4	3.2 ± 1.3
		5.4 ± 0.8	1.4 ± 0.1
		2.1 ± 0.1	5.4 ± 2.1
		1.7 ± 0.1	5.0 ± 1.0
		7.0 ± 1.0	1.5 ± 0.2
42	300 μm Preionised Foam + 10 μm Au-Foil	11.49 ± 0.04	9.42 ± 0.05
		11.07 ± 0.05	9.84 ± 0.12
		12.88 ± 0.06	10.39 ± 0.05

TABLE 4.2: Angular distribution of electrons generated in different target types. The upper part shows the estimation of the half angles plotted in fig. 4.15. The lower part shows the values from the fits in fig. 4.21 and fig. 4.28.

4.3.3 Generation of Quasi Monoenergetic Protons of few MeVs

Laser acceleration of protons or ions in NCD plasmas is a broad field studied in the recent years (Tsung et al. 2012; Wan et al. 2019; Willingale, Mangles, et al. 2006). Their application in experiments on warm dense matter was also proposed (Tauschwitz et al. 2006). The acceleration of protons or other ions was not the goal

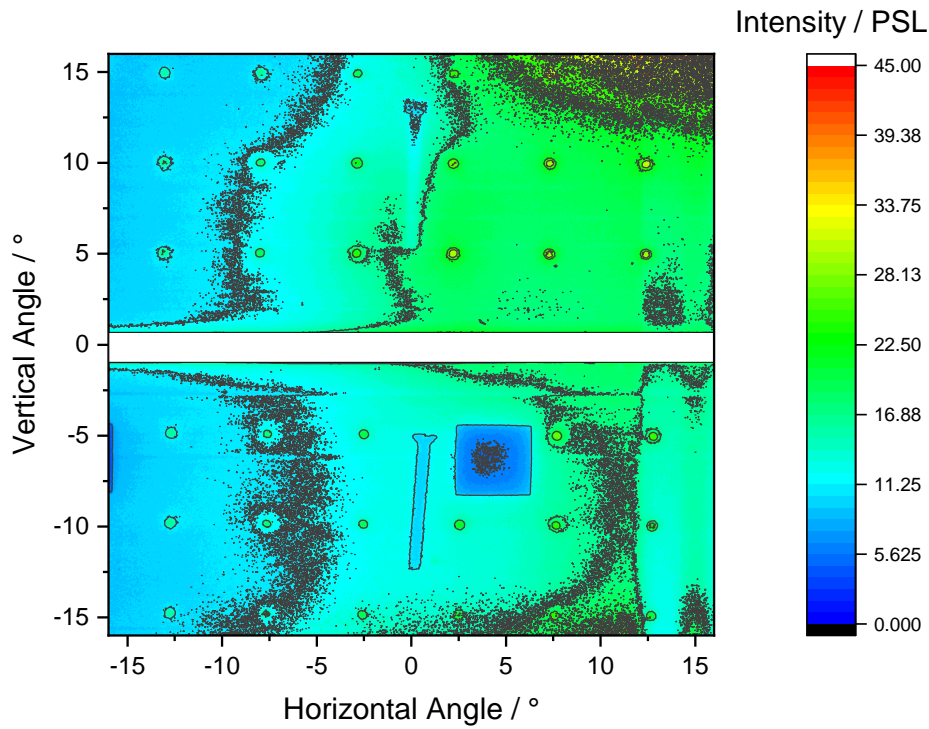


FIGURE 4.16: Angular distribution of electrons for a high contrast shot onto a $10\ \mu\text{m}$ thick gold foil. The dots show the holes drilled into the steel cylinder for angular calibration. Signal level of the first scanning procedure.

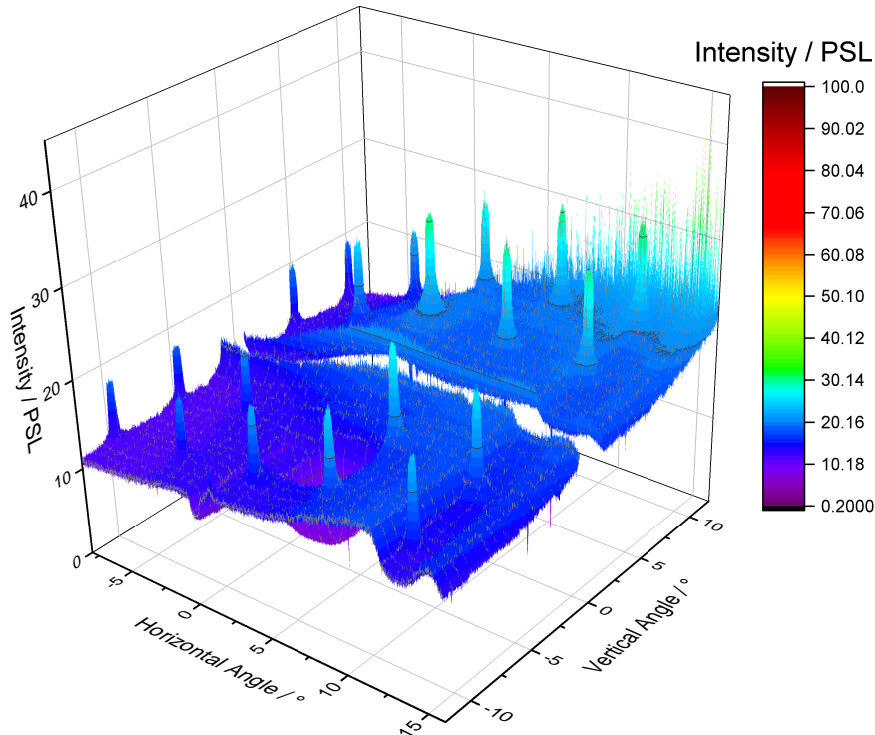


FIGURE 4.17: 3D representation of fig. 4.16.

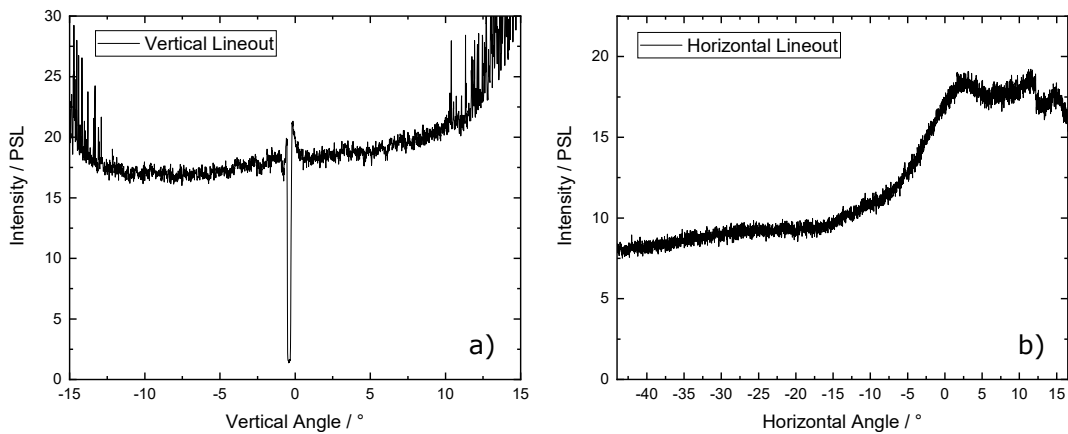


FIGURE 4.18: a) Lineout in horizontal direction at 2.5° of vertical direction of fig. 4.16. A homogeneous irradiation can be seen at angles below 0° . For higher angles the mean intensity increases by a factor of two (target rotated 0° to laser propagation direction). b) Lineout in vertical direction at 0° of horizontal direction of fig. 4.16. The irradiation in vertical direction is homogeneous as well. Only at the edges of the IP an increase in signal is visible.

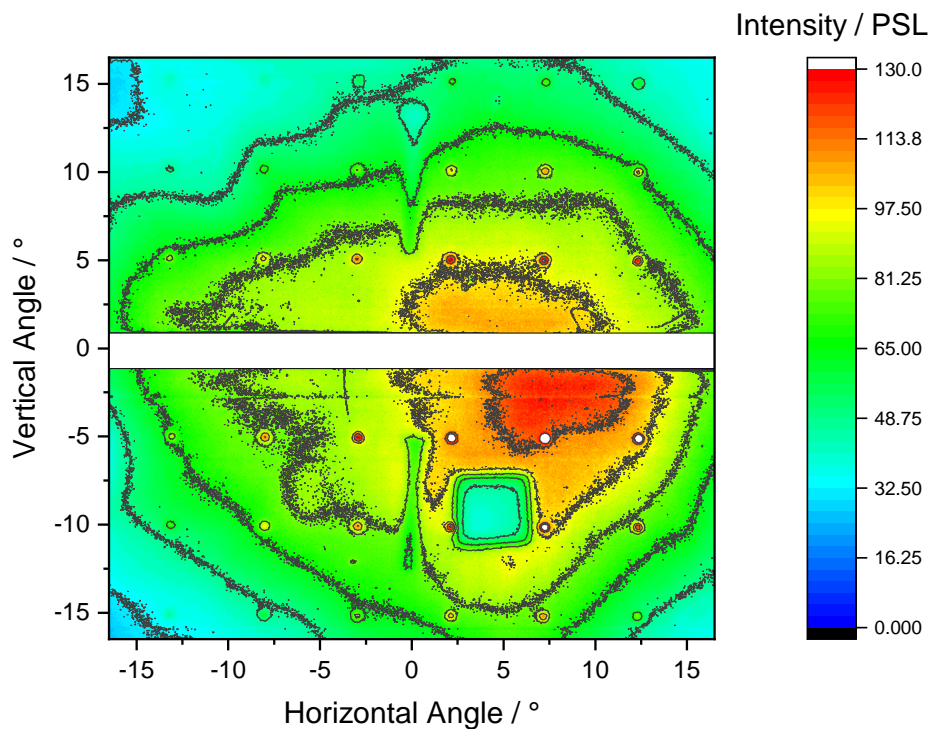


FIGURE 4.19: Angular distribution of electrons for a shot onto a preionised CHO-foam layer of thickness $300\ \mu\text{m}$. The dots show the holes drilled into the steel cylinder for angular calibration. Signal level of the third scanning procedure.

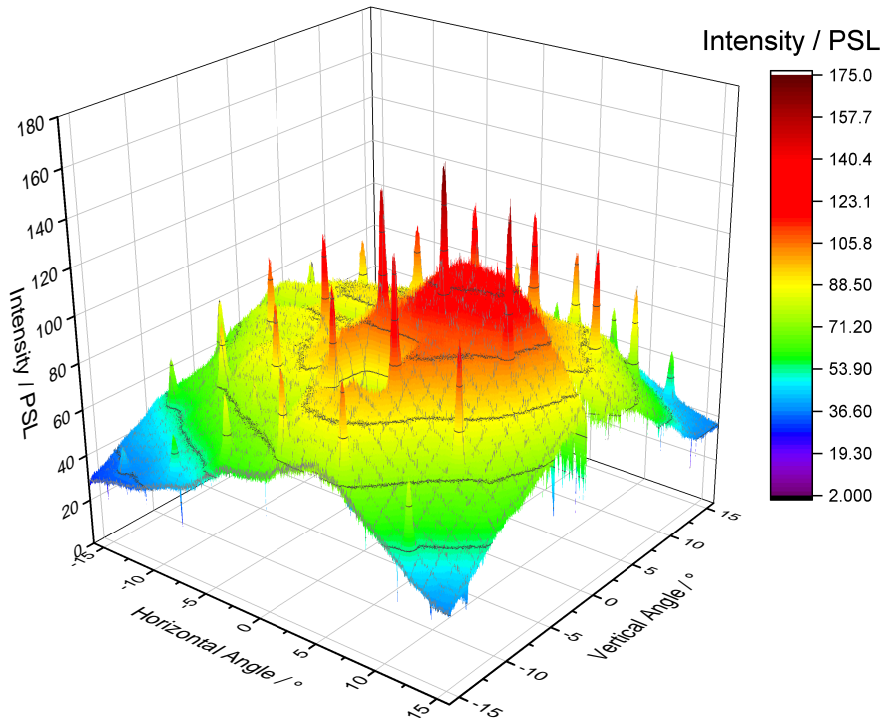


FIGURE 4.20: 3D representation of fig. 4.19.

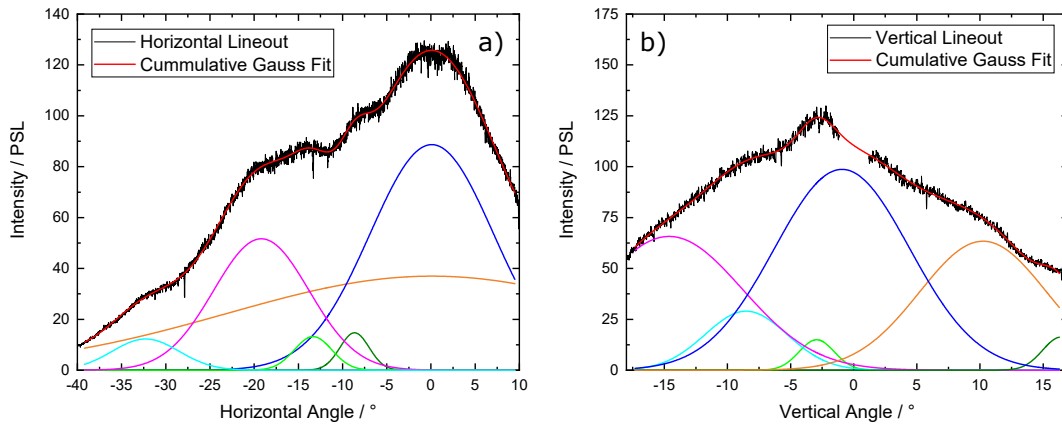


FIGURE 4.21: a) Lineout in horizontal direction at -2° of vertical direction of fig. 4.19. The signal intensity level shows a maximum in laser propagation direction (0°). As the signal is in part generated by the filamented electron beam generated in the ionised foam, multiple gaussian fits can be used to approximate the signal shape (half angles $\theta/2$: $23 \pm 16^\circ$ (orange), $3.8 \pm 0.4^\circ$ (turquoise), $5.4 \pm 0.8^\circ$ (magenta), $2.1 \pm 0.1^\circ$ (light green), $1.7 \pm 0.1^\circ$ (dark green) and $7.0 \pm 1.0^\circ$ (blue)). b) Lineout in vertical direction at 0° of horizontal direction of fig. 4.19. The signal intensity level shows a maximum in laser propagation direction (0°). As the signal is in part generated by the filamented electron beam generated in the ionised foam, multiple gaussian fits can be used to approximate the signal shape (half angles $\theta/2$: $5.8 \pm 2.3^\circ$ (magenta), $3.2 \pm 1.3^\circ$ (turquoise), $1.4 \pm 0.1^\circ$ (light green), $5.4 \pm 2.1^\circ$ (blue), $5.0 \pm 1.0^\circ$ (orange) and $1.5 \pm 0.2^\circ$ (dark green)).

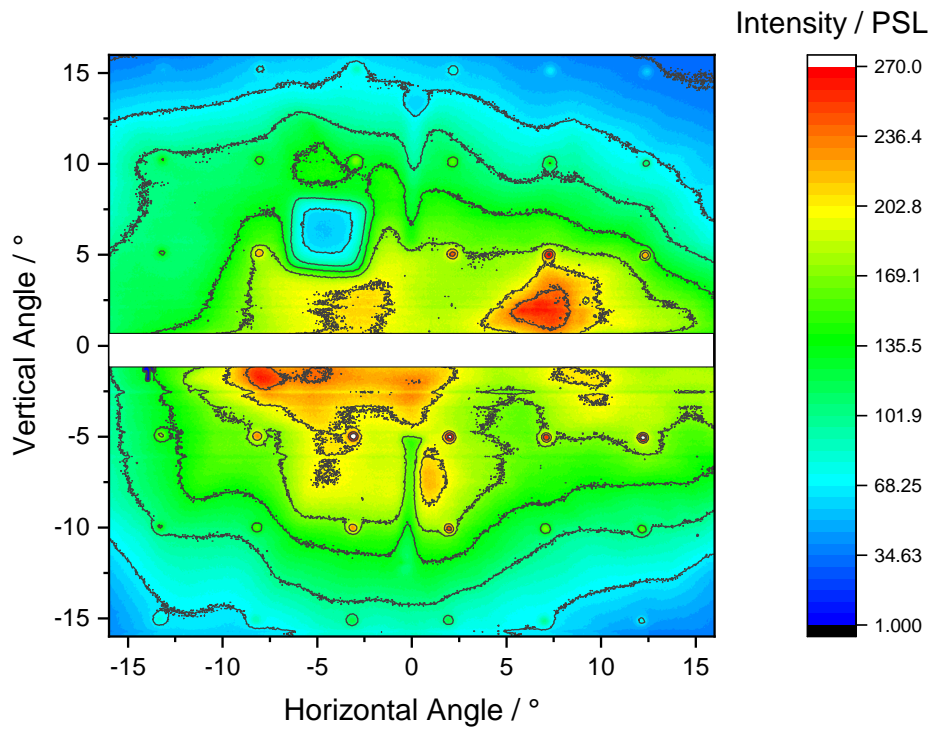


FIGURE 4.22: Angular distribution of electrons for a shot onto a preionised CHO-foam layer of thickness $300\ \mu\text{m}$. The dots show the holes drilled into the steel cylinder for angular calibration. The filamentation of the laser channel inside the plasma is illustrated by the irregularly distributed bright areas with half angles of a few degrees.

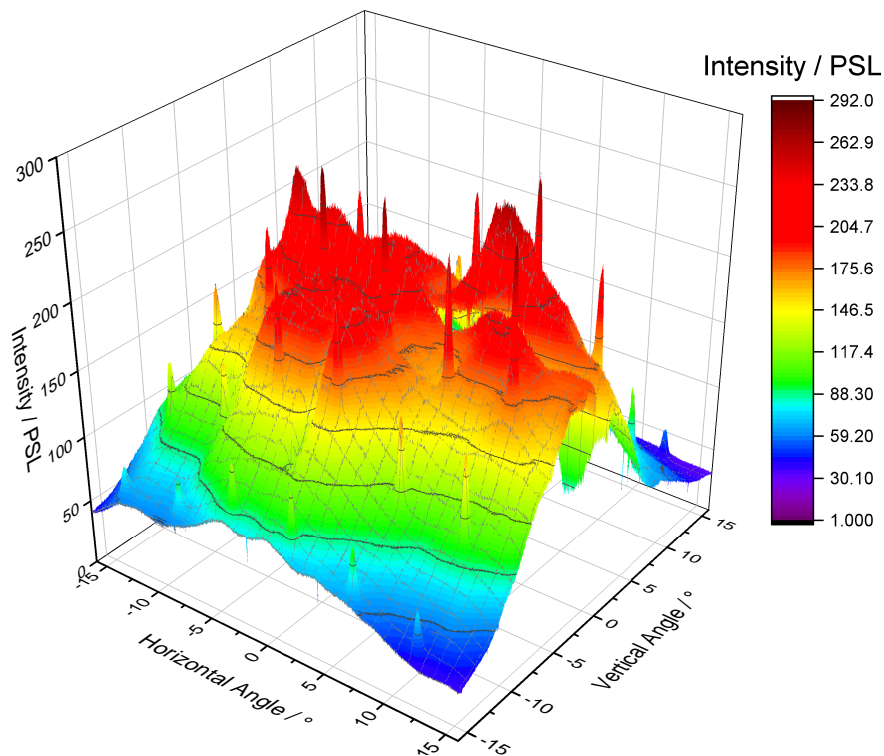


FIGURE 4.23: 3D representation of fig. 4.22.

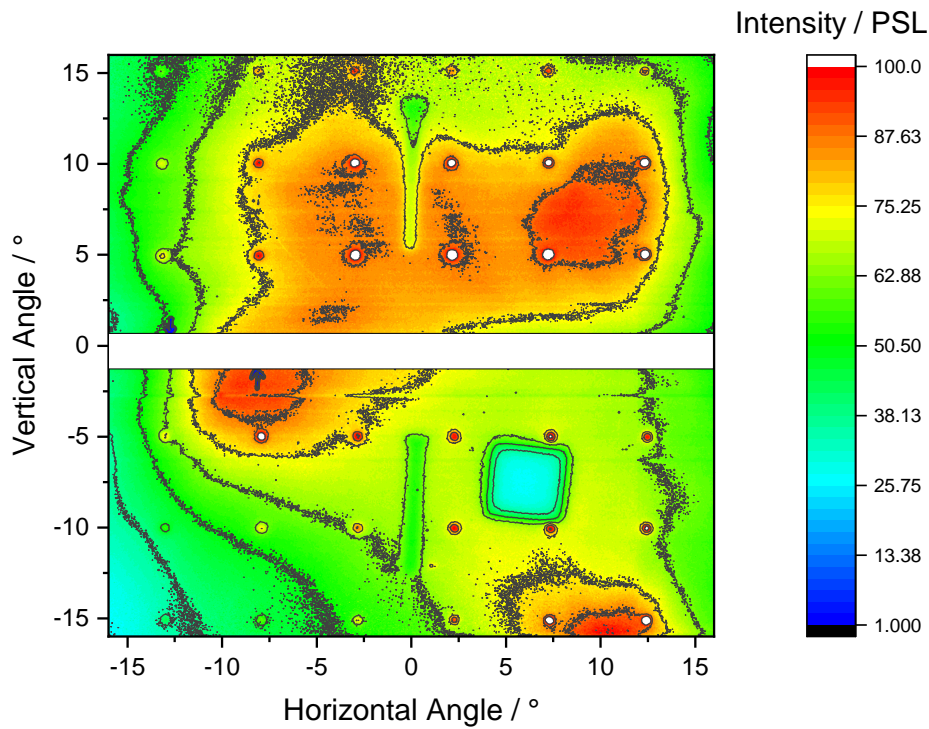


FIGURE 4.24: Distribution of electrons for a shot on a preionised CHO-foam layer of thickness $300\ \mu\text{m}$. The dots show the holes drilled into the steel cylinder for angular calibration. The filamentation of the laser channel inside the plasma is illustrated by the irregularly distributed bright areas with half angles of a few degrees.

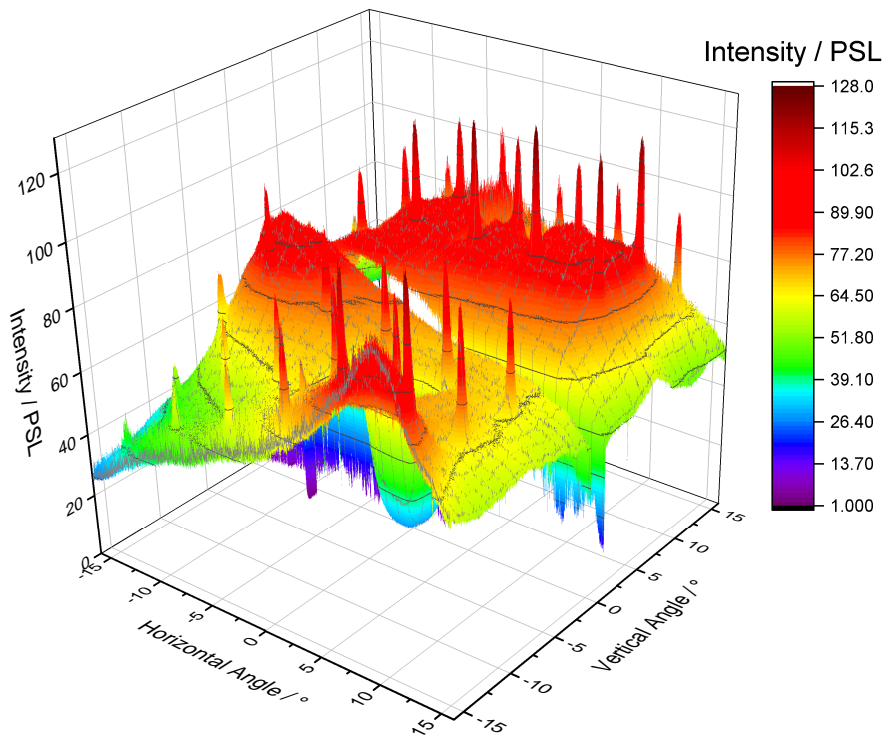


FIGURE 4.25: 3D representation of fig. 4.24.

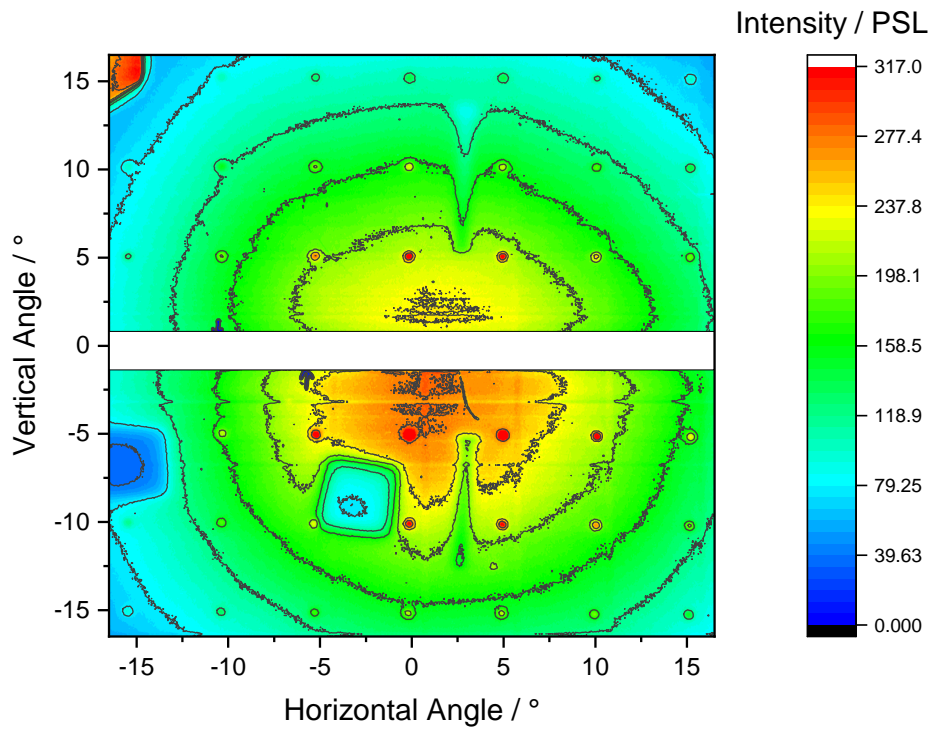


FIGURE 4.26: Angular distribution of electrons for a shot on a combination of preionised CHO-foam layer of thickness $300\ \mu\text{m}$ and a $10\ \mu\text{m}$ thick gold foil functioning as radiator. The dots show the holes drilled into the steel cylinder for angular calibration. Signal level of the third scanning procedure.

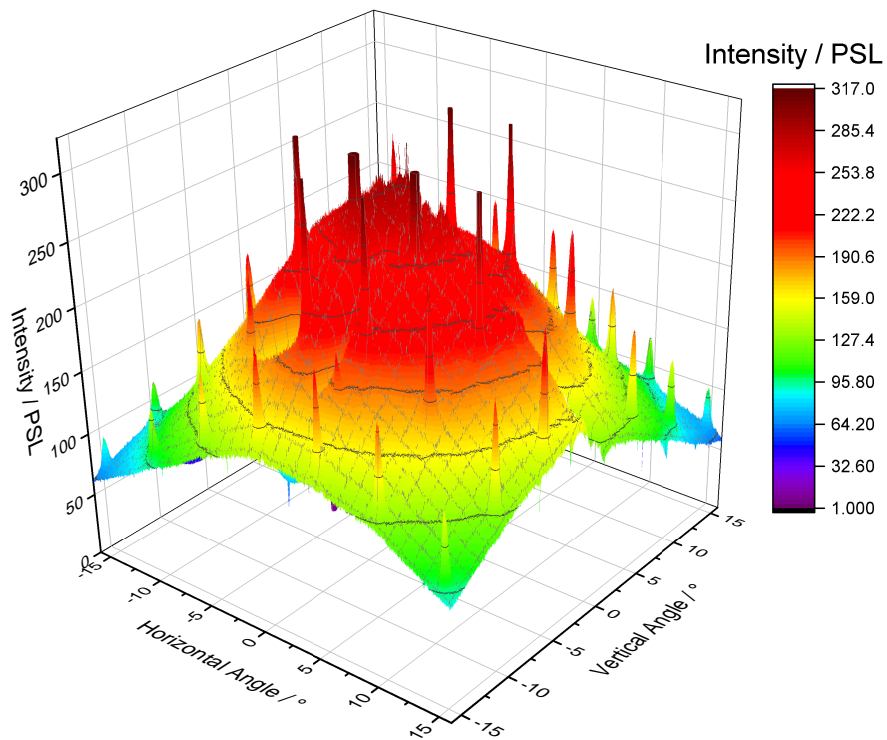


FIGURE 4.27: 3D representation of fig. 4.26.

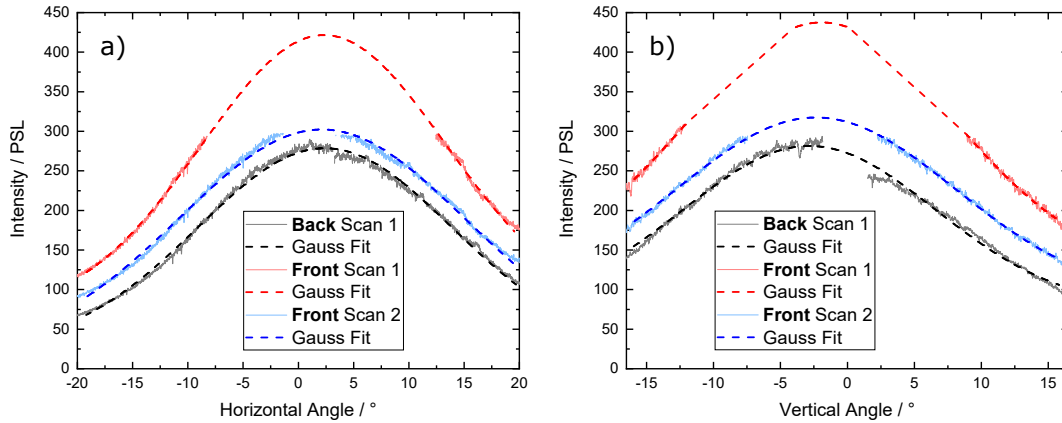


FIGURE 4.28: a) Lineout in horizontal direction at -1.6° of vertical direction of fig. 4.26. The signal intensity level shows a maximum in laser propagation direction (0°). A single gaussian fit is used to approximate the signal shape (half angles $\theta/2 = 11.728 \pm 0.047^\circ$). b) Lineout in vertical direction at 0° of horizontal direction of fig. 4.26. The signal intensity level shows a maximum in laser propagation direction (0°). A single gaussian fit is used to approximate the signal shape (half angles $\theta/2 = 9.17 \pm 0.05^\circ$).

of this work but the measurement of their energy and angular distribution can help to gain a better picture of the physical processes involved in the laser matter interaction with NCD plasmas.

Proton spectra were measured in P138 by using magnet spectrometers similar to the ones for electrons. The main laser pulse of 100 J pulse energy and an intensity of $3 \times 10^{19} - 4 \times 10^{19} \text{ W cm}^{-2}$ was shot onto 500 μm CHO-foam. A prepulse of 1 J pulse energy preceded the main pulse by 1.5 ns to ionise the foam prior to the interaction of the main laser pulse with the target.

The main differences to the measurement of the electron energy distribution are the higher magnetic field of 900 mT and the bigger geometric dimensions of the proton spectrometers. The proton spectrometers have twice the size of the electron spectrometers, both in length and width. The magnetic field polarity was inverted due to the opposite sign of the charge of the protons in comparison to electrons. A 2D map of the magnetic field was obtained using a Hall-probe. The magnetic field was more homogeneous than in the case of the electron spectrometers. Therefore the analytically calculated dispersion could be used without risking to lose precision in the measurement of the proton energies. The spectrometer was placed under 52° to laser propagation direction.

Fig. 4.29 shows the spectrum of protons measured behind a filter of 13 μm thick aluminium placed directly on top of the Imaging Plate detector. For absolute calibration, the data from fig. B.3 was used. The BAS-TR IP was used to detect the protons. This IP has a higher efficiency for very low proton energies due to the lack of a protective layer on top of the sensitive layer.

In contrast to the Target Normal Sheath Acceleration (TNSA) mechanism, where the energy of protons has a maxwellian like distribution, a quasi mono energetic

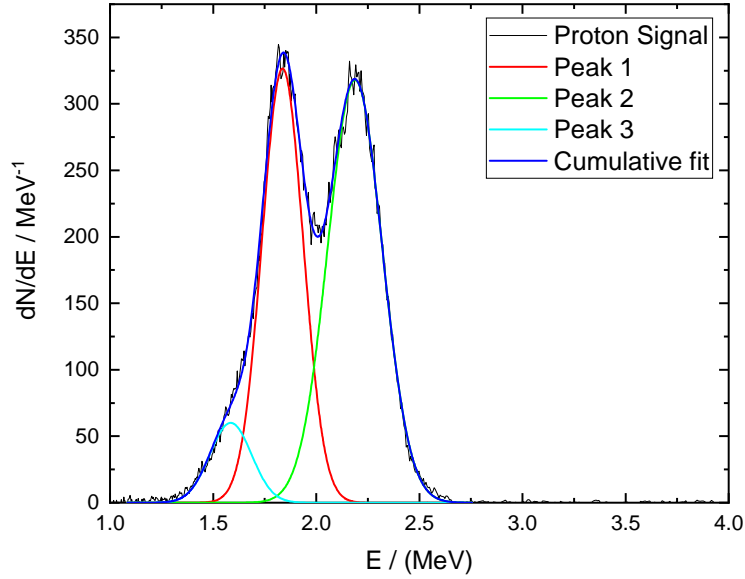


FIGURE 4.29: Proton energy distribution from a shot onto preionised foam layer. Proton spectrometer placed at 52° to laser propagation direction. The spectrometers observed a solid angle of $\Omega = 1.5 \times 10^{-5}$ sr.

energy distribution is observed. As the spectrum is not observed directly in laser propagation direction, it is further distinguished from TNSA which accelerates predominantly normal to the target surface. The spectrum (black line) can be fitted (blue line) by three Gaussian distributions (red, green and light blue lines). The mean energies of the three peaks are at $E_1 = 1.59 \pm 0.01$ MeV, $E_2 = 1.84 \pm 0.01$ MeV and $E_3 = 2.19 \pm 0.01$ MeV. The standard deviations are $\sigma_1 = 0.10 \pm 0.01$ MeV, $\sigma_2 = 0.10 \pm 0.01$ MeV and $\sigma_3 = 0.13 \pm 0.01$ MeV.

A number of 1.2×10^5 protons entered the spectrometer through the 1 mm entrance hole in P138. The spectrometers observed a solid angle of $\Omega = 1.5 \times 10^{-5}$ sr. In P176, time of flight measurements by means of diamond detectors were performed for different angles around the target. The quasi monoenergetic features of the proton energy distribution were present for all angles (-39° , 37° and 77°) while the maximum energy of the protons varied during one shot from 2.08 ± 0.01 MeV (37°) to 4.33 ± 0.01 MeV (77°). The amount of protons measured at 77° is slightly higher than at the other angles but the difference is less than one order of magnitude. Assuming an isotropic emission, the number of protons emitted in 4π measured by the magnet spectrometer is estimated to be around 10^{10} .

4.3.4 Comparison of X-Ray Radiography by X-Ray Tube and Laser Experiment

In future experiments, the spatial resolution of diagnostics based on backlighter sources is of great importance. To place a detector near the target is generally not



FIGURE 4.30: Picture of the radiography targets used in the experiments. The targets consist of several materials which allows comparison between Al, Cu, Fe and brass (alloy of Cu and Zn). The geometry of the different steps is the same (1 mm each).

possible. Therefore, a small backlighter source size is needed to obtain high spatial resolution. Additionally, to obtain a high signal-to-noise-ratio, a high dose of radiation is required. The irradiation time for reaching a sufficient amount of radiation dose using an X-ray-tube is at least a few seconds. In the case of laser based secondary backlighter sources, a high radiation dose can be deposited on a target in a much shorter time than with an X-ray-tube. High power lasers possess pulse lengths from a few 10 fs to a few 1 ps. The time resolution of such source is also in the range of pico seconds as the backlighter source only radiates during the interaction of the high power laser with the backlighter source target. In the following section, the properties of the radiation produced by an X-ray-tube is compared to the case of high power laser matter interaction.

Three different target setups are used. Firstly a 10 μm plane gold foil, secondly a 325 μm CHO-foam, and thirdly a combination of both 325 μm CHO-foam and 10 μm plane gold foil where the foil is placed at the backside of the foam. A 90–100 J, 3×10^{19} – 4×10^{19} W cm^{-2} laser pulse with 1 ps pulse length is used (see tab. 3.3). The foam targets were irradiated by a 1 J ns long pre pulse preceding the main pulse by 2.5 ns to produce homogeneous plasma conditions for the interaction of the main pulse with the target. The produced radiation passed radiography targets (see fig. 4.30). The radiography targets were placed at $62 \pm 1^\circ$ to laser propagation direction at every laser shot.

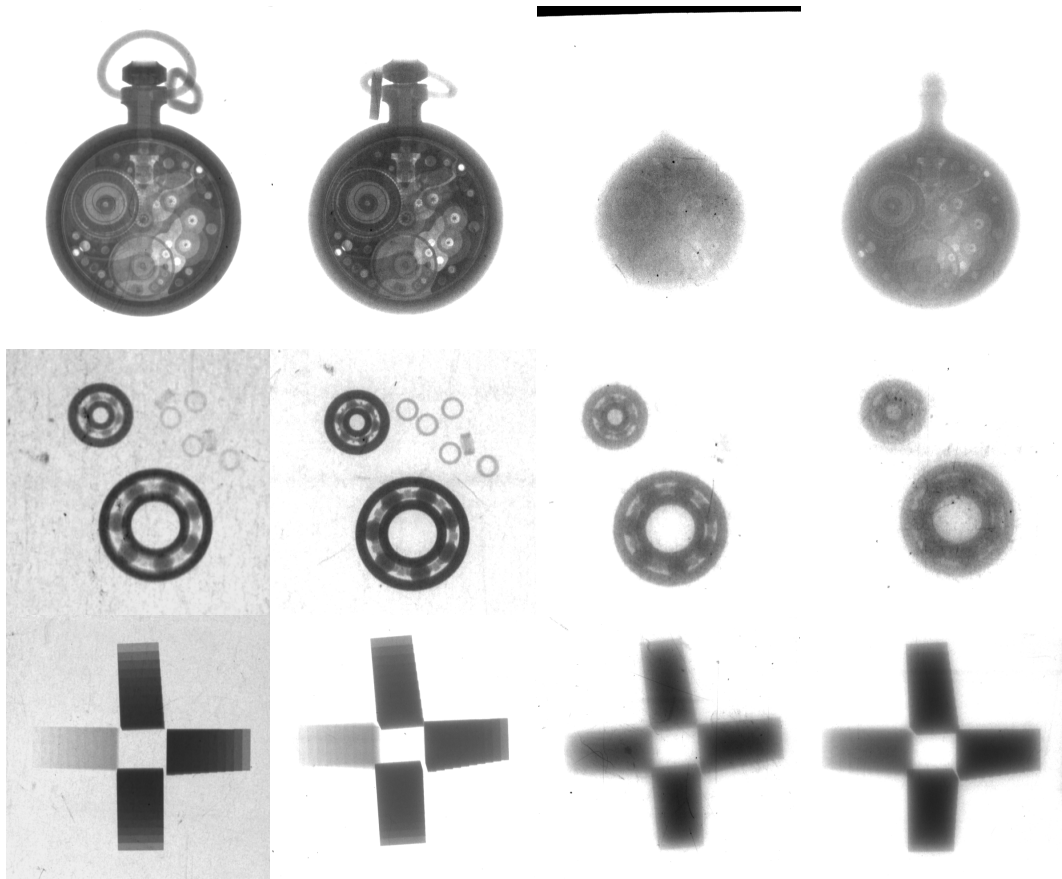


FIGURE 4.31: First column: image using an X-ray-tube. Second column: Laser shot onto foil target. Third column: Laser shot onto foam target. Fourth column: Laser shot onto combination of foam and foil target. See text for details. Colour scale adjusted to best image quality.

Fig. 4.31 shows images obtained with the different sources. The first column shows the image obtained with the X-ray-tube. The second column shows the image with a $10\ \mu\text{m}$ foil-target. The third column shows the image produced by a shot onto $325\ \mu\text{m}$ CHO-foam. The fourth column shows the results of the combination of $325\ \mu\text{m}$ CHO-foam and $10\ \mu\text{m}$ plane gold foil. The targets were placed similarly to the measurements shown in sec. B.4.2 directly on top of the IP detector only separated by $1\ \text{mm}$ of aluminium. The distance for the X-ray-tube was $400\ \text{mm}$ to the targets. In the laser experiment, the radiography targets were placed $440\ \text{mm}$ away from the laser target. The acceleration voltage of the X-ray-tube was set to $250\ \text{kV}$ and the radiography target was irradiated by a dose of $100\ \text{mGy}$. The images shown for the X-ray-tube measurements are shown in Appendix B.4.2. It is noteworthy that the image quality is increased in the shot on a combined target of foil and foam in comparison to pure foam-target. That coincides with the homogenisation shown by the cylinder diagnostic. Fig. 4.32 shows a comparison of images with the same colour scale. Therefore the signal intensity levels can be compared (see fig. 4.33).

As the source size of the X-ray-tube is non vanishing, the influence of the distances between X-ray-tube and target as well as the distance between target and imaging

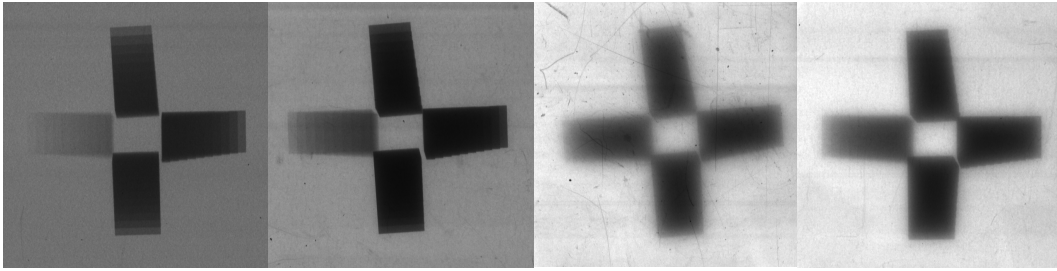


FIGURE 4.32: First column: image using an X-ray-tube with 1 mGy at 250 kV. Second column: Laser shot onto foil target. Third column: Laser shot onto foam target. Fourth column: Laser shot onto combination of foam and foil target. See text for details. Same colour scale for each image.

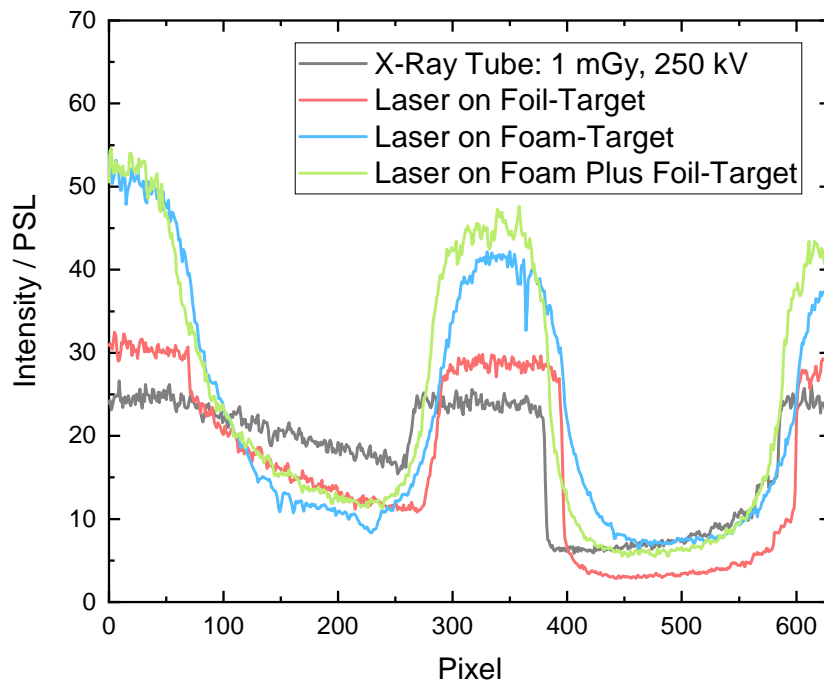


FIGURE 4.33: Lineout in horizontal direction from the images in fig. 4.32.



FIGURE 4.34: Image taken by IP with magnifications of $M = 2$. The source size of the X-ray tube leads to a washing out of the structures seen.

plate detector were tested. The acceleration voltage of the tube was chosen to be 500 kV again. The dose was reduced to 1 mGy to prevent over-saturation of the IP. The distance between the targets and the detector was fixed to 285 mm. The distance between targets and X-ray-tube was chosen to be 570 mm, 475 mm and 427 mm. That corresponds to magnifications $M = 2$, $M = 2.5$ and $M = 3$. The results are shown in fig. 4.34. There is a strong washing out of the structures seen in the the magnified images compared to the images produced when the targets are placed directly on top of the IP. This supports the assumption that the source size of the X-ray-tube is big compared to the spatial resolution of the Imaging Plate detector. In conclusion, that shows that the source size is very important in experiments where the detector cannot be placed right next to the target. Laser based X-ray sources provide the source size necessary and additionally, allow for temporal resolution up to the ps-regime.

Chapter 5

X-Ray Fluorescence of Target and Heavy-Ion Beam

The intense uranium ion beams that will be available after commissioning of the new synchrotron SIS100 at the FAIR facility in Darmstadt, Germany, can be used for experiments in High Energy Density (HED) physics. Any type of material can be heated volumetrically and extreme states of matter generated with Mbar pressures and several eV of temperature can be reached (Tahir, Deutsch, et al. 2005). One of the main goals of the plasma physics program at FAIR is the investigation of their Equations of State (EOS). One of the proposed experiments is the HIHEX-scheme (see fig. 5.1). Development of new diagnostic methods and instruments for such extreme states of matter and experimental conditions is demanded. They have to be capable to operate in an environment with a high level of radiation damage while also be able to easily allow for data collection in an irradiated environment.

Numerical simulations of the hydrodynamic response of the target on deposited energy rely heavily on the precise knowledge of the energy density distribution caused by the U-beam in the target and is therefore a very important input parameter. Fig. 5.2 illustrates the influence of the ion beam distribution on target on the number of particles actually passing the target front as shown in fig. 5.1. A Gaussian beam distribution with a *FWHM* around 1 mm is assumed (right axis). Shown are estimations for two different plane foil target thicknesses with the foils extending infinitely in the third dimension as proposed for the two different HIHEX-schemes. The fraction of the total number of beam particles interacting with the foils is shown on the left axis.

Simulations are crucial in the preparation process of an experiment and in the interpretation of obtained experimental data. The use of the target and heavy-ion beam X-ray fluorescence for the investigation of the energy density distribution in the target was proposed. For the imaging of the target expansion and mapping of the heavy-ion beam distribution in the interaction region a spatial resolution of at least 100 μm is required (O N Rosmej, S. A. Pikuz, et al. 2005; O N Rosmej, Blazevic, et al. 2005; Rzadkiewicz et al. 2010). The results further below can be scaled to high heavy-ion energies available at SIS18 and SIS100 (X. Ma et al. 2001).

In the HIHEX experiment, planned by the HED@FAIR collaboration at FAIR (V.

Mintsev et al. 2016), precise knowledge of the energy density distribution deposited by the heavy-ion beam into the target is of great importance. A heavy-ion beam experiment was performed in the frame of FAIR Phase-0 at the UNILAC facility at the GSI Helmholtz Centre for Heavy-Ion Research GmbH in Darmstadt, Germany. It was aimed at the development and application of FAIR-relevant imaging techniques of the heavy-ion beam distribution on target based on X-ray target and projectile fluorescence.

Two experimental campaigns were performed on the emission of fluorescence radiation of ion beam and target and the X-ray imaging of Cu-meshes using this fluorescence radiation (U305 in 2016 and U317 in 2019). The experiment U305 focussed on the measurement of the absolute number of fluorescence photons emitted by target and ion beam. Spectrally resolved measurements allowed to discern between the sources of that radiation and allowed to link the number of emitted photons to the heavy-ion beam charge traversing the target. The second experiment (U317) concentrated on the spatial resolving imaging techniques required in the future experiments. Both polychromatic and monochromatic imaging techniques were employed separately. The properties of Imaging Plate detectors and semiconductor based cameras (sCMOS) were compared in the polychromatic part of the experiment as well as the conversion of the X-ray radiation into visible light and its transport to the camera. 2D spatial resolving X-ray crystals allowed to obtain monochromatic images of the ion beam-target interaction region observing only the radiation of either ion beam or target by means of an X-ray CCD-camera.

The XCOT-system (X-ray Conversion to Optical radiation and Transport) was developed at the Goethe University Frankfurt in the frame of a BMBF-Project for application in Phase-0 and at FAIR (Zähler et al. 2017). Strong parasitic radiation of particles and gammas as well as activation of the experimental area is expected for experiments in the APPA-cave at FAIR (Lang et al. 2014). On one hand, existing diagnostic techniques that require access to the target area cannot be applied which emphasises the need for automation in detection and data collection. On the other hand, the experimental equipment can be destroyed due to parasitic radiation. Electronic devices are particularly in danger (Belousov 2014). Additionally, the setup has to be shielded from radiation. In the XCOT-concept, the X-ray fluorescence radiation of the ion beam-target interaction region is imaged onto a scintillator using pin-holes or crystals. The image thus converted into visible light is then transported over several meters using a telescope objective or optical fibres and registered by combination of image intensifier and a sCMOS-camera. Fig. 5.3 shows the scheme of this setup.

The XCOT-system was deployed in the experiment U317 for the first time. In the experiment, a 11.4 MeV/u Au²⁶⁺-beam was passing through different foil- and mesh-targets from few μm Al-, Cu-, Ta-foils to 10 μm thick Cu-meshes with openings of 50–190 μm and bar widths of 8–60 μm . X-ray projectile and target fluorescence produced in the interaction region was used for imaging purposes.

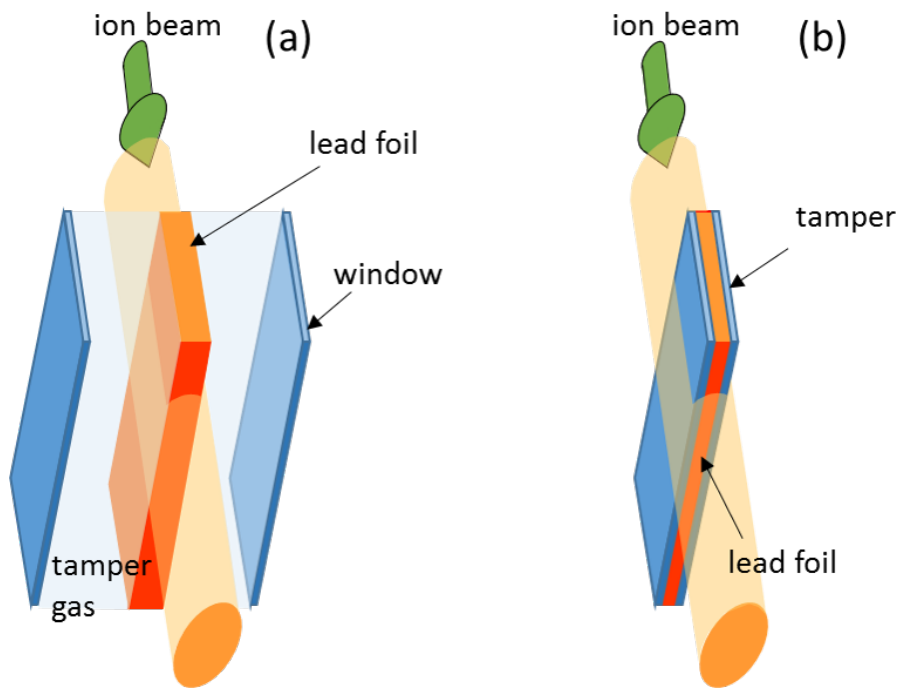


FIGURE 5.1: (a) HIHEX scheme with a thick target foil of several hundred μm thickness. A tamper gas of 100 bar pressure is planned to be used. (b) thin target foils of a few μm thickness. A solid state tamper is planned to be used in this scheme (Vincent Bagnoud 2020).

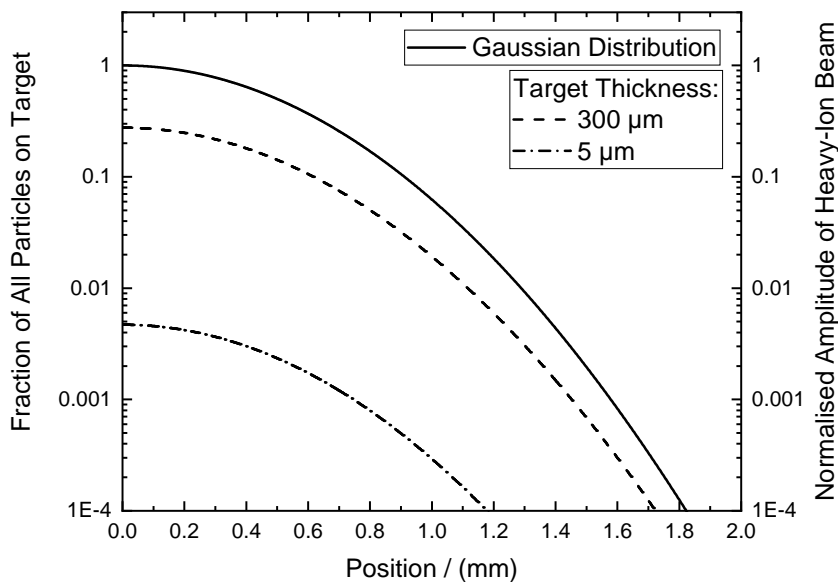


FIGURE 5.2: The fraction of heavy-ions from the beam actually passing the target front as shown in fig. 5.1. A Gaussian beam distribution with a $FWHM$ around 1 mm is assumed (right axis). Shown are estimations for two different plane foil target thicknesses with the foils extending infinitely in the third dimension as proposed for the two different HIHEX-schemes. The fraction of the total number of beam particles interacting with the foils is shown on the left axis.

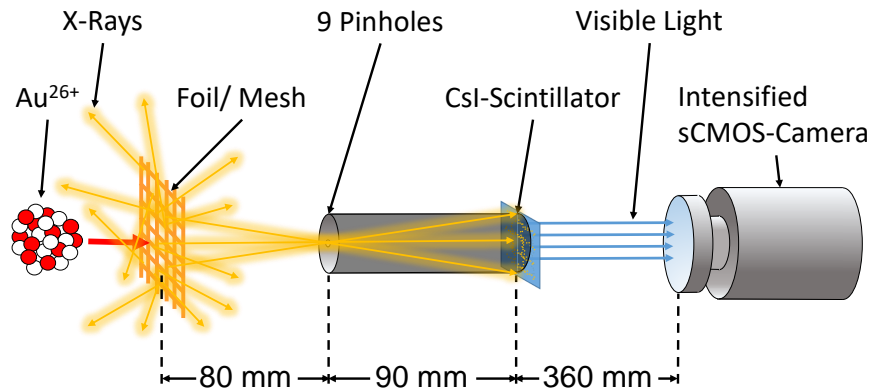


FIGURE 5.3: Schematic view of the XCOT-system. Cu-Meshes are irradiated by an Au^{26+} -beam. The Cu-meshes emit X-ray fluorescence which is imaged onto a CsI-scintillator. The scintillator converts the X-rays into visible light. That light is transported to an MCP based image intensifier and then registered by a sCMOS-camera.

5.1 Experimental Setup

Different active and passive diagnostic methods for studying the energy deposition of the ion beam in the target are discussed (see chap. 1). This experiment focuses on the passive diagnostic by measuring the X-ray target and projectile fluorescence of the target region. The experimental results on measurements and characterisation of the heavy-ion and target fluorescence using pinholes, X-ray CdTe-diodes and dispersive systems presented in this section were carried out at the Z6 experimental area which is situated after the UNILAC-accelerator facility (see sec. 3.1). In U305, a 6.5 MeV/u Au^{26+} -beam with a frequency of 3 Hz for the macro bunches, 108 MHz micro bunch structure and 2–5 μ A beam current irradiated foil-targets of different materials (Al, Cu, Ta of 6 – 10 μ m thickness). The ion beam-current was measured by Faraday-cups two m in front and three m behind the target position after passing the foil target. Polychromatic spatial resolved imaging was achieved by means of pin hole cameras. X-ray spectra were obtained using a CdTe-diode and a high resolution Highly-Oriented-Pyrolytic-Graphite-X-ray-spectrometer (HOPG). From this, the number of interactions between the ion-beam particles and the target material can be deduced.

A CdTe-diode was used to measure spectra up to 20 keV. The Au L_ *alpha* line was chosen to define the number of photons emitted in 4π per μ m target-thickness.

This shows a dependence of the X-ray fluorescence yield on the number of interacting projectiles as well as the target material and allows us to scale the results for conditions at the APPA-cave at FAIR.

This experiment demonstrated the potential of X-ray fluorescence as a diagnostic tool for future FAIR-experiments. We observed intense radiation of ionised target atoms (K-shell transitions in Cu at 8–8.3 keV and L-shell transition in Ta) as well as Doppler-shifted L-shell transitions of Au projectiles passing through foils in the photon energy region of 10 keV. This radiation can be used for monochromatic (dispersive element) or polychromatic (pin-hole) X-ray mapping of the ion beam intensity distribution in the interaction region. Using data obtained by means of CdTe X-ray spectrometer and a Faraday cup, the number of Au-L $_{\alpha}$ photons per 1 C of the Au-charge passing through Al, Cu and Ta foils and per 1 μm target-thickness in 4π could be estimated. This number allows us to conclude that 10–100 fold amplification of the signal is required in order to apply this method for U-beam intensities between 1×10^{10} – 5×10^{11} particles/pulse. 2D X-ray pinhole images of a Cu-mesh excited by an Au-ion beam, obtained with 200 μm spatial resolution, is the first promising result that was improved on in the experiment U317.

The goal of the experimental campaign U317 was to observe the ion beam intensity distribution in the target region using spatial resolving X-ray diagnostics. U317 was performed at the UNILAC-facility as well. A 11.4 MeV/u Au²⁶⁺-beam was used in contrast to U305. The fluorescence of target and ion beam only occurs during the beam-target interaction. Therefore, it is suitable for spatial resolved measurement of the energy deposition in high energy density experiments. The first part of this experiment focussed on the polychromatic imaging of the interaction region using pin hole cameras with either an imaging plate or the XCOT-System as detector (see fig. 5.4 (a) and fig. 5.4 (b)). The spatial resolution of the XCOT-system was optimised in this experiment while transporting an optical image over a long distance to the intensified camera.

The second part of the experiment discusses monochromatic imaging techniques applicable to aforementioned imaging techniques in the future (see. fig. 5.4 (b)). The advantage of monochromatic imaging is that it makes distinction between ion beam and target fluorescence possible. Leading to the measurement of the actual energy loss during the interaction time of ion beam and target.

5.2 Diagnostic Methods

A variety of radiometric (keV, particle detection (keV to MeV) and electronic diagnostics were applied at the experimental area. The photons in the range of keV energies are produced by the interaction of the ion beam with the target. For the measurement of continuous (characteristic) line radiation, electronic and crystal based diagnostics were used. As the interaction between ion beam and the target takes place in a small volume of less than a few cm^2 , radiation that was emitted has to be either transported

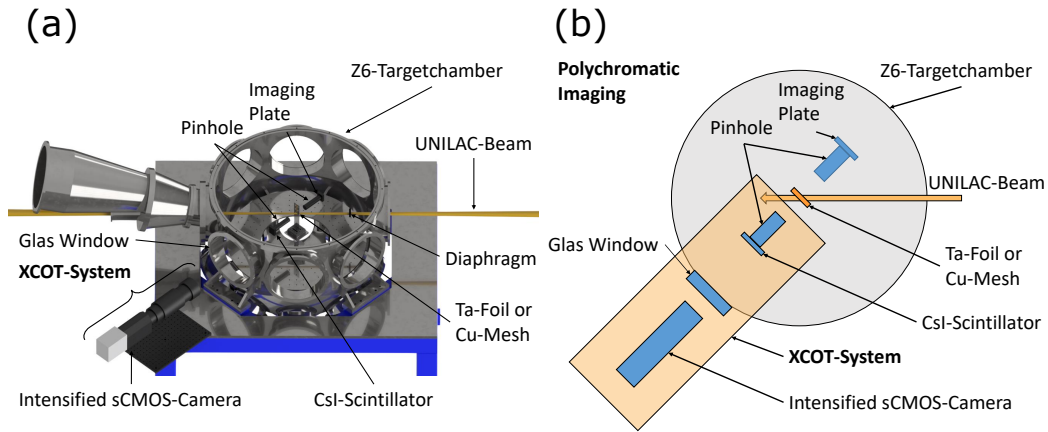


FIGURE 5.4: (a) The setup for polychromatic imaging inside the 1 m in diameter target chamber at Z6. The large tube on the left side of the chamber shows the entrance of the PHELIX-beam not used in this experiment. (b) Experimental scheme of the polychromatic imaging of the beam target interaction region using the XCOT-system and imaging plate detectors. The Au^{26+} -beam is entering the chamber from the right. The foil- or mesh-targets are placed in the center of the chamber. Also shown are the pinholes at 45° and 225° to ion-beam propagation direction. The XCOT-system is visible on the lower left outside the chamber.

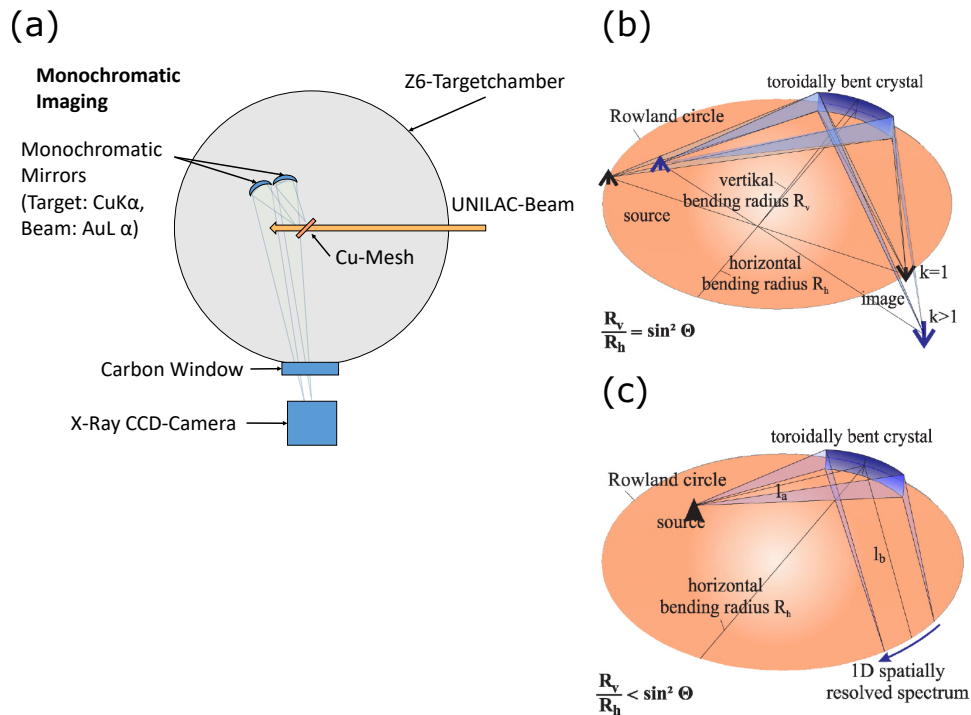


FIGURE 5.5: (a) Experimental scheme of the monochromatic imaging of the beam target interaction region using bent crystals for the imaging and an X-ray CCD-camera as detector. (b) X-ray optics with toroidally bent crystals. Imaging with source and image on the Rowland circle ($k > 1$). (c) Spectroscopy with one dimensional spatial resolution. The source lies inside and the spectrum on the circle (Lötzsch 2012).

to the diagnostics using appropriate optics or the detector has to be placed near the target. In experiments at the new FAIR facility, diagnostics have to operate under extreme conditions. In particular, electronic devices like CCD- and CMOS-Cameras can be heavily influenced by parasitic electromagnetic radiation, bombardment with high energy particles, as well as, debris and by that either the measurement process can be disrupted or the devices can be damaged. Experiments have to be performed largely without electronic measurement and readout processes near the interaction region to avoid that. Reduction of malfunctions by increasing the distance or the shielding of the diagnostics is only possible if suitable optics for the imaging of the interaction region are available for the desired spectral region. Additionally, the strong absorption of X-ray radiation in the range of up to 15 keV in air requires the transport of the radiation in vacuum. As a result, these conditions have to be considered in the development of diagnostic techniques like the XCOT-system.

Fig. xcotscheme2 shows the scheme of the XCOT-system. It consists of an X-ray imaging part which is performed by a pinhole camera in this experiment. This X-ray radiation from the beam target interaction region then imaged onto a 100 μm thick CsI-scintillator. The X-ray radiation is transformed into visible light which allows for the transport of the radiation over a large distance and through air onto a detector. In this case, the detection is facilitated by a sCMOS-camera combined with a micro channel plate based image intensifier module.

Monochromatic X-ray imaging can be performed using toroidally bent crystals as an X-ray microscope. The X-ray microscope favourably combines both the high spectral resolution of a spectrograph and the spatial one of a pinhole camera (Förster et al. 1987). It is therefore possible to get a magnified image of the emission region of a selected spectral line or of a small continuum range (see fig. 5.5). The use of Bragg reflections of two-dimensionally bent crystals enables the X-ray microscopical imaging in narrow spectral ranges ($\Delta\lambda/\lambda = 10^{-4}$ to 10^{-2}) with wavelengths $0.1 \text{ nm} < \lambda < 2.6 \text{ nm}$. The parameters of the two used crystals are shown in tab. 5.1.

Parameters of Two Toroidally Bent Crystals		
	Si	GaAs
Photon Energy / keV	8.028	13.53
Crystal Reflection	Si 444	GaAs 12 0 0
Bragg Angle $\Theta_B / ^\circ$	80.09469	76.33078
Horizontal Radius R_h / mm	200	200
Vertical radius R_v / mm	193	189.6
Magnification Factor M	6	6
Distance Source Crystal l_a / mm	114.9	113.4
Distance Crystal Detector l_b / mm	689.5	680.2
Spectral Window $\Delta\lambda/\lambda$	0.00748	0.01042
Efficiency	2.2×10^{-5}	8.1×10^{-7}

TABLE 5.1: Two toroidally bent crystals for monochromatic imaging of Cu K_α and Au L-shell emission at 13.5 keV.

5.3 Experimental Results

Two different experimental campaigns were conducted at the UNILAC-facility. The main difference was the change in energy of the particles in the gold ion-beam. In U305, a 6.5 MeV/u Au²⁶⁺-beam irradiated foil-targets of different materials (Al, Cu, Ta of 6–10 μm thickness and additionally Cu-meshes as a first step in the development of polychromatic imaging techniques for mapping of the energy deposition inside the target during the interaction with the ion beam. The X-ray fluorescence yield measurements were achieved in this experiment.

After the first experiment, the XCOT-system was set up and measurements with an X-ray-tube as radiation source were conducted to test the whole system for detection of X-rays, their conversion into visible light, and its transport and registration inside the intensified sCMOS-camera.

The second experiment at the UNILAC-facility (U317) focused on the imaging techniques desired to achieve the 100 μm spatial resolution required for energy loss measurements in the APPA-cave at the future FAIR-facility. A 11.4 MeV/u Au²⁶⁺-beam was used in contrast to U305. The spatial resolution was improved on and the XCOT-System was commissioned for the first time in a heavy-ion beam experiment.

5.3.1 Fluorescence Yield Measurements

As numerical simulation on the hydrodynamic response of the target to the energy deposited by the ion-beam depend heavily on the knowledge of the energy density distribution inside the target, the X-ray fluorescence yield of the interaction of the Au²⁶⁺-beam with foils was measured using different targets of a few μm Al-, Cu-,

Ta-foils for comparison. For such kind of diagnostic, no active backlighting is required. The X-ray-fluorescence radiation emitted by the beam-particles allows for an estimation of the number of reactions that took place during the irradiation of the target. The fluorescence radiation does only occur while ions are passing the target. No afterglow effects are present.

A single hit counting CdTe-spectrometer was used to obtain absolute numbers of fluorescence photons emitted by the target. It was placed at $55 \pm 1^\circ$ to ion-beam propagation direction and 600 ± 10 mm distant from the target. Therefore, a blue-shift of the lines emitted by the Au-ions is expected. As the target is fixed, the X-ray-lines emitted by the target materials are not shifted. A stripping of a sizeable amount of the Au^{26+} -ions to Au^{50+} is expected. The beam current of Au^{50+} ions was measured behind the target using a Faraday cup. The exposure time was in the range of one hour, which corresponds to a total number of Au^{50+} -ions passing the target foils equal to the number of U-ions expected for the APPA cave at FAIR (10^{11}).

Fig. 5.6 shows the measured X-ray spectrum. Cu and Ta lines are clearly visible. A high resolution crystal spectrometer (Highly-Oriented-Pyrolytic-Graphite (HOPG)), placed at $45 \pm 1^\circ$ and 200 ± 10 mm distant from the target, showed lines of the target materials and beam-ions according to fig. 5.7 and tab. 5.2. Lines are marked in Siegbahn notation (Verma 2007). Al was chosen for comparison as it does not show any line spectra in the observed region between 5 keV and 20 keV. The gold lines are shifted by the relativistic Doppler-shift as expected. Each spectrum for Al (black) Cu (red) and Ta (blue) shows the lines for each element respectively, but additionally, from 9 keV onwards, Doppler-shifted Au L_α , Au L_β and Au L_γ are visible in each spectrum.

Lines measured using a HOPG-crystal-spectrometer		
Type of Element	Line	E / keV
Au	L_α	9.711 (9.625)
Cu	K_α	8.047
Cu	K_β	8.904
Cu	He_α	8.390
Cu	K_α Hypersattelites (cold)	8.330–8.353 kJ
Cu	K_α Hypersattelites (Cu+Z)	8.6–8.8 kJ
Ta	L_α	8.145 (8.087)
Ta	L_β	9.341 (9.646)
Ta	L_γ	10.892

TABLE 5.2: High energy-resolution spectra obtained with HOPG-crystal shows lines for different charge states.

The Au L_α line was chosen to calculate the number of photons emitted during the beam-target interaction in 4π as it is close to the range of the relativistically Doppler

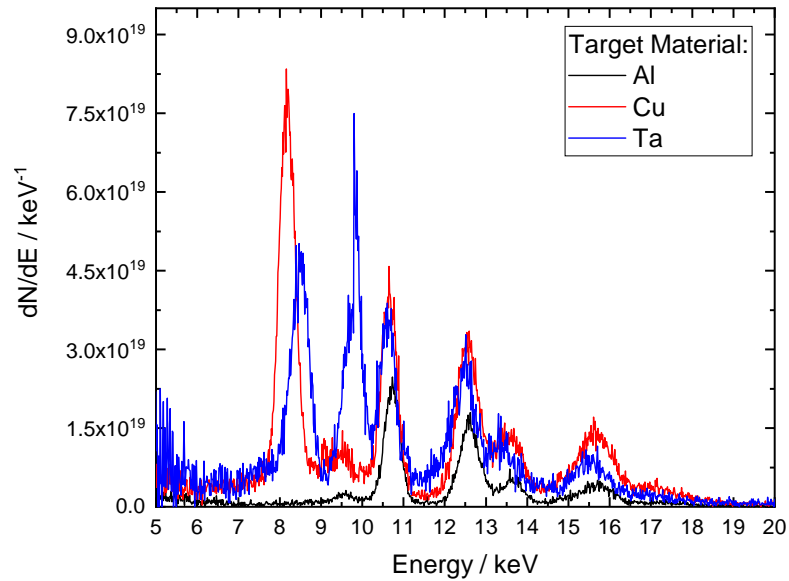


FIGURE 5.6: Fluorescence spectrum measured by CdTe-spectrometer. Spectral resolution around 1 keV. A number of 6.2×10^{13} Au-Ions passed through the foil-targets. The spectrum was normalised to the number of X-ray fluorescence photons emitted in 4π sr per C of Au^{50+} ions and per μm of target thickness.

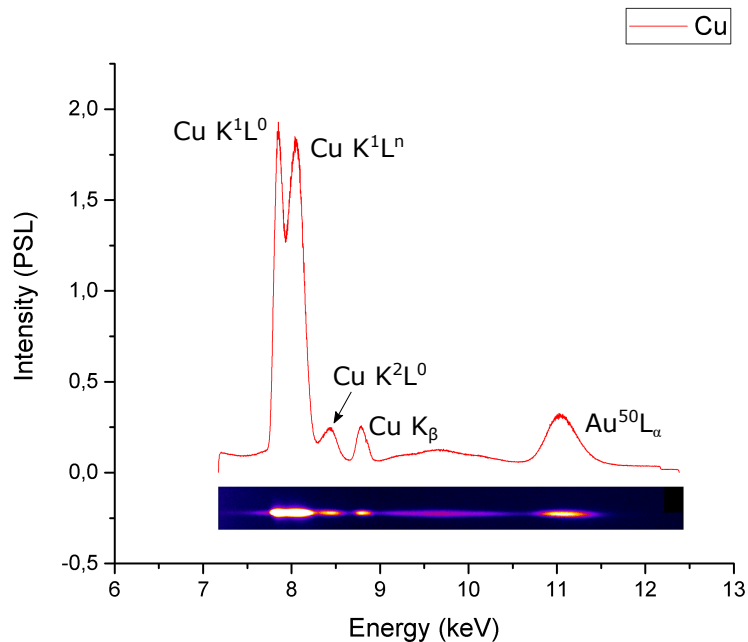


FIGURE 5.7: Fluorescence spectrum measured by HOPG-spectrometer. Cu K-shell and highly ionised Au-projectile L-shell radiation is visible.

shifted U L_α that is proposed to be used in the APPA-cave at FAIR for an angle of 50° to ion beam propagation direction (shifted U $L_{\alpha_{mean}} = 10.981$ keV and non shifted U $L_{\alpha_1} = 13.615$ keV and U $L_{\alpha_2} = 13.439$ keV). The quantum efficiency of the CdTe-spectrometer, the window material made of $500\ \mu\text{m}$ thick polymethyl methacrylate (PMMA), the foil-thickness and the self-absorption in the foils was taken into account. The results are shown in tab. 5.3.

Fluorescence Yields	
Target Material	Au L_α -radiation in 4π sr / photons/C/ μm
Al	1.66×10^{19}
Cu	2.89×10^{19}
Ta	2.05×10^{19}

TABLE 5.3: Fluorescence yield calculated from the spectrum shown in fig. 5.6.

5.3.2 Polychromatic X-Ray Fluorescence Imaging of the Ion Beam distribution on Target Using the XCOT-System

In the HIHEX experimental scheme, a U^{92+} -beam will interact with a macroscopic target (e.g. a foil with several μm thickness and mm^2 area). The beam-diameter will have a width larger than the height of the foil (see fig. 1.2) to provide homogeneous conditions for the heating of the target in lateral direction. In longitudinal direction, the high energy of the U^{92+} -beam provides for the condition that the Bragg-peak of the U^{92+} -ions slowing down in the target material is situated far behind the target. The distribution of ions in the beam hitting the target is therefore of interest. To measure this distribution, a foil might be placed in front of the actual target with the ion-beam hitting normal or with an angle to the foil surface. As the foil will be thin compared to the target-foil length (a few μm compared to mm), the ion-beam energy will not be reduced much during that interaction but a measurement of the ion beam distribution in the target region is enabled.

Since high amounts of parasitic radiation are expected for experiments at the SIS100 at FAIR, a diagnostic system for detection of X-rays and their Conversion to Optical light and Transport (XCOT-system) of the produced image was developed at the Goethe University in Frankfurt and tested at the Friedrich Schiller University in Jena (see. fig. 5.3).

The XCOT-system was developed for efficient detection of X-rays in the energy range of 10 keV to 20 keV as the relativistically Doppler shifted U L_α fluorescence radiation lies in that region (see fig. 5.8). The choice of the observed lines in the fluorescence spectrum depends on the charge state of the ion beam which is connected to the beam energy and the target thickness (Nolen and Marti 2013; Gould et al. 1984; Briand et al. 1990; Leon et al. 1998). The charge state of U-ions at energies around 400 MeV/u passing Cu of equilibrium thickness is still distributed between U^{90+} ,

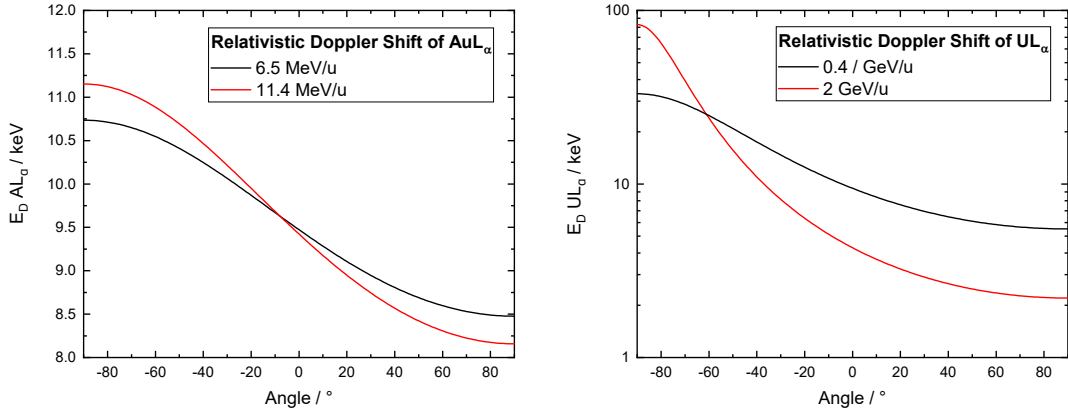


FIGURE 5.8: Relativistic Doppler shift in dependence on the angle of observation for Au L_α at the energies used in U305 (6.5 MeV/u) and U317 (11.4 MeV/u) as well as U L_α with the minimum (0.4 GeV/u) and maximum (2 GeV/u) ion beam energies expected at the APPA-cave at FAIR. Zero degrees refers to an observation angle perpendicular to the ion beam propagation direction, negative angles are in ion beam propagation direction and positive angles look along ion beam propagation direction.

U^{91+} and U^{92+} whereas in beams around 1000 MeV/u, only U^{91+} and U^{92+} are left. Ionisation and electron capture cross sections for these three charge states are similar at 400 MeV/u but differs by one order of magnitude for the higher energy with higher cross sections for ionisation (Gould et al. 1984).

A 100 μm thick CsI(Tl)-scintillator was chosen as converter for the X-rays into visible light as its maximum of conversion lies in this energy range. The signal was registered by means of a sCMOS optical camera with MCP-based image intensifier. The details about the whole XCOT-system are described in sec. C.3. The testing was conducted using an X-ray tube of the X-ray-lab at the Institute for Quantum Optics of the Friedrich Schiller University in Jena.

In U317, the XCOT-system was commissioned for the first time in an ion-beam experiment. A 11.4 MeV/u Au^{26+} -beam was used in contrast to U305. Additionally to improvement of the optical system for visible light, multi pin holes with 80 μm diameter were used for the purpose of increasing the signal intensity level on the diagnostic system and signal-to-noise ratio while keeping the spatial resolution provided by a small pin hole. A multi pin hole with nine holes was used. The distance between target and pin hole was 80 mm and between pin hole and scintillator 90 mm which results in a magnification of $M = 1.125$. The complete magnification of the XCOT-system in this setup is therefore $M = 0.685$. A Nikon 80–400 mm objective with close up lens was used to image the optical image of the ion beam intensity distribution on the Ta-foil onto the photo cathode of the image intensifier. The total distance between the by the Au-ions irradiated Ta-foil and the resulting optical image on the intensifier was around 1 m. The target was angled 45° to the ion beam propagation direction and in the direction of the XCOT-system. Using foils of 10 μm thickness, poly-chromatic X-ray images of the Au-ion beam-target interaction region

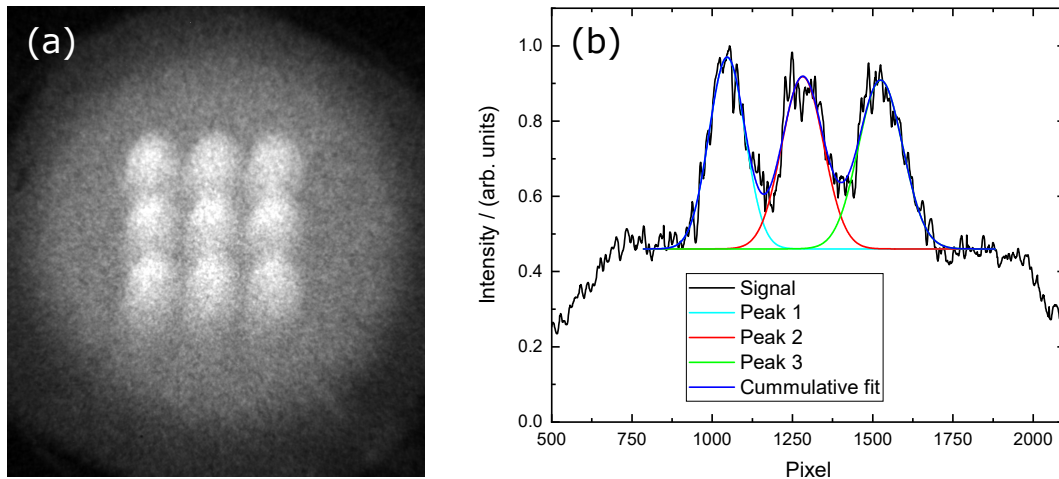


FIGURE 5.9: (a) Ion beam distribution on a Ta-foil imaged by the XCOT-system with a total exposure time of 3 s. This corresponds to a number of 1.2×10^9 Au-Ions passing through the Ta-foil. The nine images of the same distribution are created by multiple pinholes. (b) Lineout in the horizontal direction through the three middle images in (a).

in the energy range above 5 keV were taken.

Fig. 5.9 (a) and 5.10 show the image after a total exposure time of the camera for 3 s or a total number of 1.2×10^9 Au-Ions passing the target. Tab. 5.4 summarises the used beam parameters. Fig. 5.9 (b) shows the Signal-to-Noise ratio and Contrast-to-Noise ratio. Spatial integration of three of the images of the Ta-foil in Fig. 5.9 (a) result in the image shown in Fig. 5.11. The Signal-to-Noise ratio increased from 7 to 11 and the Contrast-to-Noise ratio from 7 to 10, respectively, due to the spatial integration of three of the images.

Beam Parameters	
	Ta-Foil Target
Total Number of Au-Ions	1.2×10^9 Au-Ions
Number of Au-Ions / (mm^{-2})	4.4×10^7
Number of Au-Ions / ($\text{s}^{-1} \text{mm}^{-2}$)	1.5×10^7

TABLE 5.4: Parameters of the Au-ion beam incident on the Ta-foil target.

5.3.3 Polychromatic X-Ray Fluorescence Imaging of a Cu100-Mesh Irradiated by an Ion Beam Using the XCOT-System and Imaging Plates as Detectors

In the second step of the experiment, the Ta-foil was exchanged for the Cu-meshes of 3 mm in diameter. Firstly, the Cu100-mesh was used. That corresponds to a distance of 90 μm between two meshes and a width of a single mesh of 60 μm both in x- and

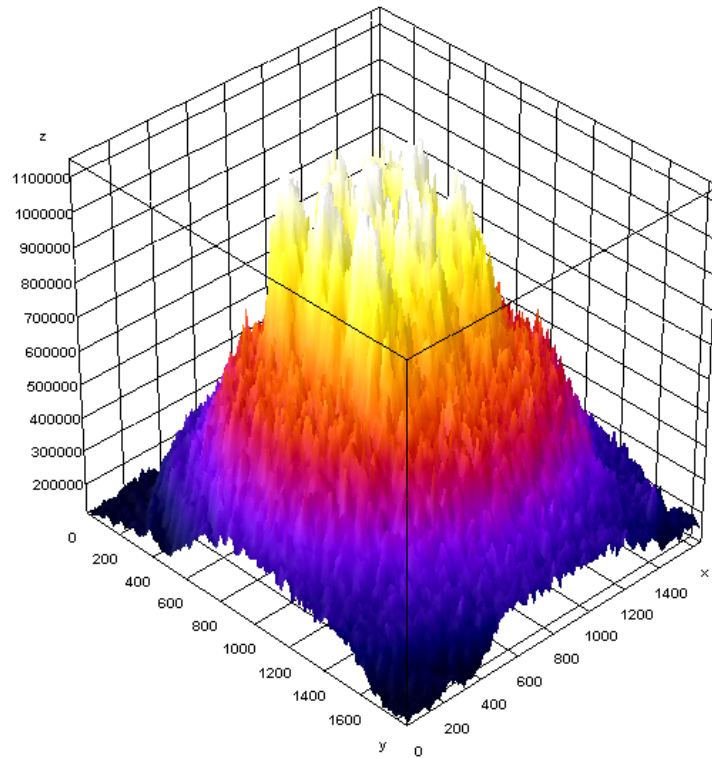


FIGURE 5.10: 3D representation of fig. 5.9 (a).

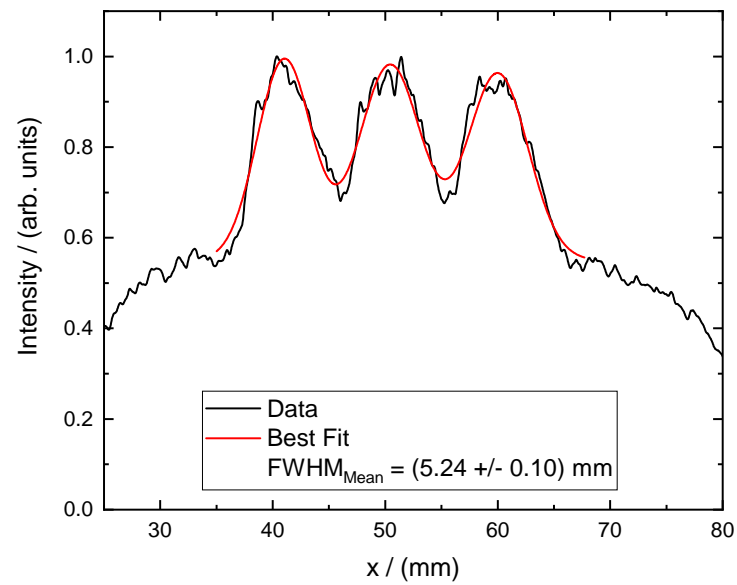


FIGURE 5.11: Lineout of the integration of three of the images in 5.9 (a).

y-direction. The filling factor of the Cu100 mesh is 42 %. The same multi pin holes with nine holes of 80 μm diameter as before (see sec. 5.3.2) were used to reduce the signal-to-noise ratio while retaining a high signal level. The signal was registered by means of a sCMOS optical camera with MCP-based image intensifier. A Nikon 80–400 mm objective with close up lens was used to image the optical image of the Cu-mesh onto the photo cathode of the image intensifier. The total distance between the by Au-ions irradiated Cu-mesh and the resulting optical image on the intensifier was around 1 m. The target was angled 45° to the ion beam propagation direction and in the direction of the XCOT-system. Polychromatic X-ray images of the Au-ion beam-target interaction region in the energy range above 5 keV were taken. Multi pin holes were used to increase the amount of registered photons during the exposition time. The XCOT-System was used as the detector.

Fig. 5.12 (a) shows an accumulation of the signal for 10 min. That corresponds to a number of 2.6×10^{11} Au-Ions in total for the Cu-mesh with 42 % areal coverage. Tab. 5.5 summarises the used beam parameters. The number of Au-ions per time and area is normalised to the beam current during the macro pulse. Temporal integration of 12 pictures similar to Fig. 5.12 (a) is shown in Fig. 5.12 (b). The accumulation time reached 120 min. That corresponds to a number of 3.1×10^{12} Au-Ions in total. Spatial integration of the six complete pictures of the meshes in Fig. 5.12 (b) result in Fig. 5.12 (c). This corresponds to a number of 1.9×10^{13} Au-Ions passing through the target. The SNR improved from 3 to 34 and the CNR from 5 to 8, respectively, due to spatial and temporal integration between fig. 5.12 (a) and fig. 5.12 (c). The magnification of the pin hole camera part of the XCOT-system was chosen to be $M = 2$ but the magnification of the whole XCOT-system can be calculated by these images to be $M = 1.37$ in this setup or, as mentioned above, by removing the magnification $M = 2$ of the pin hole from the value we gain $M = 0.685$ for the magnification of the XCOT-system from scintillator to sCMOS-camera. By taking the pixel size of 6.483 μm into account and also the minimum distance of pixels necessary to still distinguish objects in the image, we gain a number for the resolution of 35.5 μm for objects imaged onto the scintillator.

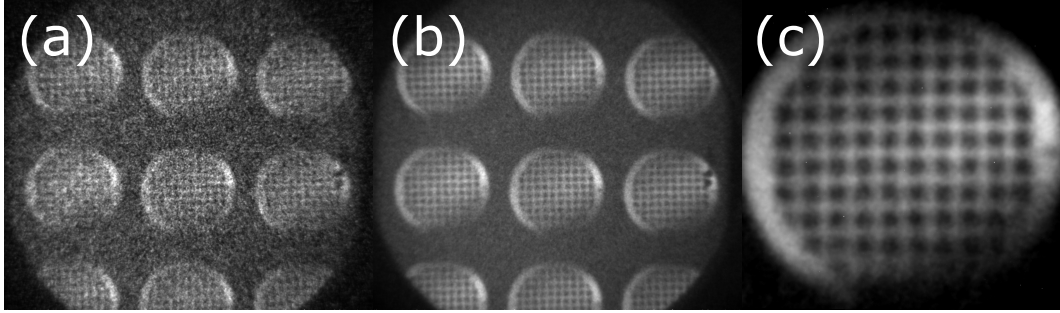


FIGURE 5.12: Shows images of a Cu100-mesh. (a) shows an accumulation of the signal for 10 min. This corresponds to a number of 2.6×10^{11} Au-Ions passing through the Cu100-mesh. (b) Temporal integration of 18 pictures similar to (a) is shown (3.1×10^{12} Au-Ions). (c) Spatial integration of the six complete pictures of the meshes in (b) result in this image. The accumulation time reached 120 min (equivalent of 1.9×10^{13} Au-Ions).

Beam Parameters			
Cu100-Mesh Target (XCOT-System)			
Exposure Time / (min)	10	120	6×120
Total Number of Au-Ions	2.6×10^{11}	3.1×10^{12}	1.9×10^{13}
Number of Au-Ions / (mm^{-2})	9.2×10^9	1.1×10^{11}	6.6×10^{11}
Number of Au-Ions / ($\text{s}^{-1} \text{mm}^{-2}$)	1.5×10^7	1.5×10^7	1.5×10^7
Cu100-Mesh Target (Imaging Plate)			
Exposure Time / (min)	225		
Total Number of Au-Ions	5.8×10^{12}		
Number of Au-Ions / (mm^{-2})	2.1×10^{11}		
Number of Au-Ions / ($\text{s}^{-1} \text{mm}^{-2}$)	1.5×10^7		

TABLE 5.5: Parameters of the Au-ion beam incident on the Cu100-mesh target applied in the experiments using the XCOT-system for imaging.

For comparison, a second pin hole camera was placed opposite to the pin hole camera of the XCOT-system on the front side of the target on an angle 135° to ion beam propagation direction. An IP detector was placed behind the pin hole. The distances of target, pin hole and detector were chosen to be the same values as for the scintillator of the XCOT-system mentioned above. Practically speaking, leading to a magnification of $M = 1$ onto the IP similar to the case with the scintillator.

Fig. 5.14(b) shows the image taken by the IP after 225 min of total accumulation time of the X-ray fluorescence radiation from the ion beam-target interaction in comparison to Fig. 5.14(a), the same image as shown in fig. 5.12 (c). That corresponds to a number of 5.8×10^{12} Au-Ions in total. On one hand, the SNR is 38 and therefore in the same range as for the six spatially and temporally integrated images of the XCOT-system ($SNR = 34$) which had only half of the exposure time

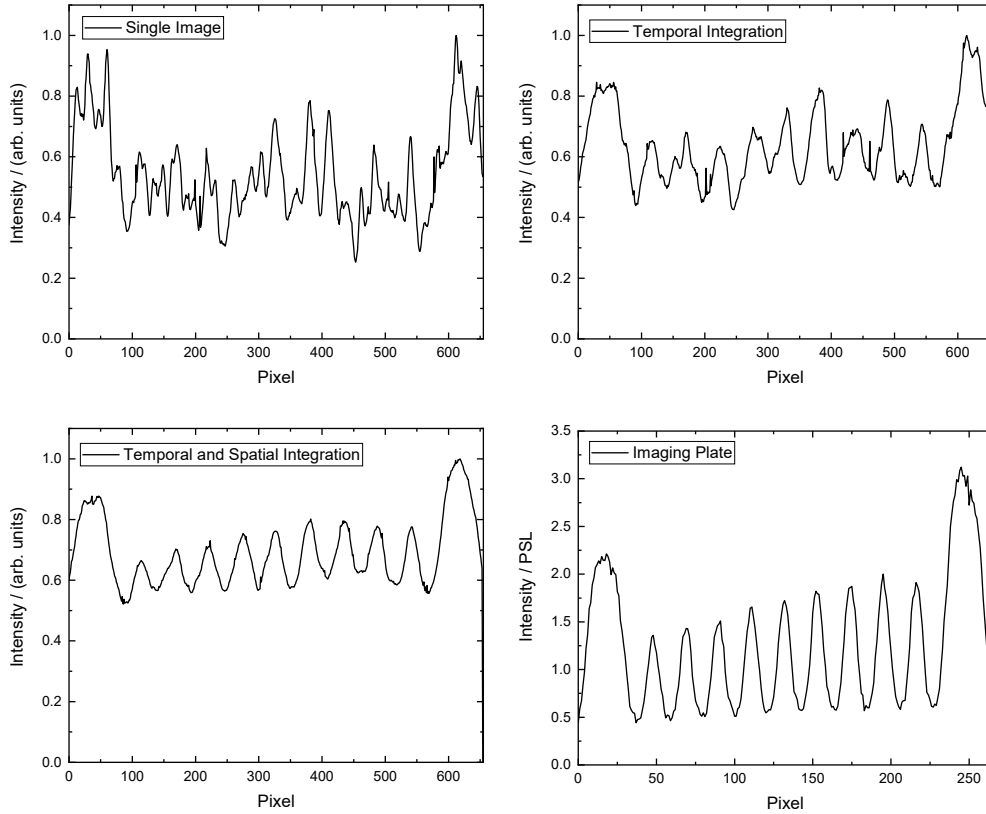


FIGURE 5.13: Horizontal lineouts of the images in fig. 5.12 (a), (b), (c) and 5.14 (b).

as the IP detector, on the other hand, the CNR was 12, which is a factor of 1.5 better than the CNR of the XCOT-system. The MTF reaches a value of 0.83. The minimum distance between two distinguishable objects is calculated to be $38\ \mu\text{m}$ for the magnification of 1.37 in this experiment mentioned above.

The spatial resolution of the XCOT-system was compared with data from the IP measurements. The mesh width of $60\ \mu\text{m}$ of the Cu100-mesh was used for this estimation. Fig. 5.15 and fig. 5.14 show lineouts from the images in fig. 5.14. The spatial resolution of the IP is slightly better ($75.9 \pm 6.2\ \mu\text{m}$) than the resolution of the XCOT-system ($91 \pm 17\ \mu\text{m}$) but the system requirements of $100\ \mu\text{m}$ are clearly met.

5.3.4 Polychromatic X-Ray Fluorescence Imaging of a Cu150-Mesh Irradiated by an Ion Beam Using the XCOT-System as Detector

Afterwards, the $3\ \text{mm}$ in diameter Cu150-mesh was used as target. That corresponds to a distance of $110\ \mu\text{m}$ between two meshes and a width of a single mesh of $15\ \mu\text{m}$ both in x- and y-direction. The filling factor of the Cu150 mesh is 23%. The rest of the setup was the same as in sec. 5.3.3. Fig. 5.17 (a) shows an image with 10 min accumulation time. That corresponds to a number of 1.3×10^{11} Au-Ions in total. Tab. 5.6 summarises the used beam parameters. The number of Au-ions per time and area is normalised to the beam current during the macro pulse. Fig. 5.17 (b) shows the

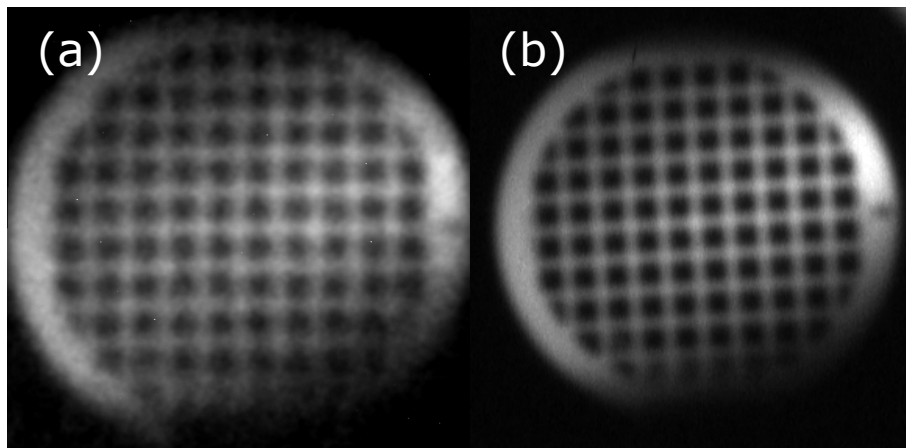


FIGURE 5.14: Shows images of a Cu100-mesh. (a) shows fig. 5.12 (c) for comparison. (b) is an image taken by an imaging plate detector after an accumulation time of 225 min which corresponds to a number of 5.8×10^{12} Au-Ions passing the Cu-mesh.

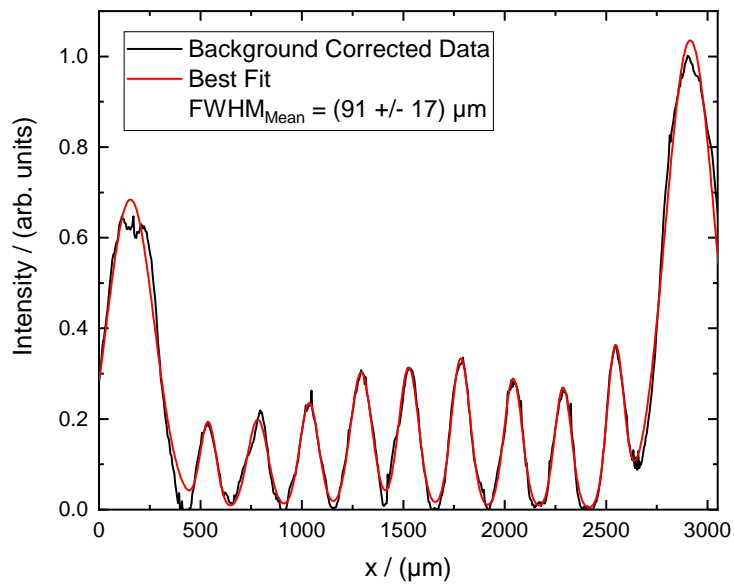


FIGURE 5.15: Background corrected data of the temporal and spatial integrated data shown in fig. 5.14.

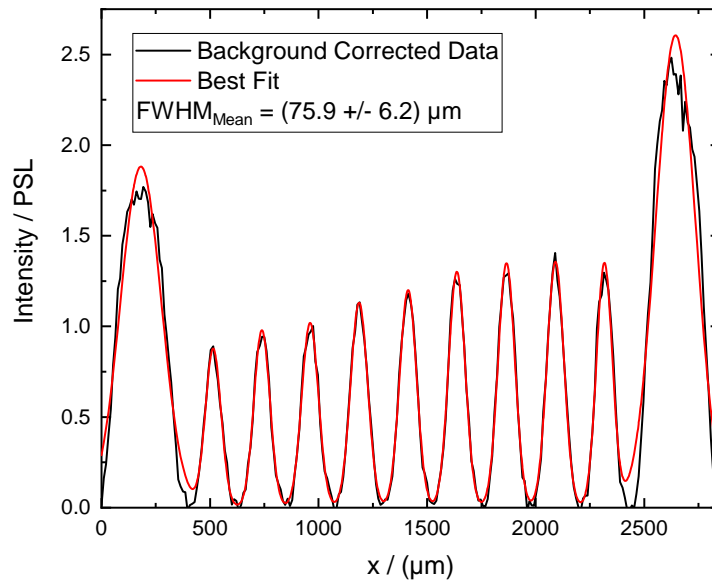


FIGURE 5.16: Background corrected data of the imaging plate data shown in fig. 5.14.

integrated image after a total accumulation time of 180 min. This corresponds to a number of 2.3×10^{12} Au-Ions in total. In fig. 5.17 (c) and fig. 5.18, six of the images shown in fig. 5.17 (b) were integrated. This corresponds to a number of 1.4×10^{13} Au-Ions in total. The SNR improved from 8 to 28 and the CNR from 3 to 10 after both spatial and temporal integration. The MTF changed from 0.52 to 0.13 after integration.

Beam Parameters			
Cu150-Mesh Target (XCOT-System)			
Exposure Time / (min)	10	180	6×180
Total Number of Au-Ions	7.6×10^6	6.3×10^{10}	5.0×10^{11}
Number of Au-Ions / (mm^{-2})	4.6×10^9	6.3×10^{10}	5.0×10^{11}
Number of Au-Ions / ($\text{s}^{-1} \text{mm}^{-2}$)	7.6×10^6	7.6×10^6	7.6×10^6

TABLE 5.6: Parameters of the Au-ion beam incident on the Cu150-mesh target applied in the experiments using the XCOT-system for imaging.

5.3.5 Monochromatic X-Ray Fluorescence Imaging Using Toroidally Bent Crystals

Monochromatic X-ray imaging techniques using toroidally bent Si- and GaAs-crystals were applied in U317 as well. The crystals were chosen in a way that one is able

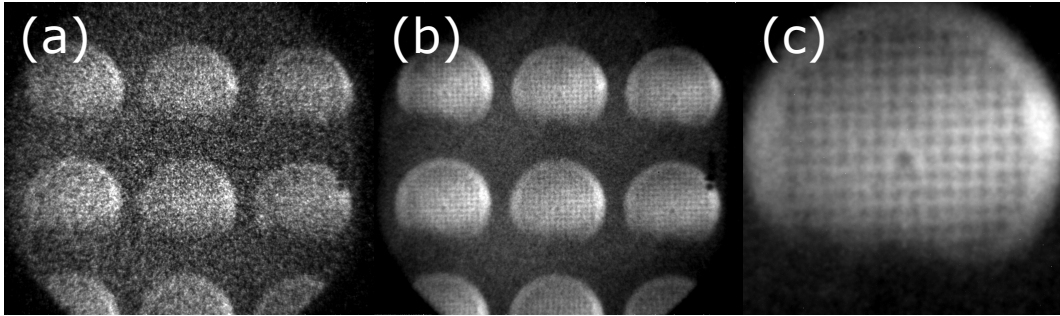


FIGURE 5.17: Shows images of a Cu150-mesh. (a) shows an image with 10 min accumulation time. This corresponds to a number of 1.3×10^{11} Au-Ions passing through the Cu150-mesh. (b) shows the integrated image after a total accumulation time of 180 min (2.3×10^{12} Au-Ions). (c) Integration of six of the images shown in (b) (equivalent of 1.4×10^{13} Au-Ions).

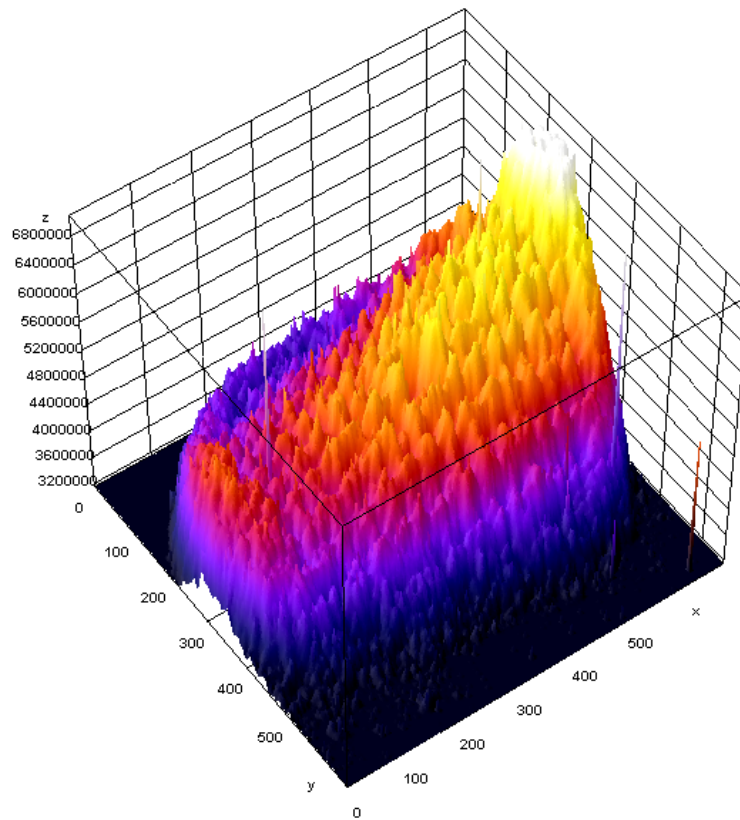


FIGURE 5.18: 3D representation of fig. 5.17.

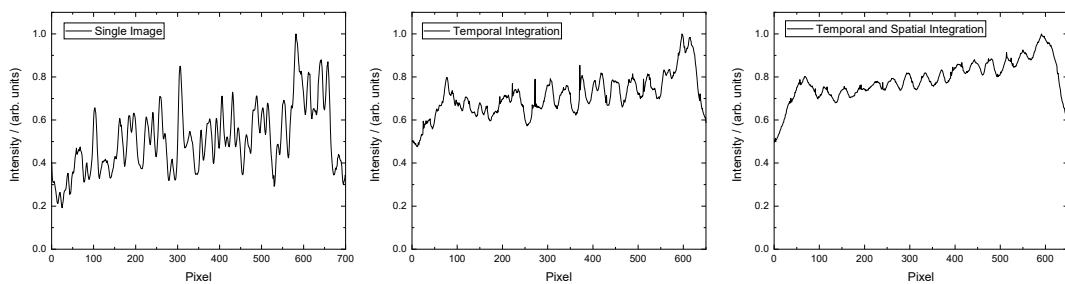


FIGURE 5.19: Horizontal lineouts of the images shown in fig. 5.17.

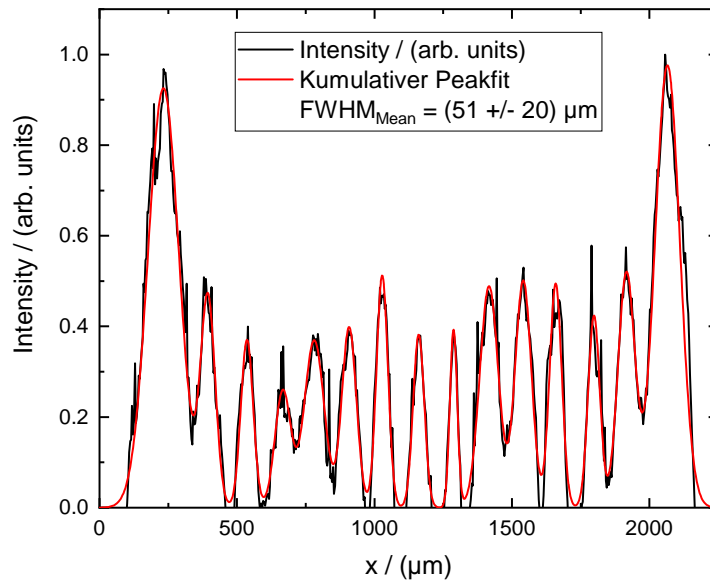


FIGURE 5.20: Background correction of the temporal and spatial integrated data shown in fig. 5.19.

to image the target (Si) and one is able to image the ion beam fluorescence (GaAs). The magnification $M = 6$ allows for a higher spatial resolution than the imaging with pinhole cameras. While the low efficiency is compensated by the higher effective area of the crystal in comparison to the pinhole size. The details about the used crystals is summarised in tab. 5.1. Filters were placed on the crystals (Si: 200 μm Mylar; GaAs: 300 μm Mylar). A carbon window of 200 μm thickness was placed in the chamber wall. The X-ray CCD-camera was covered by 200 μm Be. The same ion beam parameters as in sec. 5.3.3 were used. In addition to the Cu100 and Cu150 mesh, a Cu400 mesh was imaged. The Cu400 mesh has also a diameter of 3 mm. That corresponds to a distance of 52 μm between two meshes and a width of a single mesh of $9 \pm 1 \mu\text{m}$ both in x- and y-direction. The filling factor of the Cu400 mesh is 27%.

Fig. 5.21 (a) shows the monochromatic image of the Cu100 mesh shown with a polychromatic image in sec. 5.3.3. Due to the higher spatial resolution, the mechanical bending of the Cu100 mesh is visible at the angle of observation of around 30° to ion beam propagation direction. The total accumulation time was 15 min. That corresponds to a number of 3.1×10^{11} Au-Ions in total. Tab. 5.7 summarises the used beam parameters. The number of Au-ions per time and area is normalised to the beam current during the macro pulse. Fig. 5.21 (b) and fig. 5.21 (c) show the monochromatic images of the Cu150 mesh shown with a polychromatic image in sec. 5.3.4. The Difference is a shift in the distance between target and bent crystal by 0.5 mm. Differences in the signal intensity level are mostly due to (b) being out of focus. The integration time was 50 min in both cases. That corresponds to a number

of 4.9×10^{11} Au-Ions in total passing through the target with filling factor of 27%. The spatial resolution of the monochromatic imaging technique by toroidally bent crystals at this magnification can be estimated from fig. 5.21 (c) as well. The spatial resolution is at least 30 μm . Fig. 5.22 shows the monochromatic image of the Cu400 mesh. The total accumulation time was 70 min. That corresponds to a number of 9.1×10^{11} Au-Ions in total passing through the target with filling factor of 27%.

Beam Parameters	
Cu100-Mesh Target	
Exposure Time / (min)	15 min
Total Number of Au-Ions	3.1×10^{11}
Number of Au-Ions / (mm^{-2})	1.1×10^{10}
Number of Au-Ions / ($\text{s}^{-1} \text{mm}^{-2}$)	1.2×10^7
Cu150-Mesh Target	
Exposure Time / (min)	50
Total Number of Au-Ions	4.9×10^{11}
Number of Au-Ions / (mm^{-2})	1.7×10^{10}
Number of Au-Ions / ($\text{s}^{-1} \text{mm}^{-2}$)	1.6×10^8
Cu400-Mesh Target	
Exposure Time / (min)	70
Total Number of Au-Ions	9.1×10^{11}
Number of Au-Ions / (mm^{-2})	3.2×10^{10}
Number of Au-Ions / ($\text{s}^{-1} \text{mm}^{-2}$)	7.6×10^6

TABLE 5.7: Parameters of the Au-ion beam incident on the Cu100-, Cu150- and Cu400-mesh target applied in the experiments using bent crystals for imaging.

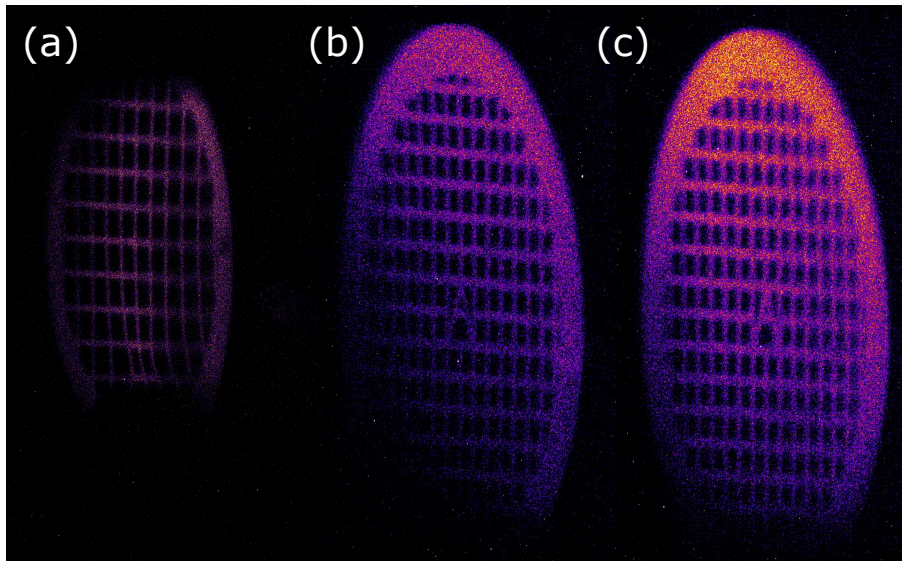


FIGURE 5.21: (a) monochromatic image of a Cu100-mesh at 8.028 keV taken by a toroidally bent Si-crystal (see tab. 5.1). The accumulation time was 15 min. This corresponds to a number of 3.1×10^{11} Au-Ions passing through the Cu-mesh. (b) and (c) image of a Cu150 mesh imaged by the same crystal as in (a). The accumulation time was 50 min (4.9×10^{11} Au-Ions). The difference between (b) and (c) is a shift of the target by 0.5 mm in respect to the crystal position. Differences in the signal intensity level are mostly due to (b) being out of focus.

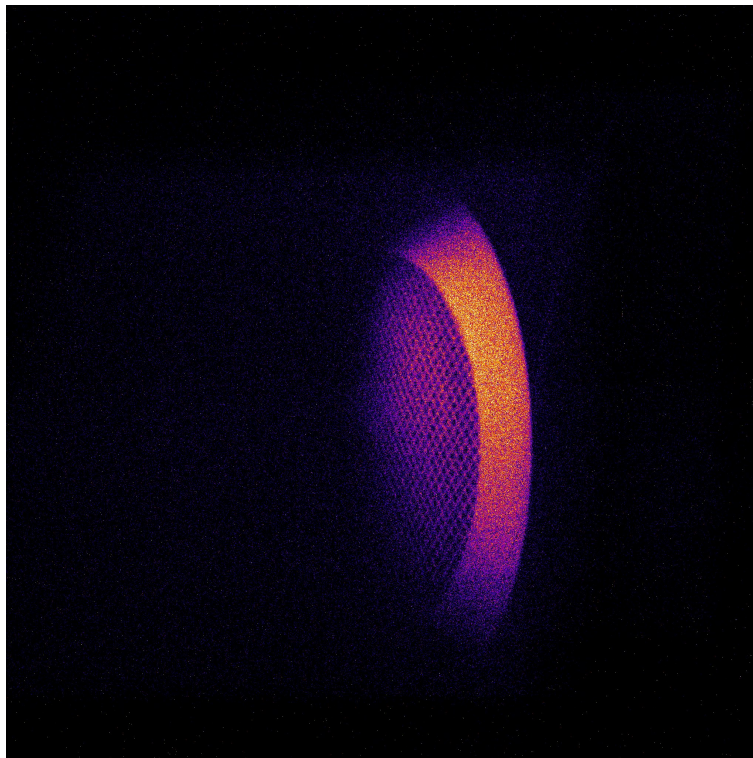


FIGURE 5.22: Monochromatic image of a Cu400 mesh at 8.028 keV with a toroidally bent Si-crystal (see tab. 5.1). The accumulation time was 70 min. This corresponds to a number of 9.1×10^{11} Au-Ions passing through the Cu-mesh.

Chapter 6

Discussion and Outlook

This chapter concludes this work with summarising remarks and will provide an outlook to the implications of the results presented above for future experiments at the HHT-cave in Phase-0 and later at the APPA-cave at FAIR as well as their value for other research areas.

6.1 Laser Generated Ultrarelativistic Electrons

It was shown that the interaction of relativistic laser pulses with foam targets of near critical density (NCD) provides an efficient conversion of the laser energy into relativistic electron beams (Pugachev, N E Andreev, et al. 2016; Pugachev and N E Andreev 2019) with energies far above those predicted by Wilks (Wilks et al. 1992). This mechanism is called direct laser acceleration (DLA). Distinctive features of these beams are their up to 100 MeV high energy accompanied by a large number of electrons (tens of nC) and a strong directionality. This prediction was realised experimentally by the application of under-dense polymer foams while keeping the laser parameters fixed (Rosmej, Olga N. et al. 2019). Our experiments were performed at the Nd:glass PHELIX-laser facility at the GSI Helmholtz Centre for Heavy-Ion Research GmbH in Darmstadt, Germany.

The goal of the performed experiments was to study the electron acceleration by intense sub-picosecond laser pulses propagating in sub-mm long plasmas of NCD and characterisation of the energy and angular distribution of super-ponderomotive electrons. Even if at this stage the application as backlighter for radiographic applications did not play a major role, first images of radiography samples were obtained.

Shots onto metallic foils and onto pre ionised foam layers were performed for comparison of the hot electron temperatures produced in the different plasma conditions. The electron and ion energy distribution measurement was performed using two electron ($\approx 18 \pm 1^\circ$ and $\approx 44 \pm 1^\circ$) and two ion ($\approx 29 \pm 1^\circ$ and $\approx 52 \pm 1^\circ$) spectrometers with static magnetic fields (see fig. 6.1). A spatial resolving cylinder diagnostic was used to measure the angular distribution of electrons. These results are summarised for comparison in fig. 6.2. It is clearly visible that temperatures of emitted relativistic electrons are isotropic for shots onto foil targets with high laser contrast. An increase of the temperatures in shots onto preionised foil-targets is achieved. These

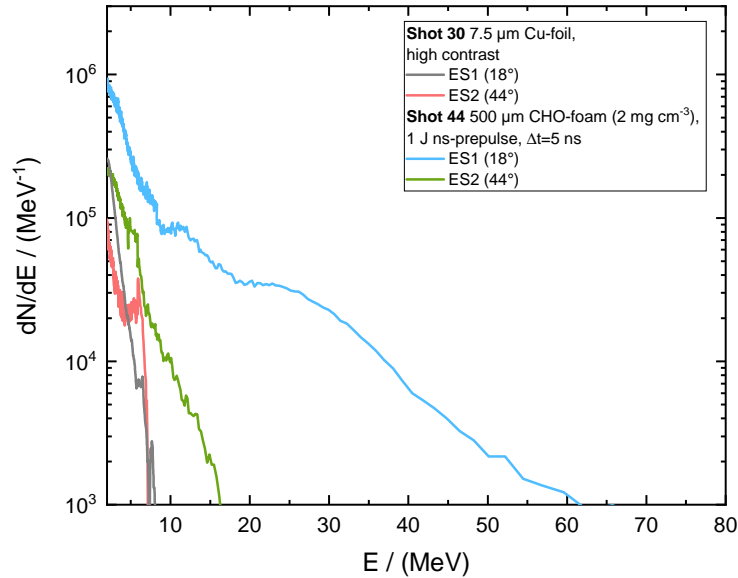


FIGURE 6.1: Electron energy distributions for different target types at same laser parameters: Cu-foil (shot 30) and 500 μm TAC-foam (shot 44). Electron Spectrometer placed at 18° (ES1) and 44° (ES2). The spectrometers observed a solid angle of $\Omega = 1.5 \times 10^{-5}$ sr.

temperatures lie between the ponderomotive- and DLA-scaling (see sec. 2.2.11). The introduction of CHO-foams as targets further increases the temperature of electrons accelerated in forward direction according to the DLA-scaling while the temperature for electrons at large angles to the laser propagation direction matches the ponderomotive scaling. This observation clearly supports the prediction of a directionality of superponderomotive electrons generated in NCD plasmas (Pugachev, N E Andreev, et al. 2016; Pugachev and N E Andreev 2019).

For comparison of the direct measurement of the electron energy distribution, gamma-yield measurements were performed by N. Zahn using a TLD-dosimeter cards based filter spectrometer. A 1000-fold increase of the measured doses in all 10 channels of the gamma-spectrometer covering the photon energy range from 30 keV up to 100 MeV was shown (Rosmej, Olga N. et al. 2019). The best fit of the measured values obtained with a deviation less than 10% resulted in $T_1 \approx 12$ MeV and $T_2 \approx 2$ –5 MeV, which is in good agreement with direct measurements made by means of two electron spectrometers. The experiment was supported by 3D-PIC simulations, that considered the used laser parameters and the geometry of the experimental set-up. The absolute number of electrons, their energy and their angular distribution could be estimated by simulations and are in good agreement with the results of the measurements as well (Pugachev, N E Andreev, et al. 2016; Pugachev and N E Andreev 2019; Rosmej, Olga N. et al. 2019).

The emission angle of the ultrarelativistic electrons can be estimated using the

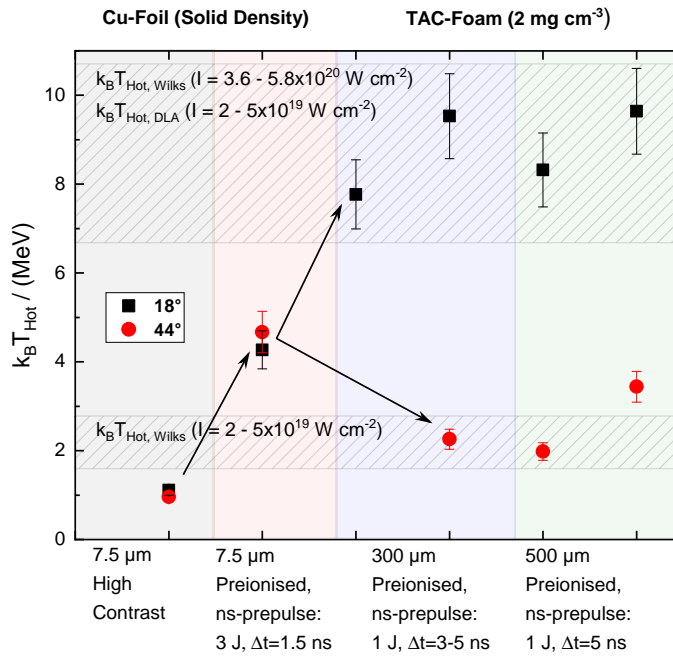


FIGURE 6.2: Comparison of the experimental results from fig. 4.9, fig. 4.10 and fig. 4.11 with the theoretical values from the diagram shown in fig. 4.12.

relativistic energy momentum relation (see. eq. 4.1) and the data from fig. 6.2. Fig. 6.3 shows these half angles in comparison to the theoretical value calculated from the ponderomotive- and DLA-scaling (half angles up to 20°) with most of the values being located in the range of up to 15° . This matches the values obtained with the cylinder diagnostic.

The formation of filamenting channels inside the plasma were observed by the cylinder diagnostic as well. The centres of these channels lay in the region of $0 \pm 15^\circ$ both in horizontal and in vertical direction while their half angles stayed below 10° . The application of a gold foil behind the CHO-foam showed low noise signal of up to 90 MeV electron energy and reduction of filamentation measured by the cylinder diagnostic. The smoothing of the filamenting structure is possibly caused by neutralisation effects of the return current in the foil. GEANT4 simulations suggest that the signal produced by electrons is one order of magnitude larger than the signal produced by gammas. Hence, any inhomogeneity of the angular distribution of electrons is still visible.

Different research areas are opened up by these first experiments on the generation of ultra relativistic electrons in underdense plasmas at the PHELIX facility. Phase contrast imaging techniques could profit from betatron radiation produced by the electrons quivering in the laser fields inside the laser channels (Johannes Wenz et al. 2015; Fourmaux et al. 2011; Cole et al. 2015). Different kinds of materials can be applied as radiators that can produce MeV gammas that in return causes nuclear reaction (Deiev et al. 2019; Günther 2011) or the ultra relativistic electrons can be

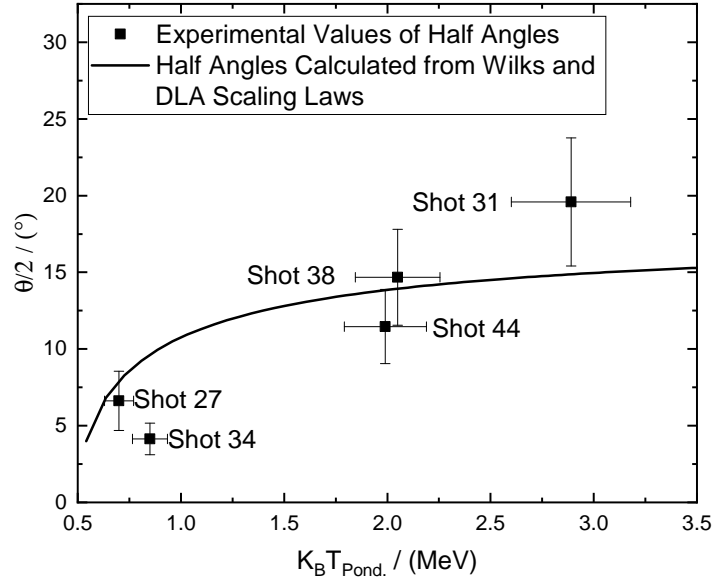


FIGURE 6.3: Half angles for shots onto different preionised target types calculated from the temperature data in tab. 4.1 depending on the values of the ponderomotive part of the spectrum. Solid line indicates the half angles calculated from the ponderomotive and DLA scaling laws.

used for bremsstrahlung driven nuclear reactions inside the targets themselves as well (Z. G. Ma et al. 2019). This is of interest in medical (Z. G. Ma et al. 2019; Deiev et al. 2019) and nuclear astrophysical applications (Huang et al. 2019). Two manuscripts covering the results of this work about the generation of ultrarelativistic electrons in underdense plasmas and additional data including data about the production of nuclear reactions from the experiment P176 are currently in preparation by O. Rosmej et al. and M. Günther et al. The hydrodynamic stability of the CHO-foam layers can be increased even further if it is not heated directly by the ns laser pulse but by X-rays generated due to interaction of ns laser pulse with an Au-hohlraum (G. A. Vergunova et al. 2013; Faik et al. 2014; O N Rosmej, Suslov, et al. 2015). Great advantage of this indirect laser heating is a very stable hydro dynamic behaviour of the plasma layer up to $10 \mu\text{s}$ after the laser energy deposition into the Au-hohlraum. This method can be applied if the energy of the ns pulse is large enough to generate a hohlraum radiation temperature above 30–40 eV. If the energy of the ns-pulse is restricted or one uses ns-prepulse to drive a super-sonic ionisation, like it was done in (Willingale, Arefiev, et al. 2018), direct laser irradiation of the foam layers has to be used (Rosmej, Olga N. et al. 2019).

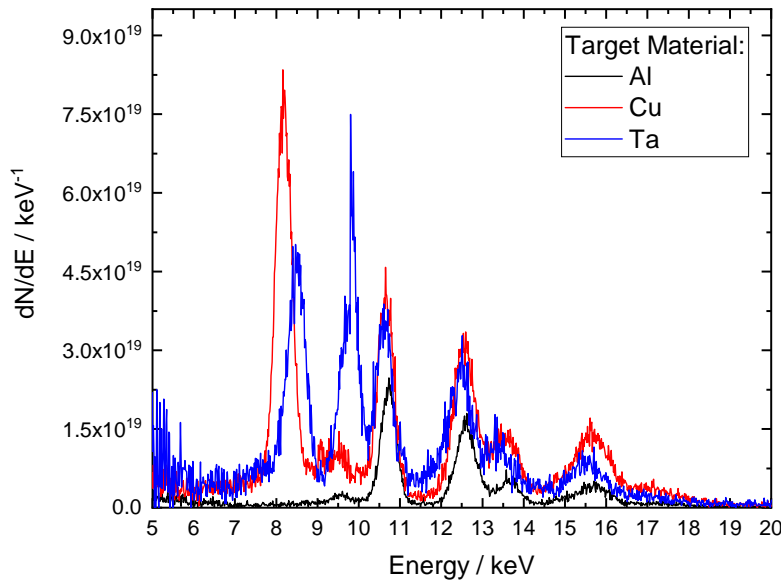


FIGURE 6.4: Fluorescence spectrum measured by CdTe-spectrometer. Spectral resolution around 1 keV. A number of 6.2×10^{13} Au^{26+} -ions passed through the foil-targets stripping them to Au^{50+} . The spectrum was normalised to the number of X-ray fluorescence photons emitted in 4π sr per keV, per C of Au^{50+} -ions and per μm of target thickness.

6.2 X-Ray Fluorescence of Target and Heavy-Ion Beam

The goal of the performed experiments was to study the possible use of projectile and target X-ray fluorescence radiation emitted during heavy-ion-target interaction for diagnostic application. X-ray spectra in the region from 5 keV to 20 keV were obtained and the interaction region was imaged both poly- and monochromatically. Our experiments were performed at the UNILAC facility at the GSI Helmholtz Centre for Heavy-Ion Research GmbH in Darmstadt, Germany.

The interaction of a 6.5 MeV/u Au^{26+} -beam with foil-targets of different materials (Al, Cu, Ta) of 6–10 μm thickness allowed to measure projectile and target X-ray fluorescence. Fig. 6.4 shows the spectrum measured by the CdTe-Spectrometer. Clearly visible are unshifted lines from target and Doppler shifted lines from beam ions. The Doppler shift allows to fine tune the observed wavelength of beam fluorescence depending on the energy of the particles. This allowed to calculate the fluorescence yield (see tab. 6.1). Therefore, X-ray fluorescence measurements allow absolute measurements of energy deposited inside the target in future experiments during Phase-0 at HHT and in the APPA-cave at FAIR.

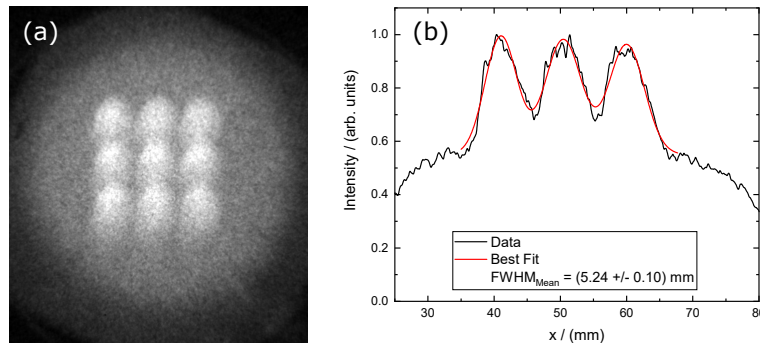


FIGURE 6.5: (a) Ion beam distribution on a Ta-foil imaged by the XCOT-system polychromatically with a total exposure time of 3s. This corresponds to a number of 1.2×10^9 Au-Ions passing through the Ta-foil. The nine images of the same distribution are created by multiple pinholes. (b) Lineout in the horizontal direction of the integration of three of the images in (a).

Fluorescence Yields	
Target Material	Au L_{α} -radiation in 4π sr / photons/keV/C/ μm
Al	1.66×10^{19}
Cu	2.89×10^{19}
Ta	2.05×10^{19}

TABLE 6.1: Fluorescence yield calculated from the spectrum shown in fig. 5.6.

In the interaction of a 11.4 MeV/u Au^{26+} -beam with foil-targets and Cu-meshes of different mesh widths, the application of X-ray fluorescence as diagnostic method was explored and the X-ray Conversion to Optical Radiation (XCOT)-system was commissioned. Measurements with foil-targets allowed to image the ion beam distribution in the plane of the foil (see fig. 6.5). The application of multi pinholes allowed to improve on the signal intensity levels, the signal-to-noise ratios and the contrast-to-noise ratios. A combination of bent crystals for imaging purposes and the XCOT-system is expected to further improve on that.

The spatial resolution of the XCOT-system was compared with data from the IP measurements. The mesh width of 60 μm of the Cu100-mesh was used for this estimation (see fig. 6.6). The spatial resolution of the IP is slightly better ($75.9 \pm 6.2 \mu\text{m}$) than the resolution of the XCOT-system ($91 \pm 17 \mu\text{m}$) but the system requirements of 100 μm are clearly met.

The spatial resolution of the monochromatic imaging technique by toroidally bent crystals at this magnification can be estimated from fig. 6.7 (c) as well. The spatial resolution is at least 30 μm . Which is a promising result for the combination of toroidally bent crystals and the XCOT-System.

These experiments demonstrated the potential of X-ray fluorescence as a diagnostic tool for future FAIR-experiments (see fig 6.8). We observed intense radiation of

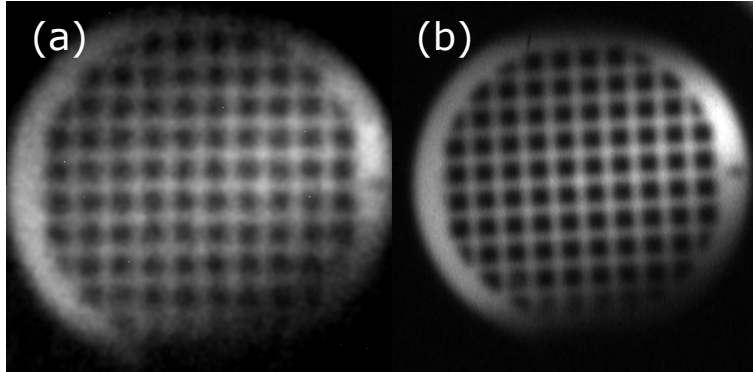


FIGURE 6.6: Polychromatic images of a Cu100-mesh. (a) Image taken by the XCOT-system. The accumulation time reached 120 min (equivalent of 1.9×10^{13} Au-Ions). (b) Image taken by an imaging plate detector after an accumulation time of 225 min which corresponds to a number of 5.8×10^{12} Au-Ions passing the Cu-mesh.

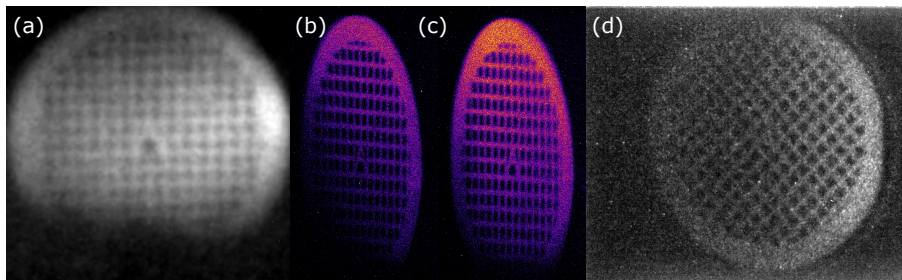


FIGURE 6.7: (a) polychromatic image of a Cu150-mesh taken with the XCOT-system. The accumulation time was 180 min (corresponding to 2.3×10^{12} Au-ions). (b) and (c) are images of the same Cu150-mesh taken by using a toroidally bent Si-crystal (see tab. 5.1). The accumulation time was 50 min (4.9×10^{11} Au-ions). The difference between (b) and (c) is a shift of the target by 0.5 mm relative to the crystal position. Differences in signal intensity levels are mainly due to (b) being out of focus. (d) shows the image of the Cu150-mesh by using a combination of the Si-crystal and the XCOT-system. The accumulation time was 25 min (1.1×10^{11} Au-ions).

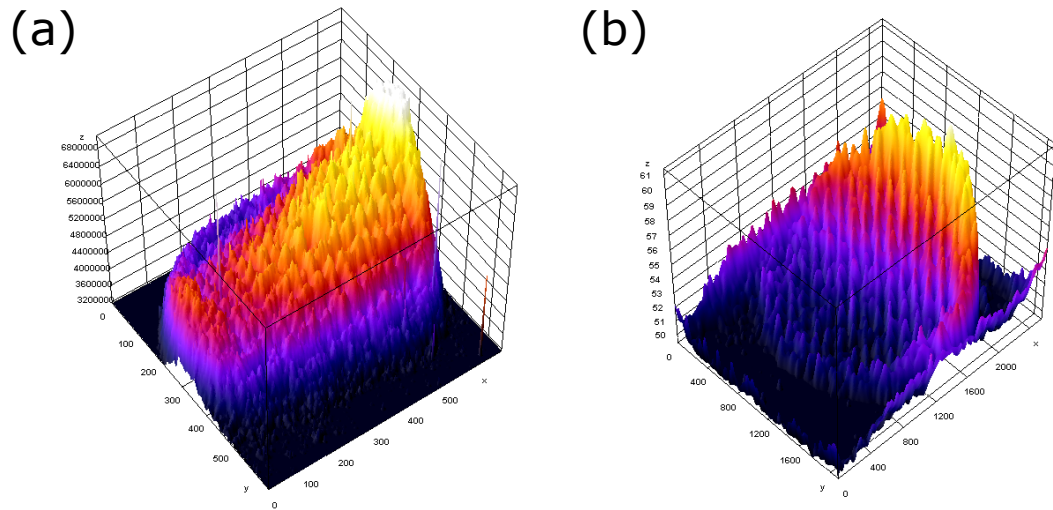


FIGURE 6.8: 3D representations of ion beam distributions on mesh-targets: (a) shows the 3D representation of fig. 6.7 (a) and (b) shows the 3D representation of fig. 6.7 (d).

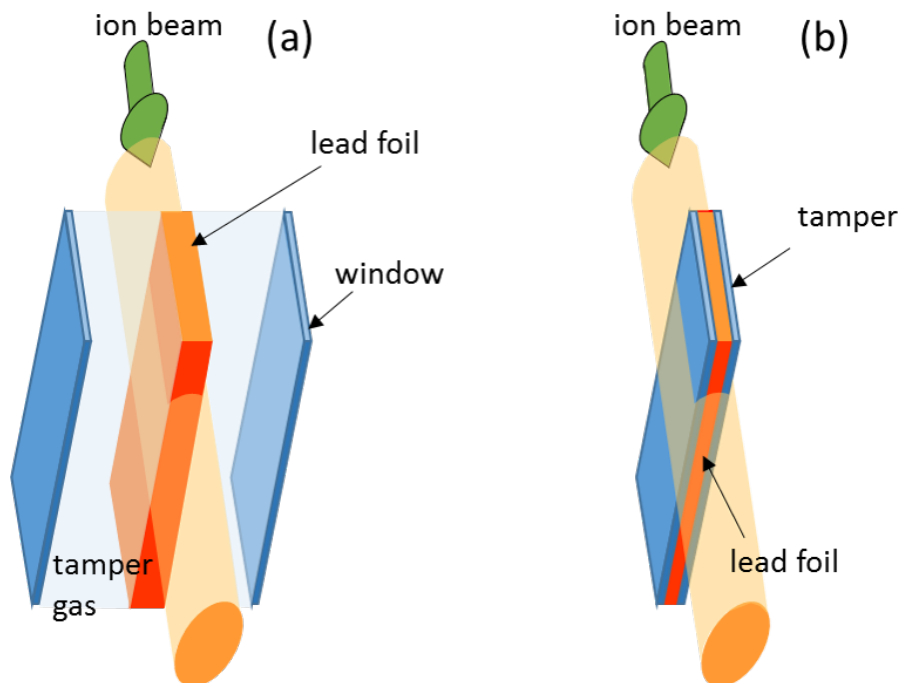


FIGURE 6.9: (a) HIHEX scheme with a thick target foil of several hundred μm thickness. A tamper gas of 100 bar pressure is planned to be used. (b) thin target foils of a few μm thickness. A solid state tamper is planned to be used in this scheme (Vincent Bagnoud 2020).

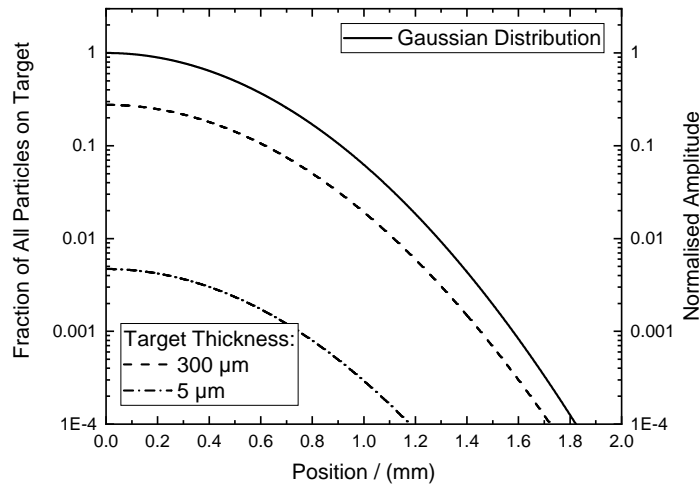


FIGURE 6.10: The fraction of heavy-ions from the beam actually passing the target front as shown in fig. 5.1. A Gaussian beam distribution with a $FWHM$ around 1 mm is assumed (right axis). Shown are estimations for two different plane foil target thicknesses with the foils extending infinitely in the third dimension as proposed for the two different HIHEX-schemes. The fraction of the total number of beam particles interacting with the foils is shown on the left axis.

ionised target atoms (K-shell transitions in Cu at 8–8.3 keV and L-shell transition in Ta) as well as Doppler-shifted L-shell transitions of Au-projectiles passing through foils and meshes in the photon energy region of 10 keV. This radiation can be used for monochromatic (dispersive element like bent crystals) or polychromatic (pinhole) X-ray mapping of the ion beam intensity distribution in the interaction region. Using data obtained by means of CdTe X-ray spectrometer and a Faraday cup, the number of Au L_{α} photons per 1 C of the Au-charge passing through Al, Cu and Ta foils and per 1 μm target-thickness in 4π could be estimated. This number allows us to conclude that 10–100 fold amplification of the signal is required in order to apply this method for U-beam intensities between 1×10^{10} – 5×10^{11} particles/pulse. In order to achieve this goal, another beamtime was performed in early 2020. The XCOT-system was coupled to the Si-crystal used in this work to improve on signal intensity level, signal-to-noise and contrast-to-noise ratio. Fig. 6.7 (d) shows the first result of a combination of the toroidally bent Si-crystal with the XCOT-system in comparison to the results from (a) the combination of XCOT-system with pinhole and (b) and (c) the Si-crystal directly on an X-ray CCD-camera. The data of this experiment is currently under evaluation and a manuscript covering the results of this work about the X-ray imaging techniques developed is in preparation by the author et al. The first result is that the optical system of the XCOT-system needs improvement for the HIHEX-experiments planned for the HHT-cave.

Appendix A

Electron and Ion Diagnostics

For the measurement of the kinetic energy of charged particles, spectrometers with static magnetic fields as dispersive elements can be applied. Charged particles that pass through electromagnetic fields are deflected in these fields according to the Lorentz force. If only a homogeneous magnetic field is present, the charged particle will perform a circular motion in the field with a turning radius called the Larmor radius. The following section describes the scheme and evaluation of the data of such a spectrometer used in the experiments described in this work.

Spectra of the hot electrons and ions leaving the target were obtained by applying a static magnetic field to disperse particles with different charge to mass ratios and energies. The detection of the particles was performed using imaging plates as detectors. The energy range of detection was up to around 100 MeV for both the electron and ion spectrometers. Fig. A.1 shows a schematic view of the used electron spectrometers (the ion spectrometers have a similar design but doubled proportions and four times higher nominal magnetic field strength). The spectrometers consist of a stainless steel box that contains two iron/neodymium magnets. Between these magnets, a static magnetic field B is present. The deflected electrons are detected by IPs on the side and in the back of the spectrometer. The geometry of the box and the nominal strength of the magnetic field is chosen according to the type of particle that the spectrometer is designed to detect. Corrections to the data were introduced considering the magnetic field inhomogeneity, non-linear dispersion, background inhomogeneity, IP-response functions, particle types, angular response, and fading.

A.1 Geometry of the magnet spectrometers

During the interaction of the main laser pulse with the target, particles are accelerated and X-rays are generated in the target. After leaving the target, they hit the front of the spectrometers (see fig. A.1). Imaging plates are used as detectors. IPs are sensitive to both particles and X-rays. Therefore, it has to be distinguished by which particle or radiation type a signal is generated. The particles and X-rays enter the spectrometer through a 2 mm aperture in a 5 mm thick steel plate. To reduce the intensity of X-rays and particles on the detectors while also improving the resolution,

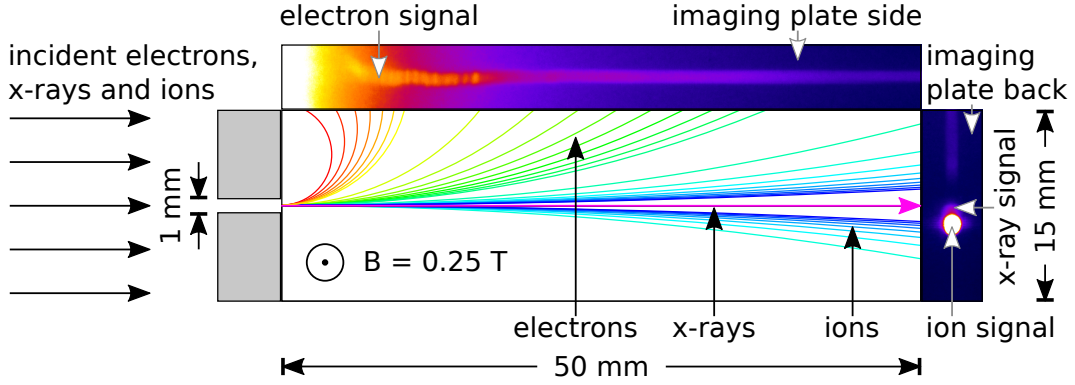


FIGURE A.1: Schematic view of the electron spectrometers used in the experiments. The ion spectrometers are similar but have bigger dimensions and a stronger nominal magnetic field.

pin holes with diameters of around 1 mm were applied in front of the apertures of the electron spectrometers. The IP on the side was placed around 7.5 mm away from the center of the entrance holes of the electron spectrometers (15 mm for ion spectrometers). The rear side with the second IP was 50 mm behind the entrance hole (100 mm for ion spectrometers).

Charged particles are forced by the Lorentz-force to travel in curved paths while the X-rays hit the backside of the spectrometer unperturbed in a straight line. Two spots can be recognised on the rear IP of the electron spectrometer as seen in fig. A.1); one for the X-rays and one for heavier positively charged particles. A line is visible on the side and rear IPs which is situated on the opposite side of the X-ray spot according to the charge of electrons. The higher the energy and the mass of a particle the closer it will get to the X-ray spot which would correspond to infinitely high energies of the particles. The size of the X-ray spot corresponds to the size of the aperture at the entrance of the spectrometer. That also holds true for the width of the electron and ion signals.

A.2 Dispersion of the magnet spectrometers

Charged particles entering the magnet spectrometers are deflected by the Lorentz-force and detected by IPs that are placed on the walls of the spectrometers. The dispersion is highly non-linear and separated into two parts as there are two detectors present that are placed perpendicular to each other. The following section shows the dispersion of the charged particles, namely electrons and protons, in the magnet spectrometers.

A.2.1 Dispersion of the magnet spectrometers assuming a homogeneous magnetic field

The dispersion of the magnet spectrometers was calculated analytically for the nominal magnetic field, a mean field, and by a numerical calculation of an interpolated

field obtained through measurements (Tavoosli 2019). The following sections describe these calculations.

Charged particles perform circular motion in static magnetic fields. The radius of these circles is called the Larmor radius r_L (F. F. Chen et al. 1984):

$$r_L = \frac{p}{eB} \quad (\text{A.1})$$

with p the momentum of the particle, e the charge of the particle, which, for this case, is the elementary charge, and B the magnetic field. The relativistic momentum p is connected to the relativistic energy E of a particle by the energy-momentum relation (Greiner 2011):

$$p = \sqrt{\frac{E^2}{c_0^2} - m_0^2 c_0^2} \quad (\text{A.2})$$

where m_0 is the relativistic rest mass of the particle.

Therefore follows for the relativistic kinetic energy E_{kin} of the same particle (Greiner 2011):

$$E_{kin} = E - E_0 \quad (\text{A.3})$$

Side-On IP

The equation of a circle states:

$$x^2 + y^2 = r_L \quad (\text{A.4})$$

A suitable geometry is chosen for the calculation of the dispersion as shown in fig. A.2. The particle entering the spectrometer is moving in y direction. The initial velocity of the particle in x direction is zero. As the particle is moving on a circular trajectory inside the magnetic field and the magnetic field is confined to the spectrometer, the center of the circle lies on the x -axis a distance r_L away from the entrance. The distance from the entrance to the walls in x direction is equal to a . Since we are interested in the position of the entering particle when it hits the detector on the wall it leads to the following:

$$x = r_L - a \quad (\text{A.5})$$

$$y = y' \quad (\text{A.6})$$

where x is the axis perpendicular to the direction of the electron motion and perpendicular to the magnetic field direction, y is the axis parallel to the direction of the electron motion and perpendicular to the magnetic field direction, a is the distance between the entrance hole of the spectrometer and the IP on the side and y'

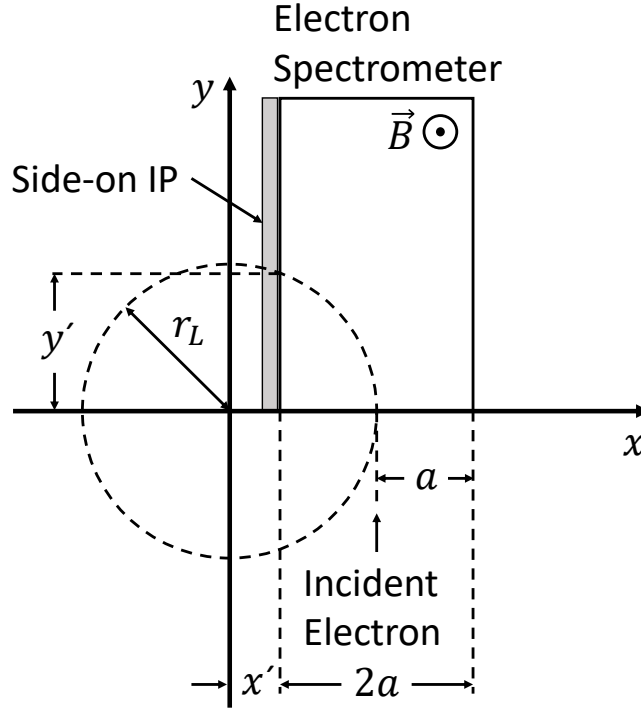


FIGURE A.2: Scheme of the geometry used for the calculation of the dispersion in the electron and ion spectrometers evaluated on the IP on the side.

is the point on the IP for which the energy of a incident particle will be calculated. Inserting this into eq. A.4 gives:

$$(r_L - a)^2 + y'^2 = r_L^2 \quad (\text{A.7})$$

$$-2ar_L + a^2 + y'^2 = 0 \quad (\text{A.8})$$

From that follows the kinetic energy E_{kin} of a particle on a point y' on the IP:

$$E_{kin} = \sqrt{\frac{(a^2 + y'^2)^2 c_0^2 e^2 B^2}{4a^2} + m_0^2 c_0^4} - m_0 c_0^2 \quad (\text{A.9})$$

Back-On IP

For the detector on the rear side of the spectrometer a different geometry is chosen as shown in fig. A.3. Here the particle has to hit the detector at a fixed distance b to the entrance hole in the y direction and the position is calculated in y direction. Therefore we get:

$$x = r_L - a + x' \quad (\text{A.10})$$

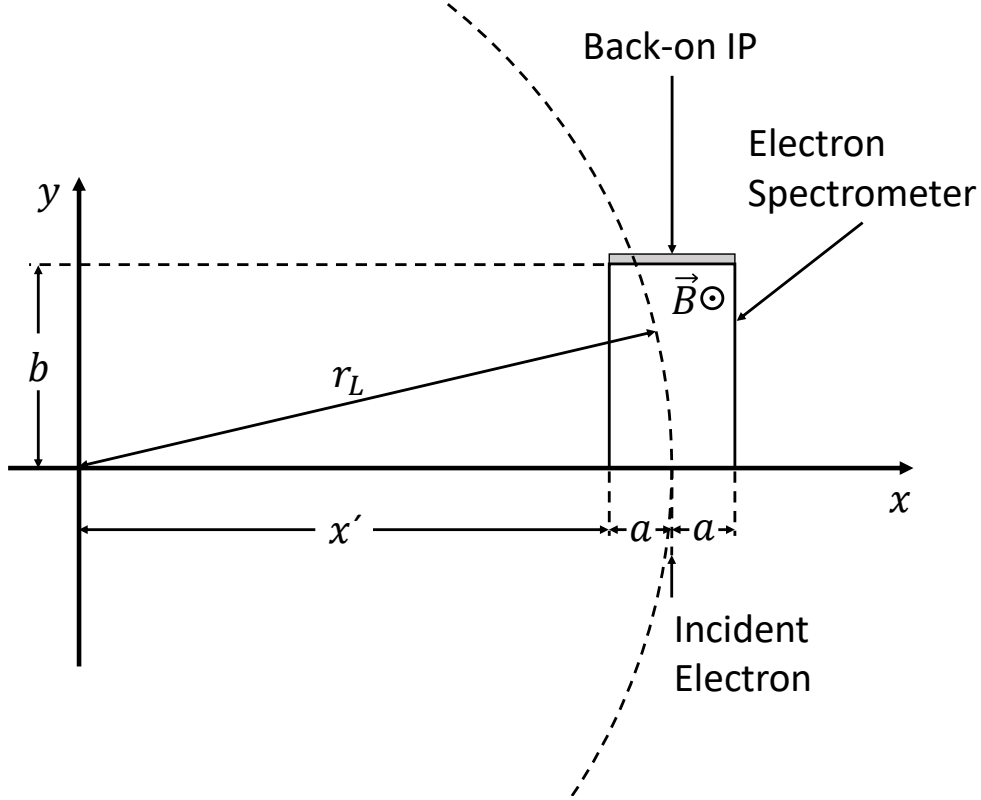


FIGURE A.3: Scheme of the geometry used for the calculation of the dispersion in the electron and ion spectrometers evaluated on the IP on the rear.

$$y = b \quad (\text{A.11})$$

Using eq. A.4 again:

$$(r_L - a + x')^2 + b^2 = r_L^2 \quad (\text{A.12})$$

$$a^2 + x'^2 + 2r_L(x' - a) - 2ax' + b^2 = 0 \quad (\text{A.13})$$

From that follows the kinetic energy E_{kin} of a particle on a point x' on the IP:

$$E_{kin} = \sqrt{\frac{\left((a - x')^2 + b^2\right)^2 c_0^2 e^2 B^2}{4(a - x')^2} + m_0^2 c_0^4 - m_0 c_0^2} \quad (\text{A.14})$$

The resulting analytical dispersion function is shown in fig. A.5.

A.2.2 Dispersion of the Magnet Spectrometers Assuming an Inhomogeneous Magnetic Field

The electron spectrometers possess a very inhomogeneous magnetic field. Therefore it was necessary to measure the magnetic field (Tavoosli 2019). Fig. A.4 shows the

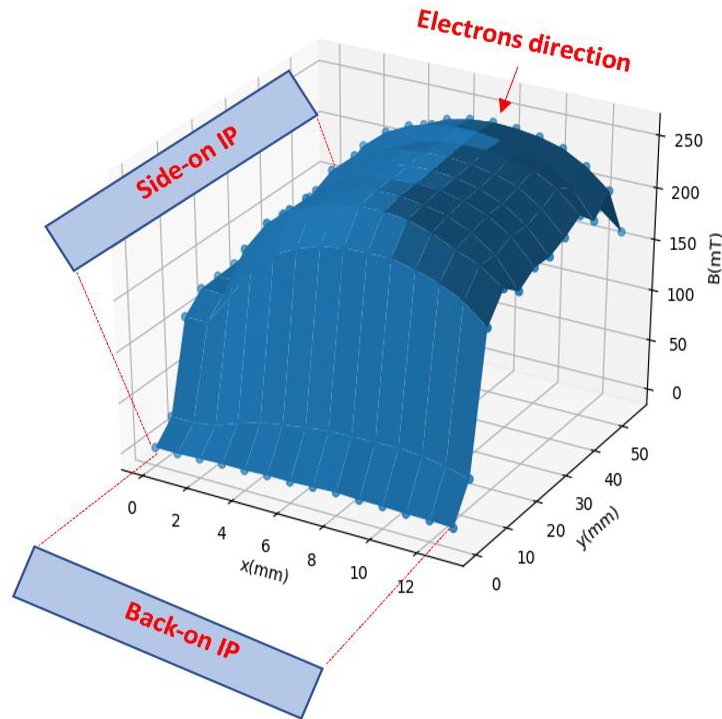


FIGURE A.4: The magnetic field distribution measured in the electron spectrometer (Tavoosli 2019).

measurement of one of the magnetic field distributions inside of the spectrometer. The magnetic field is more or less homogeneous along the propagation direction of the electron, but becomes more inhomogeneous closer to the walls. This is felt by the electron as soon as the magnetic field begins to be deflect it. The dispersion of the electrons in the magnet spectrometer is shown in fig. A.5. The analytical solution for a nominal magnetic field of 250 mT, a mean magnetic field of 215 mT and the numeric calculation for the measured magnetic field can be seen. The pixels correspond to the pixel size of 50 μm chosen for the scanning procedure. The IP on the side of the spectrometer detects the lower energetic electrons up to around 8 MeV. The X-ray spot shown in fig. A.1 allows to discern a signal on the rear IP up to pixel 135. This corresponds to an energy of over 100 MeV. Fig. A.5 shows the combined dispersion of electrons measured by both IPs. The energy resolution is higher for smaller energies. At higher energies, electrons of several MeV difference in kinetic energy are detected in one single pixel.

A.3 Normalisation due to Non Linear Dispersion

The dispersion curve of the electron spectrometer is highly non-linear. On one hand the dispersion of the magnet spectrometers mentioned in sec. A.1 is increasing monotonously. On the other hand the derivative of the dispersion seen in fig. A.5 is not monotonous. As the pixel size in the scan of an imaging plate is constant, that

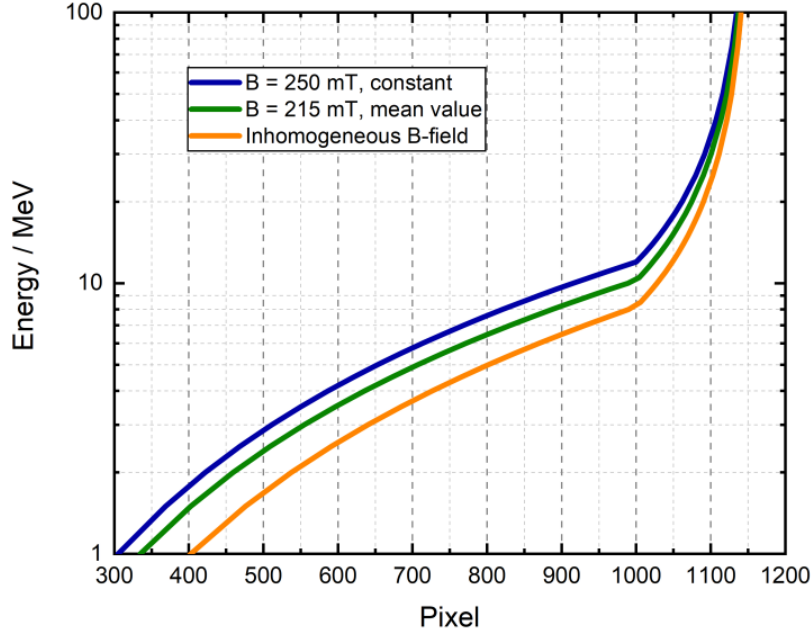


FIGURE A.5: The dispersion of the electron spectrometer. The three graphs show the analytical solution for a nominal magnetic field of 250 mT, a mean magnetic field of 215 mT and the numeric calculation for the measured magnetic field (Tavoosli 2019).

means that the signal density measured on one pixel relatively to the signal density on another pixel is in general not correct. Since dN/dx and not dN/dE is measured, the measured signal has to be corrected for this fact by a normalisation. The number of particles per energy interval dN/dE is given by (Malte Christoph Kaluza 2004):

$$\frac{dN}{dE} = \frac{dN}{dx} \frac{1}{\frac{dE}{dx}} = \frac{dN}{dx} \frac{dx}{dE} \quad (\text{A.15})$$

Therefore we have to calculate the derivative of equations A.9 and A.14. The parametrisation is according to A.2.1 and A.2.1. The derivative of eq. A.9 with respect to y' is:

$$\frac{\partial E_{kin}(y')}{\partial y'} = \frac{e^2 B^2 c_0^2 y'}{a^3 \sqrt{\frac{e^2 B^2 c_0^2 (a^2 + y'^2)}{a^3} + m_0^2 c_0^4}} \quad (\text{A.16})$$

The derivative of eq. A.14 respective to x' is:

$$\frac{\partial E_{kin}(x')}{\partial x'} = - \frac{c_0^2 e^2 B^2 (a^2 - 2ax' - b^2 + x'^2) (a^2 - 2ax' + b^2 + x'^2)}{a (a - x')^3 \sqrt{\frac{((a-x')^2 + b^2)^2 c_0^2 e^2 B^2}{4(a-x')^2} + m_0^2 c_0^4}} \quad (\text{A.17})$$

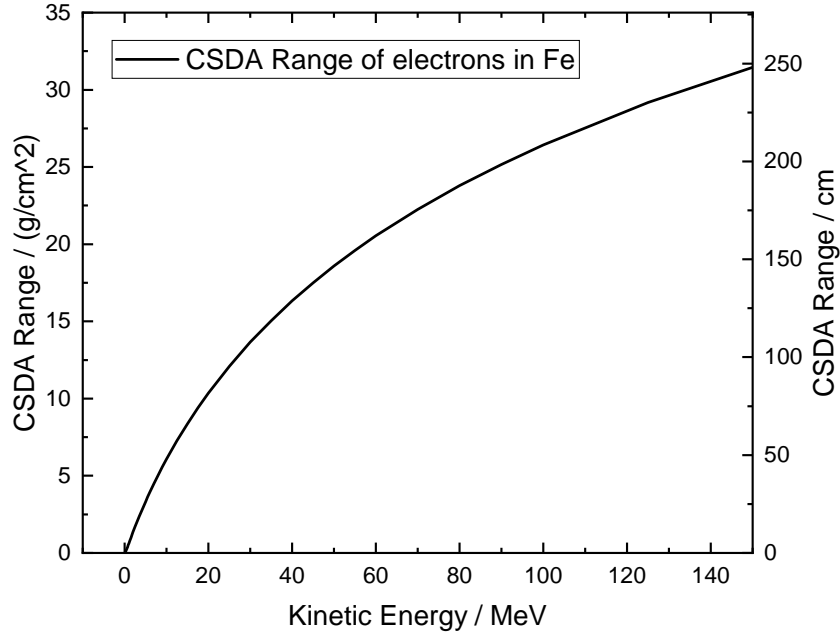


FIGURE A.6: CSDA Range of electrons in Iron.

$$\frac{\partial E(x')}{\partial x'} = -\frac{c_0^2 e^2 B^2 (a^2 - 2ax' - b^2 + x'^2) (a^2 - 2ax' + b^2 + x'^2)}{a (a - x')^3 E}. \quad (\text{A.18})$$

A.4 Background corrections

The signal on the detector shows a high proportion of background since the spectrometer consists of a front plate of 5 mm steel. We can calculate the transmission of electrons through the material with the program ESTAR (Physical Measurement Laboratory 2019a) assuming the material to consist predominantly of iron. The average path length of a charged particle travelling through the material and slowed down to rest can be approximated in the continuous-slowing-down approximation (CSDA) (Physical Measurement Laboratory 2019b). In this approximation, it is assumed that the rate of energy loss at every point along the track is equal to the total stopping power. Energy-loss fluctuations are neglected. The CSDA range is obtained by integrating the reciprocal of the total stopping power with respect to energy. The CSDA range of electrons in iron is shown in fig. A.6. From this we find that electrons with energies surpassing 8 MeV can penetrate the front plate of the spectrometer. The number of lower energy electrons will still be reduced by the front plate but electrons penetrating it can have energies up to tens of MeV left. These electrons will be deflected by the magnetic field and also hit the imaging plates.

Appendix B

Imaging Plate Detectors (IPs)

The Photostimulabel phosphor (PSP) is a two-dimensional position sensitive ionising particle detector and stores absorbed X-ray and particle energy in crystal structure traps. It is sometimes referred to as a storage phosphor. This trapped energy can be released if stimulated by additional light energy of the proper wavelength by the process of photostimulated luminescence (PSL). The unexposed PSP detector, commonly known as an imaging plate (IP), is similar in its use to X-ray screen-films. X-ray geometry and imaging techniques are also similar to screen-film acquisition. Three types of IPs produced by Fuji are mostly used by the laser community: BAS-TR, BAS-MS, and BAS-SRBonnet, Comet, Denis-Petit, Gobet, Hannachi, Tarisien, Versteegen, and Aléonard 2013. The layers these three types of IP consist of can be found in tab. B.1.

During the exposure X-rays are absorbed or particles transfer part of their kinetic energy to the IP (step 1). Energy deposited in the PSP material causes local electrons to be elevated from the ground state to a (meta-) stable state (trap) known as F-center (colour-center, german: Farbzentrum). This latent electronic image is not observable. The number of the excited electrons is proportional to the number of particles and photons incident on the IP. To produce an image the exposed IP has to be read out (step 2). The IP is raster-scanned with a highly-focussed and intense laser light of low energy (~ 2 eV). A significant number of the excited electrons are stimulated to return to lowest energy level within the phosphor, with a simultaneous release of photostimulated luminescence (PSL) of higher energy (~ 3 eV). The intensity of PSL, proportional to the number of released electrons, is optically filtered from the laser light and captured by a light guide assembly in close proximity to the IP. A photomultiplier tube (PMT) at the light guide output converts and amplifies the PSL into a corresponding output voltage. The digitisation process is performed using an analogue-to-digital converter (ADC) which produces a corresponding digital number at a specific location in the digital image matrix determined by the synchronisation of the laser beam and IP location. The IP is reusable after erasing the residual latent image information by applying an intense light (consisting of wavelengths that remove electrons from the excited states without stimulating further electron trapping). Image preprocessing (step 3) corrects the data for static light guide sensitivity variations and fixed noise patterns, so that a faithful reproduction of the imaged

object and scaling to a normalised range as raw image data is ensured.

Layer	SR	MS	TR
Protective			
Composition	C ₂ H ₂ O	C ₂ H ₂ O	No layer
Density / (g cm ⁻³)	1.273	1.66	N/A
Thickness / (μm)	6	9	0
Phosphor			
Composition	BaFBr	BaFBr _{0.85} I _{0.15}	BaFBr _{0.85} I _{0.15}
Density / (g cm ⁻³)	3.1	3.31	2.85
Thickness / (μm)	120	115	5
Support			
Composition	C ₂ H ₂ O		
Density / (g cm ⁻³)	1.273	1.66	1.66
Thickness / (μm)	188	190	250
Support			
Composition	ZnMn ₂ Fe ₅ NO ₄₀ H ₁₅ C ₁₀		
Density / (g cm ⁻³)	3.1	2.77	2.77
Thickness / (μm)	160	160	160

TABLE B.1: Atomic compositions, densities, and thicknesses of the different layers of Fuji BAS SR, MS, and TR IPs (Bonnet, Comet, Denis-Petit, Gobet, Hannachi, Tarisien, Versteegen, and Aleonard 2013).

B.1 IP Response Functions

The IP response functions for photons, electrons, and protons were calculated in the literature (Bonnet, Comet, Denis-Petit, Gobet, Hannachi, Tarisien, Versteegen, and Aléonard 2013). For the calculation it was considered that the number of FBr⁻ and FI⁻ sites generated in the phosphor layer by ionising particles is proportional to the total deposited energy in this layer. The Parameter α (PSL/keV) represents the IP responsivity and defines this proportionality. It is also considered that both the photons from the scanner and the PSL light can be absorbed when travelling either to or from the electron-hole recombination site within the phosphor layer. Therefore a second parameter, the absorption parameter L , was introduced (see tab. B.2 for protons, electrons, and photons).

Absorption Length L			
	L / (m)	α_p (10^{-4} PSL/keV)	$\alpha_{e,ph}$ (10^{-4} PSL/keV)
MS	222 ± 73	3.63 ± 0.17	6.95 ± 1.60
TR	44 ± 4	2.47 ± 0.07	4.85 ± 1.35
SR	118 ± 16	2.02 ± 0.07	3.33 ± 0.80

TABLE B.2: IP absorption lengths L and sensitivities α_p to protons, electrons and photons for different types of FUJI IPs (Bonnet, Comet, Denis-Petit, Gobet, Hannachi, Tarisien, Versteegen, and Aléonard 2013).

The attenuation of the photon fluxes at depth z in the phosphor layer is taken into account by an exponential factor to weigh the deposited energy. The response function $R(E)$ of an IP is therefore written as

$$R(E) = \alpha \int_0^W \frac{dE_{dep}}{dz} (E, z) e^{-z/L} dz \quad (\text{B.1})$$

where $\frac{dE_{dep}}{dz}$ is the amount of energy deposited by the incident and all the secondary associated particles in the phosphor layer between depths z and $z + dz$ and W is the thickness of the phosphor layer. Larger absorption lengths L ($L \gg W$) imply a larger mean free path for the scanner or PSL photons than for smaller L . Thus all the deposited energy in the phosphor layer contributes to the total number of PSL photons for larger L . Both the absorption length and sensitivity depend on the IP type, scanner and are also presumed to be dependent on the incident particle type. The yield Y of PSL photons created per second of irradiation in the whole area of the IPs was then extracted using the Fuji FLA7000 IP scanner with the scanner sensitivity 4000, latitude 5, and resolution 50 μm settings (which corresponds to the settings predominantly used in this work).

The yield Y of PSL created in a radioactive source emitting a single type of ionising particle with a continuous energy distribution per second of irradiation is related to the IP response function $R_{part}(E)$ via the folding equation:

$$Y = \int_0^\infty \frac{dN_{part}}{dE} (E) R_{part}(E) dE \quad (\text{B.2})$$

where $\frac{dN_{part}}{dE} (E)$ is the energy distribution of the particles impinging on the IP per second of irradiation. Assuming a response function following eg. B.1 with a specific sensitivity α_{part} , this yield Y can be rewritten as:

$$Y = \alpha_{part} \int_0^W \frac{dE_{dep}^{tot}}{dz} (z) e^{-z/L} dz \quad (\text{B.3})$$

$$= \alpha_{part} E_{dep}^{eff} \quad (\text{B.4})$$

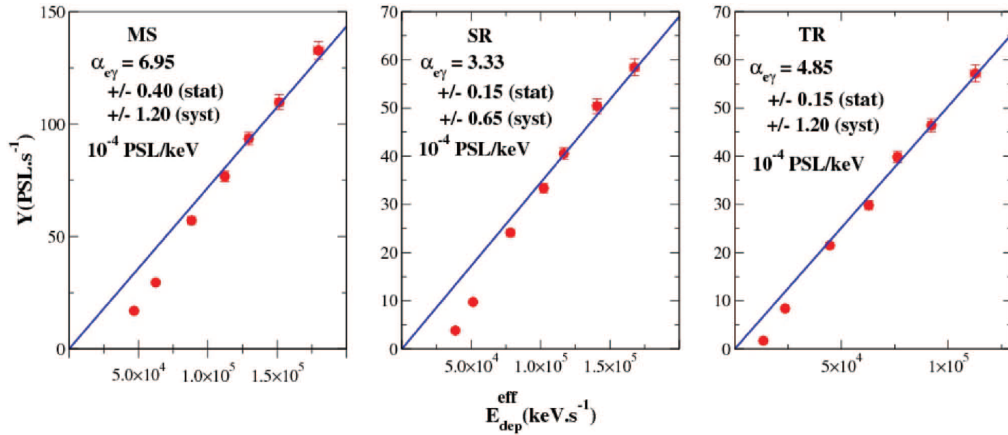


FIGURE B.1: Yield Y of measured PSL as a function of the calculated effective deposited energy for ^{60}Co irradiations with copper foils of different thicknesses (Bonnet, Comet, Denis-Petit, Gobet, Hannachi, Tarisien, Versteegen, and Aléonard 2013).

where E_{dep}^{eff} is the amount of energy deposited per second of irradiation in the IP sensitive layer between depths z and $z \pm dz$. It equals to:

$$\frac{dE_{dep}^{tot}}{dz}(z) = \int_0^\infty \frac{dN_{part}}{dE}(E) \frac{dE_{dep}}{dz}(E, z) dE \quad (\text{B.5})$$

The integral in eq. B.3 (called the effective deposited energy E_{dep}^{eff}) is calculated with the GEANT4 Monte Carlo code.

B.1.1 IP Response to Photons and Electrons

Using eq. B.1 with the values obtained for the sensitivity (see fig. B.1) and the absorption length the electron and photon response functions can be calculated. The resulting response functions to photons are shown in fig. B.2 a). The error bars (dashed area) are related to the uncertainties on the sensitivity values. This is compared to the results published by Meadowcroft et al. and Maddox et al. (Meadowcroft, Bentley, and Stott 2008; Maddox et al. 2011; Bonnet, Comet, Denis-Petit, Gobet, Hannachi, Tarisien, Versteegen, and Aléonard 2013).

The corresponding response for electrons is shown in fig. B.2 b). Those results are compared to the existing data for SR IPs published by Chen et al. (Hui Chen et al. 2008; Bonnet, Comet, Denis-Petit, Gobet, Hannachi, Tarisien, Versteegen, and Aléonard 2013).

B.1.2 IP Response to Protons

To obtain the data points for the IP response to protons monoenergetic protons ($\Delta E/E \approx 2.5 \times 10^{-5}$) were used. Protons were backscattered by the Rutherford backscattering (RBS) process and detected by the IPs. A silicon diode detector was used to measure the absolute energy distribution of protons in the experiment. The

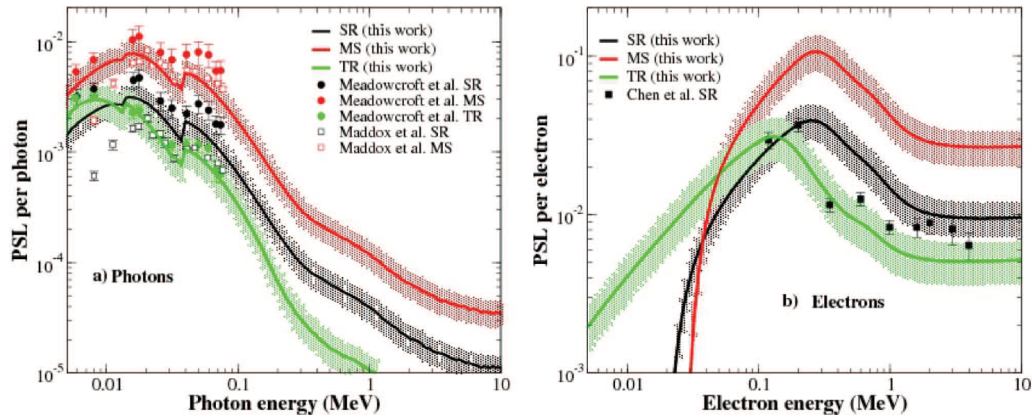


FIGURE B.2: Calculated response functions (solid lines) of MS, SR, and TR IPs for photons (left) and electrons (right) with associated uncertainties (dashed area). These responses are compared to experimental results published by Meadowcroft et al., Maddox et al., and Chen et al. (Hui Chen et al. 2008; Meadowcroft, Bentley, and Stott 2008; Maddox et al. 2011; Bonnet, Comet, Denis-Petit, Gobet, Hannachi, Tarisien, Versteegen, and Aléonard 2013)

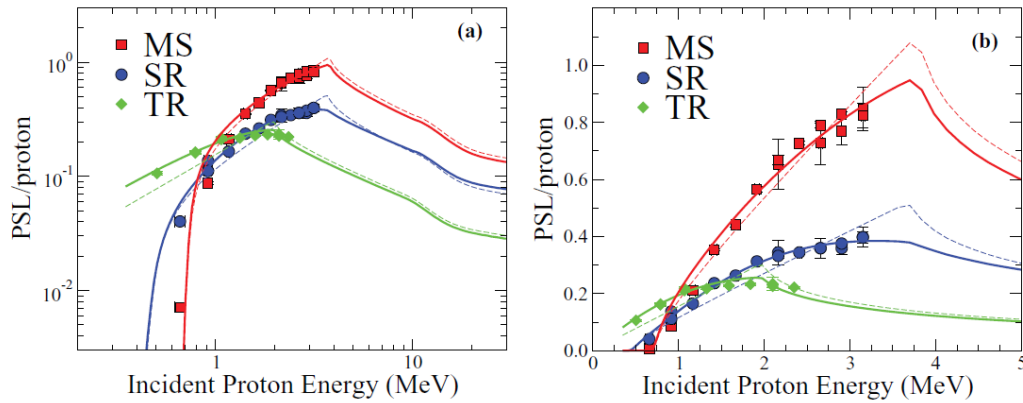


FIGURE B.3: Calculated response functions $R(E)$ of MS, SR, and TR IPs for protons. The symbols represent the experimental data. The dashed lines represent the modelled responses not taking into account the absorption of photons in the phosphor layer. The solid lines represent the modelled responses taking the absorption length L into account. (a) In logarithmic scale and (b) a magnification in linear scale (Bonnet, Comet, Denis-Petit, Gobet, Hannachi, Tarisien, Versteegen, and Aléonard 2013).

IP response for protons is shown in fig. B.3. It was calculated using the following equation:

$$R(E) = \frac{Y(E)}{N_{protons}(E)} \frac{C_{DT}C_{\sigma}(\theta_p, E)}{A} \quad (\text{B.6})$$

where $Y(E)$ is the yield of PSL per second in an area A (in mm^2) of the IP, $N_{protons}(E)$ is the number of incident protons per second and per mm^2 on the diode, C_{DT} is the correction for the dead time of the diode acquisition system and is the ratio of the RBS cross section at the IP mean angle over the RBS cross section at the diode mean angle.

As MS and SR IPs possess a protective layer, a cut-off is observed at low energies. Therefore TR IPs are more sensitive to low energies as they do not have a protective layer. As long as the protons are stopped in the phosphor layer, the response functions increase with the incident proton energy. Only for TR IPs this maximum of $R(E)$ is reached when the proton range (path length) is of the order of the phosphor layer thickness. Because only a fraction of the energy of the higher energetic protons is deposited in the phosphor layer the curves drop again. Due to the higher thickness of the phosphor layer, this maximum is not reached for MS and SR IPs. The results demonstrate that MS IPs are more sensitive than SR and TR ones.

B.2 IP Angular Response Function

Particles incident on the imaging plate will in general not hit the IP normal to the surface. That will lead to drastically different path lengths travelled by the particle through the material. Experiments were performed on this (Tanaka et al. 2005). Actually, it was discovered that the naive assumption, supposing a linear energy transfer, the angular response would only depend on the angle following a cosine law held true (see fig. B.5):

$$y = \frac{A}{\cos(Cx)} + B \quad (\text{B.7})$$

with $A = 1.15 \pm 0.265$, $B = -0.154 \pm 0.276$ and $C = 0.0164 \pm 0.0011$. From this and the dispersion function of the electron spectrometer, the relative sensitivity of the IPs can be calculated. The function is normalised to one on an incident angle of 90° . This corresponds to the calibration data of the response functions (B.1). As there are two IPs present in the spectrometer, which are placed at an angle of 90° to each other, a step in the relative sensitivity function can be seen clearly in fig. B.6.

B.3 IP Signal Fading

After exposition of the imaging plate, the spontaneous recombination of e^- /hole pairs leads to a signal loss. This behaviour of the signal is called fading. Experimental conditions often do not allow to access the IPs directly after the exposition. The time

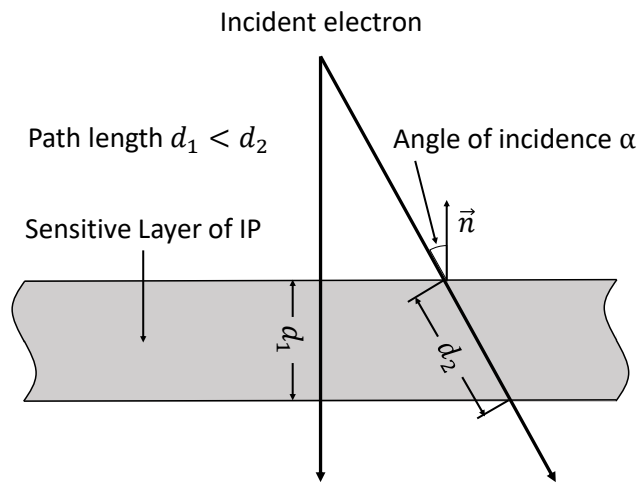


FIGURE B.4: Path length of a particle in the Imaging Plate according to angle of incidence.

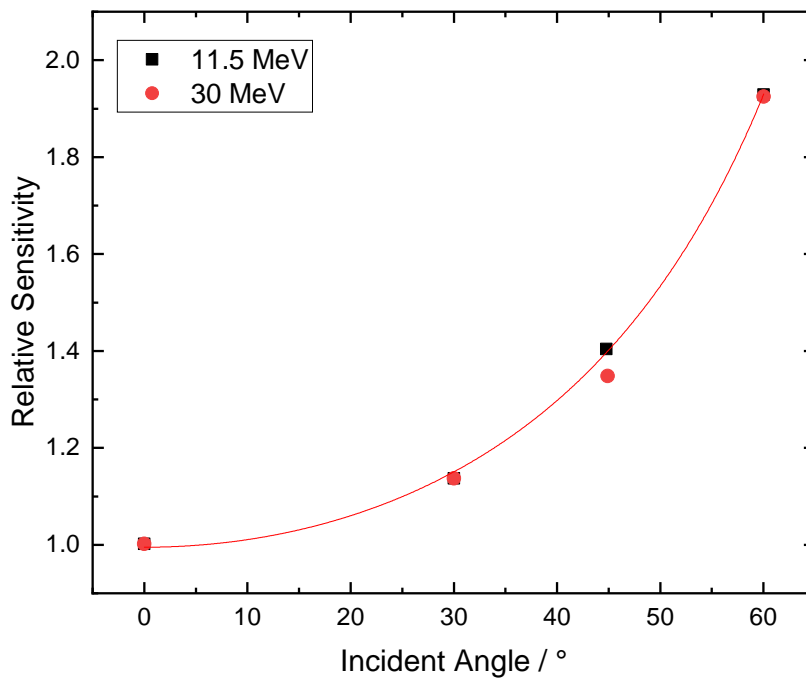


FIGURE B.5: Relative sensitivity due to incident angle.

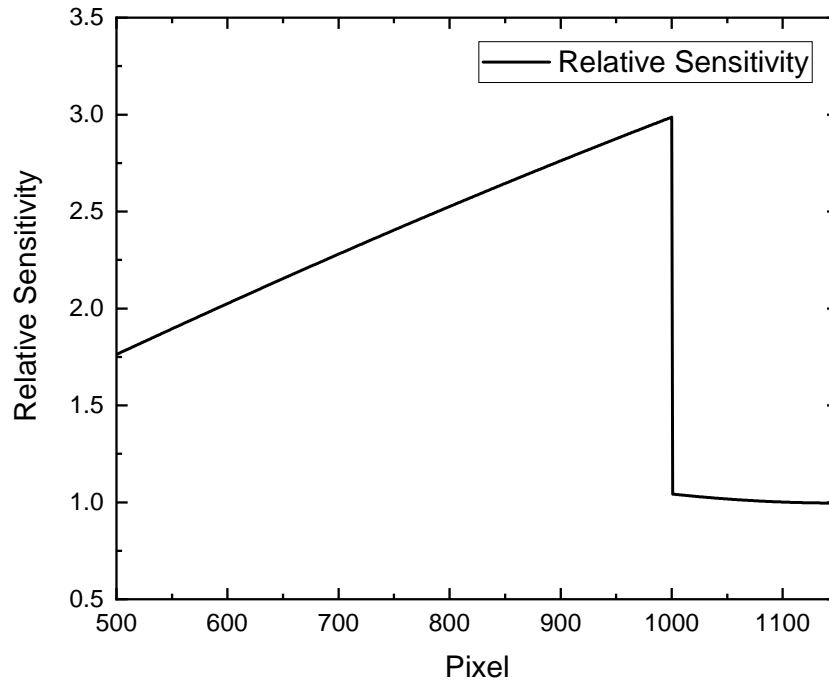


FIGURE B.6: Angular response.

from exposition to the beginning of the scanning procedure can vary from minutes to hours. At PHELIX, this time is in the order of 30 min. Other works also normalise to this time frame (Doria et al. 2015). Measurements with exposure of the IP to a ^{55}Fe radioactive source were performed in the literature. X-ray line emission in the range of 5.9 keV and 6.5 keV is emitted. The exposure time was 90 s. The signal is read out after a set of different elapsed times with the same scanner FLA-7000 and scanner settings (50 μm resolution, S4000, L5) as used in the experiments presented in this work. The fading functions are fitted with double-exponential curves:

$$f(t) = A_1 \times \exp(-t/B_1) + A_2 \times \exp(-t/B_2) \quad (\text{B.8})$$

The obtained coefficients are given in tab. B.3 and the corresponding curves in fig. B.7. The fading effect is similar for incident electrons and photons but the first temporal component decays faster in irradiations with heavier particles (Ohuchi and Yamadera 2002).

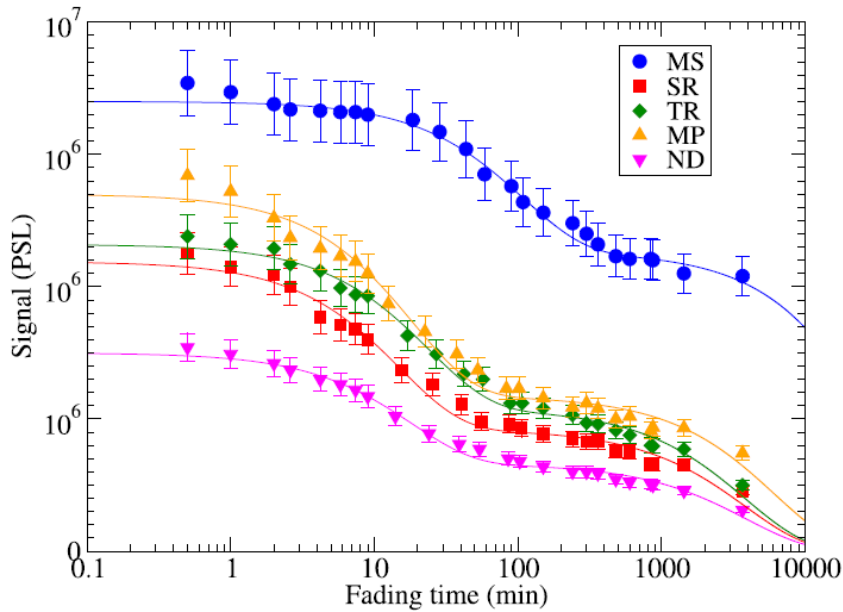


FIGURE B.7: Measured signal (PSL) using a ^{55}Fe source (80 kBq activity and 90 s exposure) for five types of IP at different fading times (Boutoux et al. 2015).

Coefficients of the Fading Functions				
A_1	B_1	A_2	B_2	
MS	0.334 ± 0.011	107.320 ± 9.661	0.666 ± 0.010	33974 ± 11235
TR	0.535 ± 0.016	23.812 ± 2.201	0.465 ± 0.012	3837.2 ± 498.1
SR	0.579 ± 0.021	15.052 ± 1.580	0.521 ± 0.013	3829.5 ± 650.9

TABLE B.3: A_i and B_i coefficients for the fading functions shown in fig. B.7 for different types of FUJI IPs (Boutoux et al. 2015). Note that B_i coefficients are given in min.

B.4 IP Properties in X-Ray Radiography Applications

It is often not possible to estimate a PSL signal level that the scanning process produces preceding an experiment. That might be due to shot to shot variations in intensity, varying experimental conditions due to different target geometries or simply because of limitations in the setup that do not allow the reduction of the expected irradiation. A over-saturation may occur. This over-saturation may originate from either saturating the sensitive layer of the IP during the irradiation or might be created in the scanning process itself and would therefore not destroy the information stored in the IP. The IPs are capable of sustaining high energy deposition but the scanning process induces such intense luminescence that the photo detectors of the

scanner become saturated even before the IP is saturated. A single scanning procedure does not erase all the original signal on an IP, it merely reduces the signal intensity level. As information remains in the IP after each scanning procedure, it is possible to reduce the signal intensity level until it is at tolerable level below the saturation level of the scanner photo detectors.

The following section shows the behaviour of the PSL signal levels in an IP after several scanning procedures and compares them. The Signal-to-Noise- and Contrast-to-Noise-ratios are introduced and compared. At last, the spatial resolution of the IP itself is shown and compared with the spatial resolution achievable with an X-ray tube.

B.4.1 Quantum Efficiency, Signal-to-Noise-Ratio (SNR) and Contrast-to-Noise-Ratio (CNR)

One important measure to evaluate the quality of an image quantitatively is noise. The kind of source of the photons has to be considered, as these sources are emitting photons homogeneously only averaged over time. The distribution over time of the emission of photons is called shot noise. Because photons are quantised, the emission of photons is subject to the Poisson-distribution. This distribution is a discrete probability distribution that expresses the probability of a certain number of events occurring in a fixed interval of time or space if these events occur with a known constant mean value and independently of each other. The probability mass function is given by (Joe and Zhu 2005):

$$P(\lambda, k) = \frac{\lambda^k e^{-\lambda}}{k!} \quad (\text{B.9})$$

with λ the expected number of events (also called the mean value) and k the number of actual events. The standard deviation of the Poisson-distribution is (D. J. Schroeder 1999):

$$\sigma_{Pois} = \sqrt{\lambda} \quad (\text{B.10})$$

This is the most fundamental reason for noise in an image, limiting the signal-to-noise-ratio (SNR) to $\lambda/\sigma_{Pois} = \sqrt{\lambda}$ (D. J. Schroeder 1999).

There is a second fact to consider, that not only the emission but also absorption of photons is a stochastic process. The difference is that the absorption process is a single particle event in contrast to the emission. The mass attenuation coefficient leads to the probability for the absorption of a photon (see. 2.3.2). Therefore, the Poisson-distribution is not applicable anymore. It is replaced by the Binomial-distribution, another discrete probability distribution, which is appropriate in cases where an event is successfully occurring with a probability p and not occurring with probability $(p - 1)$. The Binomial-distribution then gives the probability for the event to occur k times after n independent tries (Skellam 1948):

$$P(n, p, k) = \binom{N}{k} p^k (1-p)^{N-k} = \frac{n!}{k!(N-k)!} p^k (1-p)^{N-k} \quad (\text{B.11})$$

For the case of photon absorption, N_0 is the number of photons incident on the absorbing matter and $p = p_a \times p_d$ the product of absorption probability with the detection probability of the detector itself, and $N_1 p N_0$ is therefore the number of detected photons. The quantum efficiency Q is defined as the quotient of the number of detected to the number of incident photons:

$$Q = \frac{N_1}{N_0} = p \quad (\text{B.12})$$

The standard deviation of the Binomial-distribution is (Taylor 1997):

$$\sigma_{Binom} = \sqrt{pN_0(1-p)} \quad (\text{B.13})$$

Therefore, any detector with detection probability below one is subject to additional detection noise.

The highest achievable SNR in an image is subject only to the combination of shot noise and detection noise, which is calculated by the convolution of both types of noise. For large numbers of λ and N_0 , the Poisson- and Binomial-distribution converge to the Gaussian-distribution (also called normal-distribution). Hence the calculation of the total standard deviation of i sources of noise can be treated similar to that case (Timischl 2015):

$$\sigma_{conv} = \sqrt{\sum_{i=1}^n \sigma_i^2} \quad (\text{B.14})$$

As a result, even for the ideal scenario with no other noise source (e.g electronic noise, readout noise, background noise) the SNR is limited to (Welvaert and Rosseel 2013):

$$SNR = \frac{pN_0}{\sqrt{\sigma_{Pois}^2 + \sigma_{Binom}^2}} = \sqrt{\frac{p^2 N_0}{1 + p(1-p)}} \quad (\text{B.15})$$

and for solid state detectors with additional detector noise σ_{Detec} (D. J. Schroeder 1999):

$$SNR = \frac{pN_0}{\sqrt{\sigma_{Pois}^2 + \sigma_{Binom}^2 + \sigma_{Detec}^2}} \quad (\text{B.16})$$

were the number of events expected λ is equal to the number of photons N_0 incident. The fractional accuracy for a given SNR is defined as $1/SNR$, thus an observation with 1% accuracy requires a SNR of 100 (D. J. Schroeder 1999). From eq. B.16 we gather that better accuracy is achieved with smaller σ_{Detec} .

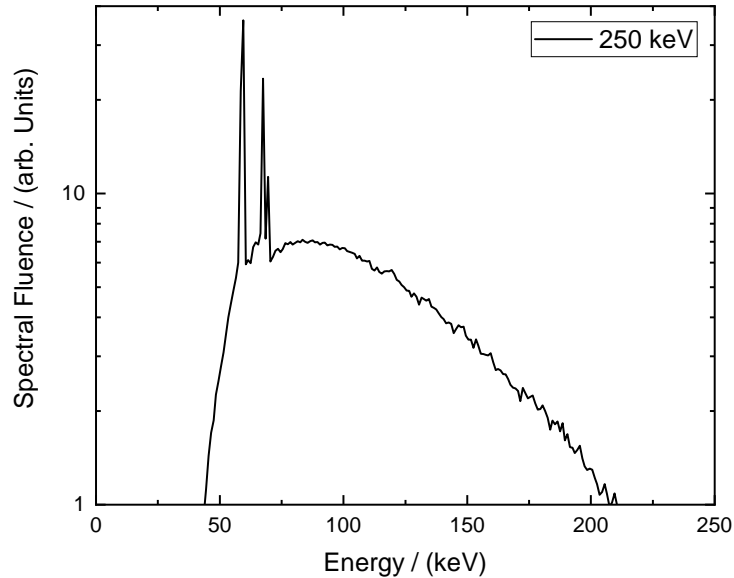


FIGURE B.8: Simulated spectrum of the used X-ray tube with an acceleration voltage of 250 kV. The low energy cut-off is due to an X-ray window between Cu-anode and detector. Calculations by Felix Horst.

Even if the SNR is a good way to evaluate the smoothness of an image, it is no measure for differentiating between objects in imaging applications like radiography. To distinguish between areas of different signal level, the Contrast-to-Noise-ratio (CNR) can be defined (Desai, Singh, and Valentino 2010):

$$CNR = \frac{|\mathcal{S}_1 - \mathcal{S}_2|}{\sigma_{1,2}} \quad (\text{B.17})$$

with \mathcal{S}_1 and \mathcal{S}_2 the mean intensity signal levels in the two regions of interest and $\sigma_{1,2}$ the noise, with the additional assumption that the noise is equal in both areas.

B.4.2 Multiple Scanning Procedures of IPs

To account for the risk of data loss, calibration measurements using a 250 kV X-ray tube (for simulated X-ray spectrum of the used tube see fig. B.8) were performed using radiography step targets of several materials (see fig. B.9 for the targets). It was observed before, that multiple scanning procedures reduce the PSL signal level stored in an IP for each subsequent scanning procedure (Khaghani 2016). Therefore the PSL signal erasing, the spatial resolution, signal-to-noise ratio and contrast-to-noise ratio were measured after 12 subsequent scanning procedures respectively. Fig. B.10 shows scan number six as an example for the relative signal levels behind different radiography targets.

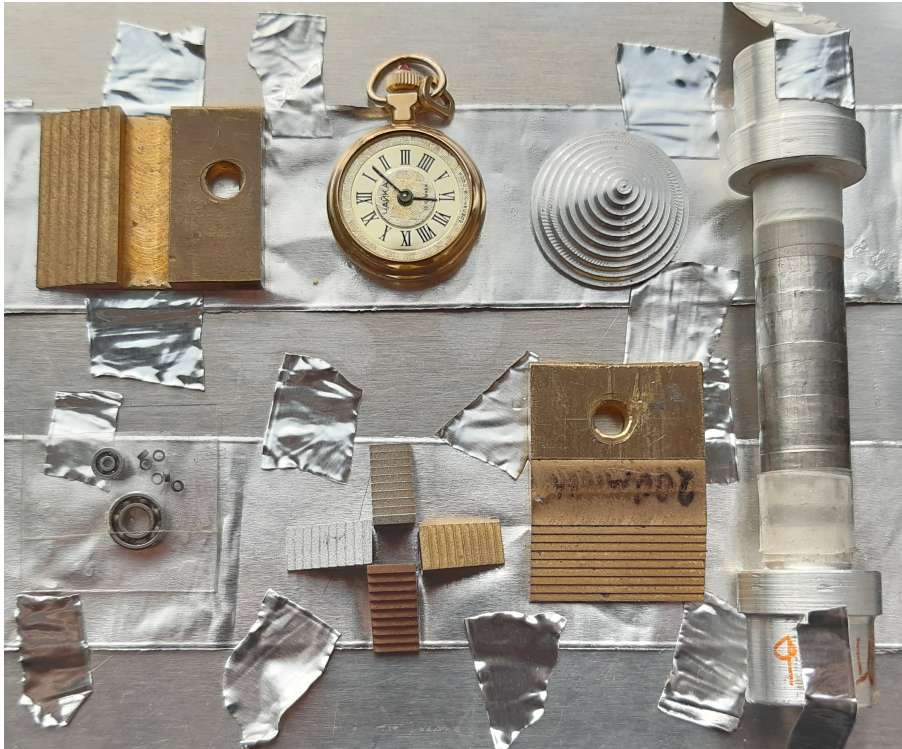


FIGURE B.9: Picture of the radiography targets used in the experiments. The targets consist of several materials which allows comparison between Al, Cu, Fe and brass (alloy of Cu and Zn). The geometry of the different steps is the same.

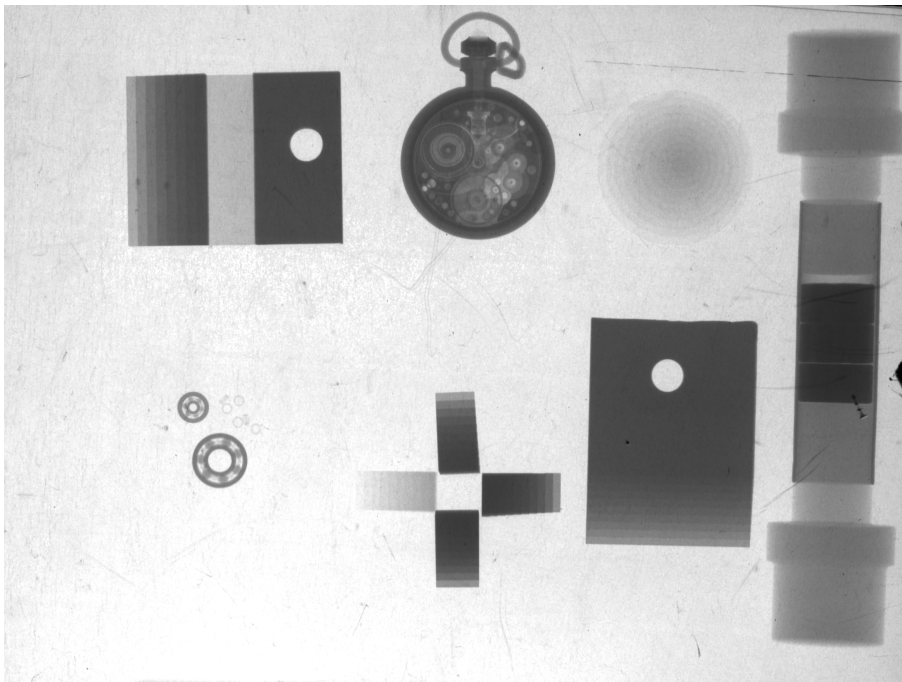


FIGURE B.10: Irradiation of the targets shown in fig. B.9 by an X-ray tube with the spectrum shown in fig. B.8. The difference in the absorption due to different material types can easily be seen.

The first step of this consideration is to irradiate the Imaging Plate detectors with a dose of X-rays that is high enough to create a situation in which the scanning process of the IP produces an over-saturated image while the IP itself is not saturated. A Dose of 100 mGy was produced using the spectrum shown in fig. B.8. The dose itself was measured below the IP. The radiography targets on top of the IP were fixed on a Al-plate of 1 mm thickness. Brass steps with thicknesses of multiples of 1 mm were used for the measurements shown below.

B.4.3 Mean Intensities in the Scanning Process of IPs

The choice of the suitable step target took two considerations into account. Firstly, the geometrical orientation to the source had to fulfil the requirement that at least one edge was exactly below the source. As the source has a size in the range of mm, the distance to the source was chosen to be 400 mm and the step targets were placed directly on top of the IP separated only by a 1 mm Al-plate as support for the targets. Secondly, the difference in the signals behind each step thickness had to be high enough to encompass a high range of PSL-intensities. Therefore, the brass step target was chosen.

Fig. B.11 shows the mean values of the intensity of an area 80 pixels in width along the direction of the steps. A factor of at least three was reached as ratio between the intensities of a 10 mm step and background level. For comparison with the scans taken in the electron acceleration experiment, the first scanning procedure was performed using 50 μm spatial resolution of the scan, sensitivity 4000 and latitude 5. This corresponds to numbers that are used in several papers concerning the calibration of Imaging Plate detectors (Bonnet, Comet, Denis-Petit, Gobet, Hannachi, Tarisien, Versteegen, and Aléonard 2013; Boutoux et al. 2015). Around 15 minutes passed from irradiation to scanning. As mentioned above, the PSL signal level was saturated in the first scan. The sensitivity was reduced to 1000 starting with the second scan. Saturation was still reached for the background level and thinner steps (up to 5 mm) for the next five scanning procedures. In total, a number of 12 scanning procedures were performed, each two to three minutes apart. Additionally, the mean signal of all 12 scanning procedures was calculated.

The mean signal intensity level per step was then calculated for each step. Reaching a statistic of around 1200 pixel (3 mm^2) for each step where edge effects in the intensity levels could be neglected. This high statistic leads to small error bars in the range of the size of the symbols plotted. The mean intensity levels are shown in fig. B.12 in logarithmic scale. As can be seen in fig. B.11, the background signal level was saturated up until scanning procedure number five. The measured signal intensity level is decreasing for each scanning procedure. Beginning with the sixth scanning procedure, a linear behaviour in the logarithmic plot starts to form. The slope for the different fits is the same within the error limits.

Corresponding to (Khaghani 2016), the erasing rate was calculated. The erasing rate compares the signal intensity level s_n of scanning step n with the signal intensity

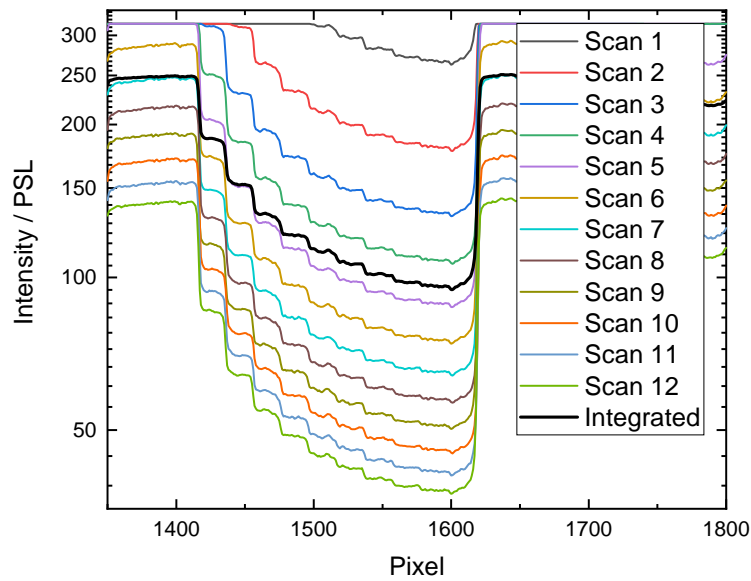


FIGURE B.11: Data for the brass steps. Mean values of the intensity of an area 80 pixels in width along the direction of the steps. The first scanning procedure was performed with $25\ \mu\text{m}$ spatial resolution, S4000 and L5 (not shown due to oversaturation of the scan). The sensitivity was reduced to S1000 and 12 more scanning procedures were performed. The black line shows the mean values of all 12 scanning procedures together.

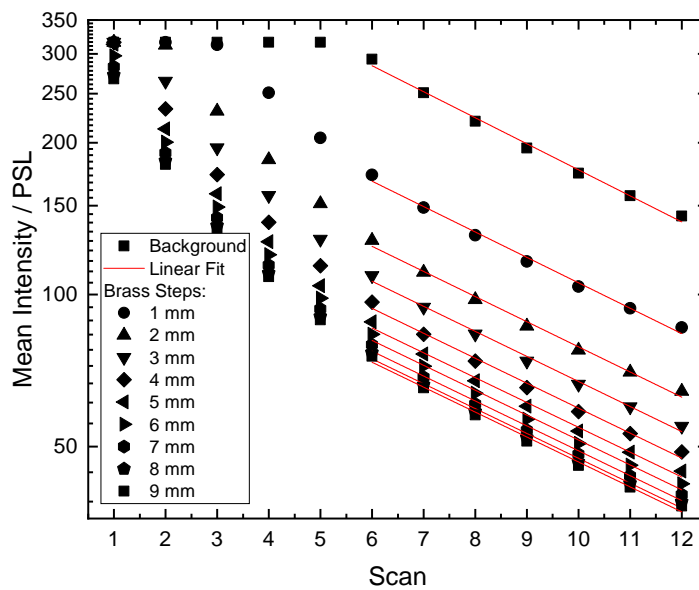


FIGURE B.12: Mean signal intensity levels for each brass step in comparison to the background intensity level. From scan six on, a linear behaviour in the signal reduction due to each scan is visible.

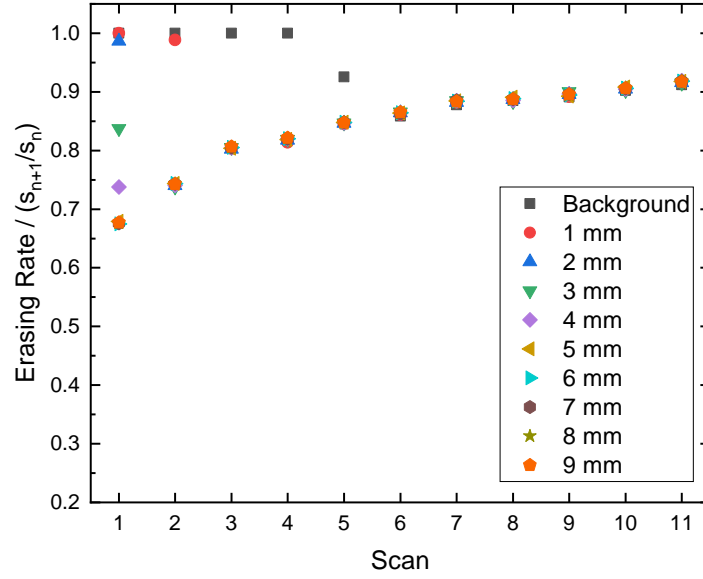


FIGURE B.13: text.

level s_{n+1} of scanning step $n + 1$. The measurement in the reference was done using protons as impinging particles. Except of the over-saturated part and the first point after leaving saturation, the erasing rate becomes constant for the different step sizes as well within the same scanning event (see fig. B.13). That is comparable to the measurement with protons.

B.4.4 Signal-to-Noise Ratio in the Scanning Process

The signal-to-noise ratio (SNR) and contrast-to-noise ratio (CNR) was measured using the same brass steps as mentioned above. Furthermore, the ratio of the signal intensity level with the background intensity level was considered:

$$Signal/Background = \frac{I_{signal}}{I_{noise}} \quad (B.18)$$

The SNR is shown in fig. B.14, CNR is shown in fig. B.16 and the ratio of signal level to background level is shown in fig. B.15. From fig. B.14 can be seen, that the SNR is only depending on the thickness of the brass steps. It does not depend on the number of scanning procedures that were performed on the IP. But for the thinner steps, a small decrease in SNR is observed for the integration of the intensity signal level of all 12 scanning procedures. But this might also be as by performing the integration over all 12 scanning procedures also included scans where the background still showed saturation. The SNR converges to around 35 for greater step sizes.

Fig. B.15 suggests that the ratio of the signal intensity level with the background intensity level is independent of the number of scanning procedures and from for thicker steps also independent from the thickness of the materia. The integrated

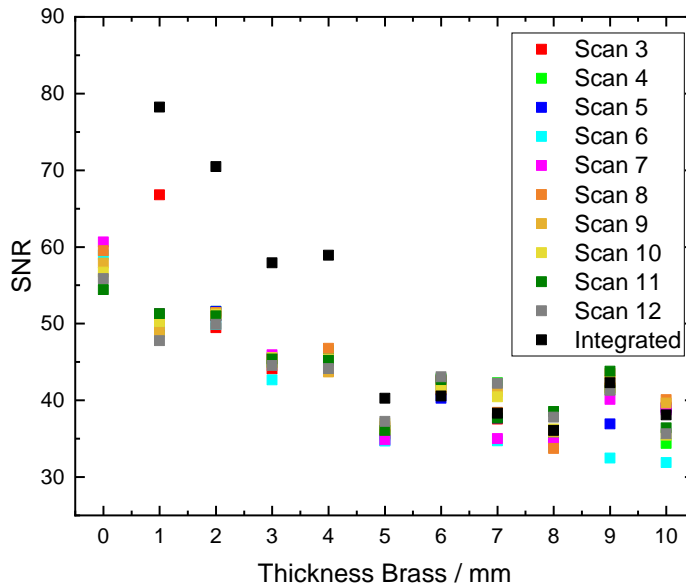


FIGURE B.14: Comparison of the signal-to-noise ratio for different step thicknesses of brass in 12 subsequent scanning procedures.

intensity signal level seems to show a higher ratio of the signal intensity level with the background intensity level for thinner target material as well as the SNR in fig. B.14. But this might be due to saturation of the background intensity level again. The CNR is shown in fig. B.16. The variance in the CNR is high for thin steps but converges to around 11 for thicker steps while the variance decreases strongly.

B.4.5 Spatial Resolution in the Scanning Process

To perform an analysis of the change in spatial resolution due to multiple scanning of the IP, the brass step was chosen according to the same reasons as before. The geometry of the experiment plays an important role for the produced image in this case. The spatial resolution could be measured to a satisfying degree as the X-ray source was situated directly above one edge of the brass step. The 10 mm step was used. The intensity signal level between background and this step was considered to measure the resolution. As shown in fig. B.17, which is a zoom-in into the right part of fig. B.11, the steps were fitted using a sigmoidal fit. In accordance with the results shown in the previous sections the reliable data begins with the sixth scan as the background signal level is saturated in the first 5 scans. The spatial resolution was defined as the 10%-90%-resolution in the following analysis. We define the spatial distance between 10% and 90% of the ratio of the signal intensity levels of the step and the background intensity level as 2σ . The spatial resolution for the twelve steps and the integration (shown as thirteenth step) is presented in fig. B.18. This diagram suggests that the spatial resolution is independent of the number of scans performed. As mentioned before, the results for the first five scanning procedures differ from the

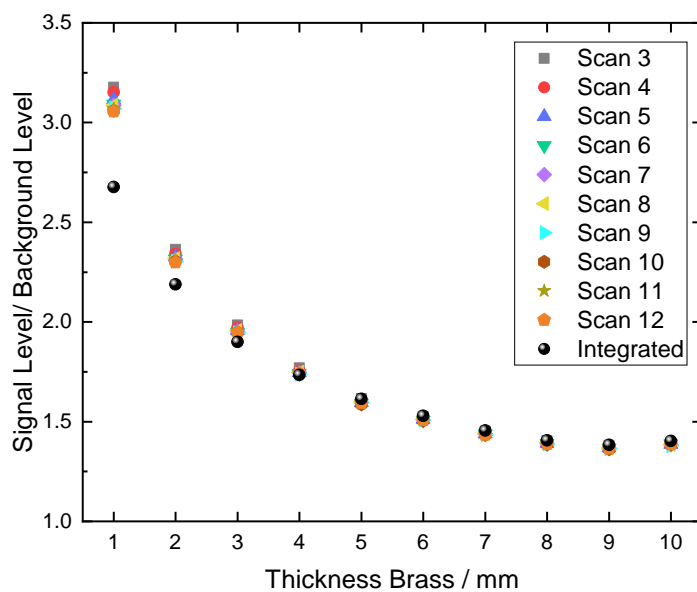


FIGURE B.15: Comparison of the ratio between signal intensity level and background intensity level for different step thicknesses of brass in 12 subsequent scanning procedures.

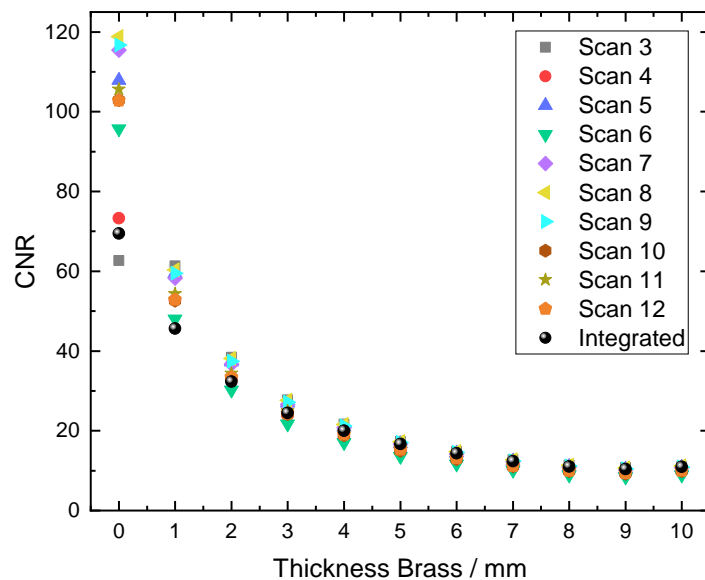


FIGURE B.16: Comparison of the contrast-to-noise ratio for different step thicknesses of brass in 12 subsequent scanning procedures.

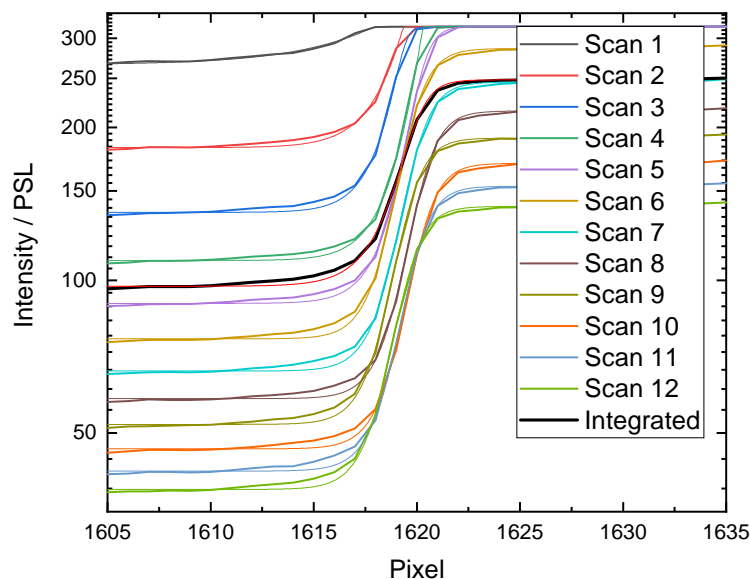


FIGURE B.17: Mean values of the intensity of an area 80 pixels in width along the direction of the brass steps. Best fits for the 10 mm step used for the estimation of the spatial resolution after each of the 12 subsequent scanning procedures shown in fig. B.18.

rest because of the saturation in the background intensity level. The spatial resolution approaches $80\ \mu\text{m}$ when the saturation effect is vanishing.

More steps of the brass target were taken into consideration in the next step of the analysis. The highest difference in the signal intensity level and background intensity level without any saturation effect is found in scan six (see fig. B.19). The spatial resolution was measured between each of these 1 mm thick steps. Fig. B.20 shows the spatial resolution for seven steps. The fitting procedure for the missing points did not reach a satisfying limit to be shown. It can be seen that the spatial resolution is $80\ \mu\text{m}$ as well as before for thin steps but is increasing from step four until reaching $220\ \mu\text{m}$ at the eighth step.

For comparison, the spatial resolution was measured by the ratio between the signal intensity level on each step and the background intensity level in the adjacent region. The mean intensity levels for the whole step width of 15 pixels are shown in fig. B.21. The first thing that can be observed is that there is a difference in the position of the two edges as the X-ray source seems to be situated above the rear and one lateral edge predominantly. Therefore the shadow of the steps seems to be cast under an angle onto the IP. This conclusion is supported by the spatial resolution data points shown in fig. B.22. The spatial resolution is $80\ \mu\text{m}$ for thin steps again but diverges for high step thicknesses. The spatial resolution is comparable for the data points on the left side and for the single steps shown in fig. B.21. It can not be excluded at this point that there is an influence of the source size to the spatial

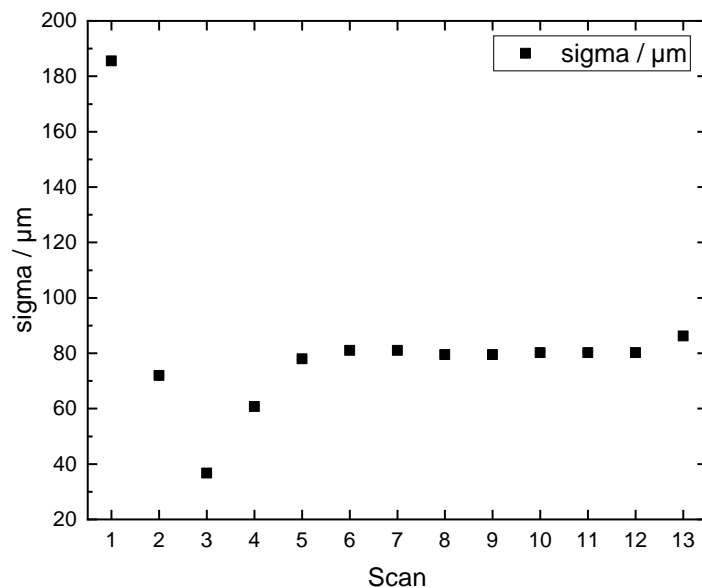


FIGURE B.18: Spatial resolution for the fits shown in B.17. The resolution is the distance between 10 % and 90 % of ratio of the background intensity level and the signal intensity level.

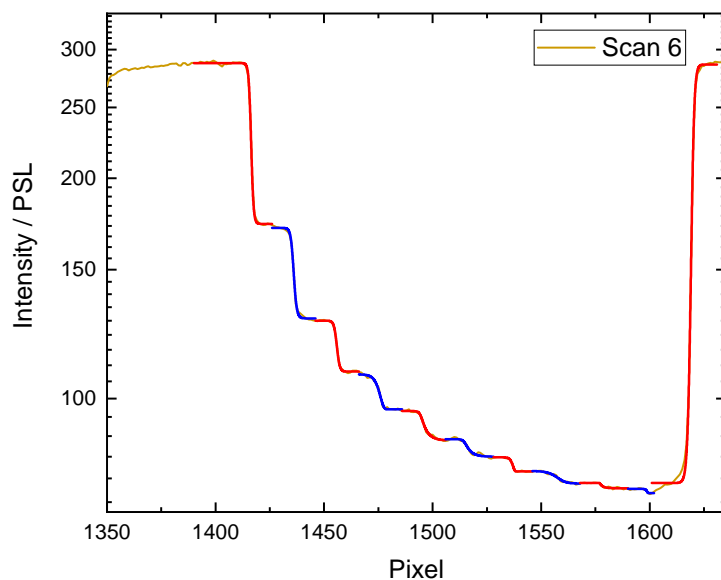


FIGURE B.19: Mean values of the intensity of an area 80 pixels in width along the direction of the brass steps. Scan six is the first scan where no oversaturation was visible. Best fits for all brass steps used for the estimation in fig. B.20 are shown.

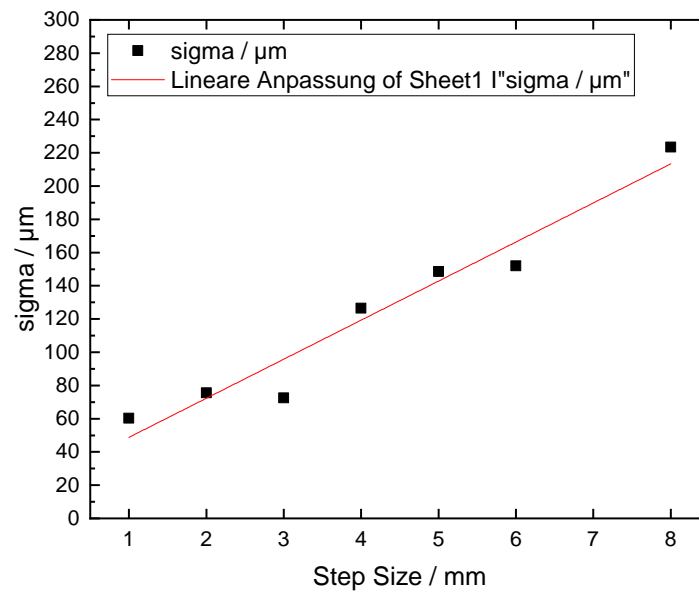


FIGURE B.20: Spatial resolution estimated by the fits shown in fig. B.19. Missing data points were not reaching a satisfying limit in the fitting procedure

resolution.

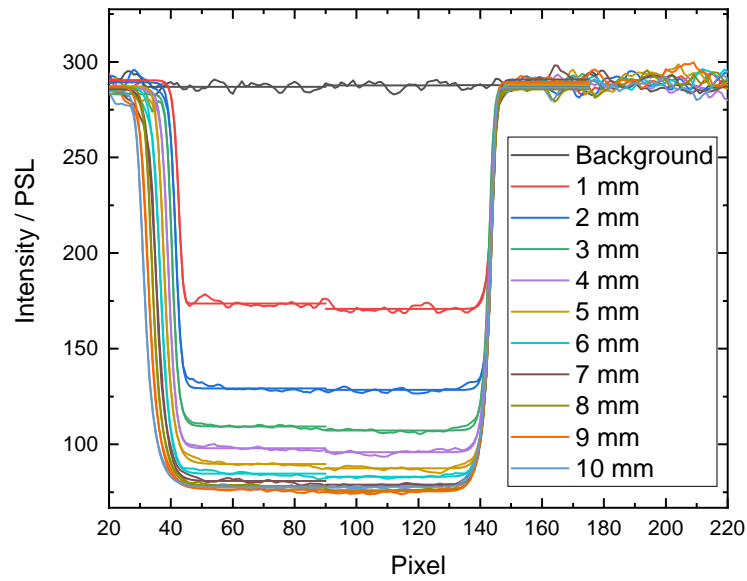


FIGURE B.21: Mean values of the intensity of an area 15 pixels in width perpendicular to the direction of the brass steps. Differences in step width is due to shadows cast by the steps onto the IP. Scan six is the first scan where no oversaturation was visible. Best fits for all brass steps used for the estimation in fig. B.22 are shown.

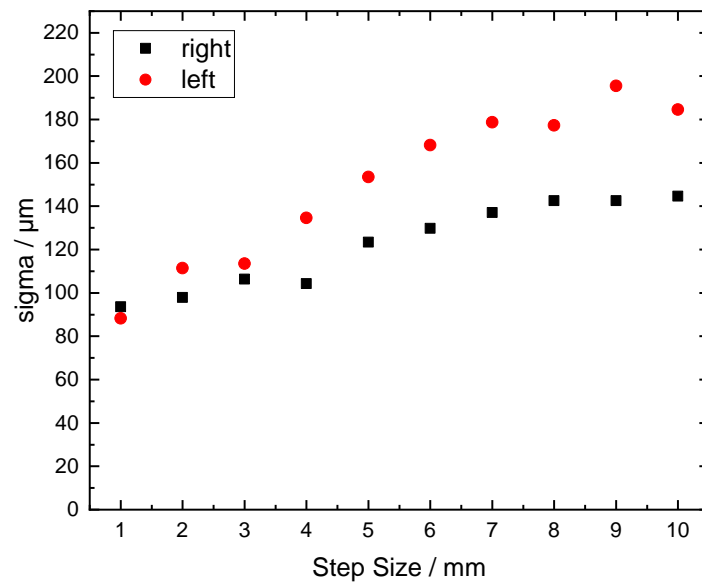


FIGURE B.22: Spatial resolution estimated by the fits shown in fig. B.21. Difference in spatial resolution between both sides of the steps is due to shadows cast by the steps themselves. Left and right refers to fig. B.21 as well.

Appendix C

X-Ray Diagnostics

For the imaging of X-ray radiation, several geometrical and X-ray optical techniques can be applied. Analogue as well as semiconductor based spatial and spectral resolving detectors were used in the experiments discussed in this work. This section describes the semiconductor based X-ray CdTe-diode spectrometer, the polychromatic imaging XCOT-system, the pinhole camera principle and the monochromatic imaging technique of the X-ray crystal microscope.

C.1 X-Ray CdTe-Diode

The XR-100CdTe-diode was used for spectrometric measurement of the X-ray fluorescence generated in the ion beam-target region. The XR-100CdTe is a thermoelectrically cooled X-ray detector and preamplifier using a $5 \times 5 \times 1$ mm CdTe diode (Amptek Inc. 2020). The photoelectric cross-section scales as Z^5 . CdTe is used instead of Si as it has a mean $Z = 50$ ($Z_{Cd} = 48$ and $Z_{Te} = 52$) instead of $Z_{Si} = 14$ (Redus 2010). The stopping power of CdTe allows for the detection of X-rays in the range up to 100 keV (see fig. C.1).

X-rays and gamma rays interact with CdTe atoms to create an average of one electron/hole pair for every 4.43 eV of energy lost in the CdTe. This energy loss is dominated by either the photoelectric effect or Compton scattering depending on the energy of the incoming radiation. The probability of detection increases with the thickness of CdTe. Therefore, the high energy response is dominated by the material thickness (1 mm) of the CdTe and the entrance window (100 μ m Be) defines the response for low energies.

C.2 HOPG X-Ray Spectrometer in von Hámos Geometry

Thin films of highly oriented pyrolytic graphite (HOPG) give the opportunity to realize crystal optics with arbitrary geometry by mounting it on a mould of any shape. A specific feature of HOPG is its mosaicity accompanied by a high integral reflectivity, which is by an order of magnitude higher than that of all other known crystals in an energy range between 2 keV up to several 10 keV. These characteristics

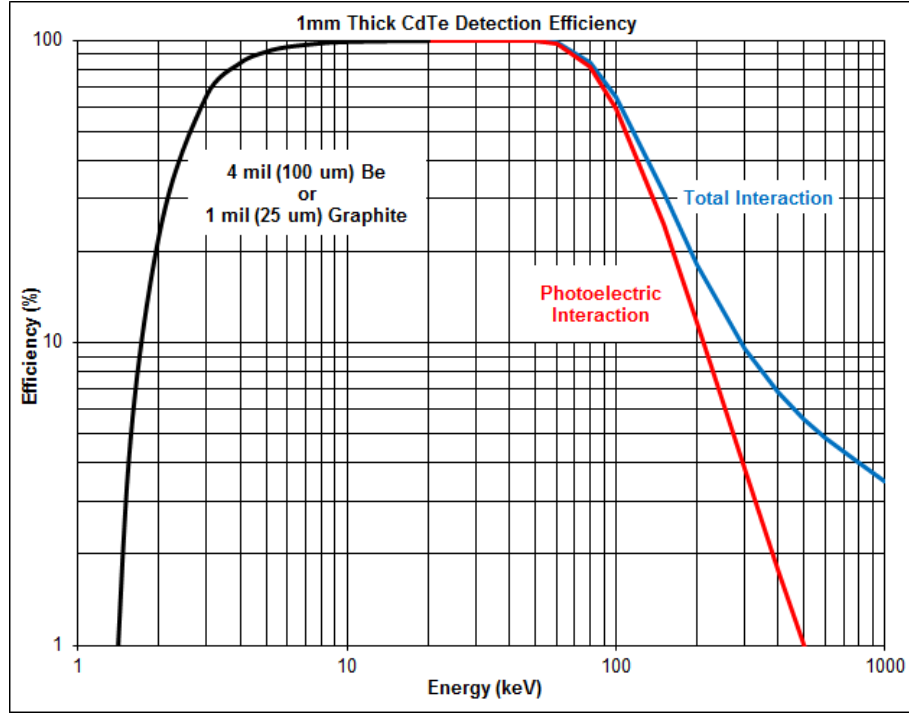


FIGURE C.1: Quantum efficiency of the CdTe-Spectrometer. Log-log plot of interaction probability between 1 keV and 1 MeV.

make it possible to realise highly efficient collecting optics (Legall et al. 2006; Arkadiey et al. 2007).

The phenomenon of Bragg reflections is used in the field of X-ray optics. Electromagnetic radiation of wavelength λ is reflected by a crystal in a narrow angular interval around the angle Θ according to Bragg's law:

$$n\lambda = 2d_{hkl} \sin \Theta, \quad (\text{C.1})$$

where d_{hkl} is the distance of the lattice planes in the crystal and n is the order of reflection. Polychromatic electromagnetic radiation will experience a dispersive effect and therefore, a crystal can be used as the dispersive element of a spectrometer.

Cylindrically bent crystals allow to focus X-rays in one dimension. This increases the intensity on a detector in the focal plane (Hámos 1932). The scheme of the optical path in the von Hámos geometry is shown in fig. C.2. X-rays entering the spectrograph through the slit S reach the bent crystal K under the Bragg angle φ , are reflected and produce the monochromatic image L on the image plane E . x_1 and y_1 are the coordinates of a point on the image L . The image of the slit S in the plane E has the shape of a sickle (Hámos 1933). The dispersion $d\lambda/dx_1$ is given by:

$$\frac{d\lambda}{dx_1} = \frac{n}{2d_{hkl}} \times \frac{\lambda^2}{2} \sqrt{1 - \left(\frac{n\lambda}{2d_{hkl}}\right)^2} \quad (\text{C.2})$$

with λ the wavelength of the electromagnetic radiation reflected, n the order of reflection, d_{hkl} the distance of the lattice planes in the crystal and x_1 the position of

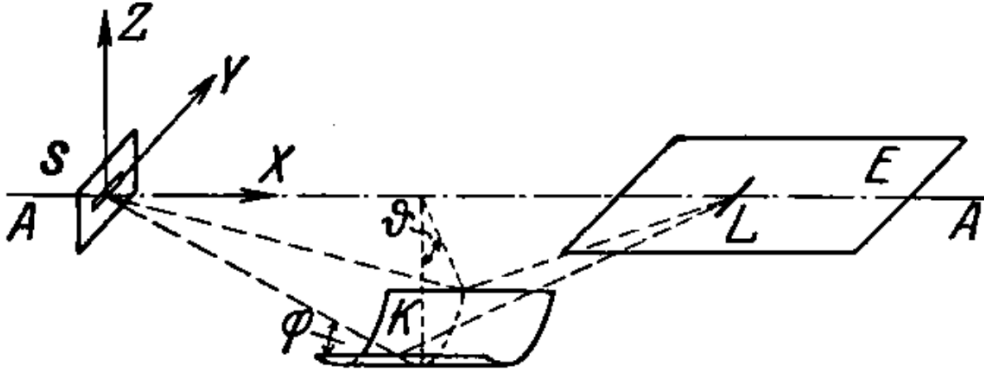


FIGURE C.2: Scheme of the optical path in the von Hámos geometry (Hámos 1934).

a point in x -direction on the image L .

The astigmatic errors are given by (Hámos 1933):

$$\Delta x_1 = 2 \cot \varphi \left(1 + \frac{1}{2 \cot^2 \varphi} \right) \sin^2(\vartheta) y^2 \quad (\text{C.3})$$

$$\Delta y_1 = -2 \sin(\vartheta) y^2 \quad (\text{C.4})$$

where $x = 0$ and y are the coordinates of a point on the slit S , x_1 and y_1 are the coordinates of a point on the image L , φ is the Bragg angle and ϑ is the azimuth.

Therefore, the spectral resolution of this geometry is governed approximately by the product $\sin^2(\vartheta) y^2$ (Hámos 1933):

$$\sin^2(\vartheta) y^2 = \frac{\Delta \lambda}{\left| 1 - \frac{1}{2} \left(\frac{n \lambda}{2d} \right)^2 \right| \lambda} \quad (\text{C.5})$$

The best achievable resolution for 8 keV X-rays is to be found $\Delta E/E \sim 10^{-4}$ (Zastrau et al. 2012).

C.3 XCOT-System

The XCOT-system (X-ray Conversion to Optical radiation and Transport) was developed as a means for the polychromatic imaging of X-ray radiation. The X-ray fluorescence radiation of the ion beam-target interaction region is imaged onto a scintillator using pin-holes or crystals. The scintillator converts the image into the visible light range. This image is transported over several meters using a telescope objective or optical fibres and registered by a combination of image intensifier and sCMOS-camera. The scheme of the complete system is shown in fig.C.3. Each single stage of the complete system is discussed in this section. After the X-ray imaging part of the system using a pinhole camera (see sec. C.4), a scintillator is placed to convert

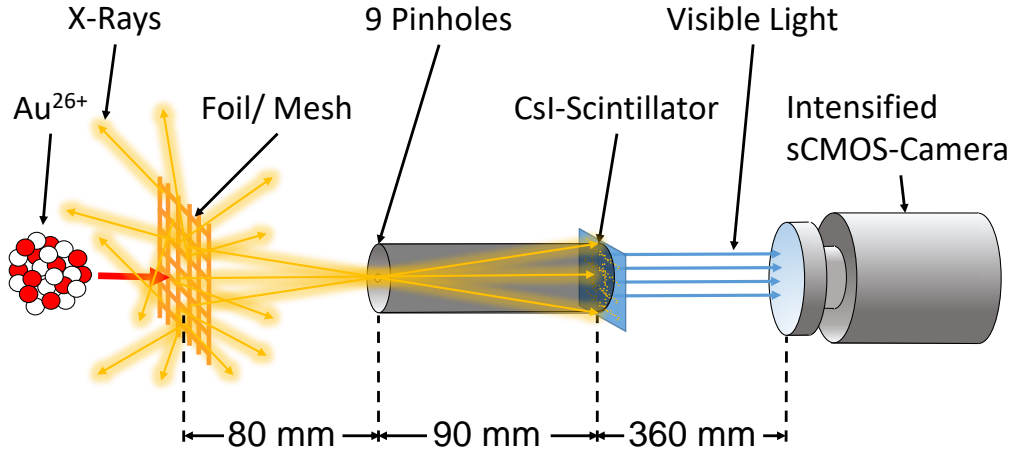


FIGURE C.3: XCOT-scheme.

the X-ray image to a visible one. A $100\ \mu\text{m}$ thick thallium ($[Tl^+]$) doped caesium iodide crystal ($CsI(Tl)$) was chosen. The typical quantum efficiency curve is shown in fig. C.4 for energies below 50 keV and fig. C.5 for energies up to 2 MeV (Collinson and Hill 1963; Gwin and Murray 1963). Fig. C.6 shows typical emission spectra of $CsI(Tl)$ scintillators depending on the concentration of the thallium dopant (Hamada et al. 2001). The maximum of the emitted intensity lies at the 480 nm band for high $[Tl^+]$ densities. The decay time of $CsI(Tl)$ is around 3–4 μs (Valentine et al. 1993).

Following the scintillator, a lens system images the visible image from the backside of the scintillator onto the photo cathode of an image intensifier (Proxiprovision, ProxiKit System, PKS 2584 BZ-V 5N). The parameters of the image intensifier were matched to those of the scintillator placed in front of it and the sCMOS-camera (Andor, Zyla5.5) behind it. As the $CsI(Tl)$ scintillator has a maximum in its emission around 480 nm, the photo cathode which is detecting the incident photons, was required to have a high quantum efficiency at that wavelength. As shown in fig. C.7 and fig. C.8 the maximum of the responsivity and quantum efficiency of the photo cathode is almost at its maximum at 480 nm. The total gain of the image intensifier can be found in fig. C.9. The emission spectrum of the phosphor P43 is shown in fig. C.10.

The last part of the setup of the XCOT-system is a sCMOS-camera. The Zyla 5.5 camera was chosen in accordance with the choice of the P43 scintillator of the image intensifier module as the maximum of the emission spectrum of P43 is around 540 nm and the maximum of the quantum efficiency of the camera lies around 580 nm.

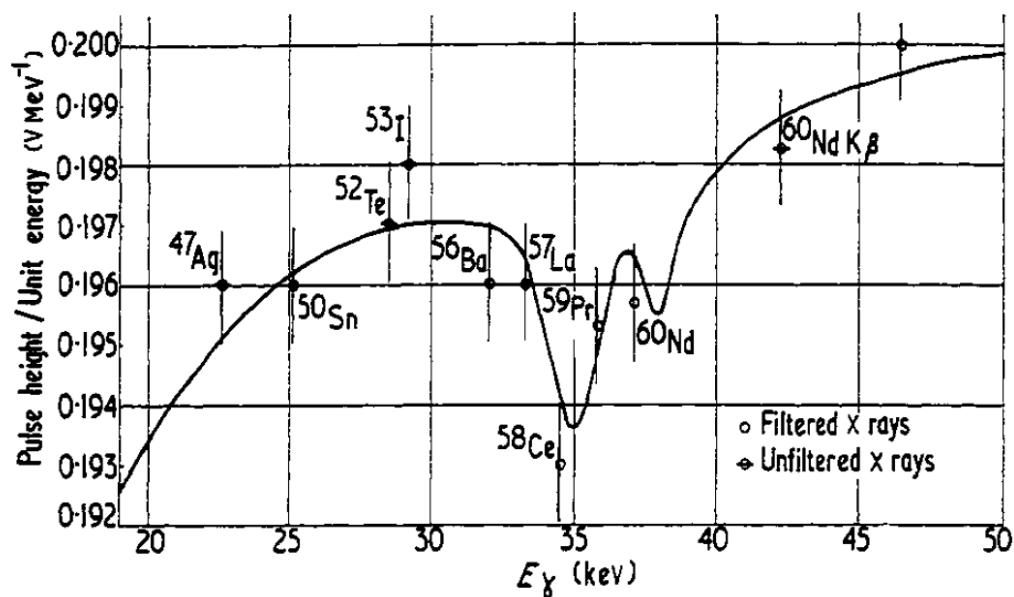


FIGURE C.4: Pulse heights/unit energy for 1 inch \times 1 inch CsI(Tl). Detail in neighborhood of iodine and caesium K-absorption edges. Experimental points and theoretical curve (Collinson and Hill 1963).

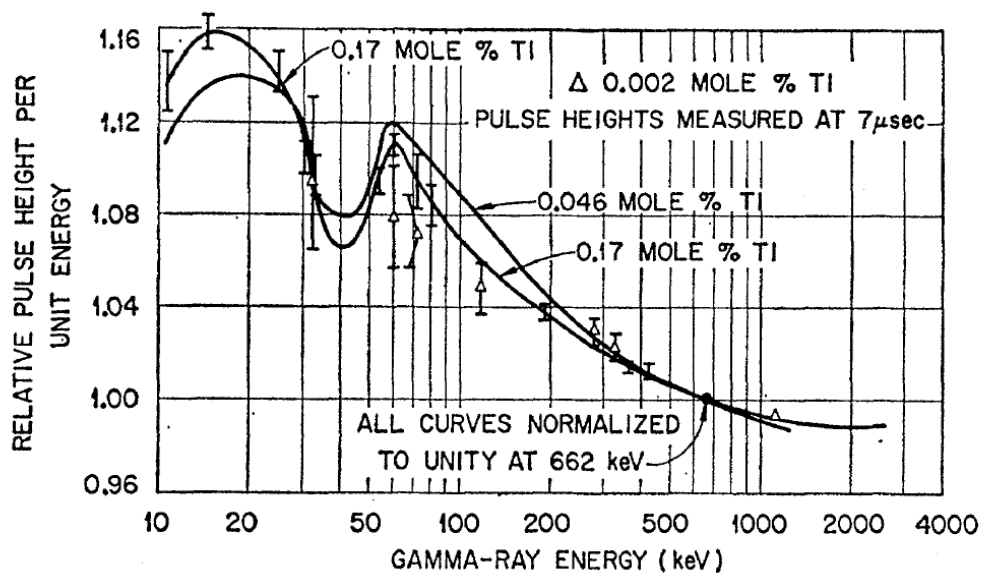


FIGURE C.5: Measured pulse height per unit energy for gamma rays on CsI(Tl) crystals of varying Tl content for a pulse-analysis time of $7\mu\text{s}$. Curves obtained with $1\mu\text{s}$ analysis are very similar. (Gwin and Murray 1963).

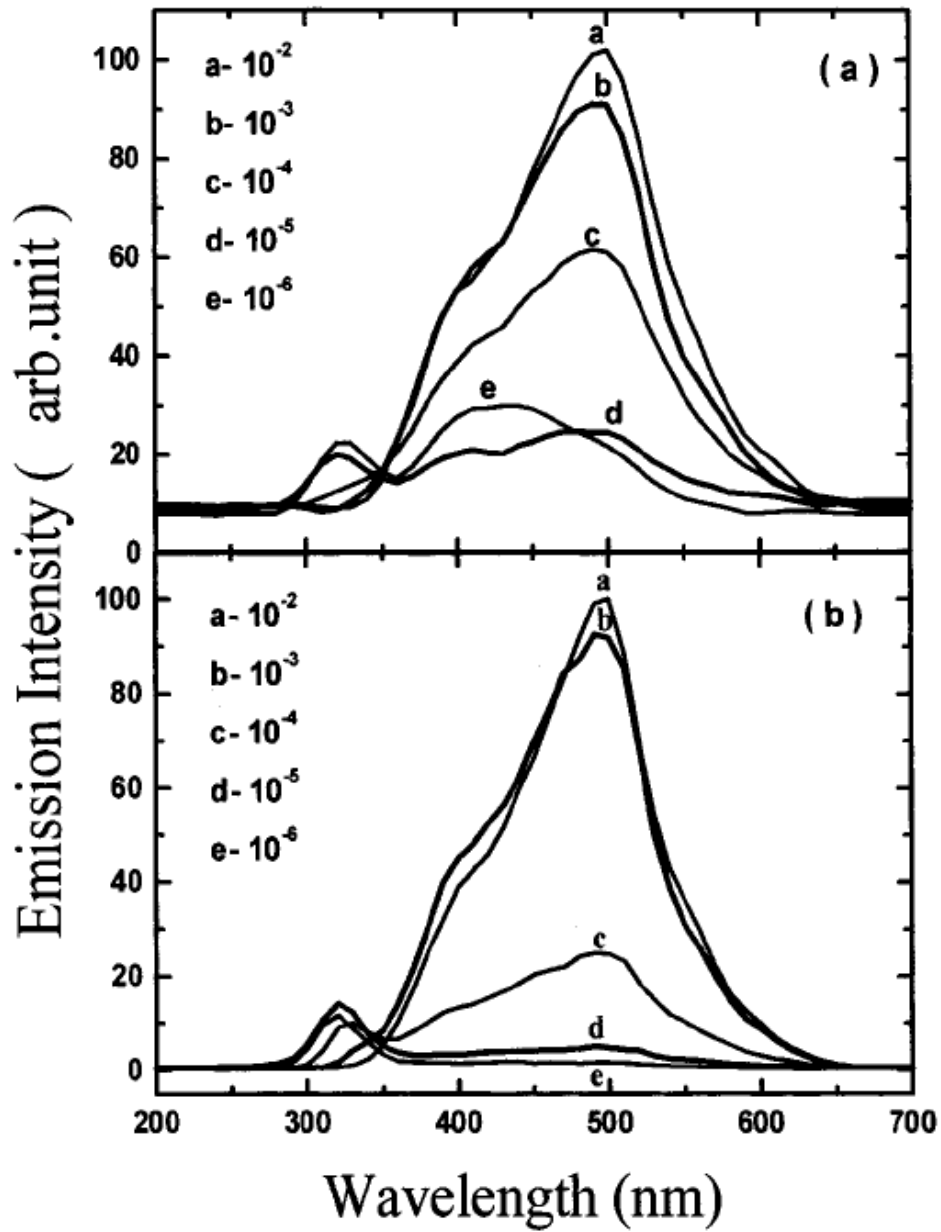


FIGURE C.6: Measured emission spectra of the CsI(Tl) crystal with [Tl⁺] of 10⁻⁶, 10⁻⁴, 10⁻³, and 10⁻² mol under (a) gamma-rays and (b) alpha particles excitations (Hamada et al. 2001).

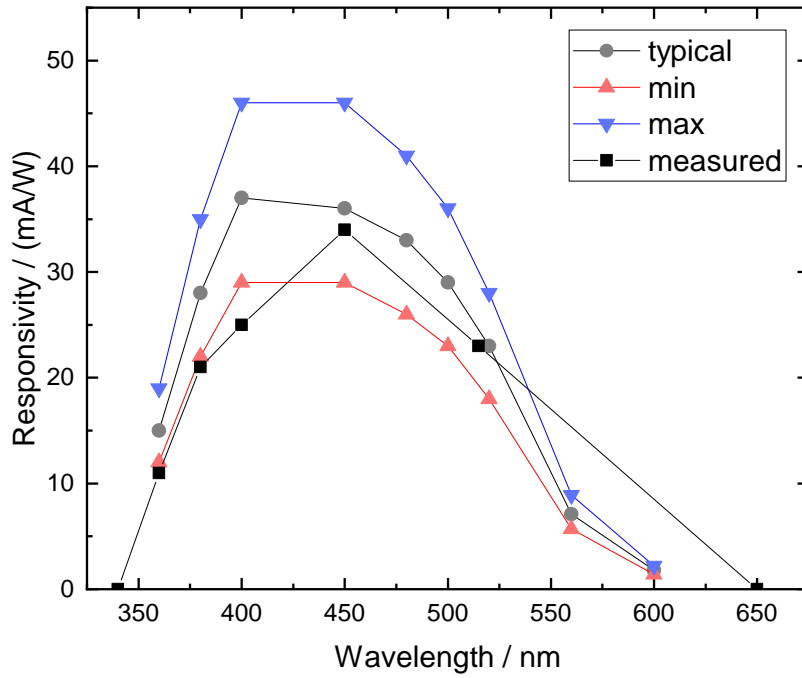


FIGURE C.7: Responsivity of the image intensifier module.

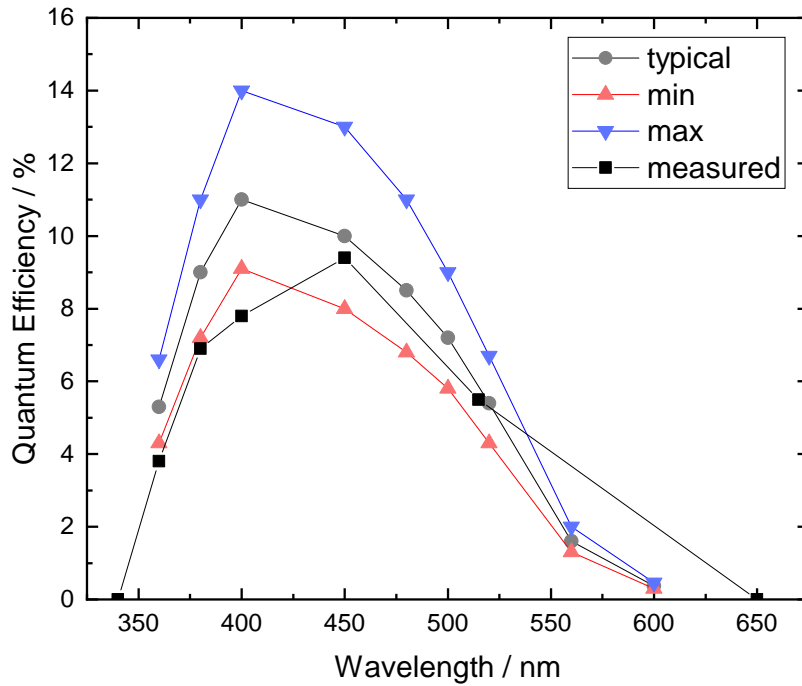


FIGURE C.8: Quantum efficiency of the image intensifier module.

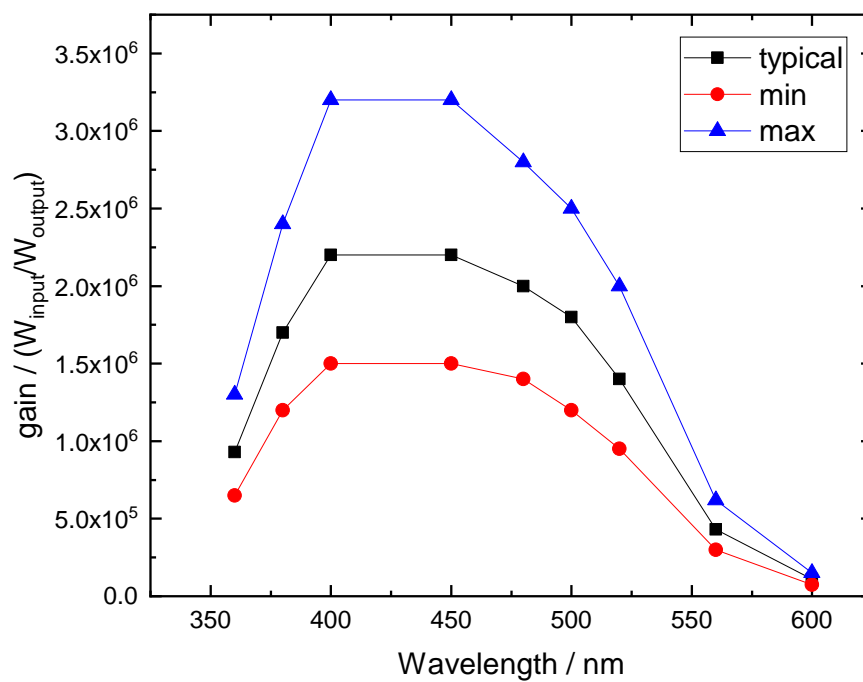


FIGURE C.9: Gain of the image intensifier module.

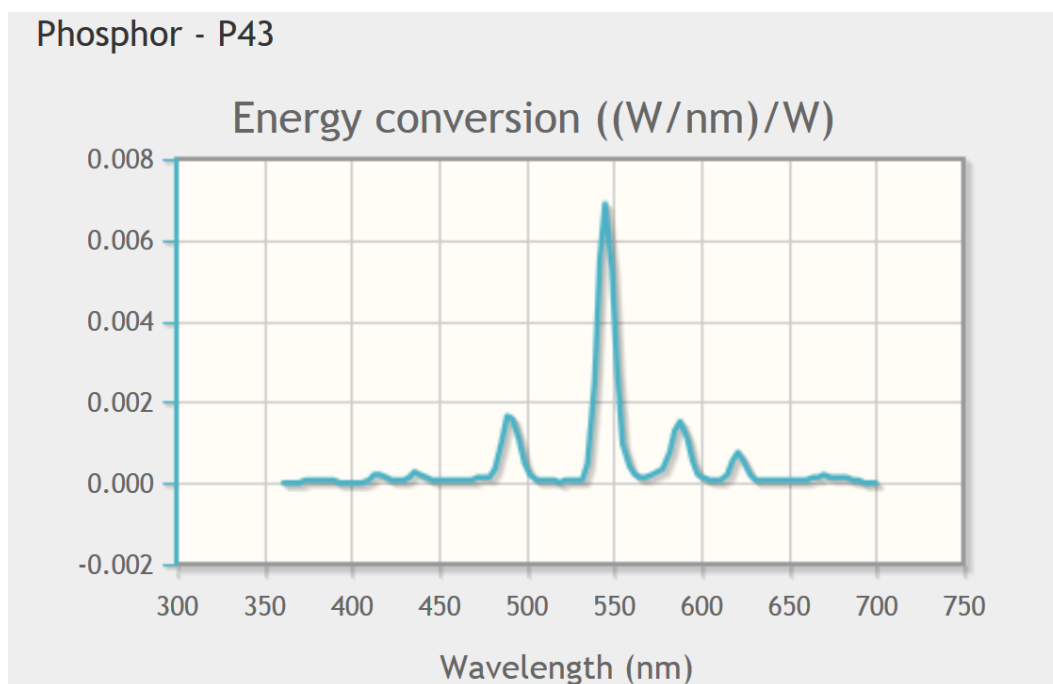


FIGURE C.10: Output spectrum of the image intensifier due to the scintillator P43.

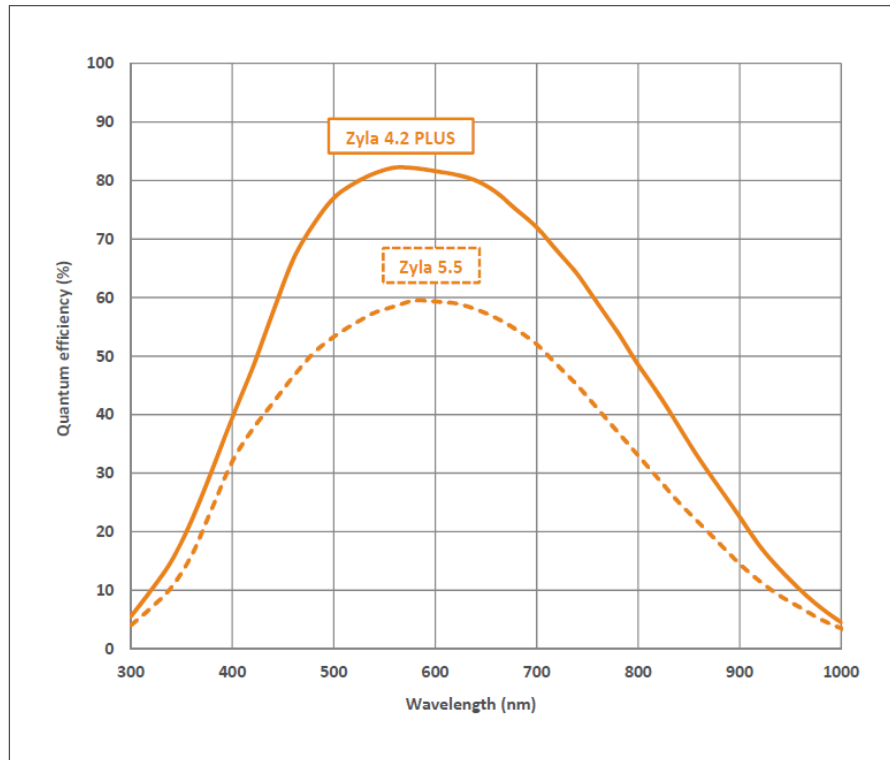


FIGURE C.11: Quantum efficiency of the used sCMOS-camera Zyla 5.5.

C.4 Pinhole Cameras

X-ray pinhole cameras are the simplest kind of X-ray optics possible to design. The pinhole camera consists of only one aperture in front of a spatial resolving detector like an imaging plate, X-ray sensitive film or camera. The imaging properties only depend on the geometry of the setup namely the size of the pinhole and the distances between source, pinhole and detector.

The image of an extended object is a collection of point images, each of which represents approximately the limit of resolution. The image of a point source is taken to be a spot with radius r . The radius of the pinhole is s . For a finite distance p between source and pinhole, we call the image distance q and define the operating focal length of the camera by $1/f = (1/p) + (1/q)$. Additionally, we define the radius g of the geometrical shadow and measure focal lengths in terms of the far-field distance $f' = s^2/\lambda$ (Matt Young 1989). f' could be called the focal length of the pinhole camera. For a small hole ($p, q > s^2/\lambda$), the image size r can be expressed in normalised fashion as $\rho = r/g = 0.61\phi$, where ρ is the image radius in units of g and $\phi = f/f'$ is the focal length in units of s^2/λ . Similarly, in geometrical optics approximation ($p, q \ll s^2/\lambda$), $r = g$, or $\rho = 1$, independent of ϕ . For the case of $\phi > 1$, the resolution limit is the Rayleigh criterion. Therefore, it is generally taken as the radius r . When $\phi \ll 1$, the resolution limit is $1.5g$ in geometrical approximation (Young 1971). Spatial resolutions of $2\mu\text{m}$ are a practical limit for pinhole images

(Förster et al. 1987). The choice of the pinhole size is not only governed by the achievable spatial resolution but often also by the photon yield necessary to obtain an image.

The focal length is $f' = 10.3 \text{ m} = 10.3 \times 10^6 \mu\text{m}$ for Cu K_α at around 8 keV and $s = 40 \mu\text{m}$. As a distance of $p = 10 \text{ cm}$ is shorter than f' , such a setup would be in the geometrical optics regime. The theoretical resolution limit for an image with magnification $M = q/p = 1$ would be $1.5g = 120 \mu\text{m}$ in that case.

A much more elegant technique for X-ray microscopy, which is also much more expensive than the pinhole system, is the Bragg-reflection microscope.

C.5 X-Ray Crystal Microscope

Monochromatic X-ray imaging can be performed using toroidally bent crystals as X-ray microscope. The X-ray microscope favourably combines both the high spectral resolution of a spectrograph and the spatial one of a pinhole camera (Förster et al. 1987). It is therefore possible to get a magnified image of the emission region of a selected spectral line or of a small continuum range. The use of Bragg reflections of two-dimensionally bent crystals enables the X-ray microscopical imaging in narrow spectral ranges ($\Delta\lambda/\lambda = 10^{-4}$ to 10^{-2}) with wavelengths $0.1 \text{ nm} < \lambda < 2.6 \text{ nm}$ (Förster et al. 1987).

A perfect point-to-point focusing is achieved by a crystal with ellipsoidally bent lattice planes, and the source as well as the image located in the two foci (Van Langevelde et al. 1990; Löttsch 2012). A toroidally bent geometry is chosen for the crystal as the theoretically perfect shape is technically not achievable (Berreman 1955). Fig. C.12 shows the principle of X-ray imaging and spectroscopy with toroidally bent crystals. As the crystal has two curvatures with bending radii R_h in the horizontal (meridional) and R_v in the vertical (sagittal) direction it has two related focal distances f_h and f_v , according to

$$f_h = \frac{(R_h \sin \Theta_B)}{2} \quad (\text{C.6})$$

$$f_v = \frac{R_v}{(2 \sin \Theta_B)} \quad (\text{C.7})$$

with Θ_B the Bragg angle of the reflection under consideration. The bending radii can be chosen in such a way that the focal distances are equal for a given wavelength and reflection. In that case

$$\frac{R_v}{R_h} = \sin^2 \Theta_B \quad (\text{C.8})$$

has to be fulfilled to have a point-to-point focussing. Magnification of the imaged source can be achieved ($k = l_a/l_b = 1$, Rowland circle geometry, or $k \neq 1$). For the case of $f_h \neq f_v$, the crystal can be used as a spectrometer with one dimensional

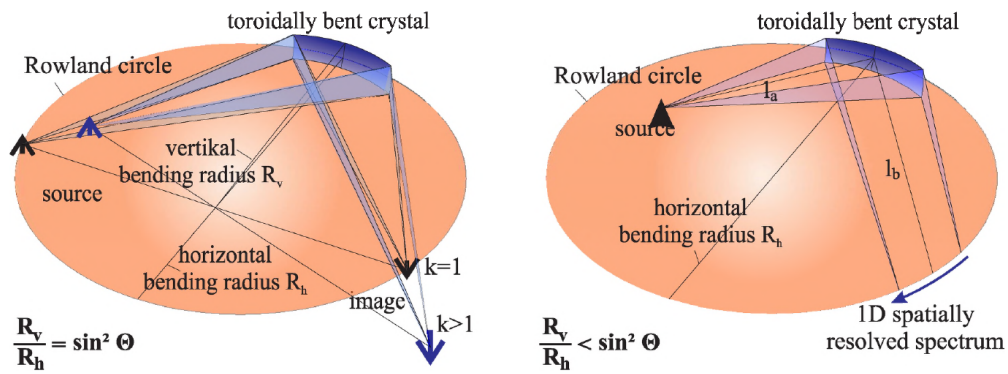


FIGURE C.12: X-ray optics with toroidally bent crystals. a) Imaging with source and image on the Rowland circle ($k > 1$). b) Spectroscopy with one dimensional spatial resolution. The source lies inside and the spectrum on the circle (Löttsch 2012).

imaging resolution. Then the distance l_a from the source to the crystal has to be chosen according to $1/l_a + 1/l_b = 1/l_v$, where l_b is the distance between the crystal and the detector which is given by $l_b = R_h \sin \Theta_B$.

Bibliography

- Amptek Inc., ed. (Jan. 8, 2020). *XR-100CdTe X-Ray & Gamma Ray Detector*. URL: <https://www.amptek.com/products/cdte-x-ray-and-gamma-ray-detectors/xr-100cdte-x-ray-and-gamma-ray-detector#Documentation>.
- Andreev, N E, S V Kuznetsov, et al. (2010). “Laser wakefield acceleration of super-short electron bunches in guiding structures”. In: *Plasma Physics and Controlled Fusion* 53.1, p. 014001.
- Andreev, N E, L P Pugachev, et al. (2016). “Electron acceleration at grazing incidence of a subpicosecond intense laser pulse onto a plane solid target”. In: *Laser and Particle Beams* 34.1, pp. 115–122.
- Appel, S., O. Boine-Frankenheim, and O. Geithner, eds. (Dec. 9, 2019). *Reference Beam Parameters of the International Facility for Antiproton and Ion Research FAIR*. URL: https://www.gsi.de/fileadmin/Beschleunigerbetrieb/FAIR_DesignStrahlParameter_2019.pdf.
- Arefiev, A V et al. (2016). “Beyond the ponderomotive limit: Direct laser acceleration of relativistic electrons in sub-critical plasmas”. In: *Physics of Plasmas* 23.5, p. 056704.
- Arkadiev, V A et al. (2007). “X-ray analysis with a highly oriented pyrolytic graphite-based von Hamos spectrometer”. In: *Spectrochimica Acta Part B: Atomic Spectroscopy* 62.6-7, pp. 577–585.
- Awaya, Y, T Kambara, and Y Kanai (1999). “Multiple K-and L-shell ionizations of target atoms by collisions with high-energy heavy ions”. In: *International journal of mass spectrometry* 192.1-3, pp. 49–63.
- Bagnoud, V. et al. (2017). *Plasma Physics at FAIR*. Ed. by V. Bagnoud.
- Bagnoud, Vincent (2020). *Private Communication*.
- Bagnoud, Vincent et al. (2010). “Commissioning and early experiments of the PHELIX facility”. In: *Applied Physics B* 100.1, pp. 137–150.
- Baron, Eric (1972). “Heavy Ion Stripping by Solid Foils between 1 and 6 MeV/Nucleon”. In: *IEEE transactions on Nuclear Science* 19.2, pp. 256–262.
- Bauer, D, P Mulser, and W-H Steeb (1995). “Relativistic ponderomotive force, uphill acceleration, and transition to chaos”. In: *Physical review letters* 75.25, p. 4622.
- Becker, F et al. (2006). “Design, development, and testing of non-intercepting profile diagnostics for intense heavy ion beams using a capacitive pickup and beam induced gas fluorescence monitors”. In: *Laser and Particle Beams* 24.4, pp. 541–551.

- Beckhoff, Burkhard et al. (2007). *Handbook of practical X-ray fluorescence analysis*. Springer Science & Business Media.
- Belousov, Anton (Nov. 25, 2014). “Radiation effects on semiconductor devices in high energy heavy ion accelerators”. PhD Thesis. Technical University Darmstadt.
- Berger, M J et al. (1993). “6. Energy-loss Straggling”. In: *Reports of the International Commission on Radiation Units and Measurements 2*, pp. 61–68.
- Berreman, Dwight W (1955). “Single Quartz Crystal Point Focusing X-Ray Monochromator”. In: *Review of Scientific Instruments* 26.11, pp. 1048–1052.
- Bethe, Hans (1930). “Zur theorie des durchgangs schneller korpuskularstrahlen durch materie”. In: *Annalen der Physik* 397.3, pp. 325–400.
- (1932). “Bremsformel für elektronen relativistischer geschwindigkeit”. In: *Zeitschrift für Physik* 76.5-6, pp. 293–299.
- Beyer, Heinrich F and Viatcheslav P Shevelko (2016). *Introduction to the physics of highly charged ions*. CRC Press.
- Bin, J H et al. (2015). “Ion acceleration using relativistic pulse shaping in near-critical-density plasmas”. In: *Physical review letters* 115.6, p. 064801.
- Bochkarev, S G et al. (2014). “Stochastic electron acceleration in plasma waves driven by a high-power subpicosecond laser pulse”. In: *Plasma Physics Reports* 40.3, pp. 202–214.
- Bonnet, T, M Comet, D Denis-Petit, F Gobet, F Hannachi, M Tarisien, M Versteegen, and M M Aleonard (2013). “Response functions of Fuji imaging plates to monoenergetic protons in the energy range 0.6–3.2 MeV”. In: *Review of Scientific Instruments* 84.1, p. 013508.
- Bonnet, T, M Comet, D Denis-Petit, F Gobet, F Hannachi, M Tarisien, M Versteegen, and M M Aléonard (2013). “Response functions of imaging plates to photons, electrons and ^4He particles”. In: *Review of Scientific Instruments* 84.10, p. 103510.
- Borghesi, M, A J MacKinnon, et al. (1997). “Relativistic channeling of a picosecond laser pulse in a near-critical preformed plasma”. In: *Physical review letters* 78.5, p. 879.
- Borghesi, M, AJ Mackinnon, et al. (1998). “Large quasistatic magnetic fields generated by a relativistically intense laser pulse propagating in a preionized plasma”. In: *Physical review letters* 80.23, p. 5137.
- Borisenko, N G, I V Akimova, et al. (2006). “Regular 3-D networks with clusters for controlled energy transport studies in laser plasma near critical density”. In: *Fusion science and technology* 49.4, pp. 676–685.
- Borisenko, N G, A M Khalenkov, et al. (2007). “Plastic aerogel targets and optical transparency of undercritical microheterogeneous plasma”. In: *Fusion science and technology* 51.4, pp. 655–664.
- Borisov, A B et al. (1992). “Observation of relativistic and charge-displacement self-channeling of intense subpicosecond ultraviolet (248 nm) radiation in plasmas”. In: *Physical review letters* 68.15, p. 2309.

- Boutoux, G et al. (2015). “Study of imaging plate detector sensitivity to 5-18 MeV electrons”. In: *Review of Scientific Instruments* 86.11, p. 113304.
- Breit, G (1967). “Virtual coulomb excitation in nucleon transfer”. In: *Proceedings of the National Academy of Sciences of the United States of America* 57.4, p. 849.
- Briand, J P et al. (1990). “Observation and measurement of $n = 2 \rightarrow n = 1$ transitions of hydrogenlike and heliumlike uranium”. In: *Physical review letters* 65.22, p. 2761.
- Brunel, F (1987). “Not-so-resonant, resonant absorption”. In: *Physical Review Letters* 59.1, p. 52.
- Chen, Francis F et al. (1984). *Introduction to plasma physics and controlled fusion*. Vol. 1. Springer.
- Chen, Hui et al. (2008). “Absolute calibration of image plates for electrons at energy between 100 keV and 4 MeV”. In: *Review of Scientific Instruments* 79.3, p. 033301.
- Cole, J M et al. (2015). “Laser-wakefield accelerators as hard x-ray sources for 3D medical imaging of human bone”. In: *Scientific reports* 5, p. 13244.
- Collinson, A J L and R Hill (1963). “The fluorescent response of NaI (Tl) and CsI (Tl) to X rays and γ rays”. In: *Proceedings of the Physical Society* 81.5, p. 883.
- Creagh, D C and J H Hubbell (1987). “Problems associated with the measurement of X-ray attenuation coefficients. I. Silicon. Report of the International Union of Crystallography X-ray Attenuation Project”. In: *Acta Crystallographica Section A: Foundations of Crystallography* 43.1, pp. 102–112.
- Danson, Colin N et al. (2019). “Petawatt and exawatt class lasers worldwide”. In: *High Power Laser Science and Engineering* 7.
- Davies, Jonathan R (2008). “Laser absorption by overdense plasmas in the relativistic regime”. In: *Plasma Physics and Controlled Fusion* 51.1, p. 014006.
- Deiev, O S et al. (2019). “Bremsstrahlung of electrons and yield of neutrons from thick converters, passing of γ -radiation and neutrons through biological shielding”. In: *Problems of Atomic Science and Technology. Series “Nuclear Physics Investigations* 3, pp. 65–73.
- Dendy, Richard O (1995). *Plasma physics: an introductory course*. Cambridge University Press.
- Desai, Nikunj, Abhinav Singh, and Daniel J Valentino (2010). “Practical evaluation of image quality in computed radiographic (CR) imaging systems”. In: *Medical Imaging 2010: Physics of Medical Imaging*. Vol. 7622. International Society for Optics and Photonics, 76224Q.
- Doria, D et al. (2015). “Calibration of BAS-TR image plate response to high energy (3-300 MeV) carbon ions”. In: *Review of Scientific Instruments* 86.12, p. 123302.
- Eichler, Jörg (1977). “Magnus approximation for K-shell ionization by heavy-ion impact”. In: *Physical Review A* 15.5, p. 1856.
- El Houssaini, Mohamed (Dec. 4, 2017). “Untersuchung emittierter Röntgenfluoreszenzstrahlung bei der Wechselwirkung von Goldionen mit verschiedenen Festkörpertargets”. Master Thesis. Goethe University Frankfurt.

- Esarey, Eric, C B Schroeder, and W P Leemans (2009). “Physics of laser-driven plasma-based electron accelerators”. In: *Reviews of modern physics* 81.3, p. 1229.
- Faik, Steffen et al. (2014). “Creation of a homogeneous plasma column by means of hohlraum radiation for ion-stopping measurements”. In: *High energy density physics* 10, pp. 47–55.
- Faure, Jérôme et al. (2004). “A laser–plasma accelerator producing monoenergetic electron beams”. In: *Nature* 431.7008, p. 541.
- Forslund, D W, J M Kindel, and K Lee (1977). “Theory of hot-electron spectra at high laser intensity”. In: *Physical Review Letters* 39.5, p. 284.
- Förster, E et al. (1987). “Investigation of X-ray Emission from Plasmas Created by NIXE 6-nsec Nd: Glass Laser System”. In: *Annalen der Physik* 499.1, pp. 61–73.
- Foster, C et al. (1976). “An estimate of direct Coulomb K-shell vacancy production in heavy ion-atom collisions”. In: *Journal of Physics B: Atomic and Molecular Physics* 9.11, p. 1943.
- Fourmaux, S et al. (2011). “Single shot phase contrast imaging using laser-produced Betatron x-ray beams”. In: *Optics letters* 36.13, pp. 2426–2428.
- Freeman, R R, P H Bucksbaum, and T J McIlrath (1988). “The ponderomotive potential of high intensity light and its role in the multiphoton ionization of atoms”. In: *IEEE journal of quantum electronics* 24.7, pp. 1461–1469.
- Gesell, Daniel (2018). “Entwicklung und experimentelle Erprobung der Komponenten des XCOT-Systems zur Umwandlung & Transport von Röntgenstrahlung in sichtbares Licht für Diagnostiken an FAIR”. Bachelor Thesis. Goethe University Frankfurt.
- Gibbon, Paul (2004). *Short pulse laser interactions with matter*. World Scientific Publishing Company Singapore.
- Golubev, A A and V B Mintsev (2012). “Study of the fundamental properties of matter at high energy density created by an intense ion beam”. In: *Atomic Energy* 112.2, pp. 147–155.
- Gordienko, S and A Pukhov (2005). “Scalings for ultrarelativistic laser plasmas and quasimonoenergetic electrons”. In: *Physics of Plasmas* 12.4, p. 043109.
- Gould, Harvey et al. (1984). “Electron Capture by U^{91+} and U^{92+} and Ionization of U^{90+} and U^{91+} ”. In: *Physical Review Letters* 52.3, p. 180.
- Gray, R J et al. (2014). “Laser pulse propagation and enhanced energy coupling to fast electrons in dense plasma gradients”. In: *New Journal of Physics* 16.11, p. 113075.
- Greiner, Walter (2011). *Quantum mechanics: an introduction*. Springer Science & Business Media.
- Gryaznykh, D A, Ya Z Kandiev, and V A Lykov (1998). “Estimates of electron-positron pair production in the interaction of high-power laser radiation with high-Z targets”. In: *Journal of Experimental and Theoretical Physics Letters* 67.4, pp. 257–262.

- GSI Helmholtz Centre for Heavy-Ion Research GmbH, ed. (May 29, 2018). *PHE-LIX Lasersystem*. URL: <https://www.gsi.de/work/forschung/appamml/plasmaphysikphelix/phelix.htm>.
- ed. (Dec. 8, 2019a). *HED at FAIR*. URL: https://www.gsi.de/en/work/research/appamml/plasma_physicsphelix/hed_at_fair.htm.
- ed. (Dec. 6, 2019b). *The "Machine"*. URL: https://www.gsi.de/en/research%20accelerators/fair/the_machine.htm.
- ed. (Dec. 8, 2019c). *Z6 – a unique facility offering ion and laser beams for combined experiments*. URL: https://www.gsi.de/work/forschung/appamml/plasmaphysikphelix/anlagen_in_der_experimenthalle_z6.htm.
- ed. (Feb. 11, 2020). *Nominal Beam Parameter for Operation 2021-2022*. URL: https://www.gsi.de/en/work/accelerator_operations/operation.htm?C=1.
- Günther, Marc (2011). “Investigation of Laser Interaction with Nano-/Micro-Structures for Ion Acceleration, Intense X-Ray Production & High Energy Density Generation”. PhD Thesis. Technical University Darmstadt.
- Gus’kov, S Yu et al. (2011). “Laser-supported ionization wave in under-dense gases and foams”. In: *Physics of plasmas* 18.10, p. 103114.
- Gwin, R and R B Murray (1963). “Scintillation process in CsI (Tl). I. Comparison with activator saturation model”. In: *Physical Review* 131.2, p. 501.
- Gyrdymov, Mikhail (May 20, 2019). “Charakterisierung und Optimierung einer sCMOS-Kamera mit Verstärker zur Diagnostik der Ionenstrahlintensitätsverteilung für Experimente während Phase-0 und an FAIR”. Bachelor Thesis. Goethe University Frankfurt.
- Hamada, Margarida M et al. (2001). “Dependence of scintillation characteristics in the CsI (Tl) crystal on Tl/sup+/concentrations under electron and alpha particles excitations”. In: *IEEE Transactions on Nuclear Science* 48.4, pp. 1148–1153.
- Hámos, L von (1932). “Röntgenspektroskopie und Abbildung mittels gekrümmter Kristallreflektoren”. In: *Naturwissenschaften* 20.38, pp. 705–706.
- (1933). “Röntgenspektroskopie und Abbildung mittels gekrümmter Kristallreflektoren. I. Geometrisch-optische Betrachtungen”. In: *Annalen der Physik* 409.6, pp. 716–724.
- (1934). “Röntgenspektroskopie und Abbildung mittels gekrümmter Kristallreflektoren II. Beschreibung eines fokussierenden Spektrographen mit punktgetreuer Spaltabbildung”. In: *Annalen der Physik* 411.3, pp. 252–260.
- Haug, Eberhard and Werner Nakel (2004). *The elementary process of bremsstrahlung*. Vol. 73. World Scientific.
- Hoffmann, D H H et al. (2002). “Unique capabilities of an intense heavy ion beam as a tool for equation-of-state studies”. In: *Physics of Plasmas* 9.9, pp. 3651–3654.
- Horst, Felix et al. (2015). “A TLD-based ten channel system for the spectrometry of bremsstrahlung generated by laser-matter interaction”. In: *Nuclear Instruments*

- and Methods in Physics Research Section A: Accelerators, Spectrometers, Detectors and Associated Equipment* 782, pp. 69–76.
- Huang, Meirong et al. (2019). “Nuclear Astrophysics with Lasers”. In: *Nuclear Physics News* 29.3, pp. 9–13.
- Jackson, John David (1999). “Classical Electrodynamics 3rd ed John Wiley & Sons”. In: *Inc., New York, NY*.
- Jenkins, Ron (2012). *X-ray fluorescence spectrometry*. Vol. 265. John Wiley & Sons.
- Joe, Harry and Rong Zhu (2005). “Generalized Poisson distribution: the property of mixture of Poisson and comparison with negative binomial distribution”. In: *Biometrical Journal: Journal of Mathematical Methods in Biosciences* 47.2, pp. 219–229.
- Ju, J et al. (2014). “Analysis of x-ray emission and electron dynamics in a capillary-guided laser wakefield accelerator”. In: *Physical Review Special Topics-Accelerators and Beams* 17.5, p. 051302.
- Kadhane, Umesh, C C Montanari, and Lokesh C Tribedi (2003). “K-shell processes in heavy-ion collisions in solids and the local plasma approximation”. In: *Physical Review A* 67.3, p. 032703.
- Kaluza, Malte (n.d.). *High Intensity Physics. lecture notes*. FSU Jena.
- Kaluza, Malte Christoph (June 14, 2004). “Characterisation of Laser-Accelerated Proton Beams”. PhD Thesis. Technical University Munich.
- Keldysh, L V et al. (1965). “Ionization in the field of a strong electromagnetic wave”. In: *Sov. Phys. JETP* 20.5, pp. 1307–1314.
- Key, M H et al. (1998). “Hot electron production and heating by hot electrons in fast ignitor research”. In: *Physics of plasmas* 5.5, pp. 1966–1972.
- Khaghani, Dimitri (Nov. 25, 2016). “Investigation of Laser Interaction with Nano-/Micro-Structures for Ion Acceleration, Intense X-Ray Production & High Energy Density Generation”. PhD Thesis. Goethe University Frankfurt.
- Khalenkov, A M et al. (2006). “Experience of micro-heterogeneous target fabrication to study energy transport in plasma near critical density”. In: *Laser and Particle Beams* 24.2, pp. 283–290.
- Khudik, Vladimir et al. (2016). “Universal scalings for laser acceleration of electrons in ion channels”. In: *Physics of Plasmas* 23.10, p. 103108.
- Kluge, T et al. (2011). “Electron temperature scaling in laser interaction with solids”. In: *Physical review letters* 107.20, p. 205003.
- Krause, Manfred Otto (1979). “Atomic radiative and radiationless yields for K and L shells”. In: *Journal of physical and chemical reference data* 8.2, pp. 307–327.
- Lang, R et al. (2014). *Radiation protection update for the FAIR APPA building*. Research rep. GSI Helmholtz Centre for Heavy-Ion Research GmbH.
- Langdon, A Bruce (1980). “Nonlinear inverse bremsstrahlung and heated-electron distributions”. In: *Physical Review Letters* 44.9, p. 575.
- Le Pape, Sebastien et al. (2010). “X-ray radiography and scattering diagnosis of dense shock-compressed matter”. In: *Physics of Plasmas* 17.5, p. 056309.

- Leemans, W P et al. (2014). “Multi-GeV electron beams from capillary-discharge-guided subpetawatt laser pulses in the self-trapping regime”. In: *Physical review letters* 113.24, p. 245002.
- Legall, H et al. (2006). “High spectral resolution x-ray optics with highly oriented pyrolytic graphite”. In: *Optics express* 14.10, pp. 4570–4576.
- Leon, A et al. (1998). “Charge state distributions of swift heavy ions behind various solid targets ($36 \leq Z_p \leq 92$, $18 \text{ MeV/u} \leq E \leq 44 \text{ MeV/u}$)”. In: *Atomic Data and Nuclear Data Tables* 69.2, pp. 217–238.
- Li, K et al. (2014). “Developments toward hard X-ray radiography on heavy-ion heated dense plasmas”. In: *Laser and particle beams* 32.4, pp. 631–637.
- Lötzsch, Robert (Nov. 8, 2012). “Bent crystal X-ray optics for the diagnosis and applications of laser-produced plasmas”. PhD thesis. Friedrich Schiller University Jena.
- Ma, X et al. (2001). “State-selective electron capture into He-like U^{90+} ions in collisions with gaseous targets”. In: *Physical Review A* 64.1, p. 012704.
- Ma, Zhi Guo et al. (2019). “Photonuclear production of medical isotopes 62 , ^{64}Cu using intense laser-plasma electron source”. In: *Matter and Radiation at Extremes* 4.6, p. 064401.
- Maddox, B R et al. (2011). “High-energy x-ray backlighter spectrum measurements using calibrated image plates”. In: *Review of Scientific Instruments* 82.2, p. 023111.
- Major, Zsuzsanna et al. (2019). *A High-Energy Laser Beamline for plasma physics experiments – from PHELIX to the HHT-cave at GSI*. Research rep. GSI Helmholtz Centre for Heavy-Ion Research GmbH.
- Malka, G et al. (1997). “Suprathermal electron generation and channel formation by an ultrarelativistic laser pulse in an underdense preformed plasma”. In: *Physical review letters* 79.11, p. 2053.
- Max, Claire Ellen, Jonathan Arons, and A Bruce Langdon (1974). “Self-modulation and self-focusing of electromagnetic waves in plasmas”. In: *Physical Review Letters* 33.4, p. 209.
- Meadowcroft, A L, C D Bentley, and E N Stott (2008). “Evaluation of the sensitivity and fading characteristics of an image plate system for x-ray diagnostics”. In: *Review of Scientific Instruments* 79.11, p. 113102.
- Meyerhof, W E and Knud Taulbjerg (1977). “K-shell ionization in heavy-ion collisions”. In: *Annual Review of Nuclear Science* 27.1, pp. 279–332.
- Mintsev, V et al. (2016). “Non-Ideal Plasma and Early Experiments at FAIR: HIHEX-Heavy Ion Heating and EXpansion”. In: *Contributions to Plasma Physics* 56.3-4, pp. 281–285.
- Morace, A et al. (2014). “Development of x-ray radiography for high energy density physics”. In: *Physics of Plasmas* 21.10, p. 102712.
- Moseley, Henry Gwyn Jeffreys (1913). “XCIII. The high-frequency spectra of the elements”. In: *The London, Edinburgh, and Dublin Philosophical Magazine and Journal of Science* 26.156, pp. 1024–1034.

- Mourou, Gerard A, Toshiki Tajima, and Sergei V Bulanov (2006). “Optics in the relativistic regime”. In: *Reviews of modern physics* 78.2, p. 309.
- Mulser, P, S M Weng, and Tatyana Liseykina (2012). “Analysis of the Brunel model and resulting hot electron spectra”. In: *Physics of Plasmas* 19.4, p. 043301.
- Mulser, Peter and Dieter Bauer (2010). *High power laser-matter interaction*. Vol. 238. Springer.
- Nicolai, Ph et al. (2012). “Experimental evidence of foam homogenization”. In: *Physics of Plasmas* 19.11, p. 113105.
- Nolen, Jerry A and Felix Marti (2013). “Charge strippers of heavy ions for high intensity accelerators”. In: *Reviews of Accelerator Science and Technology* 6, pp. 221–236.
- Nuclear Data Services (Nov. 28, 2019). *Electronic Stopping Power of Matter for Ions*. Ed. by International Atomic Energy Agency. URL: https://www-nds.iaea.org/stopping/stopping_heav.html.
- Ohuchi, H and A Yamadera (2002). “Dependence of fading patterns of photo-stimulated luminescence from imaging plates on radiation, energy, and image reader”. In: *Nuclear Instruments and Methods in Physics Research Section A: Accelerators, Spectrometers, Detectors and Associated Equipment* 490.3, pp. 573–582.
- Physical Measurement Laboratory (Aug. 2, 2019a). *ESTAR: Stopping Powers and Ranges for Electrons*. Ed. by National Institute of Standards and Technology. URL: <https://physics.nist.gov/PhysRefData/Star/Text/method.html>.
- (Aug. 2, 2019b). *PSTAR and ASTAR Databases for Protons and Helium Ions*. Ed. by National Institute of Standards and Technology. URL: <https://physics.nist.gov/PhysRefData/Star/Text/appendix.html>.
- Pratt, R H et al. (1977). “Bremsstrahlung energy spectra from electrons of kinetic energy $1 \text{ keV} \leq T_1 \leq 2000 \text{ keV}$ incident on neutral atoms $2 \leq Z \leq 92$ ”. In: *Atomic Data and Nuclear Data Tables* 20.2, pp. 175–209.
- Protopapas, M, Christoph H Keitel, and Peter L Knight (1997). “Atomic physics with super-high intensity lasers”. In: *Reports on Progress in Physics* 60.4, p. 389.
- Pugachev, L P and N E Andreev (2019). “Characterization of accelerated electrons generated in foams under the action of petawatt lasers”. In: *Journal of Physics: Conference Series*. Vol. 1147. 1. IOP Publishing, p. 012080.
- Pugachev, L P, N E Andreev, et al. (2016). “Acceleration of electrons under the action of petawatt-class laser pulses onto foam targets”. In: *Nuclear Instruments and Methods in Physics Research Section A: Accelerators, Spectrometers, Detectors and Associated Equipment* 829, pp. 88–93.
- Pugacheva, Darya Valer’evna and Nikolai Evgen’evich Andreev (2018). “Effect of synchrotron radiation on the dynamics of electron spin precession in the process of laser-plasma acceleration”. In: *Quantum Electronics* 48.4, p. 291.
- Pukhov, A and J Meyer-ter-Vehn (1996). “Relativistic magnetic self-channeling of light in near-critical plasma: three-dimensional particle-in-cell simulation”. In: *Physical review letters* 76.21, p. 3975.

- (1997). “Laser hole boring into overdense plasma and relativistic electron currents for fast ignition of ICF targets”. In: *Physical review letters* 79.14, p. 2686.
- (1998). “Relativistic laser-plasma interaction by multi-dimensional particle-in-cell simulations”. In: *Physics of Plasmas* 5.5, pp. 1880–1886.
- Pukhov, A, Z-M Sheng, and J Meyer-ter-Vehn (1999). “Particle acceleration in relativistic laser channels”. In: *Physics of Plasmas* 6.7, pp. 2847–2854.
- Pukhov, Alexander (2003). “Strong field interaction of laser radiation”. In: *Reports on progress in Physics* 66.1, p. 47.
- (2019). *Private Communication*.
- Randall, R R et al. (1976). “Experimental impact-parameter-dependent probabilities for K-shell vacancy production by fast heavy-ion projectiles”. In: *Physical Review A* 13.1, p. 204.
- Ravasio, A et al. (2008). “Hard x-ray radiography for density measurement in shock compressed matter”. In: *Physics of Plasmas* 15.6, p. 060701.
- Redus, Bob (May 25, 2010). *Efficiency and Attenuation in CdTe Detectors*.
- Rolfs, Claus E, William S Rodney, and William S Rodney (1988). *Cauldrons in the cosmos: Nuclear astrophysics*. University of Chicago press.
- Rosmej, Olga N. et al. (2019). “Interaction of relativistically intense laser pulses with long-scale near critical plasmas for optimization of laser based sources of MeV electrons and gamma-rays”. In: *New Journal of Physics* 21.4, p. 043044.
- Rosmej, O N, A Blazevic, et al. (2005). “Charge state and stopping dynamics of fast heavy ions in dense matter”. In: *Physical Review A* 72.5, p. 052901.
- Rosmej, O N, S A Pikuz, et al. (2005). “Radiation dynamics of fast heavy ions interacting with matter”. In: *Laser and Particle Beams* 23.1, pp. 79–85.
- Rosmej, O N, N Suslov, et al. (2015). “The hydrodynamic and radiative properties of low-density foams heated by x-rays”. In: *Plasma Physics and Controlled Fusion* 57.9, p. 094001.
- Rosmej, Olga N (2016). *Experiment U305 X-Ray Spectroscopy*. Talk.
- Rzadkiewicz, J et al. (2010). “Interpretation of the Si K α x-ray spectra accompanying the stopping of swift Ca ions in low-density SiO₂ aerogel”. In: *Physical Review A* 82.1, p. 012703.
- Sayer, R O (1977). “Semi-empirical formulas for heavy-ion stripping data”. In: *Revue de physique appliquée* 12.10, pp. 1543–1546.
- Schoenberg, K et al. (2020). “High-energy-density-science capabilities at the Facility for Antiproton and Ion Research”. In: *Physics of Plasmas* 27, p. 043103.
- Schönlein, A et al. (2016). “Generation and characterization of warm dense matter isochorically heated by laser-induced relativistic electrons in a wire target”. In: *EPL (Europhysics Letters)* 114.4, p. 45002.
- Schroeder, Daniel J. (Sept. 27, 1999). *Astronomical Optics*. 2nd ed. Academic Press. 478 pp. ISBN: 978-0-12-629810-9. URL: <https://proquest.tech.safaribooksonline.de/book/electrical-engineering/optical-electronics/9780126298109/>

- firstchapter#X21udGVybmFsX0J2ZGVwRmxhc2hSZWFkZXI/eG1saWQ90Tc4MDEyNj%20I50DEwOS80MjY=.
- Seltzer, Stephen M and Martin J Berger (1985). “Bremsstrahlung spectra from electron interactions with screened atomic nuclei and orbital electrons”. In: *Nuclear Instruments and Methods in Physics Research Section B: Beam Interactions with Materials and Atoms* 12.1, pp. 95–134.
- Sigmund, P (2006). *Particle penetration and radiation effects, vol. 151 of Springer Series in Solid-State Sciences*.
- Skellam, John Gordon (1948). “A probability distribution derived from the binomial distribution by regarding the probability of success as variable between the sets of trials”. In: *Journal of the Royal Statistical Society. Series B (Methodological)* 10.2, pp. 257–261.
- Sternheimer, R M, S M Seltzer, and M J Berger (1982). “Density effect for the ionization loss of charged particles in various substances”. In: *Physical review B* 26.11, p. 6067.
- (1983). “Erratum: Density effect for the ionization loss of charged particles in various substances”. In: *Physical Review B* 27.11, p. 6971.
- Sternheimer, Rudolph M (1952). “The density effect for the ionization loss in various materials”. In: *Physical Review* 88.4, p. 851.
- Stöhlker, Th et al. (2015). “APPA at FAIR: From fundamental to applied research”. In: *Nuclear Instruments and Methods in Physics Research Section B: Beam Interactions with Materials and Atoms* 365, pp. 680–685.
- Sun, Guo-Zheng et al. (1987). “Self-focusing of short intense pulses in plasmas”. In: *The Physics of fluids* 30.2, pp. 526–532.
- Swinehart, D F (1962). “The beer-lambert law”. In: *Journal of chemical education* 39.7, p. 333.
- Tahir, N A, A Adonin, et al. (2005). “Studies of heavy ion-induced high-energy density states in matter at the GSI Darmstadt SIS-18 and future FAIR facility”. In: *Nuclear Instruments and Methods in Physics Research Section A: Accelerators, Spectrometers, Detectors and Associated Equipment* 544.1-2, pp. 16–26.
- Tahir, N A, C Deutsch, et al. (2005). “Proposal for the study of thermophysical properties of high-energy-density matter using current and future heavy-ion accelerator facilities at GSI Darmstadt”. In: *Physical review letters* 95.3, p. 035001.
- Tahir, N A, Th Stöhlker, et al. (2010). “Ultra-high compression of water using intense heavy ion beams: laboratory planetary physics”. In: *New Journal of Physics* 12.7, p. 073022.
- Tanaka, Kazuo A et al. (2005). “Calibration of imaging plate for high energy electron spectrometer”. In: *Review of scientific instruments* 76.1, p. 013507.
- Tauschwitz, Anna et al. (2006). “Laser-produced proton beams as a tool for equation-of-state studies of warm dense matter”. In: *High Energy Density Physics* 2.1-2, pp. 16–20.

- Tavoosli, Sahar (Nov. 22, 2019). “Influence of B-Field Inhomogeneity on Measurements of Relativistic Laser Accelerated Electrons Energy Distribution”. Master Thesis. Goethe University Frankfurt.
- Taylor, John R (1997). “Error analysis”. In: *Univ. Science Books, Sausalito, California*.
- Timischl, F (2015). “The contrast-to-noise ratio for image quality evaluation in scanning electron microscopy”. In: *Scanning* 37.1, pp. 54–62.
- Toncian, T et al. (2018). “Non-Maxwellian electron distributions resulting from direct laser acceleration in near-critical plasmas”. In: *Matter and Radiation at Extremes* 1.1, p. 82.
- Tsai, Yung-Su (1974). “Pair production and bremsstrahlung of charged leptons”. In: *Reviews of Modern Physics* 46.4, p. 815.
- Tsung, F et al. (2012). “CO₂ Laser acceleration of forward directed MeV proton beams in a gas target at critical plasma density”. In: *Journal of Plasma Physics* 78.4, pp. 373–382.
- Tzeng, K-C, W B Mori, and T Katsouleas (1999). “Self-trapped electron acceleration from the nonlinear interplay between Raman forward scattering, self-focusing, and hosing”. In: *Physics of Plasmas* 6.5, pp. 2105–2116.
- Valentine, John D et al. (1993). “Temperature dependence of CsI (Tl) gamma-ray excited scintillation characteristics”. In: *Nuclear Instruments and Methods in Physics Research Section A: Accelerators, Spectrometers, Detectors and Associated Equipment* 325.1-2, pp. 147–157.
- Van Langevelde, F et al. (1990). “Ellipsoid X-ray focussing for synchrotron-radiation microprobe analysis at the SRS, Daresbury, UK”. In: *Nuclear Instruments and Methods in Physics Research Section A: Accelerators, Spectrometers, Detectors and Associated Equipment* 292.3, pp. 719–727.
- Varentsov, D et al. (2008). “Transverse optical diagnostics for intense focused heavy ion beams”. In: *Contributions to Plasma Physics* 48.8, pp. 586–594.
- Vergunova, G A et al. (2013). “Mathematical modeling of gas-dynamic and radiative processes in experiments with the use of laser and heavy-ion beams”. In: *Plasma physics reports* 39.9, pp. 755–762.
- Verma, H R (2007). “X-ray fluorescence (XRF) and particle-induced X-ray emission (PIXE)”. In: *Atomic and Nuclear Analytical Methods: XRF, Mössbauer, XPS, NAA and B63Ion-Beam Spectroscopic Techniques*, pp. 1–90.
- Wagner, F et al. (2014). “Temporal contrast control at the PHELIX petawatt laser facility by means of tunable sub-picosecond optical parametric amplification”. In: *Applied Physics B* 116.2, pp. 429–435.
- Walker, P A et al. (2013). “Investigation of GeV-scale electron acceleration in a gas-filled capillary discharge waveguide”. In: *New Journal of Physics* 15.4, p. 045024.
- Wan, Y et al. (2019). “Two-stage laser acceleration of high quality protons using a tailored density plasma”. In: *Physical Review Accelerators and Beams* 22.2, p. 021301.

- Warczak, A et al. (1983). “K and L X-ray excitation in very-heavy-ion-atom collisions near KL level matching”. In: *Journal of Physics B: Atomic and Molecular Physics* 16.9, p. 1575.
- Watson, R L, J M Blackadar, and Vladimir Horvat (1999). “Projectile Z dependence of Cu K-shell vacancy production in 10-MeV/amu ion-solid collisions”. In: *Physical Review A* 60.4, p. 2959.
- Weick, H et al. (2002). “Energy-loss straggling of (200–1000) MeV/u uranium ions”. In: *Nuclear Instruments and Methods in Physics Research Section B: Beam Interactions with Materials and Atoms* 193.1-4, pp. 1–7.
- Welvaert, Marijke and Yves Rosseel (2013). “On the definition of signal-to-noise ratio and contrast-to-noise ratio for fMRI data”. In: *PloS one* 8.11, e77089.
- Wenz, Johannes et al. (2015). “Quantitative X-ray phase-contrast microtomography from a compact laser-driven betatron source”. In: *Nature communications* 6, p. 7568.
- Wharton, K B et al. (1998). “Experimental measurements of hot electrons generated by ultraintense ($>10^{19}$ W/cm²) laser-plasma interactions on solid-density targets”. In: *Physical Review Letters* 81.4, p. 822.
- Wiesemann, K (2014). “A short introduction to plasma physics”. In: *arXiv preprint arXiv:1404.0509*.
- Wilks, S C et al. (1992). “Absorption of ultra-intense laser pulses”. In: *Physical review letters* 69.9, p. 1383.
- Willingale, L, A V Arefiev, et al. (2018). “The unexpected role of evolving longitudinal electric fields in generating energetic electrons in relativistically transparent plasmas”. In: *New Journal of Physics* 20.9, p. 093024.
- Willingale, L, S P D Mangles, et al. (2006). “Collimated multi-MeV ion beams from high-intensity laser interactions with underdense plasma”. In: *Physical review letters* 96.24, p. 245002.
- Willingale, L, P M Nilson, et al. (2011). “High-power, kilojoule laser interactions with near-critical density plasma”. In: *Physics of Plasmas* 18.5, p. 056706.
- Willingale, L, A G R Thomas, et al. (2013). “Surface waves and electron acceleration from high-power, kilojoule-class laser interactions with underdense plasma”. In: *New Journal of Physics* 15.2, p. 025023.
- Wollersheim, Hans-Jürgen (2011). “Relativistic Coulomb Excitation: From Rising to PreSPEC.” In: *Acta Physica Polonica B* 42.
- Young, M (1971). “Pinhole optics”. In: *Applied Optics* 10.12, pp. 2763–2767.
- Young, Matt (1989). “The pinhole camera: Imaging without lenses or mirrors”. In: *The Physics Teacher* 27.9, pp. 648–655.
- Zähler, Sero et al. (2017). *High energy resolution spectroscopy of the target and projectile X-ray-fluorescence*. Research rep. GSI Helmholtz Centre for Heavy-Ion Research GmbH.
- Zastrau, U et al. (2012). “Focal aberrations of large-aperture HOPG von-Hamos x-ray spectrometers”. In: *Journal of Instrumentation* 7.09, P09015.

Acknowledgements

Last but not least, I would like to thank so many people for a variety of things that have influenced my life in ways I am aware of but they might not have perceived. Unfortunately, the space is limited so I have to restrain myself.

I would like to thank (in no specific order other than loosely alphabetical)...

- Alexander Engeda and Alexander Müller-Münster for showing me how to connect to people on a whole new level.
- Alexander Pukhov and Sergey Rykovanov for discussions involving the direct laser acceleration mechanism.
- Andre Michel for showing me how to dress as a pirate...
- and Bernhard Bohlender for teaching me the scoundrel fun of it.
- Andreas Schönlein for showing me that sacrificing your own security can have a huge impact on not only your own life but also the lives of people around you.
- Astrid Hergt who is the heart and soul of the plasma physics working group in Frankfurt.
- Claire-Anne Reidel, Elena Hartmann, Francesca Luoni, Marius Dehmer, Markus Baschke, Monika Hölscher-Brinkmann and Sophia Böhm for holding me responsible for finishing this whole damn thing.
- Dimitri Khaghani for seeing things in me that I didn't see.
- Dylan Ćetković for stepping into the tension of reading this giant mountain of paper with care.
- Emma Ford, Gerhard Burau, Henner Büsching, Mike Rawlins and the HGS-HIRE-Team for showing me how to find my path without despair.
- Joachim Jacoby for giving me the chance to tread this path by inviting me into the plasma physics working group in Frankfurt.
- Jochen Wieser for discussions involving the construction of a self-made X-ray tube.
- Jörg Schreiber und Malte Kaluza for discussions involving electron diagnostics.
- Julia Höhler for trusting me without question.

- Kristina Zerbe for kicking me to take responsibility for myself when my life went from order to chaos.
- Leonardo Krivic for kicking me to start doing sports again. . .
- Dennis Ammon for holding me accountable for keeping up doing it. . .
- and Mario Sauer for providing me with the environment where I learned to have fun with it again.
- Marcus Iberler for providing the great working atmosphere I enjoyed over the years in the plasma physics group in Frankfurt.
- Nikolai Andreev for discussions involving the simulations for the laser experiments.
- Olga Rosmej for expecting more from me than I would grant myself to be capable of and therefore starting to become the best version of myself.
- Paul Neumayer for discussions involving imaging techniques.
- the PHELIX- and UNILAC-teams without whom this work would have been impossible.
- Philipp Beloiu for showing me how to begin a tradition.
- Tanja Lucas who accompanied me on a significant part of my journey and influenced me more than most other people I know.
- Tim Rienecker for being a paragon in mastering beamtimes with fun.
- Vincent Bagnoud for having faith in my abilities, being patient and paving the way for new challenges for me even before I finished this work.
- Daniel Gesell, Mikhail Gyrdymov, Nadiya Zahn, Parysatis Tavana and Sahar Tavoosli whose own works got intermingled with mine.
- all the colleagues from Darmstadt, Frankfurt, Frascati, Jena and Moscow with whom I had great experiences in our collaboration and working group over the years.
- all my friends that make my life to be a lot of fun.
- my family for everything that allowed me to start this journey in the first place.

Şero Jakob Zähler

Curriculum Vitae

Personal Information

Date of Birth 27.07.1987
Place of Birth Frankfurt am Main

Academic Studies

- since 2016 **Doctoral Studies**, *Goethe University*, Frankfurt, Title: *Development of FAIR-Relevant X-Ray Diagnostics Based on the Interaction of Lasers and Particle Beams with Matter*.
Supervisor: Apl. Prof. Dr. Olga Rosmej, Reviewers: Apl. Prof. Dr. Olga Rosmej, Prof. Dr. Joachim Jacoby
- 2013 – 2016 **Master Studies**, *Goethe University*, Frankfurt, Title: *Aufbau und Charakterisierung eines Detektors zur Untersuchung der Wechselwirkung niederenergetischer Ionenstrahlen mit einem Gastarget*.
Supervisor: Behrooz Fathinejad, Reviewers: Dr. Marcus Iberler, Prof. Dr. Joachim Jacoby
- 2008 – 2013 **Bachelor Studies**, *Goethe University*, Frankfurt, Title: *Aufbau und Kalibrierung eines Vakuum-Ultraviolett-Spektrometers*.
Supervisor: Andreas Schönlein, Reviewers: Dr. Marcus Iberler, Prof. Dr. Joachim Jacoby

Civilian Service

2007 – 2008 **Civilian Service**, *ZSP Hochtaunus - Klinik Bamberger Hof*, Frankfurt am Main.

Education

2004 – 2007 **High School**, *Ernst-Reuter-Schule I*, Frankfurt am Main.
1998 – 2004 **Secondary School**, *Ernst-Reuter-Schule II*, Frankfurt am Main.
1993 – 1998 **Primary School**, *Holzhausenschule*, Frankfurt am Main.

Publications

- 2019 ROSMEJ, O. N., et al. Interaction of relativistically intense laser pulses with long-scale near critical plasmas for optimization of laser based sources of MeV electrons and gamma-rays. *New Journal of Physics* 21 (2019) 043044
- 2018 ROSMEJ, O. N., et al. Generation of keV hot near-solid density plasma states at high contrast laser-matter interaction. *Physics of Plasmas* 25 (2018) 083103
- 2015 ROSMEJ, O. N., et al. The hydrodynamic and radiative properties of low-density foams heated by x-rays. *Plasma Physics and Controlled Fusion* 57 (2015) 094001

Reports

- 2018 ZAHN, N., et al. Application of a TLD-based ten channel system for the spectrometry of bremsstrahlung generated by laser-matter interaction. *GSI Scientific Report 2017* (2018) 242.
- ZÄHTER, S., et al. Optimization of laser based sources of electrons and gammas for backlighting of high areal density targets at FAIR. *Annual Report HI Jena and GSI Scientific Report 2017* (2018) 243.
- 2017 CISTAKOV, K. et al. Investigation on the theta pinch plasma as application for an ion stripper for FAIR. *GSI Scientific Report 2016* (2017) 292.
- ZÄHTER, S., et al. High energy resolution spectroscopy of the target and projectile X-ray-fluorescence. *GSI Scientific Report 2016* (2017) 296.
- ZÄHTER, S., et al. Generation of keV hot near solid density plasma at high contrast laser-matter-interaction. *Annual Report HI Jena and GSI Scientific Report 2016* (2017) 288.
- 2015 XU, G., et al. Beam transmission for inductively coupled plasma stripper. *GSI Scientific Report 2014* (2015) 290.
- XU, G., et al. Beam transmission for a plasma stripper device. *High Energy Density Generated by Heavy Ion and Laser Beams* (2015) 17.
- MAEDER, R., et al. Measurements of the Heavy Ion Stopping in X-ray heated low-density nanostructured targets. *High Energy Density Generated by Heavy Ion and Laser Beams* (2015) 24.
- 2013 MARTSOVENKO, D., et al. Comparison of measured time resolved hohlraum radiation temperature with data produced by RALEF II-Code. *GSI Scientific Report 2012* (2013) 338.